FACULTEIT WETENSCHAPPEN

Vakgroep fysica en sterrenkunde

THE PANCHROMATIC INTERPLAY BETWEEN STARLIGHT AND DUST IN ANDROMEDA AND THE LOCAL UNIVERSE

Sébastien Viaene

Dissertation for the degree of Doctor of Science: Astronomy

Supervisors: Prof. Dr. Maarten Baes and Prof. Dr. Jacopo Fritz

Supervisors:

Prof. Dr. Maarten Baes
Vakgroep fysica & sterrenkunde
Universiteit Gent

Prof. Dr. Jacopo Fritz
Instituto de Radioastronomía y Astrofísica
Universidad Nacional Autónomia de México

Jury members:

Prof. Dr. Jan Ryckebusch (President)
Vakgroep fysica & sterrenkunde
Universiteit Gent

Prof. Dr. Sven De Rijcke (Secretary)
Vakgroep fysica & sterrenkunde
Universiteit Gent

Prof. Dr. Herwig Dejonghe
Vakgroep fysica & sterrenkunde
Universiteit Gent

Prof. Dr. Gianfranco Gentile
Vakgroep fysica & sterrenkunde – Universiteit Gent
Vakgroep fysica – Vrije Universiteit Brussel

Prof. Dr. Haley Gomez
School of physics and astronomy
Cardiff University

Dr. Bart Vandenbussche
Afdeling Sterrenkunde
KU Leuven

Acknowledgements

Astronomy is like a sport. You need a coach, a team you can trust, and lots of supporters on the side. I was lucky to have all of that during my years as a PhD student. At the beginning of this dissertation, I wish to express my sincere gratitude to all of them.

This investigation was conceived by my two wonderful supervisors Maarten Baes and Jacopo Fritz. To them I am deeply grateful. They were always there for me with advise or a joke to put things in perspective. Thanks to their thrust, I was able to develop myself as a scientist. Thanks to their generosity, I could meet many interesting people and see the world of astronomy. To Jacopo in particular, I want to say thank you for the close guidance in my first years and the Skype-guidance beyond that. To Maarten I just want to say you couldn't have been a better supervisor and I hope you continue to do that for many more starting astronomers.

I also want to thank the members of my jury, for reading through my first submission and helping me to make this a solid and consistent work. Hopefully, you enjoyed process and the end result. I certainly gained new insights from the stimulating discussions in the past month.

Astronomy is not possible without a capable team and a good atmosphere in the office. So a big shoutout to eveyone I've shared an office with in the past years: Bert, Gert, Ilse, Jacopo, Peter, and also my current office mates: Pieter and Aleksandr. One by one I thank you for the fun times and the times you endured my whining. But of course, we are part of a bigger group. A great team full of brilliant people: Steven, Flor, Gianfranco, Marjorie, Sam, Christian, Robbert, Sven. I enjoyed the countless lunches, ping-pong sessions and coffee breaks so much that working at S9 was far better than working at home. I also want to stress my gratitude towards the supporting staff: Inge, Gerbrand, Guy. Without you I would still be working on my first draft.

Outside the Ghent astronomy group, I also received a lot of support from the people in Tartu Observatory. In particular from Antti and Elmo, it was a pleasure to work with other Andromeda fanatics. I will never forget the cold, cosy and fun few months I spend in Estonia. The list of other colleagues and collaborators is long and I am grateful to all my co-authors for the elaborate feedback and good conference moments. I wish to especially thank the people from the former HeViCS team and from DustPedia, I am proud to be part of your team.

Astronomy is also not possible when you do it 24/7. I feel lucky because I was able to keep the balance and spend a lot of time with my friends. To my old fysicasa comrades: thank you for your support and interest in my work, but also for all the good times we had so far in Ghent and beyond. The same goes for the wonderful people from Wunder, whom I don't see as much as I would like to. However, every time we meet is good fun and I hope we can extrapolate these moments as far as possible.

It almost goes without saying, but some special people definitely need to be mentioned here. Mom and dad, brother and sister. You are the best. You are the main reason I succeeded in my studies and you know you have my eternal gratitude. A big thank you as well to all my family members and soon-to-be family. I always look forward to the next meetup and enjoy the moments you ask about my work or about deep astronomy questions in general.

And then finally, and deeply, I want to thank my lady, my daily go-to support, my best friend and my wife-to-be. She's the one that shared all the highs and lows of a PhD study. She keeps my feet on the ground or lifts my spirit if needed. It's astonishing how much energy she used to help me during these four years. Elina, I can't thank you enough, you are truly, purely amazing.

Sébastien

Contents

List of Figures

List of Tables

Part I

Introduction

Galaxies, stars and dust

1

In the beginning there was nothing, which exploded.

Terry Pratchett

1.1 The Local Universe

Galaxies. Mysterious nebulous objects in space, colourful and diverse. But what are they? What is the reason for their variety in shape and appearance? An observer on Earth can only see a handful of galaxies with the naked eye: Andromeda, the Magellanic clouds, and of course the Milky Way, the galaxy in which we live. However, there are many more. The systems mentioned above reside in the Local Group, within 1 Mpc (mega-parsec, $\sim 10^{22}$ m). It hosts about 50 galaxies, most of them small. If we go out to 10 Mpc, which defines the Local Volume, over 500 galaxies can be found (Koribalski & Jerjen 2008). In a sphere of 100 Mpc around the Sun, which we consider here as the border of the 'Local Universe', over 70 000[1] galaxies are found. Many of these can be imaged using decent ground-based optical telescopes. But it is only with professional large telescopes on Earth and space telescopes, that their true detail can be exposed. Especially if one is interested in their appearance across the electromagnetic spectrum.

1.1.1 Building a galaxy

Each galaxy is made up of several basic components: gas, stars, dust and dark matter (see Fig. 1.1). Gas (helium and hydrogen) contributes most to the baryonic mass and can naively be considered as the fuel of a galaxy. It comes in multiple phases depending on the local environment. At the lowest densities, most of the gas is in a hot phase, where temperatures can reach 10^7 K. In the warm neutral and warm ionized medium, typical temperatures lie around

[1] NASA Extragalactic Database. http://ned.ipac.caltech.edu

8 000 K. When the gas cools down it gets denser and becomes part of the cold neutral medium ($\sim$ 80 K). At even higher densities, and temperatures around 10 K, there is a transition to the molecular (H_2) phase.

The next component are the stars. which are the main source of radiation in galaxies. They are formed from the gas and convert it into heavier elements (metals) through nuclear fusion. Stars dominate the ultra-violet (UV), optical and near-infrared (NIR) regime. The wavelength regime where the emission of a star peaks depends on its mass, age and fraction of heavier elements (metallicity). High-mass stars ($\gtrsim 10\,M_\odot$) are short-lived and radiate most of their energy in the UV. Low-mass ($\lesssim 0.8\,M_\odot$) stars are brightest in the NIR, while stars of intermediate mass (like our Sun) dominate the optical spectrum. Stellar age and metallicity have a similar effect on a population of stars. The younger or more metal-poor the stellar population is, the bluer its colour will be, i.e. it will be relatively more luminous at shorter wavelengths. Vice versa, old or metal-rich stellar populations are usually redder, i.e. their emission is more luminous at longer wavelengths.

The third building block, and most important for this investigation, is dust. Dust is a mix of sub-micrometer sized grains mainly made of silicates and carbon. It constitutes only a small fraction of the total galaxy mass, but can be found almost everywhere in a galaxy. Dust can be traced indirectly through its extinction of background UV/optical/NIR light, and directly, through its emission in the mid-infrared(MIR), far-infrared (FIR) and sub-millimeter (submm) regime.

The most massive component in galaxies is not considered here: dark matter. To this date, dark matter has not been detected, but there are several indications of its presence. Dark matter is thought to only interact with baryonic matter through the gravitational force. Therefore, it can not be detected in any regime of the electromagnetic spectrum. Fortunately, this is also the reason we can 'ignore' its presence when studying the interaction of dust and starlight.

1.1.2 Galaxy classification

Depending on the relative proportions of the above components, all galaxies differ from each other. Not a single galaxy is the same as they all have a unique mix, but there are several ways to group them; by shape, size, or other properties. The common approach to classify large galaxies is in the Hubble diagram following Hubble (1936). An example of such a classification is shown in Fig. 1.2. In this tuning-fork diagram, galaxies are classified as early-type (left) or late-type (right). Early-type galaxies (ETGs) range from purely round (E0), to very elliptical shapes (E7), with no distinct features. Late-type galaxies (LTGs) have spiral arms. They are discriminated by having a bar or a regular bulge in the center, forming the two arms of the tuning fork. They can be further subdivided, from bulge-dominated (Sa,SBa) towards disk-dominated (Sd, SBd) spiral galaxies. In the middle between ETGs and LTGs are the lenticular galaxies. They have a

Figure 1.1: A partial view of the Milky Way in optical and infrared filters. The blue and yellow light comes from stars in our galaxy. They are partially obscured by the dark dust features. Clouds of ionized gas are shown in red. What is invisible in this picture is the neutral gas, which emits mostly at radio wavelengths, and the dominating presence of dark matter.
Image courtesy: Greg Bradley

clear disk, but no sign of spiral arms. Several galaxies do not fall within this diagram because of their irregular shape. This is often caused by a past or ongoing interaction with another galaxy. They are labelled as peculiar galaxies (Pec) or irregular galaxies (Irr). An important class of galaxies is not included in the Hubble diagram: dwarf galaxies. These objects are typically an order of magnitude smaller (in diameter as well as number of stars) than the typical 'large' galaxies. Like their bigger counterparts, dwarf galaxies can have several morphologies (elliptical, spheroidal, spiral, irregular,...). In this work, we do not consider dwarf galaxies and focus on normal, 'large' galaxies.

The above classification is purely based on the optical morphology of the galaxies. Another way is to discriminate on the basic kinematics of the stars inside the galaxies. There are two main types of motions for stars within a galaxy: organized and random. Organized motion is known in the form of rotation. These galaxies are usually disk-dominated. A galaxy dominated by random motion in the stellar component will not have a coherent rotation and will be a bulge-dominated system. The ATLAS^{3D} consortium proposed a classification based on fast and slowly rotating galaxies (Cappellari et al. 2011). In the fast-rotating subgroup, a separation can be made by level of spiral structure (see Fig. 1.3). This ranges from fast-rotating, but bulge-dominated systems (analogous to lenticular galaxies) to fast-rotating spiral galaxies, with an intermediate stage called *anaemic* spirals. The kinematic classification mechanism can be naturally extended towards dwarf galaxies. It can thus give a more complete classification of the galaxy population.

Classifying galaxies according to different schemes not only underlines their diversity, it also provides insights into the evolution of the general population. The current understanding of

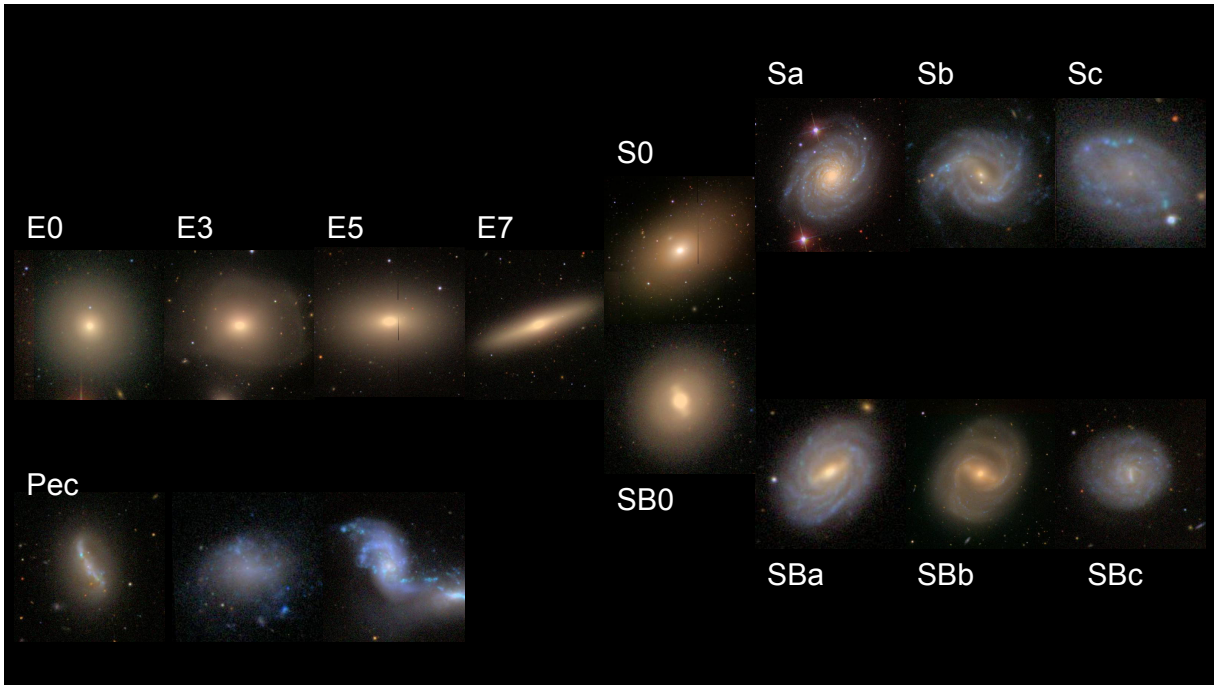

Figure 1.2: A Hubble tuning-fork classification with a selection of galaxies from the Herschel Reference Survey (HRS, Boselli et al. 2010b). The images are synthetic RGB images made from SDSS observations. Morphological classifications range from elliptical (E) over lenticular (S0, SB0) to spiral (S, SB) with the 'B' indicating a bar in the center. In the lower left corner, a few examples of peculiar morphologies are shown.

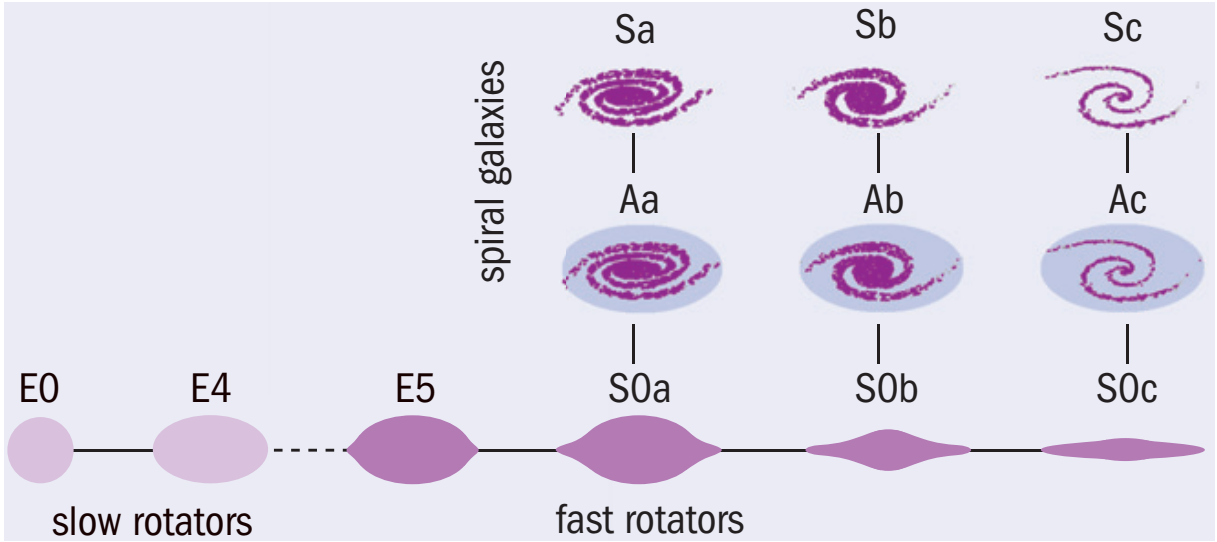

Figure 1.3: The ATLAS^{3D} 'comb' classification scheme. Galaxies are divided into fast and slow rotators based on their stellar kinematics. The fast rotators are then further split according to their spiral structure into spiral (S), anaemic (A) and lenticular (S0) galaxies. *Image Courtesy: The ATLAS^{3D} team.*

galaxy evolution is one of star formation and merging. Proto-galaxies in the early universe are thought to be gravitationally bound clouds of gas. Stars convert this gas into heavier elements through nuclear fusion. They are consequently viewed as the cosmic factories that drive galaxy evolution. From these heavier elements, dust is formed. A young galaxy will thus form stars, placing itself on the right side of the Hubble sequence (confusingly labelled late-type galaxy). The gravitational collapse of gas-rich proto-galaxies into disks causes them to start rotating due to the conservation of angular momentum. This rotation, combined with the feedback of star formation, leads to the observed structure in spiral galaxies.

Major and minor mergers between galaxies are also an important ingredient of galaxy evolution. The early universe was significantly more dense than today so galaxies lived closer together. Consequently, the chance of galaxy interactions was much higher. Mergers or interactions have the potential to stir up, or shut down star formation. They can also disrupt the galactic disks, or disturb the rotation pattern. These violent events will speed up the evolution of disk galaxies towards bulge-dominated systems. Galaxy merging happens more often in denser regions such as in the universe, or in present day clusters of galaxies. In these clusters, we see more ETGs in the center, and LTGs in the outskirts, where they are still moving towards the core.

The present universe has passed its most violent phases of galaxy evolution. Madau & Dickinson (2014) recently reviewed the star formation history of the observable universe, and confirmed that the universe was most active around redshifts 2-3. This is in line with the observation that the universe was more dusty in the past (Dunne et al. 2011; Rowlands et al. 2014). Due to the expansion of the universe, galaxies keep moving away from each other, decreasing the overall chance of interactions. In groups and clusters, however, the density of galaxies is still high enough for these events to occur. In the Local Universe, the situation is rather calm now. Most local galaxies are forming stars at a moderate pace, or have stopped doing so altogether. Extreme objects, such as galaxies with strong bursts of star formation or with active galactic nuclei (AGN) are less common. It is thus certainly worthwhile to study 'normal', star forming galaxies in the Local Universe. Precisely because they are the most common objects among the large galaxies.

1.2 Star formation

The cycle of star formation starts and ends in the interstellar medium (ISM, see Fig. 1.4). The ISM harbours a rich mixture of matter that interacts through multiple chemodynamical processes. Hydrogen is by far the most abundant element and occurs primarily in its neutral form, varying from warm ($\sim$ 8 000 K) to cold gas ($\sim$ 80 K). In the very cold and dense environments, it is converted into molecular hydrogen (H_2). In local galaxies, the gas has been enriched by star formation throughout the life of the galaxy. There is consequently a small, percentage-

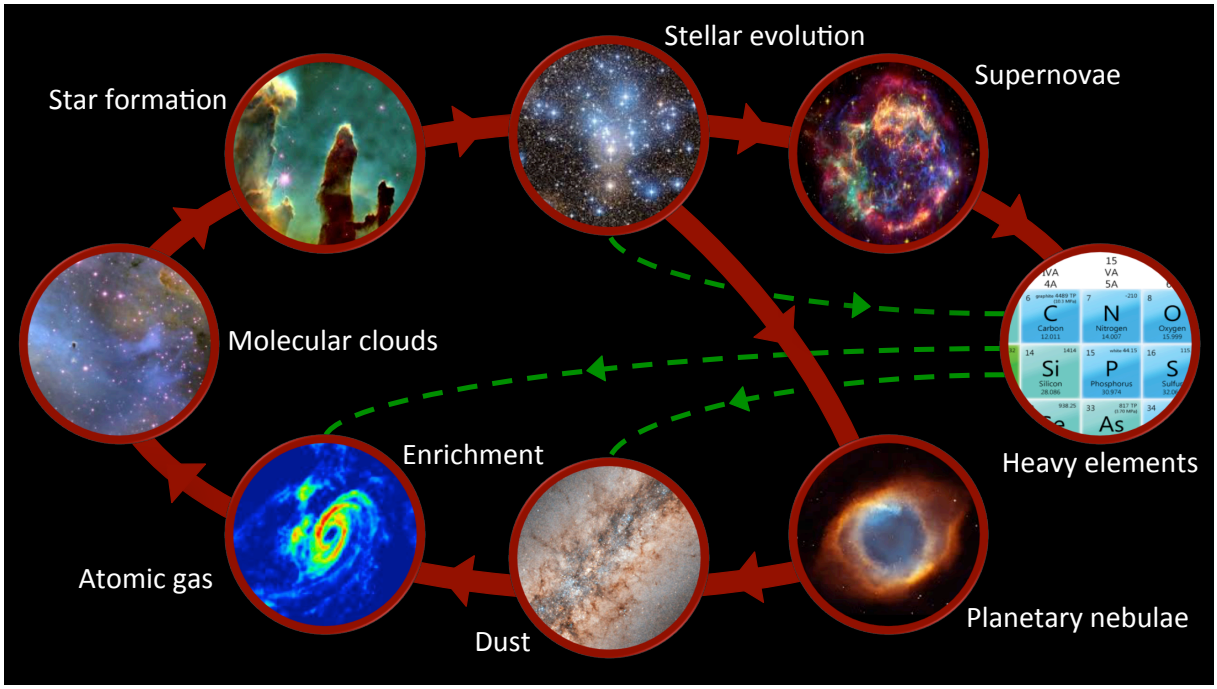

Figure 1.4: The cycle of matter processing in the ISM. Atomic gas is converted into molecular gas and starts forming stars. The stars evolve and explode to produce heavy elements, or they die out and produce dust. Metals can coagulate and form dust grains as well. Dust and metals enrich the gas and catalyse the formation of molecular clouds.

level, fraction of metals in the gas. The most abundant metals are oxygen and carbon. They act as important coolants for the gas, and allow it to become even more dense. At some point, molecular gas clouds will collapse under their own gravity and form stars.

The process of star formation is understood up to a certain resolution. There are several open questions such as how the cloud collapse takes place, how cooling in this phase works, and what the roles are of turbulence and magnetic fields. However, for the global picture of star formation in galaxies, the qualitative description given above (and summarized in Fig. 1.4) is sufficient. Star formation only occurs when sufficient dense gas is present in the galaxy. The Kennicutt-Schmidt law (Schmidt 1959; Kennicutt 1998) describes how much star formation is to be expected from a quantity of gas surface density. Beside the fuel content, the level of star formation will depend on the efficiency to form stars. Several events may trigger star formation: mergers, tidal interactions, supernova shock waves,... The key ingredients are shocks that propagate through the interstellar medium and compress the gas beyond the limit of gravitational collapse.

The number of newly formed stars follows an initial mass function (IMF). This function describes how many stars of a certain mass are formed when a stellar population is born. Depending on galaxy and environment, IMFs can vary from top-heavy (many high-mass stars are formed) to bottom-heavy (more low-mass stars are formed). The most popular IMF models

are those proposed by Salpeter (1955), Kroupa (2001), and Chabrier (2003). Throughout this investigation, we make use of the Chabrier (2003) IMF, which is similar to the Kroupa (2001) IMF. Both functions are more top-heavy compared to the Salpeter (1955) IMF.

Star formation has several important consequences for a galaxy. One of them is the production of dust, which we will discuss at length in the next section. Another consequence is the fact that gas is consumed and party converted into electromagnetic radiation. This produces feedback on the environment. The radiation of young stellar populations is mostly in the UV. Photons with wavelength below $\sim 0.1\,\mu$m can ionize neutral hydrogen atoms. The presence of ionized hydrogen (HII) increases as new, massive stars irradiate the neutral gas. Recombination emission of this ionized gas can serve as an indirect tracer of star formation. Young, high-mass stars die in violent supernova explosions and cause a second form of feedback: shocks. They may trigger new star formation when they compress the matter in the ISM. Supernovae also enrich the ambient gas again with heavy elements, which makes it easier to cool the gas. After about 10 Myr after the birth of a stellar population, the radiation of the stellar population is dominated by heavy stars that are below the ionizing limit. However, they still produce strong UV radiation which heats their environment. As time goes by, the stars of intermediate and (eventually) solar mass will dominate the radiation field. These stars radiate most of their energy in the optical and NIR regime. Their combined radiation field will act as a second heating mechanism for the ISM.

Star formation is thus a vital process for the evolution of a galaxy from a giant gas reservoir to a chemically rich, multiphase environment. Needless to say, it will have important consequences on the appearance and properties of a galaxy, and in particular on our research topic: the influence of starlight and dust on each other.

1.3 Dust in galaxies

1.3.1 Production and destruction

As already mentioned in the previous section, dust is an important by-product of star formation. The exact process of dust production is, however, still not clear. Several mechanisms are proposed, but all fall short, individually, to explain the amount of dust we observe (e.g. Tielens et al. 2005; Gomez & Matsuura 2012; Rowlands et al. 2014). Therefore, a combination of several mechanisms is likely.

A first option is direct production in evolved stars (e.g. Morgan & Edmunds 2003; Gail et al. 2009; Ladjal et al. 2010; Rowlands et al. 2014). When low and intermediate mass stars approach the end of their lifetime, their atmospheres are cool and enriched with heavier elements. These are environments suitable to lock metals into dust grains. A second option for dust production

is more violent and happens during supernovae explosions (e.g. Todini & Ferrara 2001; Gomez et al. 2012; Matsuura et al. 2015). These energetic events expel a large amount matter into the ISM, including many heavy elements that can be converted into dust grains. A third form of dust production is more indirect. Star formation enriches the ISM with heavy elements due to stellar winds and supernovae. The ISM is a turbulent environment, so these elements can collide and stick to form molecules and small grains. Grain coagulation can then further grow dust grains to larger sizes (e.g. Ossenkopf 1993; Stepnik et al. 2003; Ormel et al. 2009; Hirashita & Kuo 2011; Köhler et al. 2012).

Galaxies with little star formation (ETGs) usually do not hold a lot of dust, or are even devoid of dust. For example, Smith et al. (2012d) only detected dust in 24% of elliptical galaxies. This leads to the conclusion that dust must be destroyed somehow (for a review, see Jones 2004). Indeed, the ISM can be a hostile environment. Dust grains are bombarded with cosmic rays, atoms, ions and electrons that fly through the ISM. This process is often referred to as sputtering (see e.g. Jones 2004; Serra Díaz-Cano & Jones 2008; Bocchio et al. 2012, 2014). Shocks can further aggravate these violent collisions, shattering the dust grains instead of coagulating them. Eventually, dust grains get destroyed over a time scale of a few Myr, depending on the environment (see e.g. Jones 2004; Bocchio et al. 2014). The fact that dust is still so abundant and visible in all active galaxies is actually a clear case for its efficient production, or less efficient dust destruction.

1.3.2 Dust grain types

The different dust production mechanisms occur each in their suitable environment. Other mechanisms process (and destroy) existing dust grains. It is thus not surprising that a variety of grains are present in the ISM. A first type of dust, at the smallest end of the scale, are actually just metals. In astrophysics, metals are essentially all atoms and ions of elements heavier than helium. The most abundant metals that can get locked into dust grains are oxygen, carbon, iron, nitrogen, silicon and magnesium. Metals themselves are not able to reprocess the continuum of starlight because they are small and have discrete energy levels. They are more likely to be collisionally excited by the abundant hydrogen and helium atoms. By radiating this collisional energy away, they act as coolants for the gas in the ISM.

A second type of dust is the family of aromatic molecules labelled PAHs. They are the smallest class among the actual dust grains (i.e. those who can reprocess continuum radiation). PAHs in the strict chemical sense are Polycyclic Aromatic Hydrocarbons, a suite of large molecules consisting mainly out of carbon and hydrogen atoms. These molecules were long thought to be the only aromatic molecules responsible for the MIR line emission. However, recent studies (Kwok & Zhang 2011, 2013; Jones et al. 2013) paved the way for other aromatic molecules as well. In the astrophysical context, the term ‘PAH’ has become an umbrella for several classes

of aromatic molecules.

As a third type of dust, there are also small grains that do not hold aromatic features. They consist mainly out of amorphous carbon and are about 1-20 nm in size. Small grains and PAHs will react heavily on the absorption of UV photons. A single photon can be energetic enough to catapult the small grain to an excited state far higher than its surroundings. These grains are therefore not in local thermal equilibrium. This process is called stochastic heating, and is difficult to model accurately (Camps & Baes 2015). We further discuss the modelling of PAHs and small grains in Sect. 1.5. The main observational consequence of such heating, are the peaks of emission in the MIR (see also Smith et al. 2007; Tielens 2008).

The last broad class of dust are any larger grains. Small grains can coagulate and grow in the ISM, becoming more efficient at absorbing radiation from the UV to the NIR. Stochastic events can no longer suddenly heat them to temperatures above the local thermal equilibrium. The grains can be carbonaceous or silicic in nature, and have size distributions peaking around 200 nm according to the most popular dust models (e.g. Zubko et al. 2004; Draine & Li 2007; Jones et al. 2013). The largest silicates can be doped with iron atoms, and can even have a mantle of ice or small carbon grains around them. These little additions dramatically change their scattering and absorption properties. It is therefore difficult to investigate exactly how they are composed, or even what they are composed of.

Another unknown, aside for the chemical composition, is the shape of dust grains. Modelling dust grains is a tedious task, and is often simplified by assuming spherical or spheroidal grains. It is unclear whether dust grains are actually spheroidal, especially the smaller ones. In fact, dust grains may be amorphous or 'fluffy' due to various radiative and collisional processes. Such hypotheses are hard to test because samples of cosmic dust are limited to the neighbourhood of the Earth. Fig. 1.5 shows two dust grains found on Earth, but of extraterrestrial origin. The left image shows a smooth and almost spherical dust grain of a few μm in diameter. Such a size is rather large, but the shape corresponds roughly to the assumptions made in theoretical dust models. This grain is thought to be pre-solar (Clayton & Nittler 2004). Similar grains could be present in the ISM, albeit of smaller size due to the less favourable environment for grain growth. An example of interplanetary dust is shown in the right image of Fig. 1.5. It is rather porous or fluffy, and again much larger ($>$ 1 micron) than dust models predict for ISM dust. This grain seems to be a loose aggregate of smaller, sub-μm sized particles. It is possible that these are the kind of dust grains that can be expected in the ISM. It is near impossible to collect grains of interstellar origin on Earth, which limits interstellar dust models to assumption-based models. On top of that, the ISM can differ significantly from galaxy to galaxy and even within a single galaxy. It is thus far from certain that a dust model that works in one location is applicable for all local galaxies. This is an important caveat, which one must be aware of when investigating dust in the Local Universe.

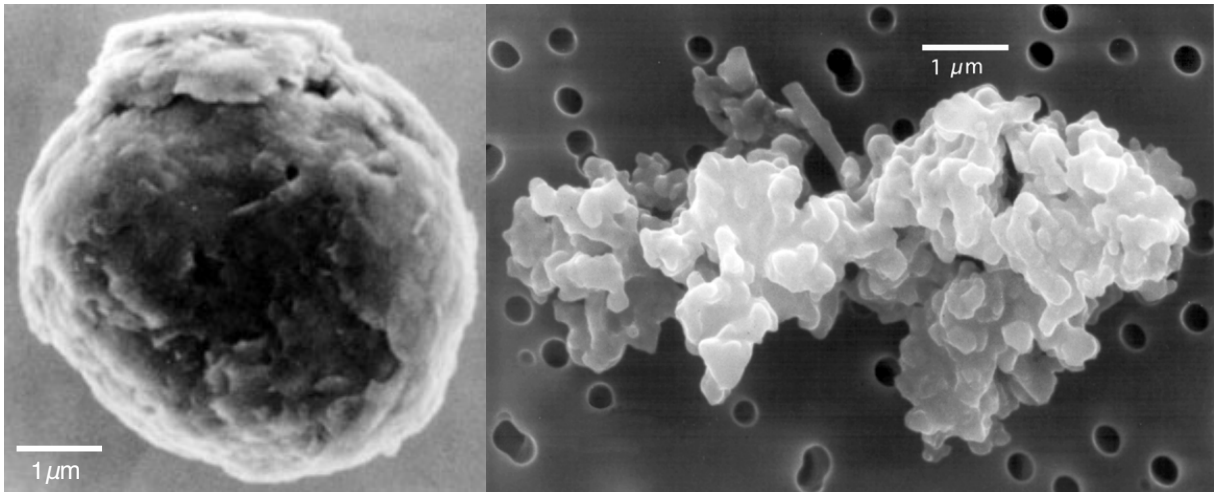

Figure 1.5: Two examples of dust grains from electron microscope scans. Left: A smooth and spherical graphite grain from the Murchison meteorite of which the origin is thought to be pre-solar (Clayton & Nittler 2004). *Image courtesy: S. Amari.* Right: Porous chondrite interplanetary dust particle collected from Earth's stratosphere. This is a loose aggregate of sub-μm-sized grains. *Image courtesy: D. E. Brownlee and E. Jessberger.*

1.3.3 Effects of dust in a galaxy

The effects of dust in a galaxy are immense and vital for the galaxy's evolution. We already mentioned the absorption and scattering that occurs when short-wavelength photons interact with dust grains. This is the major effect dust has on the visible image of galaxies, since it attenuates roughly one third of the starlight (Popescu et al. 2002; Skibba et al. 2011). Scattering also causes polarisation, which in turn hides (or encrypts) information from the stellar and AGN components in a galaxy (see e.g. Zubko & Laor 2000; Draine 2003b; Goosmann & Gaskell 2007, and references therein). In general, if one considers a line of sight from observer to a galaxy, several processes will alter the observed intensity of a source of radiation. First, there is direct emission that is unblocked by dust. In the presence of dust, the radiation from the source can be absorbed or scattered out of the line of sight. Conversely, radiation from other directions can be scattered into the line-of-sight, towards the observer.

For an observer, the amount of radiation that is lost due to dust is referred to as extinction. This only includes absorption and scattering out of the line-of-sight. The extinction efficiency is an intrinsic property of the dust composition. Grain-specific properties such as the absorption coefficient and the scattering albedo contribute to the probability of an incoming photon to be absorbed or scattered. Extinction is often measured by comparing nearby stars with those of the same spectral type, but further away. Unfortunately, this is only possible for the most nearby galaxies. An extinction curve shows the variation of extinction with wavelength (see Fig. 1.6). It is usually characterized by strong extinction in the UV domain, and lower in the NIR. Extinction curves from different lines-of-sight or different galaxies are usually not the

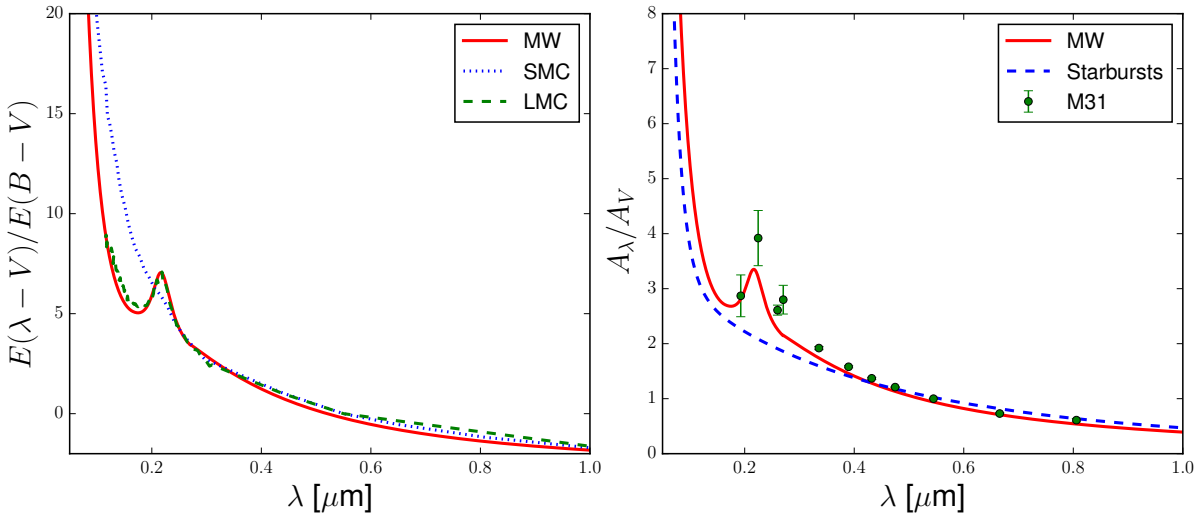

Figure 1.6: Examples of extinction and attenuation curves. Left: Wavelength-dependent extinction relative to extinction in the B-V colour for the SMC (bar region) and LMC (average) from Gordon et al. (2003), and the average Milky Way model from Fitzpatrick & Massa (2007). Right: Attenuation relative to the *V* band from the same model of Fitzpatrick & Massa (2007) for the Milky Way, for semi-empirical measurements for M31 (Dong et al. 2014), and a sample of starburst galaxies (Calzetti et al. 1994).

same. They may differ in global slope or in smaller features (Gordon et al. 2003; Fitzpatrick & Massa 2007; Wild et al. 2011; Battisti et al. 2016). This is one of the strongest proofs that dust is not the same across the Local Universe.

The difference between the emitted radiation, and the observed radiation is then called attenuation. This consists of extinction, which is an inherent property of the dust. But it also includes scattering into the line of sight, and unblocked stellar light that radiates towards the observer. Note that the latter can also originate from sources in front of the dust. Attenuation should thus be seen as a convolution of extinction and the relative geometry of dust and stellar sources. Attenuation is much more difficult to measure than extinction since it requires information on the intrinsic emission sources. A certain distribution of dust along the line of sight must be assumed to convert an extinction curve to an attenuation curve. Alternatively, attenuations are computed from theory or simulations. Some examples are shown in Fig. 1.6. Determining the attenuation in galaxies is necessary to derive reliable estimates on the intrinsic stellar populations in the galaxy, such as mass, age, metallicity, and the formation rate of new stars.

There are other, less obvious processes attributed to dust that are just as important:

- *H_2 formation.* Atomic hydrogen in the gas phase can condense on a dust grain. When two hydrogen atoms merge on a dust grain, H_2 is formed and the excess of energy is deposited on the dust grain (see e.g. Gould & Salpeter 1963; Vidali et al. 2004; Bron et al. 2014, and references therin). This way, dust acts as a catalyst in the formation of H_2, which is crucial in the star formation process.

- *Shielding.* By absorbing the hard radiation of young stars, dust actively shields the already formed molecules in the ISM. This allows the gas to cool further down, which facilitates the formation of stars.
- *Gas heating.* Non-ionizing photons can hardly heat the ISM gas, because atomic hydrogen only has discrete energy levels to absorb them. Ionizing photons are more efficient because they can produce free electrons in the gas. Even more efficient is to knock electrons out of the dust grains through the photoelectric effect. These electrons interact more strongly with the gas, expending their energy and heating the gas. (see e.g. Watson 1972; Croxall et al. 2012; Hughes et al. 2015, and references therein).
- *Gas cooling.* Gas cools through the metals and small dust grains that are intermixed with the hydrogen and helium. Hot gas is more turbulent and so hydrogen atoms collide more frequently with dust grains. The hydrogen atoms lose kinetic energy (and cool), while dust grains heat up. In contrast to hydrogen atoms, dust grains can more easily get rid of this excess energy by emission of long-wavelength photons.

1.4 Andromeda as our laboratory

In short, it is clear that the universe would look and behave quite differently without dust. Therefore, it is important to continuously refine our knowledge of this small, but vital component. Especially, how it behaves in different astrophysical environments and how it reprocesses starlight. Ideally, we would like to study dust in a galactic context and with sufficient detail. Our own Galaxy offers the necessary detail. It is easy to resolve star forming clouds at all wavelengths. However, because we are inside the Milky Way, we cannot see the global picture. If we look at galaxies that are too far away, we see the global picture, but lack the detail to study the internal processes.

The Andromeda galaxy (M31) meets both of the above criteria. It is the closest large galaxy at a distance $D_{\mathrm{M31}} = 785$ kpc (McConnachie et al. 2005), which means every arcsecond on the sky corresponds to 3.8 pc along the major axis of M31. Due to the inclined view we have of this galaxy, this translates to 17.6 pc along the minor axis. This gives us the necessary detail, while maintaining the global picture. Classified as a SAb-type LINER galaxy, M31 is a slow-star forming spiral (SFR $= 0.20\ M_{\odot}\mathrm{yr}^{-1}$, Ford et al. 2013) with an inclination of 77.5° and a position angle of its major axis of 38° (McConnachie et al. 2005; Corbelli et al. 2010; Kirk et al. 2015). As the only large galaxy visible with the naked eye, it appears smooth and yellowish to the observer. Through specialized telescopes, it looks rather different (see Fig. 1.7). In the optical, the galaxy is dominated by its large bulge. The smooth disk is intersected by several dark lanes where dust obscures the starlight (Tempel et al. 2010). The dark dust patches in the disk coincide with bright emission in the MIR (Barmby et al. 2006; Gordon et al. 2006; Jarrett

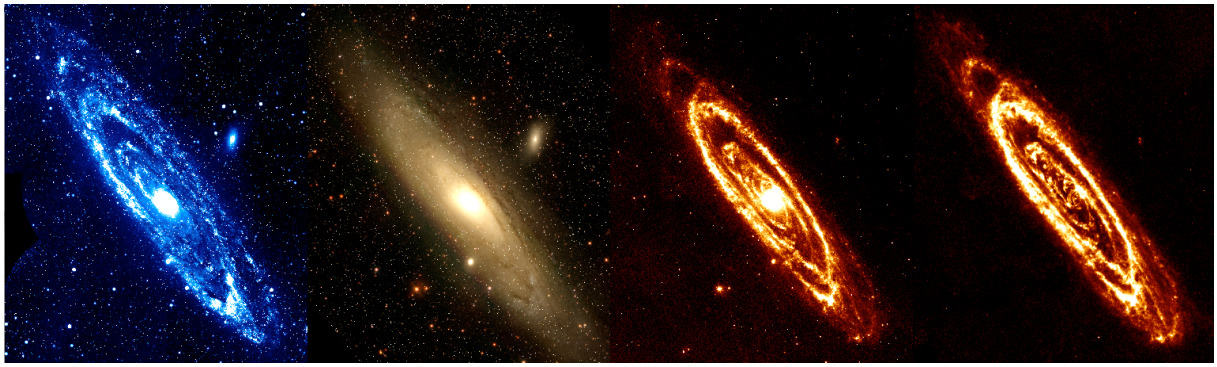

Figure 1.7: The Andromeda galaxy seen in several wavelength domains. Left to right: near-UV image from GALEX (Martin et al. 2005; Thilker et al. 2005), *gri* colour composition based on SDSS observations (York et al. 2000; Tempel et al. 2011), MIR view from the WISE satellite (Wright et al. 2010; Jarrett et al. 2013), submm view from the Herschel Space Observatory (Pilbratt et al. 2010; Fritz et al. 2012).

et al. 2013), and the bulge is still prominent at these wavelengths. In the FIR and submm, the bulge is much dimmer, and Andromeda looks like a mix of rings and filaments of cold dust (Fritz et al. 2012; Smith et al. 2012c; Groves et al. 2012). On the other side of the spectrum, in the ultra-violet (UV), a striking similarity with the MIR morphology is observed (Thilker et al. 2005). The morphological (anti-)correlations are a manifestation of intricate interactions between dust and starlight.

An interesting feature is the hole in the star forming ring at 10 kpc from the center. This is observed in several wavelength regimes and is though to be caused by an interaction with its satellite M32. Block et al. (2006) used numerical N-body simulations to model the effect of the passage of M32 through Andromeda's disk. Beginning with a model with two spiral arms, they end up with a morphological structure closely matching the 10 kpc ring and the hole. Similarly, Gordon et al. (2006) argued that a head–on encounter with M32 might have resulted in star forming waves propagating through the 10 kpc ring. These results were confirmed by Dierickx et al. (2014), although they find that a head-on collision is not necessary to create the observed structure of M31 and M32. However, recent results from the PHAT survey (Dalcanton et al. 2012; Lewis et al. 2015) suggest that this collision is unlikely to be the origin of the 10 kpc ring. Nevertheless, this collision has surely shaken up M31, so we can expect a large variety of physical environments inside the galaxy. This also makes M31 an obvious choice as our cosmic laboratory.

Andromeda allows us to investigate the starlight-dust interaction at a local scale, and couple it to the galaxy as a whole. Subsequently, we can see how the dust properties of M31 as a galaxy compare to a representative sample of galaxies in the Local Universe. The sample used in this thesis is the *Herschel* Reference Survey (HRS, Boselli et al. 2010b), a *Herschel* guaranteed-time key programme that targeted a sample of 322 galaxies in the Local Universe. The sample covers

a wide range of densities, from the field to the centre of the Virgo Cluster, and spans the entire range of morphological types, from ellipticals to late-type spirals. Thanks to the proximity (all galaxies are between 15 and 25 Mpc) and the completeness of the sample, the HRS can be used both for detailed studies of individual galaxies (e.g. Gomez et al. 2010; Cortese et al. 2010a; Roussel et al. 2010; Pohlen et al. 2010; De Looze et al. 2012a) as well as statistical analyses (e.g. Boselli et al. 2010a, 2012; Cortese et al. 2012b; Smith et al. 2012d; Ciesla et al. 2014). Thousands of nearby galaxies have been observed by *Herschel* as part of several large surveys, and for many of these surveys complementary data are available from UV to MIR wavelengths. The reason we chose the HRS in particular is because of the volume-limited selection, making it a complete sample, representative for 'normal' galaxies in the Local Universe.

A potential caveat is that the sample is still K-band or stellar mass selected. This criterion favours evolved systems with relatively low gas fractions (Cortese et al. 2012b; Clark et al. 2015). In particular, ETGs are picked up very easily this way. That is why we focus on the LTGs in the HRS sample for this thesis.

1.5 Modelling a galaxy's emission

It is a great challenge to correctly model the emission of galaxies across the electromagnetic spectrum. The multitude of components (stars, metals, dust, gas, dark matter) in different substructures make galaxies extremely complex ensembles. These components then interact with one another, both gravitationally and electromagnetically. The result is a galaxy's emission that varies strongly with wavelength. Encoded in this Spectral Energy Distribution (SED), is a treasure of information about the galaxy.

1.5.1 Model assumptions

A first step towards a manageable model is to simplify the general galaxy model to a static configuration of stars and dust. Stars emit light, which is partly absorbed or scattered by dust. Dust gets heated by this starlight and re-emits this energy at longer wavelengths. The main assumption here is that light travel times are much smaller than the lifetimes of dust and stars, and than dynamical timescales in galaxies. In other words: the configuration does not change when considering the dust-starlight interaction.

A second step is to limit the considered wavelength range to the problem that has to be addressed. Stars radiate in the UV-MIR, while dust is visible in the MIR-submm domain. In the interplay between those two components, it is possible to neglect the role of gas. Gas in galaxies are either hydrogen and helium, or H_2 molecules. These constituents can be ionized or radiatively excited, but the latter is only possible with photons of specific wavelength.

This discrete absorption of stellar energy is negligible compared to the continuous absorption by dust. In emission, gas dominates the radio and X-ray domain through mechanisms like bremsstrahlung and synchrotron radiation. In the UV-submm regime, gas is no dominant emitter nor absorber.

AGN can also contribute significantly to the SED, or even dominate it. Especially in the radio or X-ray regime, but sometimes in the UV-submm SED as well. An example of SEDs containing an AGN component is shown in Fig. 1.8. We do not consider AGN in this thesis because it significantly complicates the picture. AGN are an extra source of UV-optical radiation (the accretion disk) and FIR-submm emission (the dusty torus around the accretion disk). There is evidence that AGN may contribute to dust heating beyond the inner parts of the galaxy (see e.g. Wu et al. 2007; Kirkpatrick et al. 2012; Schneider et al. 2015). However, this effect is limited and certainly not common for the bulk of local galaxies. Including AGN in our samples and modelling would cause degeneracies between properties of the AGN and the host galaxy. A proper study of AGN and their host galaxies requires an analysis of line emission from spectra of multiple locations. This data is not always available, and such an analysis falls beyond the scope of this thesis. Fortunately, AGN are not very common in the Local Universe. For example, there are only 18 strong AGN among the HRS late-type galaxies. These rare systems are consequently not representative for the Local Universe. We chose to look at galaxies without an AGN so we can concentrate purely on the stars and dust.

It therefore makes sense to limit our study to the UV-submm range and investigate the processing of starlight by dust, and consequently, dust heating where these processes are most visible. In the rest of this work, we refer to 'panchromatic' and 'UV-submm' as the wavelength range between 0.1 and 1000 μm. The relative contribution of both components in this regime depends strongly on morphological type. Fig. 1.8 shows an example SED for an ETG and an LTG. ETGs are usually older, and host more evolved stars. They will outshine the relatively small amount of dust that is still present. On the other hand, the dust peak is quite strong in most LTGs.

1.5.2 Stars and dust extinction

In the panchromatic study of galaxies, stars are usually modelled as simple stellar populations (SSPs). These models are based on an IMF, from which an ensemble of stars is 'born'. The SED of an SSP is then computed based on emission models of the individual stars, and evolved in time. An SSP of a certain age and metallicity has an SED associated to it. Usually, these SEDs span UV-MIR wavelengths, with negligible emission at longer wavelengths. The most widely used SSP models are those from Bruzual & Charlot (2003) and Maraston (2005). SSP models compute the intrinsic light emitted by stars. In a realistic configuration, part of the light will be absorbed by dust residing in between the source of emission and the observer. On the other hand, scattering in and out of the line of sight will also influence the flux that is observed.

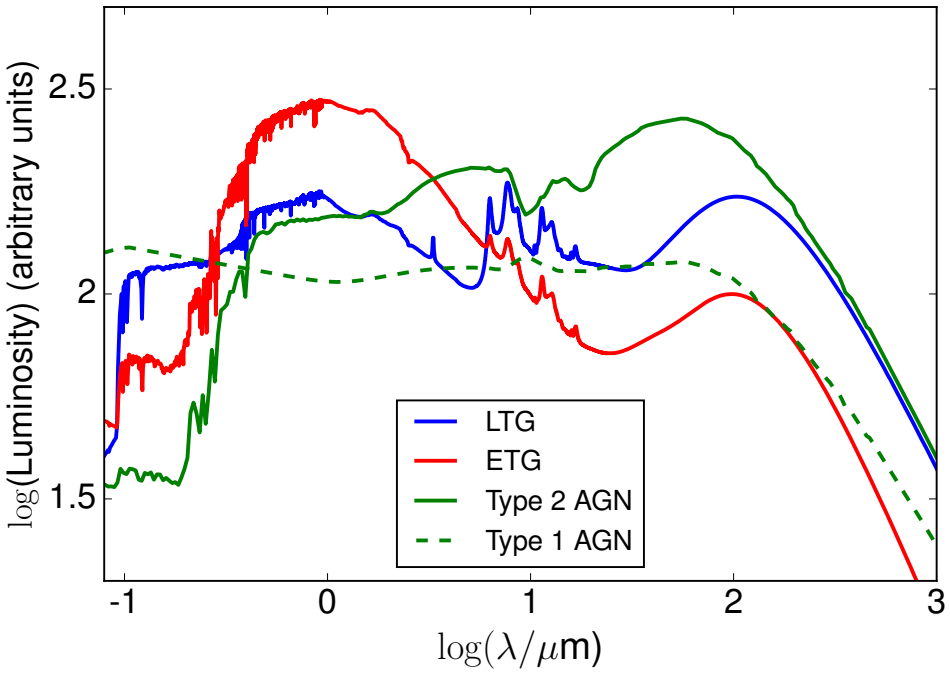

Figure 1.8: Example SEDs of different galaxy classes: A quiescent early-type (ETG), a star-forming late-type (LTG), a galaxy hosting a type 2 AGN and a galaxy hosting a strong (type 1) AGN. The SEDs are theoretical templates from MAGPHYS (da Cunha et al. 2008) and Fritz et al. (2006). They are normalised to the same bolometric luminosity for comparison.

In the current panchromatic SED fitting routines, scattering on dust grains is not treated directly. They are parametrized by applying an attenuation law. For a direct treatment of scattering, one must resort to radiative transfer calculations, an issue which we address in Sect. 1.6.

The effects of dust on the stellar SED can be implemented by applying an age-dependent attenuation model. Here, the dust attenuation levels depend on the age of the stars. This follows from the fact that young stars are obscured by their birth clouds, while the flux from evolved stars is only influenced by the diffuse interstellar dust. The most notable example is the two-component model by Charlot & Fall (2000). The main drawback of this approach is that the configuration is isotropic, and dust is distributed in a thin shell around the sources. This is of course a huge simplification of the real situation. Another way to implement the effects of dust is through the application of a single attenuation law for all ages. However, the attenuation law should then incorporate a more realistic geometry than a thin slab of dust. Attenuation laws are usually derived empirically, and one must be careful in applying them on galaxies that have different star-dust geometries than the calibration sample. Some of the most widely used attenuation models are those from Calzetti et al. (1994), Gordon et al. (2003), and Fitzpatrick & Massa (2007).

1.5.3 Thermal re-emission by dust

Dust is heated by starlight, and consequently re-emits this energy. Two main emission regimes can be distinguished: local thermal equilibrium (LTE) and non-local thermal equilibrium (NLTE). In the latter case, the dust grains are very small and can be excited to high energy levels by a single UV photon. The dust grains are then no longer in thermal equilibrium with their environment, and their emission properties are harder to compute. This phenomenon is called stochastic heating. Dust emission from stochastic heating can be computed directly based on the dust grain properties and size distributions, together with the conditions of the local radiation field. For a thorough overview, we refer the reader to Camps et al. (2015). The alternative to direct calculations is to use observational or pre-computed template spectra. This is usually done in SED fitting without radiative transfer simulations (Dale et al. 2001; Draine & Li 2007; Groves et al. 2008; da Cunha et al. 2008; Noll et al. 2009).

Dust in LTE is basically the limiting case of stochastic heating, towards larger dust grains. Due to their larger size, they are no longer excited by a single UV photon. The various dust grains are then in thermal equilibrium with their environment. The dust grains of a certain subcomponent (which are roughly equal in size, shape and chemical composition) will radiate as a *modified* black body function (Hildebrand 1983). This means that the emission j_λ from such a component will follow

$$j_\lambda = \kappa_\lambda^{\mathrm{abs}} \rho B_\lambda(T_{\mathrm{dust}}), \tag{1.1}$$

where ρ is the dust density and $B_\lambda(T_{\mathrm{dust}})$ is the Planck function of a standard black body of temperature T_{dust}. The main difference with a normal black body function lies in the absorption coefficient $\kappa_\lambda^{\mathrm{abs}}$, which is proportional to $\lambda^{-\beta}$ in the FIR/submm. β is called the emissivity index and reflects an extra wavelength dependence of the black body function. Every subcomponent will have its own total intensity and temperature. Since there are many grain populations, the resulting SED will be the sum of these modified black bodies. In practice, this is modelled by reducing the MIR-to-submm SED to a small number of dust components, each of them at a different temperature. The notion of temperature here no longer reflects a physical temperature. It should be seen as a parametric average temperature of the various dust grain populations that make up the dust component.

Several dust models treat both LTE and NLTE emission in a single dust emission template (e.g. Dale et al. 2001; Draine & Li 2007). These models are tuned to match the observed FIR SEDs using dust compositions based on the solar neighbourhood. They have a small number of free parameters, and allow a fast and physically motivated fit to the data. However, they sometimes do not give a good representation of the data, especially when the same dust model also has to match the attenuation of the stellar SED (Jones et al. 2013; Planck Collaboration 2014; Rémy-Ruyer et al. 2015).

1.5.4 A panchromatic framework

Panchromatic SED fitting has been the subject of intense research in the past few years, combining the above models (for an overview, see Walcher et al. 2011; Conroy 2013). Various powerful libraries and fitting tools have become available to analyse the observed SEDs from UV to submm wavelengths (Groves et al. 2008; da Cunha et al. 2008; Noll et al. 2009; Serra et al. 2011; Silva et al. 2011, Boquien et al. in prep). The key point is that the energy balance is respected. This means that the energy from the stellar component that is absorbed by dust, is again re-emitted by the dust component. This self-consistent treatment of the galaxy UV-submm SED can break several degeneracies involving extinction, dust temperature, and dust mass. It allows for a better determination of these parameters, but also provides better constraints on the intrinsic properties of the stellar component.

Additionally, the number of galaxies for which the entire UV-submm spectral energy distribution has been sampled accurately and densely, has increased enormously in the past few years. Concerning the stellar part of the SEDs, thousands of nearby galaxies have been imaged in the UV by the Galaxy Evolution Explorer (*GALEX*, Martin et al. 2005), in the optical by the Sloan Digital Sky Survey (SDSS, York et al. 2000) and in the near-infrared by the Two-Micron All Sky Survey (2MASS, Skrutskie et al. 2006). Even more important for our goal is the spectacular increase in the coverage of the infrared part of the SED. Mid-infrared imaging is now available for the entire sky thanks to the WISE survey (Wright et al. 2010), and many nearby galaxies have been imaged by *Spitzer* (Werner et al. 2004), *Akari* (Murakami et al. 2007) and *Herschel* (Pilbratt et al. 2010) at longer wavelengths. The latter mission is particularly useful for our goals as *Herschel* is the first large-scale mission to cover the submm region at wavelengths beyond 200 μm, where the emission from cool dust dominates. At even longer wavelengths, there is the all-sky survey by *Planck* (Planck Collaboration 2011), which can provide additional flux constraints, independent of *Herschel*.

Thus, we are now in the situation where panchromatic datasets can be combined with advanced panchromatic SED models. This paves the way for dedicated research on the interaction of starlight and dust, and on the intrinsic links between physical properties of galaxies.

1.6 Radiative transfer models of galaxies

An alternative and independent way to study the interaction between dust and starlight is through radiative transfer simulations. The technique of 3-D radiative transfer offers several advantages over panchromatic SED fitting as in Sect. 1.5. The 3-D nature allows for a realistic distribution of stars and dust. Additionally, RT simulations can correctly take scattering effects into account. Scattering and the relative star-dust geometry are the two elements required to accurately determine dust attenuation.

Unfortunately, RT simulations are computationally expensive. In particular, the computation is orders of magnitude slower than panchromatic SED fitting when dust heating and emission is included. In general, SED fitting is useful when modelling a large sample of galaxies. This method can then provide relatively accurate estimates, suitable for statistical analysis. Radiative transfer can be used to model individual galaxies at higher complexity, and give more detailed insights in the dust properties. For a more technical description of the radiative transfer method, we refer the reader to App. A.1.

The first radiative transfer galaxy models were constructed using forward radiative transfer. In this case, the starting point is a star-dust geometry and the result is an artificial image projected on the sky. Byun et al. (1994), Witt & Gordon (2000) and Baes & Dejonghe (2001) modelled galactic environments using different basic geometries, and studied the effect on the attenuation for the observer. In subsequent studies (e.g. Misiriotis & Bianchi 2002; Pierini et al. 2004; Tuffs et al. 2004; Möllenhoff et al. 2006; Gadotti et al. 2010; Pastrav et al. 2013a,b) more complex geometries were tested, which underlined the importance of clumping and multiple stellar populations. Not only analytical geometries can serve as the starting point for radiative transfer simulations (see App. A.1). Jonsson (2006) demonstrated how to use the output of hydrodynamical simulations as more arbitrary distributions for stars or dust. This has become one of the fastest growing sub-fields in dust radiative transfer (see e.g. Domínguez-Tenreiro et al. 2014; Natale et al. 2015; Saftly et al. 2015; Schaye et al. 2015). Forward radiative transfer is thus a suitable method to study the processes of emission, absorption and scattering from a theoretical point of view.

Alternatively, radiative transfer simulations can be used to model the spectral and morphological appearance of real galaxies. This is often referred to as *inverse* radiative transfer. In this case, the starting point is an observed image (or a set of images), and the end point is a parameter set describing the 3D geometry and luminosity of the model components. Pioneering work in inverse radiative transfer modelling of galaxies was done by several teams (Kylafis & Bahcall 1987; Xilouris et al. 1999; Bianchi 2007). These studies focussed on the extinction and scattering of optical light in edge-on spiral galaxies. The choice of edge-on galaxies is obvious. The dust is clearly visible in extinction and they have a regular geometry. Often, they can be simplified to an exponential disk for dust and stars, with the addition of a Sérsic bulge (Sérsic 1963) of stars.

In the past decade, more complex modelling of edge-on galaxies became possible including clumpy disk or ring-geometries (see e.g. Bianchi 2008; Baes et al. 2010; Popescu et al. 2011; MacLachlan et al. 2011; De Looze et al. 2012b,a; Schechtman-Rook et al. 2012; Shinn & Seon 2015, and references therein). These studies provided important insights in the distribution and mass of dust in edge-on spirals. The biggest technical advancement here was the computation of the FIR emission of dust. This was an important step towards self-consistent, panchromatic SED modelling.

Interestingly, these studies found that there is a dust energy balance problem in these systems. When modelling observations in the optical, the energy absorbed by dust could be derived. Upholding the principle of energy conservation, the absorbed energy must be re-emitted in the FIR/submm. However, predictions from radiative transfer simulations systematically underestimated the observed FIR/submm fluxes for these edge-on galaxies. A possible explanation is that dust is more clumped than previously thought. Cold, compact clumps or filaments are not expected to contribute to the large-scale attenuation, but can contribute to the FIR emission. Alternatively, there may be obscured star formation going on in the disk of the galaxy. The strong UV radiation of new stars will not be visible through the dust lane, but the dust will be heated by these new stars, producing more FIR emission.

The above efforts all rely on manually tuning the free parameters to obtain a galaxy model. Often, a good parameter set was found, but perhaps not the best possible parameter set for a given analytical configuration. Ideally, we would like to obtain the best set of parameters that fit a radiative transfer model to the observations. Set to both investigate the dust energy balance in edge-on galaxies, and to provide a better, unbiased way to model galaxies, De Geyter et al. (2013, 2014) took a leap forward. They performed radiative transfer simulations for a set of edge-on galaxies. Their method automatically retrieves the best fitting parameter set for the model. Saftly et al. (2015) used the same code, but applied it to synthetic edge-on images of simulated galaxies. Both studies show that such an approach can give stronger constraints on both stellar and dust parameters, specially when multiple wavebands are fitted at the same time. Imaging in blue bands is ideal for investigating the extinction properties of dust, but it hides information on the underlying stellar distribution. The red bands, on the other hand, provide more accurate information on the stellar distribution, but make it more difficult to study the dust-extinction effects. A combined fit to all bands can alleviate these degeneracies, as shown by De Geyter et al. (2014). This procedure is called oligochromatic radiative transfer fitting. An additional benefit is the more stable convergence towards the optimal solution, particularly for low S/N observations (Häußler et al. 2013; Vika et al. 2013).

In a follow-up analysis, De Geyter et al. (2015) showed that the predicted FIR/submm emission again underestimates the observations for the two galaxies they could test it for. The fact that unbiased, automatic modelling also yields a dust energy balance problem suggests more detailed models are necessary. In this respect, radiative transfer of face-on galaxies may provide an answer. The line-of-sight averaging for face-ons is much smaller than for edge-on galaxies. On the downside, face-on spiral galaxies show much more structure which makes them difficult to model. Bianchi et al. (2000) used analytical geometries to reproduce the FIR emission and dust temperature of the nearby face-on NGC 6946. However, their model requires high face-on optical depths and they were unable to retrieve the observed FIR scale length of the dust disk. The inverse radiative transfer modelling of face-on galaxies was put on hold for more than a decade due to its complexity and lack of computing power. De Looze et al. (2014)

revived the investigation by modelling M51, a nearly face-on galaxy. The big novelty in their work was the use of observed images as input geometries, which naturally yields more realistic distributions for the galaxy components. The 2-D images were converted to 3-D distributions by deprojecting them and adding an exponential vertical profile. They consider three stellar components (ionizing stars, young stars, and evolved stars) and one dust component. The use of multiple stellar components allows for a better reconstruction of the internal radiation field. Consequently, they were able to reproduce the observed FIR/submm emission.

1.7 This thesis

There are still several open questions related to the topics we described in the previous sections. The most fundamental issue is the composition of dust. Except for a handful of interstellar dust grains found in the solar system, all data on cosmic dust is indirect. It is fairly established that interstellar dust in Milky Way is a mix of silicates and carbonaceous material, with a small amount of other elements. However, the true composition of the molecules and grains is uncertain. Additionally, it is likely that the dust mixture in the Milky Way is location dependent, with grain size distributions depending on radiation field in a complex way. Therefore, dust in other galaxies is potentially quite different from Milky Way dust. One way to investigate these questions further is through attenuation and extinction curves.

Related to the composition of dust are the production and destruction mechanisms. The are three likely production scenarios (supernova, AGB stars, grain growth), but their relative weight is not really known. Here again, it is possible that their contribution is location dependent. There are many ways to destroy dust, which strongly depend on radiation field and density of the local environment. Further insights in this area could be obtained by investigating dust extinction and emission for a wide range of environments, and through numerical simulations or chemical evolution modelling.

Another important uncertainty is the energy balance between absorbed starlight and dust emission. On a global galaxy scale, the energy balance is thought to be respected in the local universe. The radiation field in galaxies is dominated by the stars (and possibly by AGN) in the galaxy itself, with a negligible contribution of the intergalactic background. It is unclear however, at which scale this energy balance breaks down. One can expect, that dust in molecular clouds is heated by the newly formed stars inside them, but also by the radiation field of the general stellar population surrounding the cloud. Answers to these questions lie in detailed radiative transfer studies and scaling relation on local scale. They can help to quantify the effect of dust on the SED of a galaxy or a galactic region. This information is only qualitatively known and vital to derive stellar properties and star formation rates.

The goal of this thesis is to gain insights in the energy balance between starlight and dust in

galaxies. At the start of this investigation, the first results of the *Herschel* mission provided several new insights in global dust attenuation (e.g. Skibba et al. 2011; Boquien et al. 2012), dust scaling relations (e.g. Cortese et al. 2012b), radiative transfer modelling (e.g. De Looze et al. 2012a; De Geyter et al. 2013), and dust heating (e.g. Bendo et al. 2012a). These new results form the foundation and motivation for deeper studies on larger samples, with the aim of quantifying the more qualitative picture we have now.

Our investigation covers both global and on local scales in nearby galaxies. We aim to measure the attenuation levels stellar radiation, determine the contribution of different sources to dust heating, and determine the importance of the geometric distribution of dust. Additionally we will look for reliable methods to derive physical properties from galaxies and relate those properties to each other. We focus in particular on normal, large galaxies in the Local Universe because they are spatially resolved and high-quality data is available across the electromagnetic spectrum. It is also our goal to look at the differences and similarities between trends for galactic regions and for global galaxy properties. To this end, we will explore the capabilities of panchromatic SED fitting (part II) and radiative transfer simulations (part III). Part IV presents our main conclusions and looks at what lies ahead in the field.

Chapter 2 addresses the question of global dust attenuation in galaxies. The starting point here are the spiral galaxies in the HRS sample. To model the panchromatic SED in these systems, we adopt the Bayesian SED fitter MAGPHYS (da Cunha et al. 2008). A detailed description of this code can be found in App. A.3. Using the model for both the observed and intrinsic galactic SED, three attenuation parameters are defined and investigated. The bolometric attenuation and the fraction of UV photons to this bolometric attenuation are correlated against several main galaxy properties. The attenuation levels in the FUV waveband are linked to the β-ratio (TIR/FUV) and recipes are provided to determine the intrinsic FUV emission for different bins of the observable $NUV - r$ colour.

In chapter 3, dust scaling relations and their underlying processes are investigated on a local and global scale. We perform a systematic pixel-by-pixel SED fit of the Andromeda galaxy using MAGPHYS. The quality of our fits is investigated and caveats to applying this method on sub-kpc scales are outlined. In a subsequent section, a wide set of physical properties are analysed. We discuss their spatial variation across the galaxy and search for dust scaling relations. The dust scaling relations derived at a local scale in Andromeda are compared to the global trends found for the HRS galaxies. In a final analysis, some indications on the dust heating mechanisms are discussed.

In a critical comparison, chapter 4 deals with our ability to infer dust properties from resolved galaxies. This study focuses entirely on the nearby edge-on lenticular galaxy NGC 4370. We discuss its morphology and apply methods of different complexity to determine the distribution and total mass of dust in this system. Colour maps and multi-Gaussian expansion models are

used to determine the attenuation and dust mass from optical data. Using *Herschel* data as well, the dust mass is derived from SED fitting. We then use FitSKIRT (De Geyter et al. 2013, see App. A.2) to automatically fit a 3-D radiative transfer model to the galaxy. We test the difference between an exponential disk and a ring geometry for the dust, and investigate the influence of a possible nuclear stellar disk in the galaxy.

Chapter 5 turns back to the Andromeda galaxy and seeks to quantify the dust heating mechanisms in the galaxy. Using the knowledge and data products of the previous chapters, a realistic and highly detailed radiative transfer model of M31 is constructed. We discuss the set-up of our model and outline the caveats. The model is then tested against a range of observable constraints, and a face-on view of Andromeda is discussed. In a dedicated analysis, the contribution of the different stellar populations to the dust heating is quantified. We outline the differences between 3-D and 2-D dust heating properties and provide recipes to estimate the dominant dust heating sources.

Part II

Panchromatic SED fitting

Dust attenuation in the local universe

2

In order for the light to shine so brightly, the darkness must be present.

Francis Bacon

2.1 Introduction

The obscuring power of cosmic dust has a significant effect on our view of the Universe. Dust grains in all environments absorb a portion of the light emitted by stars and active galactic nuclei (AGN). This energy is reprocessed and makes dust the prime source of emission in the far-IR (FIR) and sub-millimetre (submm) regimes. For a given galaxy, it is hard to measure exactly how much of the starlight is attenuated by dust and how this amount differs with wavelength and environment. These are useful quantities to know, for example when constructing luminosity functions and colour-magnitude diagrams and when determining star formation rates (SFRs) or stellar masses. Additionally, it can play a key role in comparing simulated galaxies or universes with our own Universe. In a broader context, the average fraction of absorbed energy (and the corresponding dust luminosity) allows estimates of the extragalactic background light (see e.g. Skibba et al. 2011).

Several studies in the 1990s attempted to determine the bolometric luminosity in nearby galaxies based on data from the IRAS mission, and they found a typical number of about 30% for the fraction of the bolometric luminosity absorbed and re-emitted by dust (Soifer & Neugebauer 1991; Xu & Buat 1995). A dedicated study was performed by Popescu & Tuffs (2002). Their work was based on a sample of 28 spiral galaxies with multi-band optical and ISOPHOT FIR observations. They found the same percentage of attenuation: on average, interstellar dust absorbs and re-emits about 30% of the bolometric luminosity of late-type galaxies.

Chapter based on Viaene et al. (2016).

While the study of Popescu & Tuffs (2002) was a significant step forward in determining the bolometric attenuation compared to IRAS-based estimates, their work still suffered from a number of limitations. Their sample size was modest, which limits a detailed statistical study. Moreover, the wavelength range on which their analysis was based was rather limited. Optical data were available for all galaxies, but UV[1] data were not. In the near-IR (NIR), only *K*'-band magnitudes were available (*H*-band data for only a few galaxies). But more importantly, the dust luminosity was estimated using only three FIR bands centred at 60, 100, and 170 μm. The lack of data beyond 170 μm and in the mid-IR (MIR) region puts limitations on a secure determination of the dust luminosity. Finally, only Virgo Cluster galaxies were included in the study, which may cause significant bias (e.g. due to the dense cluster environment).

More than a decade later, we are now in a situation where we can eliminate most of these concerns. Most importantly, there is now a significant number of galaxies with accurate photometric measurements across the UV-submm SED. This is thanks to all-sky and wide-field surveys such as SDSS, 2MASS, WISE and Planck, and several targeting telescopes such as GALEX, Spitzer and *Herschel*. The latter is particularly useful for our goals as *Herschel* is the first large-scale mission to cover the submm region at wavelengths beyond 200 μm, where the emission from cool dust dominates. In addition to the availability of large samples of galaxies with high-quality SED data, we now also have the advantage that advanced tools have become available for analysing observed SEDs (see chapter. 1.5).

Consequently, the exercise of determining the bolometric absorption by dust was repeated in the *Herschel* era. Skibba et al. (2011) investigated the dust/stellar flux ratio for the KINGFISH sample (Kennicutt et al. 2011). Only considering the spiral galaxies of their sample, they find an equivalent of 31% for the bolometric attenuation. Although this is a comforting confirmation of previous studies, it was still derived in a rather empirical way from (as they state) a relatively small and incomplete sample.

The combination of high-quality SED data and advanced panchromatic SED fitting tools implies that we can extend our analysis beyond only determining the bolometric attenuation in galaxies. First, we can correlate the bolometric attenuation with fundamental physical galaxy properties derived from the SED modelling, such as stellar masses and SFRs. Second, it also allows a more detailed investigation of the absorbed energy spectrum. This can be used to quantify the importance of different heating sources for the dust in normal spiral galaxies. This question has been the subject of quite some debate in the recent past, and different approaches have been used to tackle this problem (e.g. Draine et al. 2007; Rowan-Robinson et al. 2010; Boselli et al. 2010a, 2012; Bendo et al. 2010a, 2012a, 2015; Boquien et al. 2011; Popescu et al. 2011; De Looze et al. 2012a,b; Hermelo et al. 2013). The results from these studies are mixed: it seems that in normal spiral galaxies, both young and evolved stellar populations can dominate the dust

[1] Following Xu & Buat 1995, we define the UV domain as the wavelength range up to 3650 Å

heating budget.

Another important attenuation-related quantity is the attenuation in the *GALEX* FUV band, A_{FUV}. Estimating the attenuation in this wavelength range is extremely useful if one wants to determine the SFR of galaxies, often probed by the FUV flux. Closely related to A_{FUV} is the ratio of the total IR (TIR) and the FUV luminosity; IRX. The IRX ratio is one of the best, geometry-independent methods to determine the UV attenuation in galaxies (see e.g. Buat & Xu 1996; Meurer et al. 1999; Gordon et al. 2000, and references therein). Recent studies have attempted to calibrate this relation based on theoretical models and observations (Cortese et al. 2008; Hao et al. 2011). Boquien et al. (2012) investigated the IRX-β relation at sub-galactic scales for a sample of seven face-on galaxies. They made use of the powerful tool of panchromatic SED fitting to provide a consistent picture of the attenuation and its link to observational quantities. Their approach relies on CIGALE (Noll et al. 2009), which is based on the same concept as MAGPHYS. A calibration of A_{FUV} for a large and representative sample of local galaxies using this technique would prove its worth. With our panchromatic SED modelling and information on the intrinsic flux of each galaxy, we obtain an independent measurement of A_{FUV}. This allows us to revisit previous calibrations and provide a new calibration based on physically consistent parameters for a representative set of local galaxies.

This chapter aims to provide a better determination of three main attenuation-related galaxy parameters and to understand how these parameters are related to global galaxy properties. This is done in a self-consistent model framework and through panchromatic SED fitting. Our goal is to quantify how much of the starlight is absorbed by dust, both in total energy and in the UV domain, where the effect of extinction and dust heating is the greatest. In Section 2.2 we present the sample we use for this study and the available data. In Section 2.3 we discuss the methods we use for our analysis and define three main attenuation parameters: the bolometric dust fraction $f_{\rm dust}$, the UV heating fraction $\xi_{\rm UV}$, and the FUV attenuation A_{FUV}. Our results are presented in Section 2.4. Section 2.5 discusses the correlations found and highlights some of the model caveats. We conclude in Section 2.6.

2.2 Sample selection and data

This analysis is based on the *Herschel* Reference Survey (HRS), which is described in section 1.4. Our approach requires a representative sample of nearby galaxies with accurate photometry from the UV to submm wavelengths. We chose the HRS in particular is because of the K-band and volume-limited selection, making it a complete sample, representative of 'normal' galaxies in the local universe. Note that the HRS favours evolved galaxies with low gas fractions (Cortese et al. 2012b; Clark et al. 2015) due to the K-band (or stellar mass) selection. To partly alleviate this bias, we focus on the late-type galaxy subsample (types Sa and later, galaxy types are taken

from Table 1 in Cortese et al. (2012a)). We exclude the galaxies without *Herschel* PACS or SPIRE fluxes (HRS 104, 116, 164, 195, 225, 228, 229, and 291) or without *GALEX* fluxes (HRS 4, 5, 10, 38, 73, 76, 238, 254, 259). Additionally, we remove HRS 284 (no SDSS) from our sample. Of the remaining galaxies, 14 were found to have a strong AGN. The AGN classification was done through analysis of optical spectral lines of the galaxy nuclei and will be presented in Gavazzi et al. (in prep.). We plot them separately in section 2.4. However, we do not treat them as a separate subsample because, as we show, their attenuation properties are not fundamentally different.

The final sample counts 239 galaxies. The spread over the different morphological types can be found in Table 2.1. The HRS was originally proposed to acquire *Herschel* observations, but now a vast set of ancillary data is available. In this work, we focus on the broad-band data (see list below), but there is also narrow band photometry in Hα (Boselli et al. 2015), optical spectroscopy (Boselli et al. 2013; Hughes et al. 2013), and atomic and molecular gas data (Boselli et al. 2014a). For the present study we use integrated flux densities over the UV-submm range:

- *GALEX FUV* and *NUV* and SDSS *gri* flux densities are taken from Cortese et al. (2012a);
- 2MASS *J*, *H*, and K_s data from the 2MASS archive (Skrutskie et al. 2006);
- *Spitzer* IRAC 3.6 and 4.5 μm flux densities from the S^{4}G project (Sheth et al. 2010);
- WISE 12 and 22 μm data taken from Ciesla et al. (2014);
- Integrated *Spitzer* MIPS 24, 70 and 160 μm fluxes are taken from Bendo et al. (2012b);
- *Herschel* PACS 100 and 160 μm flux densities are taken from Cortese et al. (2014);
- *Herschel* SPIRE 250, 350, and 500 μm flux densities are taken from Ciesla et al. (2012). Correction factors to convert them to the latest SPIRE calibration and beam factors are taken into account. An additional calibration error of 7% was added to the tabulated flux uncertainties.

For many galaxies in the sample, additional data are available that could be added to the database. To have a database that is as uniform as possible for all galaxies in the sample, we limited our database to these data. Note that we do not correct these fluxes for extinction by Milky Way dust. One of the selection criteria for the HRS was a low Galactic extinction $A_B < 0.2$ mag. The survey is centred in and around the Virgo Cluster, which lies at high Galactic latitude ($b > 70°$). The reddening effects due to Milky Way dust are thus relatively weak.

2.3 Dust attenuation analysis

We make use of the MAGPHYS (described in appendix A.3) to perform the panchromatic SED modelling. The code has been used extensively in recent years and has proved reliable

(see e.g. Michałowski et al. 2014; Hayward & Smith 2015; Smith & Hayward 2015, and references therein). For the HRS, cold dust temperatures were found to lie within the 10-30K range based on modified black body fitting (Cortese et al. 2014). We therefore make use of the extended version of the code, which has a wider temperature range for the warm and cold dust component. This extended version work well at sub-kpc scales (see chapter 3), but also for integrated galaxy SEDs (Agius et al. 2015, Papallardo et al. in prep.).

A representative SED fit is shown in Fig. 2.2, together with several parameter PDFs. The overall χ^2 distribution is shown in Fig. 2.1, where we multiplied the MAGPHYS output-χ^2 with the number of bands to obtain an unreduced χ^2. It resembles a classic χ^2 distribution, with a clear peak and a tail towards higher values. To estimate the significance for our model, we rely on the work of Smith et al. (2012a). They investigated the effective degrees of freedom (DOF) for MAGPHYS based on the number of bands. We use their formula B2 and find (for 20 bands) $\sim 14^{+5}_{-6}$ DOF. The uncertainty on this number is based on bootstrapping simulations performed by these authors.

In Fig. 2.1, we also show the corresponding theoretical distributions for unreduced χ^2 and several DOF. The best estimate DOF of 14 yields a curve which is less broad than the observed curve. It also peaks at significantly shorter χ^2 values. Even the optimistic DOF estimate of the Smith et al. (2012a) equation (DOF=19) still shows this behavior. While it is difficult to treat the MAGPHYS-χ^2 value as a classical χ^2, the numbers we find are higher than expected from theory. This indicates that a) our model is not adequate for the sample of galaxies considered, or b) the uncertainties on the observed fluxes are underestimated. Even though MAGPHYS adds a 5% uncertainty to each flux by default, this may not be sufficient if the calibration errors for certain observations are too optimistic.

Setting a blind χ^2 cut-off for bad fits is not advisable because this value only reflects how well the best-fit template model matches the observations. In fact, the shape of the parameter PDFs holds more information on the uncertainty for each parameter. We therefore visually inspect the SED fits and the parameter PDFs for all galaxies, especially those at the high end of the χ^2 distribution (i.e. where our distribution has a higher number of galaxies in a particular bin than the theoretical curve with DOF$=$ 14). The correspondence between best-fit curve and observed data points is usually excellent, without strong offsets. The PDFs are generally well behaved (no bimodalities) and have a certain width (a width of only one bin indicates MAGPHYS has no room to try other options, which points to an underestimate of the observational errors).

There is only one object in our sample that shows strong offsets between model and observations: HRS 142. This source has an exceptionally broad FIR peak and was identified as a peculiar galaxy with a strong AGN. We omit HRS 142 from our sample because MAGPHYS is unable to fit the FIR SED with this library of SED templates at hand. We chose to keep the remainder of the galaxies in our sample, despite the higher χ^2 for some fits. However, we rely

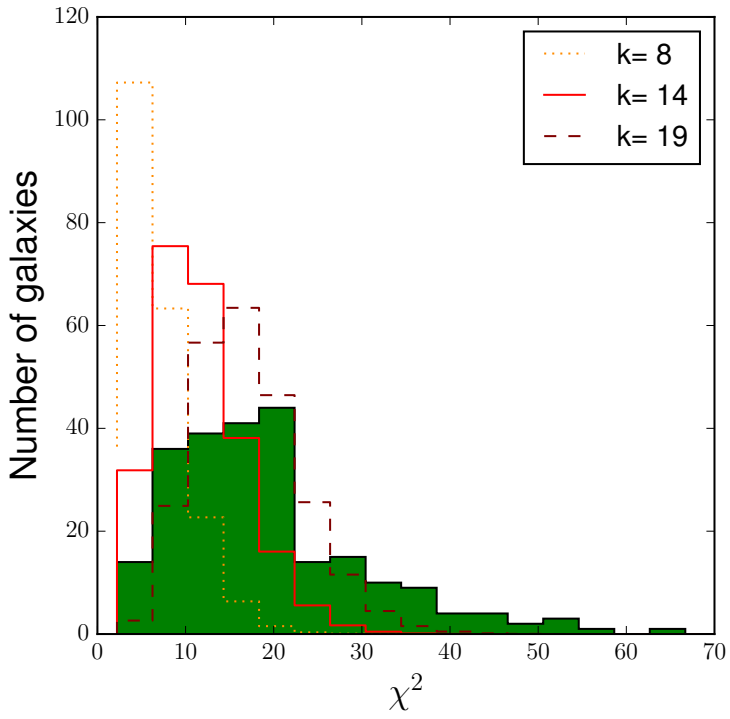

Figure 2.1: χ^2 distribution of the best fit SED models for our galaxy sample (green). The orange, red and brown histograms show the expected theoretical distribution for different degrees of freedom.

on the Bayesian framework of MAGPHYS, so that these fits can still provide an estimate for the main parameters.

The above considerations should be seen as a caveat of the MAGPHYS code. However, it is to date one of the best available tools to model the panchromatic emission from galaxies and galactic regions. To better constrain this model, one ideally would need more observational bands and a more conservative approach to calibration uncertainties. That is why, in the following analysis, we will limit ourselves to the main stellar parameters of MAGPHYS ($M_\star$, SFR, sSFR), which are proved to be well constrained (da Cunha et al. 2008; Smith et al. 2012a; Michałowski et al. 2014; Hayward & Smith 2015; Smith & Hayward 2015).

MAGPHYS allows us to determine basic galaxy parameters, such as stellar mass ($M_\star$), SFR averaged over the last 100 Myr, and dust luminosity ($L_{\rm dust}$). In this work, we use the median of the PDFs as estimates for these properties. Additionally, it provides us with the unattenuated SED. Upon comparing this intrinsic SED (without dust attenuation) with the 'normal', attenuated SED, the wavelength dependence of dust attenuation can be investigated.

In this work, we make use of MAGPHYS' capacity to provide an attenuated and unattenuated SED. We focus on three attenuation-related quantities: 1) the bolometric attenuation $f_{\rm dust}$ or the fraction of the bolometric luminosity that is absorbed by dust, 2) the UV heating fraction $\xi_{\rm UV}$, which is the fraction of UV radiation to the total absorbed luminosity, 3) A_{FUV}, the attenuation in the FUV band.

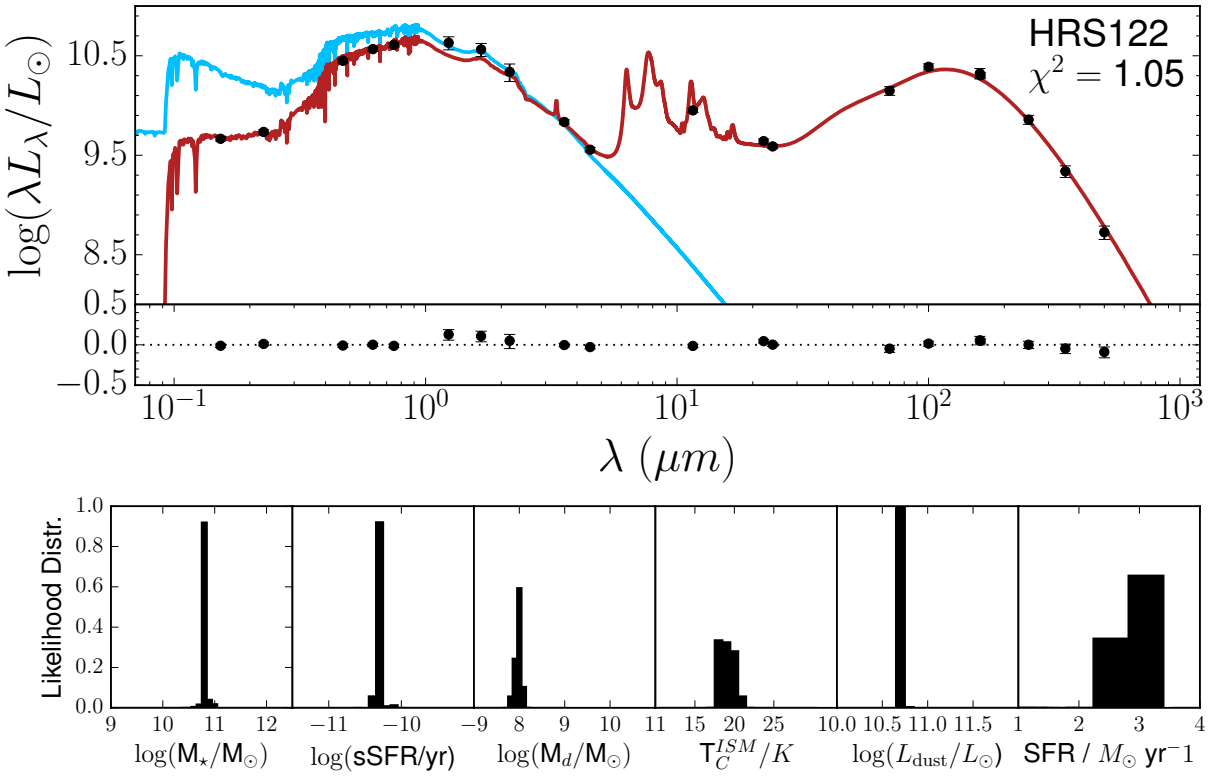

Figure 2.2: SED and model of HRS 122 (M 100), which is representative for the sample. The top panel shows the data (black dots with error bars), the best fitting panchromatic SED fit (red line) and the intrinsic stellar SED (blue line). The residuals between data and best fitting model are shown below the SED. The bottom row shows the corresponding PDFs for several key parameters of the model.

From the attenuated and unattenuated SED provided for each galaxy, we can directly calculate $f_{\rm dust} = L_{\rm dust}/L_{\rm bol}$. We can also easily calculate the detailed SED of the radiation absorbed by dust, i.e. $L_\lambda^{\rm abs}$. From this absorbed SED we calculate the contribution due to UV radiation as

$$\xi_{\rm UV} = \frac{\int_{\rm UV} L_\lambda^{\rm abs}\,{\rm d}\lambda}{\int L_\lambda^{\rm abs}\,{\rm d}\lambda} = \frac{1}{L_{\rm dust}}\int_{\rm UV} L_\lambda^{\rm abs}\,{\rm d}\lambda \tag{2.1}$$

where the integral in the numerator covers the UV domain ($\lambda < 3650\,$Å). Finally, A_{FUV} is computed by convolving both the attenuated and the unattenuated best fit SED with the *GALEX* FUV filter response curve and computing

$$A_{FUV} = -2.5\log(L_{FUV}^{\rm att}/L_{FUV}^{\rm unatt}). \tag{2.2}$$

In the subsequent analysis, we correlate $f_{\rm dust}$ and $\xi_{\rm UV}$ to a number of other global physical galaxy parameters, such as stellar mass, SFR, and specific star formation rate (sSFR), which is often used in the context of galaxy evolution. We also re-calibrate the often studied relation between IRX vs. the A_{FUV} relation, where we define IRX as TIR/$FUV = L_{\rm dust}/L_{FUV}^{\rm att}$. Our calibration is done in a self-consistent framework and provides a method for determining A_{FUV} from empirical, observational data, which are relatively easy to obtain. All of these quantities are directly derived from the MAGPHYS model. MAGPHYS has been thoroughly tested, and we limit ourselves to those parameters that are known to be determined well by the fitting, given a good panchromatic wavelength coverage. However, these parameters can still be model dependent. We come back to this in Sect. 2.5.

The uncertainties on the attenuation parameters and on the physical quantities $L_{\rm dust}$, $M_\star$, SFR, and sSFR are derived through a Monte Carlo bootstrapping method. For each galaxy, we alter the observed fluxes by choosing a random value from a normal distribution centred on the observed flux and with the flux uncertainties as standard deviation. We then re-run the MAGPHYS fitting and derive all our parameters again from the output. We perform 100 iterations per galaxy, which gives a good estimate of the effect of the observational uncertainties on the resulting parameters. It must be noted that these uncertainties can be underestimated (see the discussion on the χ^2 distribution above).

2.4 Results

2.4.1 The bolometric attenuation

The top left-hand panel of Figure 2.3 shows a histogram of the bolometric attenuation for all the galaxies in the sample. The mean value obtained for our sample is $\langle f_{\rm dust}\rangle = 32\%$, which basically reproduces the value obtained by previous studies (Soifer & Neugebauer 1991; Xu

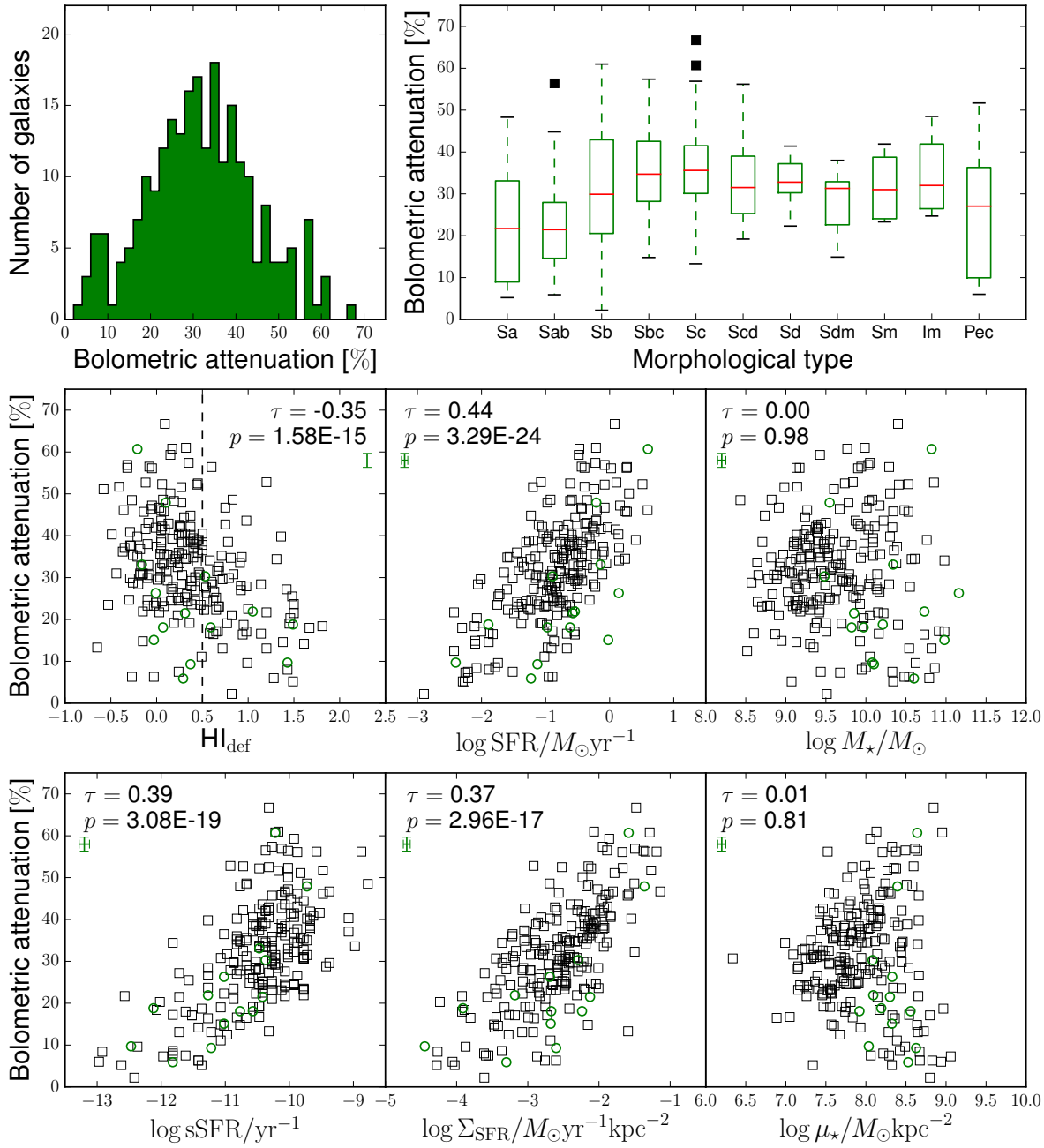

Figure 2.3: Top left: Histogram of the bolometric attenuation $f_{\rm dust}$ for the galaxies in the sample. Top right: Box plots of $f_{\rm dust}$ for different morphological types. Red lines indicate the median values, boxes the 1st and 3rd quantiles. Outliers are plotted as black squares. Middle row: Correlations between the bolometric attenuation and HI deficiency, SFR, and stellar mass. Bottom row: Correlations between the bolometric attenuation and sSFR, SFR surface density, and stellar mass surface density. Green circles are classified as strong AGNs. The Kendall's τ correlation coefficients and corresponding p-values are indicated for each scatter plot. Average error bars are shown in green.

& Buat 1995; Popescu & Tuffs 2002; Skibba et al. 2011). Soifer & Neugebauer (1991) used the integrated optical and FIR luminosity density of the 60 μm-selected IRAS Bright Galaxy Atlas (BGS, Soifer et al. 1987) to estimate $f_{\rm dust}$. Xu & Buat (1995) and Buat & Xu (1996) improved on this study by using a sample of nearby spiral galaxies that were detected by IRAS and observed in the UV. To correct for the thermal emission from cool dust beyond the IRAS cut-off at 120 μm and in the MIR region, they used empirical correction factors based on a small sample of 13 nearby galaxies observed in the submm.

Popescu & Tuffs (2002) used ISO data out to 170 μm, so they could actually trace the cool dust component in the individual galaxies. These authors attributed their finding the same value of 30% as obtained by Soifer & Neugebauer (1991) to two factors that work in opposite directions. On the one hand, the BGS is biased towards FIR-bright galaxies, as already mentioned, and thus favours galaxies that have more dust than the average local spiral galaxy population. On the other hand, estimating the dust luminosity from only IRAS flux densities misses the bulk of the cold dust in galaxies, which implies that the estimates of the bolometric attenuation in Soifer & Neugebauer (1991) are an underestimate of the true bolometric attenuation. It seems a happy coincidence that these two factors, which work in opposite directions, cancel out exactly.

More recently, Skibba et al. (2011) have analysed the dust/stellar flux $F_d/F_\star$ for the KINGFISH galaxies. For their subset of 35 nearby spirals, they find that $\langle \log(F_d/F_\star) \rangle = -0.35$. This is equivalent to $\langle f_{\rm dust} \rangle = 31\%$. Their method was purely observational, integrating the UV to submm SED through simple linear interpolation. However, they indicate that their sample was not statistically complete.

That we again recover essentially the same number as these earlier studies is remarkable and requires further exploration. First, one would expect that the ISO-based estimates of the dust luminosity might be an underestimate of the real dust luminosity in spiral galaxies. Indeed, most spiral galaxies still have significant dust emission beyond 170 μm, so FIR/submm data beyond this wavelength are required to correctly recover the dust temperature distribution, hence dust mass and luminosity (e.g. Gordon et al. 2010; Galametz et al. 2011). Skibba et al. (2011) note that the lack of SPIRE data led to the underestimation of the total dust luminosity by 17%. On the other hand, they do retrieve the same average value for $f_{\rm dust}$. But then again their sample is relatively small and contains objects in different environments than the ones from Popescu & Tuffs (2002). Additionally, one could expect the mean value of the bolometric luminosity of our study to be higher than the 30% value obtained by Popescu & Tuffs (2002) because their sample contained only Virgo Cluster galaxies. It is well-known that spiral galaxies in the Virgo Cluster are generally deficient in atomic gas (Davies & Lewis 1973; Giovanelli & Haynes 1983), which is considered to be due to ram pressure stripping by the hot cluster gas. Recent observations suggest that the same accounts for interstellar dust: Virgo Cluster galaxies contain on average less interstellar dust than similar galaxies in sparser environments (Boselli & Gavazzi 2006; Gomez et al. 2010; Cortese et al. 2010b, 2012b).

To investigate whether this has an effect on the mean bolometric attenuation, we plotted the bolometric attenuation as a function of the *H*I deficiency ($\mathrm{def_{HI}}$) in the middle left-hand panel of Fig. 2.3. This parameter was determined as the difference (in logarithmic space) between the expected and observed *H*I mass of a galaxy. The expected *H*I content was estimated from galaxies of similar morphological type and angular size as described in (Haynes & Giovanelli 1984). The *H*I reference sample for the HRS galaxies are taken from the ALFALFA survey (see Boselli & Gavazzi 2009). For more information on the HI data for the HRS and the computation of $\mathrm{def_{HI}}$, we refer to Boselli et al. (2014a). To quantify the strength of the correlations presented in this chapter, we computed Kendall's rank coefficient τ (Kendall 1938; Kendall & Gibbons 1990). This non-parametric correlation coefficient is derived from the number of concordant (C) and discordant (D) pairs upon ranking the data: $\tau = \frac{C-D}{C+D}$. A τ value of one points towards a perfect correlation, while $\tau = -1$ indicates an anti-correlation. The coefficient is zero when no correlation is present. For each τ, an associated p-value can be computed that reflects the chance that the null hypothesis (no correlation) is true. This formalism allowed us to directly compare the correlations we present in this work and quantify the chances of a genuine link between physical parameters.

The correlation between f_{dust} and $\mathrm{def_{HI}}$ is weak, and we find that Kendall's $\tau = -0.35$. However, the chance of no correlation is small ($p = 1.58 \times 10^{-15}$). Most of the HI deficient galaxies ($\mathrm{def_{HI}} > 0.5$) do occupy the region where $f_{\mathrm{dust}} < 30\%$. In fact, for the HI deficient galaxies, the average $\langle f_{\mathrm{dust}} \rangle = 0.25$ with a standard deviation of 0.11. On the other hand, galaxies with $\mathrm{def_{HI}} < 0.5$ have $\langle f_{\mathrm{dust}} \rangle = 0.34$ with a standard deviation of 0.13. A Kolmogorov-Smirnov (K-S) test showed that the probability of both samples coming from the same distribution is 7.35×10^{-8}. This means the bolometric attenuation properties of HI deficient and non-deficient galaxies are significantly different. The trend could indicate that environment and galaxy interactions play a role in governing the amount of starlight that is attenuated. This is in line with the findings of Cortese et al. (2010b) and Boselli et al. (2014b) and can be interpreted in two ways. One possibility is that rapid quenching of the star formation occurs. When this happens (which is usually the case in a cluster environment), the UV energy output by new stars drops dramatically. Consequently, less energy is absorbed, and the bolometric attenuation fraction drops. Galaxies with quenched star formation due to interactions are usually deficient in atomic gas as well, hence the observed trend. Alternatively, dust may simple get stripped when a galaxy enters a dense environment. This directly causes a decrease in attenuation fractions.

That star formation affects the bolometric attenuation fraction is clear from the middle panel in Fig. 2.3. We observe a positive correlation between f_{dust} and SFR, with $\tau = 0.44$ and $p = 3.29 \times 10^{-24}$. Still there is quite some scatter on the relation: e.g. for Milky Way type galaxies with a SFR of the order of 1 $M_{\odot}$ yr^{-1}, there are galaxies with bolometric attenuation below 20% and others with values up to almost 60%. It has been shown that galaxies with high $\mathrm{def_{HI}}$ usually have low SFR (see Boselli & Gavazzi 2006, for a review). This is an intuitive link

as gas content and SFR are strongly connected through the Schmidt-Kennicutt law (Schmidt 1959; Kennicutt 1998). Because SFR anti-correlates with $\mathrm{def_{HI}}$ and positively correlates with f_{dust}, the observed trend between f_{dust} and $\mathrm{def_{HI}}$ may just be an indirect correlation.

Interestingly, there is a 98% chance of no correlation ($\tau = 0.00$) with stellar mass, another key parameter in galaxy evolution (Fig 2.3, middle right panel). There is a known positive trend between SFR and galaxy mass (see e.g. Speagle et al. 2014, and references therein). Following the above reasoning, one might expect an indirect correlation between $M_\star$ and f_{dust}. It appears that the indirect links are not strong enough to exhibit a trend between those two quantities. This indicates that galaxy mass is no indication of how much of the starlight is absorbed by dust. Wang & Heckman (1996) investigated this indirectly through the correlation between the $F_{\mathrm{UV}}/F_{\mathrm{FIR}}$ flux ratio and ΔV_{HI}, the velocity dispersion of HI gas. They interpret ΔV_{HI} as a proxy for stellar mass and the $F_{\mathrm{UV}}/F_{\mathrm{FIR}}$ flux ratio as a tracer of the fraction of light from young stars that is escaping the galaxy. In a way, this is the inverse of the attenuation (which is the light not escaping). Their results suggest we should at least see some trend between f_{dust} and $M_\star$. However, both relations are difficult to compare, not only because different parameters are used, but also because the sample of Wang & Heckman (1996) is quite different. They investigated nearby galaxies with IRAS detection, while the HRS is K-band-selected. This way, early-type spirals are under-represented in their sample. These objects are usually more massive and lower in attenuation, which would contradict the trend they observe.

We investigated the changes in bolometric attenuation for different morphological types. Popescu & Tuffs (2002) claimed a strong dependence of the bolometric attenuation on morphological type. For early-type spirals, they found a mean bolometric attenuation of only 15%, whereas this rose to 30% for late-type spirals. The top right-hand panel of Figure 2.3 shows the distribution of the bolometric attenuation as a function of the morphological type of the galaxies in our sample. The average value of f_{dust} does increase from 23% for Sa galaxies to 37% for Sc galaxies and then remains more or less flat. For each individual class of galaxies, however, there is a significant spread in the values. Even for the Sa class, for example, the values vary between 5% and 50%. In fact, for each morphological class, the mean value for f_{dust} is compatible with the global mean value of 32% within one standard deviation (see Table 2.1).

The variation is particularly high for galaxies classified as peculiar (Pec). While their median bolometric attenuation fraction is roughly consistent with late-type spirals, this subsample ranges between 5% and 50% in f_{dust}. Naively, one would expect higher values, since galaxy mergers are usually associated with peculiar morphologies. Mergers can trigger star formation, which in turn boosts dust production, and can cause more attenuation. We visually inspected these galaxies and found that they cover a wide variety in shape and colour. Some have disk and spiral arms, and others are dust lane elliptical galaxies. None of them, however, show ongoing interaction with another galaxy. Their NUV-r colours range from 2.1 to 5.8, which illustrates the diversity in this class. We therefore do not consider them when investigating trends with

morphology.

We ran a K-S test to investigate whether the $f_{\rm dust}$ values for Sa-Sab galaxies, on one hand, and Scd-Sd, on the other, stem from the same distribution. The chance that both samples are the same is 7.50×10^{-4}. We can thus state a slight increase in bolometric attenuation going from early-type spirals to late types. This is consistent with the previous claims by Popescu & Tuffs (2002). The conclusion is that it is impossible to make a sensible estimate of the bolometric attenuation for individual galaxies based on their morphological type. Even for statistical studies, this cannot be done without introducing large errors.

Global extensive parameters, such as stellar mass and SFR, can be prone to scaling effects. A galaxy may contain much dust or form quite a few stars, but if the galaxy is a large and extended object, this will not translate into a strong attenuation. On the other hand, intensive parameters (such as sSFR = SFR/ $M_\star$ and surface density quantities) do hold information about the internal proportions of dust and starlight. One can naively expect galaxies with high sSFR to have more SFR per stellar mass, hence more dust. These objects are denser, which naturally induces more attenuation by dust.

With this motivation, we have plotted the bolometric attenuation as a function of parameters related to the internal galaxy environment in the bottom row of Fig. 2.3. The sSFR is provided by MAGPHYS, and we computed the stellar mass surface density $\mu_\star$ and the SFR surface density $\Sigma_{\rm SFR}$ using the i band half-light radius following Cortese et al. (2012a). There is an upward trend between $f_{\rm dust}$ and the sSFR, with $\tau = 0.39$ and $p = 1.58 \times 10^{-15}$. The correlation with $\Sigma_{\rm SFR}$ is about as strong ($\tau = 0.37$ and $p = 2.96 \times 10^{-17}$) as with sSFR, but weaker than with SFR. We find no correlation with stellar mass surface density ($\tau = 0.01$ and $p = 0.81$).

The galaxies classified as strong AGNs by Gavazzi et al (in prep.) do not exhibit different values for $f_{\rm dust}$. They occupy the same ranges in all of the correlations of Fig. 2.3. This suggests that the central activity does not contribute significantly to the attenuation properties of the galaxy as a whole. For this reason, we did not treat them as a separate subsample when computing the correlation coefficients or mean attenuation values.

From our analysis with a statistically representative sample of the local universe, we can now confirm that one third of the produced starlight is attenuated by dust. For the bolometric attenuation, we find no tight correlation with main galaxy evolutionary parameters. The strongest trend is an increasing bolometric attenuation with increasing SFR, which proves that more energy is absorbed in the more active galaxies.

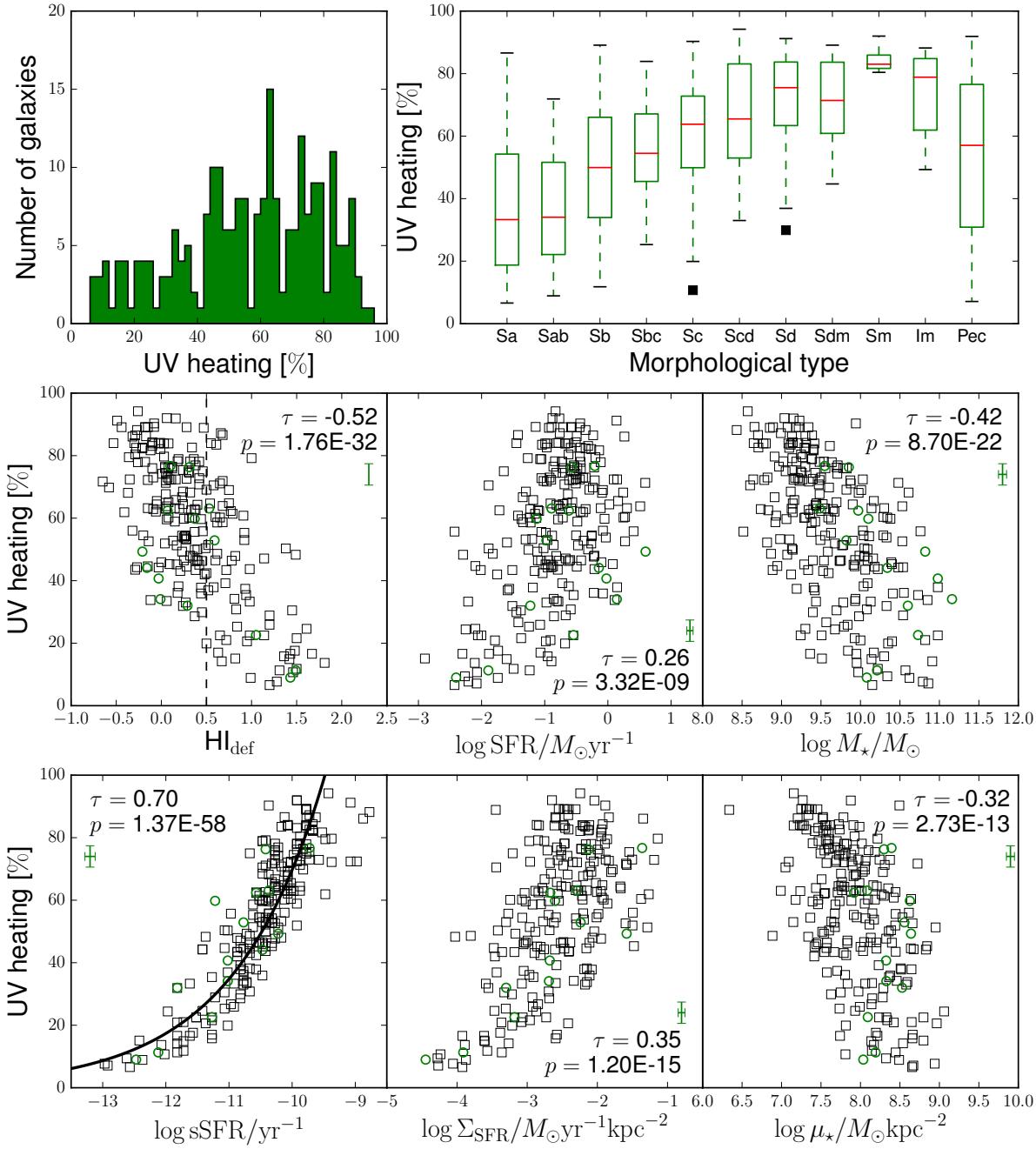

Figure 2.4: Top left: Histogram of the UV heating fraction $\xi_{\rm UV}$ for the galaxies in the sample. Top right: Box plots of $\xi_{\rm UV}$ for different morphological types. Red lines indicate the median values, boxes the 1st and 3rd quantiles. Outliers are plotted as black squares. Middle row: Correlations between the UV heating and HI deficiency, SFR, and stellar mass. Bottom row: correlations between the UV heating and sSFR and between the SFR surface density and stellar mass surface density. Green circles are classified as strong AGNs. The Kendall τ correlation coefficients and corresponding p-values are indicated for each scatter plot. Average error bars are shown in green.

Table 2.1: Mean value and the standard deviation of the bolometric attenuation $f_{\rm dust}$ and the UV heating fraction $\xi_{\rm UV}$ as a function of the morphological type.

type	$N_{\rm gal}$	$f_{\rm dust}$ mean ± std	$\xi_{\rm UV}$ mean ± std
Sa	23	0.23 ± 0.14	0.38 ± 0.24
Sab	20	0.23 ± 0.12	0.36 ± 0.19
Sb	48	0.32 ± 0.15	0.50 ± 0.21
Sbc	31	0.36 ± 0.10	0.56 ± 0.15
Sc	37	0.37 ± 0.11	0.61 ± 0.17
Scd	29	0.34 ± 0.10	0.67 ± 0.16
Sd	18	0.33 ± 0.06	0.70 ± 0.19
Sdm	10	0.28 ± 0.08	0.71 ± 0.14
Sm	4	0.32 ± 0.08	0.85 ± 0.04
Im	8	0.35 ± 0.09	0.74 ± 0.13
Pec	10	0.26 ± 0.15	0.53 ± 0.29
total	238	0.32 ± 0.13	0.56 ± 0.22

2.4.2 The heating of dust in spiral galaxies

The corresponding results concerning the UV heating fraction (i.e. the percentage of dust luminosity that comes from absorbed UV photons) are shown in Figure 2.4. The top left-hand panel shows the histogram of $\xi_{\rm UV}$ for the 221 galaxies in the sample. The histogram shows a broad distribution that is peaked around 65%, but it is skewed towards lower values, such that the average value is only 56%. Notably, the full range of values between 0 and 100% is covered: in some galaxies nearly all of the luminosity absorbed by the dust is optical and NIR radiation, whereas in other galaxies, the dust heating is powered almost exclusively by UV radiation. The distribution of $\xi_{\rm UV}$ over the different morphological types (top right panel) now shows a clear trend, with the average value increasing from less than 40% for the earliest type spirals to 85% for the Sm galaxies. Within every morphological class, however, there is no uniformity, and a broad range of values is found. We performed the same K-S test as for $f_{\rm dust}$, i.e. between the combined Sa-Sab sample and the Scd-Sd sample. The probability that both samples are statistically equivalent is 1.15×10^{-5} for the $\xi_{\rm UV}$ parameter. Potentially, the trend with morphology may be caused by the fact that early-type spirals have larger bulges and so contain more evolved stars relative to the ongoing star formation. The evolved stars then act as a second heating mechanism in the galaxy, causing the UV heating fraction to go down.

The middle left-hand panel of Fig. 2.4 shows that this time there is an anti-correlation with HI

deficiency. The trend is stronger than with $f_{\rm dust}$ ($\tau = -0.52$ and $p = 1.76 \times 10^{-32}$), albeit still with some scatter. We find $\langle \xi_{\rm UV} \rangle = 0.40$ with a standard deviation of 0.23 for HI deficient galaxies ($\rm def_{HI} > 0.5$) and $\langle \xi_{\rm UV} \rangle = 0.63$ with an rms of 0.19 for galaxies with $\rm def_{HI} < 0.5$. A K-S test showed that the change of both samples coming from the same distribution is 4.02×10^{-8}. It appears that the environment has a stronger effect on the UV heating fraction than on the bolometric attenuation. We can again interpret this trend in the context of star formation quenching as described in section 2.4.1 or as an effect of dust stripping. This process shuts down an important source of UV light, causing the UV contribution to the total attenuation to go down. This is in line with a significant (but weaker than with $f_{\rm dust}$) positive trend with SFR ($\tau = 0.26$ and $p = 3.32 \times 10^{-9}$).

In the middle right-hand panel in Fig. 2.4, an inverse trend between $\xi_{\rm UV}$ and stellar mass can be noted with $\tau = -0.42$ and $p = 8.70 \times 10^{-22}$. UV radiation dominates the absorbed luminosity in the less massive galaxies, and this portion decreases gradually if we move to higher stellar masses. The picture does not really improve when plotting the surface density parameters $\Sigma_{\rm SFR}$ and $\mu_\star$ in the bottom row (middle and right panels). In the correlation with the UV heating fraction and $\mu_\star$, the trend is steep and we find $\tau = -0.32$ with $p = 2.73 \times 10^{-13}$. That would mean the stellar density has very little influence on the attenuation in the UV. Considering that $\mu_\star$ indirectly traces the radiation field of the older stellar populations, this is not surprising. Old stars in general do not dominate the UV radiation field. The trend between $\Sigma_{\rm SFR}$ and $\xi_{\rm UV}$ is stronger ($\tau = 0.35$ and $p = 1.20 \times 10^{-15}$) than the one with SFR. When more stars are formed per unit of area, the UV radiation field is higher and more UV light can be absorbed.

Most interesting is the correlation between $\xi_{\rm UV}$ and the sSFR, as shown in the bottom left-hand panel. Here we obtain a tight correlation, with $\tau = 0.70$ and a very low $p = 1.37 \times 10^{-58}$. Galaxies with a low sSFR ($\rm sSFR < 10^{-11}\ yr^{-1}$) all have low UV heating, whereas in all galaxies with $\rm sSFR \gtrsim 10^{-10}\ yr,^{-1}$ the absorbed dust luminosity is dominated by UV radiation. Since the scatter on this trend is much smaller compared to the other trends, sSFR seems like the best option for tracing the UV heating in spiral galaxies. A similar trend was also identified by De Looze et al. (2014). They used radiative transfer simulations to quantify the dust heating fraction due to young stars and found that high heating fractions correspond with high levels of sSFR and vice versa. We quantified our relation by fitting a power law function to the data points and find

$$\xi_{\rm UV} = 7.3^{+1.7}_{-1.4} \times 10^4\, \rm sSFR^{0.3017 \pm 0.0086}, \tag{2.3}$$

which gives $\xi_{\rm UV}$ in percentage points for a sSFR in $\rm yr^{-1}$. Uncertainties on the coefficients were derived through a Monte Carlo method with 1000 iterations.

Both parameters are related to the excess in UV emission to the emission of the evolved stellar population. The more stars that are formed per unit of stellar mass, the stronger the radiation field. This will heat the dust (mainly through absorption of UV photons) and produce more

MIR and FIR dust emission. On the other hand, we do not find a strong correlation with SFR. This is consistent with the fact that galaxies in our sample with higher SFR are simply larger (higher $M_\star$) galaxies. The intrinsic properties of the radiation field are less influenced by this scaling effect. In this case, it is thus more valuable to look at sSFR than at extensive parameters, such as SFR or $M_\star$.

We again note that the AGNs do not stick out as having different $\xi_{\rm UV}$ values. They follow the trends of the other galaxies in Fig. 2.4. In our subsequent analysis, we no longer plot them as a separate subsample.

2.4.3 Calibrating the IRX vs. A_{FUV} relation

Our models allow us to revisit the IRX vs. A_{FUV} relation for late-type galaxies. There is a strong trend between those two properties, but also a wide spread (see Fig. 2.5). The main difficulty for constructing this relation is a reliable measurement of A_{FUV}. This quantity requires information of the intrinsic, unattenuated SED, which has, up to now, not been easy to obtain. Therefore, previous calibrations of the IRX vs. A_{FUV} relation started from the well-studied and observable IRX vs. β relation, where β is the slope of the UV SED (Calzetti et al. 1994; Meurer et al. 1999; Kong et al. 2004; Cortese et al. 2008; Hao et al. 2011). They then rely on theoretical or semi-empirical considerations to derive A_{FUV}. More recently, Boquien et al. (2012) have demonstrated that it is possible to use panchromatic SED fitting as a way to determine A_{FUV} independently and link it to the IRX - β relation.

Cortese et al. (2008), hereafter C08, find that the spread on the IRX-A_{FUV} relation was closely related to the star formation history. They assumed a SFH 'a la Sandage' in the formalism of Gavazzi et al. (2002), which is parametrized by τ, the time after formation at which the star formation in the galaxy peaks. This parameter is related to the sSFR, which is easier to derive from observations. To provide a more empirical calibration of the scatter in the TIR/FUV vs. A_{FUV} relation, we make use of the close correlation of $NUV-r$ and sSFR. The former is easy to obtain, even without making any model asumptions. In our model, we define IRX $\equiv$ TIR/FUV $= L_{\rm dust}/L^{\rm att}_{FUV}$. And A_{FUV} was derived using Eq. 2.2, which is a direct determination, without having to work through the IRX-β relation.

We plot the correlation between IRX and A_{FUV} in Fig. 2.5 and colour code them according to $NUV-r$ colour. A clear, nonlinear but monotonic trend is indeed visible. Galaxies with a high FUV attenuation also have a high TIR/FUV ratio. The scatter in the plane correlates well with $NUV-r$, with blue galaxies exhibiting more FUV attenuation than redder galaxies. The trends make sense in the picture where more active galaxies are bluer and hold relatively more dust (hence more attenuation). This dust is heated to higher temperatures because star formation acts as a second dust heating source. Consequently, the IRX ratio increases. Additionally, we plot the relations found by C08 for $\tau = 2.8$, 4.0, and 7.0, corresponding to galaxies of old,

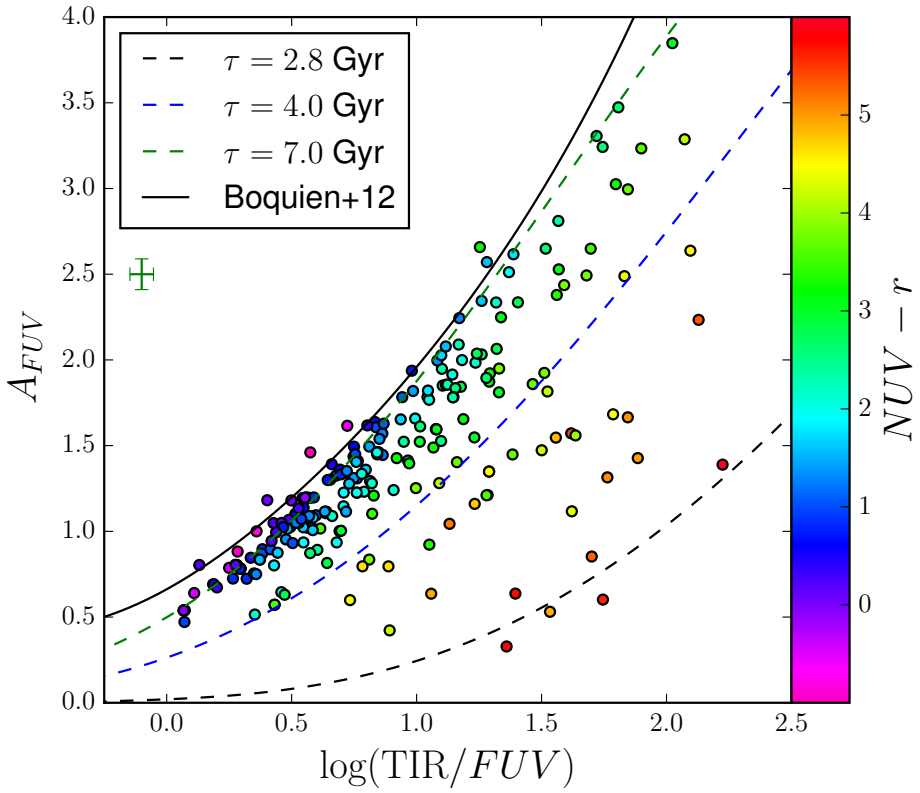

Figure 2.5: A_{FUV} vs. $\log(\mathrm{TIR}/FUV)$ relation for the HRS late-type galaxies, colour-coded according to $NUV - r$ colour. For comparison, a few relations from the calibration by C08 are plotted as dashed lines. Average error bars are shown in green.

Table 2.2: Conversion relations for the $\log(\mathrm{TIR}/FUV)$ vs. A_{FUV} relation for different bins of $NUV-r$. The last column shows $\langle \Delta A_{FUV} \rangle$, the average absolute deviation in A_{FUV} from the polynomial relation.

$\langle NUV-r \rangle$		$A_{FUV} = a_1 + a_2 x + a_3 x^2, x = \log(\mathrm{TIR}/FUV)$			
mean	std	a_1	a_2	a_3	$\langle \Delta A_{FUV} \rangle$
0.66	0.25	0.48309	1.12325	0.60186	0.05
1.05	0.11	0.49580	0.86097	0.63454	0.02
1.34	0.06	0.45683	0.77105	0.73777	0.04
1.57	0.08	0.41163	0.88936	0.55688	0.04
1.79	0.06	0.65207	0.03586	1.13833	0.04
2.00	0.07	0.42749	0.58636	0.71669	0.05
2.21	0.07	-0.01291	1.39637	0.26219	0.05
2.51	0.11	0.34217	0.40083	0.73603	0.06
2.86	0.09	0.62276	0.05598	0.74223	0.14
3.26	0.12	0.84988	-0.68556	0.94567	0.21
3.86	0.21	0.70715	-0.43529	0.56733	0.29

intermediate, and young stellar populations. The theoretical relations by C08 follow the trend closely. The relation for galaxies with old (young) stellar populations follows the data points with high (low) NUV-r colours. This is again comforting for our model, but also opens the opportunity to calibrate this correlation. Finally, in Fig.2.5, the relation found by Boquien et al. (2012) is shown. This relation was derived from seven local face-on spirals, and they found a strong similarity ($-0.3 < \Delta A_{FUV} < 0.16$) between their relation and previous parametrisations of the IRX-A_{FUV} relation from different samples (Burgarella et al. 2005; Buat et al. 2011; Hao et al. 2011). These relations are consistent with the blue HRS galaxies ($NUV-r \approx 0$), but do not follow the IRX-A_{FUV} trend for redder galaxies. This again calls for a parametrisation depending on $NUV-r$ or sSFR.

We divided our sample in 11 bins of 20 galaxies according to their $NUV-r$ colour. We chose to fit a second-order polynomial to the data in each bin. The number of data points did not allow us to go to higher order polynomials. Unfortunately, adding more galaxies per bin would increase the spread on $NUV-r$ within one bin. To fit with more general functions (with more free parameters), we need to increase the number of galaxies per bin without increasing the spread on $NUV-r$. This is currently not possible with our dataset. However, we consider this a good trade-off, which covers a wide range in $NUV-r$ with sufficient resolution to be applicable on other sets of late-type galaxies. Figure 2.6 shows the best fit polynomial for each sSFR bin, together with a few relations from C08. The best fit parameters are listed in Table 2.2.

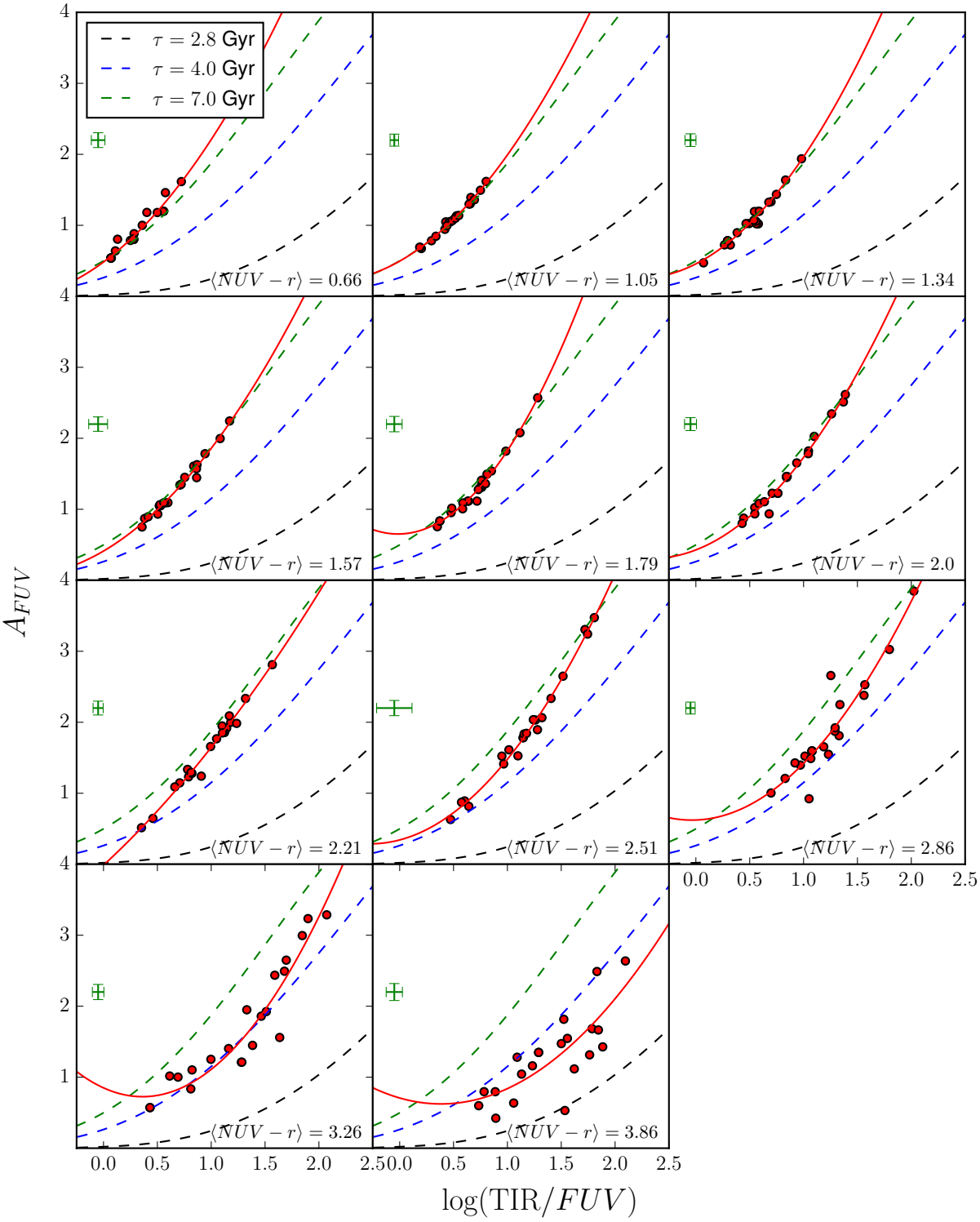

Figure 2.6: A_{FUV} vs. $\log(\mathrm{TIR}/FUV)$ relation separated in different bins of $NUV - r$ colour. The points in each bin are fitted with a second-degree polynomial (solid line). For comparison, a few relations from the calibration by C08 are plotted as dashed lines. Average error bars per bin are shown in green.

This framework provides a physical relation between IRX, $NUV - r$, and A_{FUV} and a more direct way to estimate the attenuation in the FUV band. Both $NUV - r$ and TIR/FUV are relatively easy to determine for large samples of galaxies (e.g. following Galametz et al. 2013; Chang et al. 2015). Our calibration allows computing the intrinsic FUV radiation and gives insight into the dust attenuation in a galaxy. On the other hand, if A_{FUV} can be derived (following our approach or any other) together with the $NUV - r$, our relations give a rather precise value for the total infrared luminosity. This quantity is important for studying galaxies near and far, but it is only available for a part of the galaxies in the observed universe.

We do not claim that these polynomial relations are physically motivated. They were used to give a good functional representation of the observed relations. In this respect, they hold within the parameter range of the calibrating data and can be used to interpolate within this range. We caution against extrapolating beyond the calibrated parameter ranges or applying these relations on objects with highly different properties than our calibration sample.

2.5 Robustness of the results

Our results were derived by a physically motivated model for a galaxy's SED. In the first place, our goal was to investigate whether there are observable trends and which ones are worth pursuing. In that aspect, MAGPHYS provides self-consistent results that can be used to probe these correlations. However, the absolute values of the best fit parameters may differ from those derived from single-band tracers or alternative methods. It is worth investigating model dependencies that can influence our results.

As a first test, we derived the bolometric attenuation from pure observable quantities without any underlying model assumptions. To do this, we did a linear interpolation (in log-space) between the FUV-500 μm data points. The purely empirical SED was then integrated from the UV to the submm to obtain $L_{\rm bol}$. Similarly, we integrated the purely empirical SED from 4 μm to the submm data points to compute $L_{\rm IR}$. The bolometric attenuation can then be estimated as $f_{\rm dust} \approx L_{\rm IR}/L_{\rm bol}$. The top left-hand panel in Fig. 2.7 shows a very tight correlation between the empirical and model $f_{\rm dust}$. The Pearson correlation coefficient r (aimed at probing linear relations) is close to unity, and the chance p of no linear correlation is virtually zero. However, the trend does not follow a strict 1:1 relation; MAGPHYS produces slightly higher $f_{\rm dust}$ fractions.

The underlying reason for this situation is that the $L_{\rm dust}$ from MAGPHYS is systematically higher than the observed $L_{\rm IR}$. The bolometric luminosities do match closely. This discrepancy is most likely linked to the integration interval. For the observed $L_{\rm IR}$, we integrated from 4 μm to the last available submm data point (500 μm in most cases). This is less straightforward in the case of MAGPHYS, where the dust SED is defined from $0.1 - 1000$ μm. Although the SED

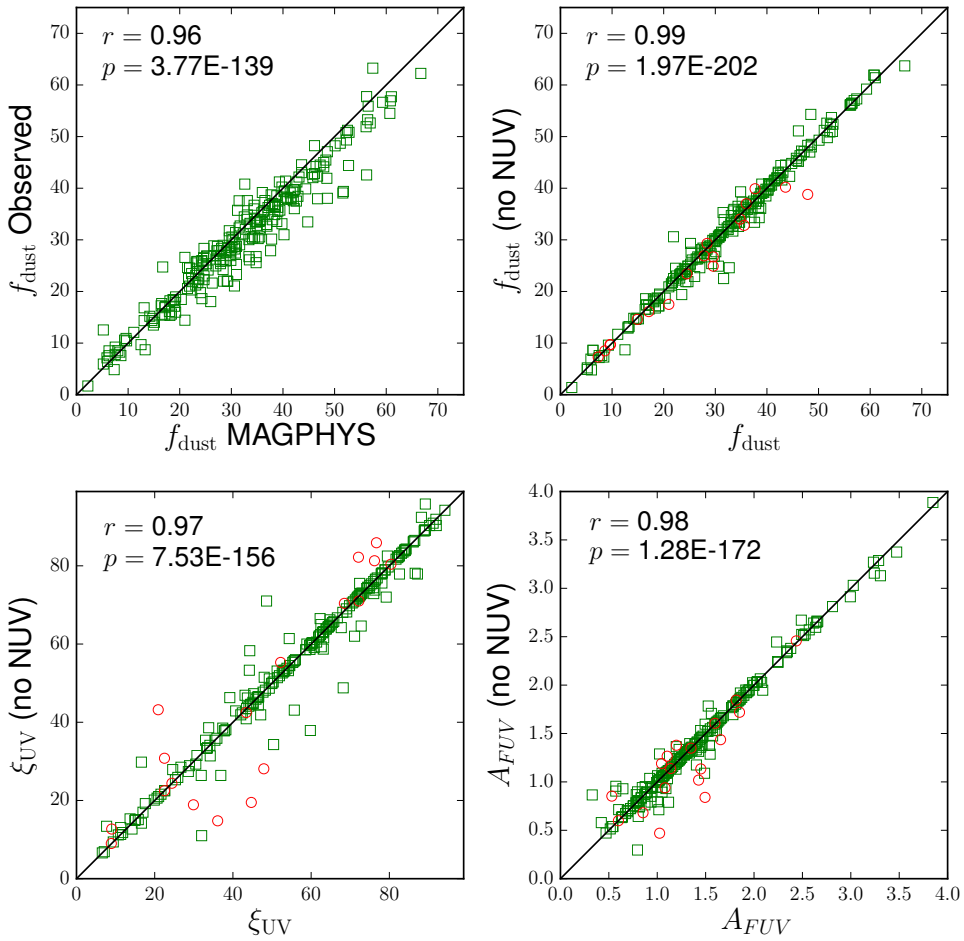

Figure 2.7: Checks to trace potential systematic errors in our method. Top left: $f_{\rm dust} \approx L_{\rm IR}/L_{\rm bol}$ as derived from integrating the observed SED plotted against $f_{\rm dust}$ derived from our fitted model SEDs. Top right: $f_{\rm dust}$ as derived from the MAGPHYS fits with (ordinate) and without the NUV data point. Red circles indicate galaxies with no UV data after removing the NUV band. Bottom: Results for $\xi_{\rm UV}$ (left) and A_{FUV} (right) of the same run without the NUV flux.

is virtually zero in the 0.1 – 4 micron regime, some flux from hot dust can contribute to the total $L_{\rm dust}$ that is not captured in our $L_{\rm IR}$. Likewise, the observed estimates lack the contribution from the 500 – 1000 μm regime since there are no data points there. Additionally, PAH peaks are included in the MAGPHYS model, but not in the observed SED owing to a lack of spectral resolution. As a result it is not surprising that MAGPHYS produces slightly higher total dust luminosities. This is also one of the reasons for choosing for a full SED model, rather than an ad hoc integration of the observed SED. The correlations we examined in the previous section still hold when using the empirical $f_{\rm dust}$ because the link with the MAGPHYS $f_{\rm dust}$ is tight and linear.

In a second test, we verified the validity of the MAGPHYS attenuation model of Charlot & Fall (2000). Interstellar and circumstellar dust extinction are described by a few parameters, and

their relative contribution is also a free parameter (for more details, see da Cunha et al. 2008). This parametrization creates enough diversity in the attenuation curves to cover a realistic range of attenuation levels. The dust model in MAGPHYS is a rather ad hoc, but physically motivated dust emission model. The dust SED is a combination of modified black bodies with different temperatures and emissivities, and a template for the PAH features based on M17 (da Cunha et al. 2008). It is difficult to compare this to self-consistent, physical dust models from e.g. Zubko et al. (2004), Draine & Li (2007) or Jones et al. (2013). Those models naturally yield extinction properties that (together with the dust distribution) lie at the basis of the attenuation curve. In MAGPHYS, the extinction model and the dust emission model are in fact two different entities. A handful of dust-related free parameters determine the shape of the MIR-submm SED, but it is the forced coupling with the absorbed starlight that drives the total dust luminosity. This so-called energy balance was modelled so that the total dust luminosity falls within 15% of the total absorbed stellar energy. The attenuation curve is consequently shaped by this combination of stellar and dust SEDs, not by imposing an attenuation or extinction law beforehand. For example, for galaxies with the same optical SED, the galaxy with the highest dust luminosity will have higher values of attenuation.

The reliability of MAGPHYS for different intrinsic galaxy attenuation curves has been studied by Hayward & Smith (2015). They performed MAGPHYS fits of synthetic galaxies created by a combination of radiative transfer and hydrodynamical simulations, where the intrinsic SED is known. They found that MAGPHYS was able to reproduce the intrinsic SED quite well if the attenuation curve did not deviate significantly from the true attenuation curve. In their tests, MW and LMC curves returned reliable fits, while SMC-type attenuation curves showed more discrepancy. It is not possible to measure the true attenuation curve for our sample, but we can argue that these local, star forming galaxies are not particularly low in metallicity (Hughes et al. 2013) and fall in the same class of large spirals like the MW. It is therefore likely that they will not have an SMC-like attenuation curve and our models provide a good estimate of the attenuation curve. It is difficult to quantify these model uncertainties, but this falls beyond the scope of this work.

The MAGPHYS extinction model does not include a bump at NUV wavelengths, as observed for the Milky Way or the LMC (Gordon et al. 2003; Fitzpatrick & Massa 2007). The absence or presence of an NUV bump will affect the model NUV flux. To check any influence on the determination of our attenuation parameters, we re-ran the fitting excluding the NUV data point from the SED of all galaxies. From the new set of models, we again computed $f_{\rm dust}$, $\xi_{\rm UV}$, and A_{FUV}. These NUV-less quantities are compared to their original values in Fig. 2.7. The bolometric attenuation is relatively unaffected by the exclusion of the NUV point. We find a Pearson coefficient r of 0.99. This is expected because the additional extinction by the NUV-bump is relatively small compared to the total absorbed energy. The effect is greater for the UV heating fraction, although MAGPHYS still retrieves the same best fit model in most cases and

$r = 0.97$. For 18 galaxies, no UV data points are left after removing the NUV point. This leaves only little constraint on the UV attenuation curve, making comparison difficult. Consequently they make up half of the scatter in the plots in the bottom row of Fig. 2.7. The determination of A_{FUV} appears to be quite robust against the exclusion of the NUV point, especially for higher values of attenuation. At the low attenuation side, MAGPHYS is more likely to find a different best fit model. However, these models still yield an attenuation that is relatively close to the old one, and no outliers are found. This results in a comforting r value of 0.98.

A final concern is whether MAGPHYS is able to capture the star formation history (SFH) of the galaxies in our sample. MAGPHYS adopts an exponentially declining SFH with a random chance of starbursts occurring over the lifetime of the galaxy. The reliability of this formalism has been tested by Smith & Hayward (2015) for the same set of hydrodynamical simulations as Hayward & Smith (2015) in the discussion above. Although they are able to retrieve the intrinsic SFHs for normal galaxies, it requires marginalising over the library of fitted SEDs. In fact, they find that the SFH of the best fit model is not reliable. Unfortunately, they do not test the influence of the SFH discrepancy on any of the MAGPHYS output parameters, such as stellar mass and SFR. Additionally, for more complex SFHs such as strong bursts and mergers, MAGPHYS is not able to retrieve the SFH even when marginalising over the fitted SEDs. In contrast, when star formation is quenched in a galaxy, a truncated SFH model is necessary according to Ciesla et al. (submitted). They fitted their truncated SFH model to the same sample as ours (HRS late-type galaxies) using CIGALE (Noll et al. 2009). They found little difference with fitting results of a double exponentially declining SFH with a short burst for normal spirals. However, HI deficient spirals were usually better fitted by the truncated SFH, with the main difference being a better fitting UV part. However, the SFH they compare with differs from the MAGPHYS SFH, which uses an exponential model with random short bursts. Without this addition of multiple short bursts, it appears to be difficult to produce an UV SED that fits both *GALEX* data points. In our MAGPHYS fits, even for the HI deficient galaxies, the SED matches the *GALEX* observations for virtually all galaxies.

From these two recent studies, it is not clear how strong the influence of the SFH is on the key parameters we use in this work. MAGPHYS has been tested and proved to give consistent estimates of main galaxy parameters for various samples of local star forming galaxies (e.g. da Cunha et al. 2008, 2010; Smith et al. 2012d; Driver et al. 2016, and reference therin). Although the SFH can influence parameters, such as stellar mass and SFR during the evolution of a galaxy, there is a strong degeneracy, and many SFH models can reproduce the same observed $M_\star$ and SFR.

Michałowski et al. (2014) investigated the effect of the SFH parametrisation on stellar mass for a set of simulated submm galaxies. They found that MAGPHYS slightly overestimates the true stellar masses. We can compare the SFRs from this work with the ones derived in Boselli et al. (2015). They determined the SFR for HRS late-type galaxies using several observational

tracers and also using SED fitting. We find strong correspondence in SFR across the sample, with Pearson's correlation coefficients over 0.85. There is, however, a systematic offset of about 0.1-0.3 dex between our values (which are lower) and the different tracers from Boselli et al. (2015). Without going into detail, we attribute these systematic offsets to differences in the modelling. This includes different assumptions in the SFH and has also been found by Pacifici et al. (2015) for a sample of galaxies at redshifts 0.7-2.8. On the other hand, Buat et al. (2014) investigated the SFR for a sample of $z > 1$ galaxies using SED fitting again with different SFHs. They found that the SED-derived SFRs are slightly *higher* than the classical IR+FUV tracer. The bottom line here is that while this may influence the absolute location of the correlations in the plots with $f_{\rm dust}$ and $\xi_{\rm UV}$, it does not neutralise the trends we found.

It is even more difficult to quantify how the SFH influences the attenuation curve and the derived parameters $f_{\rm dust}$, $\xi_{\rm UV}$, and A_{FUV}. There is a strong need for more research in this area. In particular, the mutual influence of the dust model and the SFH model on retrieving the correct attenuation curve of galaxies is an important question to address in the future.

2.6 Conclusions

We have performed panchromatic (UV-submm) SED modelling of the HRS late-type galaxies. Our main goal was to quantify the total amount of absorbed energy by dust. We used the power of MAGPHYS to investigate the difference between the observed and the intrinsic (dust free) SEDs of our sample and derive three key parameters; the bolometric dust fraction $f_{\rm dust}$, the UV heating fraction $\xi_{\rm UV}$, and the FUV attenuation A_{FUV}. We connected these quantities to key parameters of galaxy evolution, such as $M_\star$, SFR, and sSFR. Our main conclusions are:

- The mean bolometric attenuation $\langle f_{\rm dust} \rangle$ is 32% for our sample. For local, star forming galaxies about one third of the energy produced by stars is absorbed by dust. This number is, quite surprisingly, in line with previous estimates derived from small and incomplete samples.
- We confirmed a weak trend between $f_{\rm dust}$ and morphological type. A broad range of $f_{\rm dust}$ values were found for each type of galaxy. The strongest correlation ($\tau = 0.44$) was found with SFR, but still with significant scatter.
- The mean UV heating fraction $\langle \xi_{\rm UV} \rangle = 0.56$, but with a broad distribution. For our sample, more than half of the stellar energy is absorbed in the UV domain.
- There is a clear trend between $\xi_{\rm UV}$ and morphological type with significantly higher UV heating in galaxies of later type. We also found a strong correlation with sSFR, a known indicator of the heating of dust. The relation is not linear, and we provided a power law fit in equation 2.3.

- We find no evidence that the presence of a strong AGN in a galaxy affects the attenuation properties that galaxy.
- We revisited the IRX vs. A_{FUV} relation with both quantities derived directly from the best fit models, offering a self-consistent framework. We calibrated this relation for different values of $NUV - r$, using a second-order polynomial. The best fitting relations are given in Table 2.2. This framework allows to estimate A_{FUV} based on quantities that are relatively easy to obtain and to determine the FIR properties of galaxies lacking observations in this regime.

The HRS is designed to provide a concise view of the large galaxies in our local universe. The results of this work should therefore be representative for nearby spirals. The derived relations can be applied to a larger set of local galaxies and can be compared with a similar analysis at higher redshift. The latter in particular could yield important insight into the evolution of energy absorption and reprocessing by dust.

MAGPHYS and other energy balance codes are ideal tools for performing this kind of study in a relatively fast and straightforward way. However, the results are still an interpretation through the underlying galaxy model inherent to the code. While the results appear to be robust, it is still uncertain how well the star formation history and the attenuation curve are reproduced. The effect of a discrepancy in one or both of these two key elements on our parameters is difficult to quantify and requires a more dedicated investigation.

Dust scaling relations in Andromeda

3

How many times must a man look up before he can see the sky?

Bob Dylan

3.1 Introduction

The effect of dust on the observation of starlight is evident from our results in chapter 2. These effects must be taken into account when deriving galaxy properties. Panchromatic SED fitting is a powerful method to do this, and provide reliable estimates of main galaxy parameters such as star formation rate (SFR), stellar mass, dust temperature, and dust mass.

Correlations between the main properties of dust, gas, and stars, also known as *scaling relations*, define a tight link between these constituents. In the past, relations between the dust-to-gas ratio on the one hand and metallicity or stellar mass on the other hand were the only notable relations that were being investigated (Issa et al. 1990; Lisenfeld & Ferrara 1998; Popescu et al. 2002; Draine & Li 2007; Galametz et al. 2011). Only recently were other scaling laws more systematically investigated. Namely, the ratio of dust to stellar mass, the specific dust mass, which was found to correlate with the specific star formation rate (i.e. star formation rate divided by the stellar mass, Brinchmann et al. 2004; da Cunha et al. 2010; Rowlands et al. 2012; Smith et al. 2012b), NUV–r colour (i.e. the difference in absolute magnitude between the GALEX NUV and SDSS r band), and stellar mass surface density $\mu_\star$ (Cortese et al. 2012b; Agius et al. 2013).

Each of the above scaling laws was derived on a galaxy-galaxy basis, considering galaxies as independent systems in equilibrium. In order to fully understand the coupling of dust with stars and the ISM, we must zoom in on individual galaxies. This is however troublesome at FIR/submm wavelengths because of the limited angular resolution. Only in the last few years,

Chapter based on Viaene et al. (2014).

we have been able, thanks to *Herschel*, to observe nearby galaxies in the FIR and submm spectral domain whilst achieving sub-kpc resolutions for the closest galaxies (< 5.7 Mpc) in the 500 μm band. Dust scaling relations on subgalactic scales were thus so far limited to gas-to-dust ratios for a handful of local galaxies (see e.g. Muñoz-Mateos et al. 2009a; Bendo et al. 2010b; Magrini et al. 2011; Sandstrom et al. 2013; Parkin et al. 2012).

Today, exploiting PACS and SPIRE, plus the 3.5-metre mirror onboard *Herschel*, IR astronomy has gone a leap forward. Spatial resolutions and sensitivities have been reached that allow us, for the first time, to accurately characterise the dust emission in distinct regions of nearby galaxies. To properly investigate scaling relations on a local scale, one would ideally need a self–consistent model to derive the desired physical quantities. The complexity of a full stellar and chemical evolution model for galaxies, however, requires some simplifications. The models should treat both stellar and dust components, taking into account their influence on each other (the so–called dust energy balance). Panchromatic emission modelling of subgalactic regions has been carried out by Mentuch Cooper et al. (2012) for the Whirlpool galaxy (M51). However, the stellar and dust components were treated separately. Boquien et al. (2012, 2013), have performed panchromatic pixel-by-pixel fits of nearby star forming galaxies using CIGALE (Noll et al. 2009), which does include a dust energy balance. They showed that most of the free parameters could accurately be constrained, given a sufficiently large range of priors.

The proximity of ISM regions is crucial in order to obtain the desired, sub-kpc spatial resolution. The closest giant molecular cloud systems are of course in our own Milky Way, but it is not possible to probe the entire Galaxy. The Magellanic clouds are the nearest galaxies as they are close satellites of the Milky Way. These objects are, however, quite irregular and lower in metallicity and in total mass, hence they do not represent the well–evolved ISM of virialised large galaxies. Andromeda (M31) is the closest large galaxy to our own Milky Way, As described in section 1.4, it lies at a distance $D_{\mathrm{M31}} = 785$ kpc (McConnachie et al. 2005), which means every arcsecond on the sky corresponds to 3.8 pc along the major axis of M31. The gas and dust components of Andromeda have been extensively studied in the past (e.g., Walterbos & Schwering 1987; Montalto et al. 2009; Tabatabaei & Berkhuijsen 2010) using low–resolution data at FIR wavelengths and simplified models.

Although mapped in all wavelengths from UV to the FIR in the past, high–quality submm observations are thus far not available, yet these wavelengths are crucial to constraining the properties of the cold dust. The *Herschel* Exploitation of Local Galaxy Andromeda (HELGA, Fritz et al. 2012, hereafter HELGA I) is the first programme that mapped M31 from 100 μm to 500 μm with *Herschel*, covering a large $5.5^\circ \times 2.5^\circ$ field centred around the galaxy. Even at the sparsest *Herschel* resolution ($36''$ at 500 μm), physical scales of only 140 pc are resolved. Andromeda is consequently the best suited object for studying the ISM in great detail while allowing at the same time, the comparison with global properties.

In Smith et al. (2012c) (hereafter HELGA II), we performed a pixel-by-pixel SED fit to the *Herschel* data and mapped dust properties of Andromeda. Ford et al. (2013) (hereafter HELGA III) investigated the star formation law in M31 on both global and local scales. A catalogue of giant molecular clouds was recently constructed by Kirk et al. (2015) (hereafter HELGA V).

We aim to expand on this work by carrying out an in-depth investigation of the dust scaling relations in Andromeda. We do this by fitting the panchromatic SED of each statistically independent 36–arcsecond region in the galaxy with MAGPHYS. This will produce the largest and most complete view of the stars and ISM dust in a large spiral galaxy.

The arrangement of this study is as follows. In Sect. 3.2 we give an overview of the data used. Section 3.3 goes into more detail on the processing of multi-wavelength data. The results are given in Sect. 3.4, along with the parameter maps of Andromeda. We analyse the dust scaling relations of Andromeda in Sect. 3.5. In Sect. 3.6 we present our discussion and main conclusions.

3.2 The dataset

Modelling the full spectrum of a galaxy requires a fair number of free parameters and consequently sufficient data points to sample the problem in a meaningful way. The Andromeda galaxy has been observed by many space borne telescopes such as the GALEX, *Spitzer*, and WISE. Recently, the *Herschel* Space Observatory was added to this list and has been the main drive for this investigation. Ground–based observations from SDSS complete our panchromatic dataset. A detailed account on the data treatment, including uncertainty estimates, for each of the observations is given in Section 3.3.

3.2.1 Infrared data

Far-Infrared and submillimetre observations with the *Herschel* Space Observatory catch the peak in emission of the diffuse interstellar dust. This component plays an essential role in the energy balance of the SED. Andromeda was observed with both PACS and SPIRE instruments in parallel mode. Because of the large extent of the galaxy, observations were split into two fields. Both fields were combined during data reduction, resulting in $\sim 5.5^\circ \times 2.5^\circ$ maps at 100, 160, 250, 350, and 500 μm. In the overlapping area of the two fields, the signal-to-noise ratio is slightly higher. The full width half maximum (FWHM) of point sources in the final PACS maps are 12.5″ and 13.3″ at 100 μm and 160 μm, respectively (Lutz 2010). The resulting SPIRE maps are characterised by beams with a FWHM of 18.2″, 24.5″, and 36.0″ at 250, 350, and 500 μm (Herschel Space Observatory 2011). Galactic dusty structures tend to cause

foreground emission when observing nearby galaxies. The north-east part of the M31 disk clearly suffers from this kind of cirrus emission. Following a technique devised by Davies et al. (2010b), Galactic cirrus emission was disentangled from the light of the M31 disk. A detailed description of the data reduction process, including cirrus removal, can be found in HELGA I. The authors performed the cirrus subtraction before dedicated maps from the *Planck* mission became available. These maps could provide additional constraints on the cirrus subtraction, despite their lower resolution. Nevertheless, an independent effort (Draine et al. 2014) produced cirrus-subtracted maps which are consistent with the ones from HELGA I, which we will use in this chapter.

The Multiband Imaging Photometre of *Spitzer* (MIPS; Rieke et al. 2004) observed the mid-infrared and far-infrared light of M31 in its three bands (24, 70, and 160 μm). Gordon et al. (2006) made a complete data reduction of the observations, covering a $1^\circ \times 3^\circ$ area along the major axis of the galaxy. The images have standard MIPS FWHM values of 6.4″, 18.7″, and 38.8″ at 24, 70, and 160 μm, respectively (Rieke et al. 2004). Both MIPS and PACS cover a wavelength range around 160 μm. While this could be used to more accurately estimate the uncertainties at this wavelength, it limits our working resolution. Both MIPS and PACS measurements come with a total uncertainty of $\sim$ 10% in their 160 μm band so they can be considered equally sensitive. We therefore opted to omit the MIPS 160 μm image from our sample.

The same area of M31 was also mapped in all four bands of the *Spitzer* Infrared Array Camera (IRAC; Fazio et al. 2004). The complete data reduction, including background subtraction, was carried out by Barmby et al. (2006). Their final, background subtracted frames have the standard FWHM values of 1.6, 1.6, 1.8, and 1.9 arcseconds in the 3.6, 4.5, 5.8, and 8 μm wavebands, respectively.

Complementary to the IRAC/MIPS observations, the mid-infrared part of M31 has been observed by WISE as part of an all-sky survey at 3.4, 4.6, 12, and 22 μm. High–quality mosaics of M31 were provided by the WISE Nearby Galaxy Atlas team (Jarrett et al. 2013). Recent results from these authors have proven the possibility of enhancing the resolution of WISE using deconvolution techniques. Here, however, we use the mosaics with the standard beams because we will have to degrade the resolution to the SPIRE 500 μm beam in order to remain consistent. The FWHM of the WISE beams are 6.1, 6.4, 6.5, and 12.0 arcseconds at 3.4, 4.6, 12, and 22 μm, respectively (Wright et al. 2010).

Several WISE and Spitzer bands lie close to each other in central wavelength. This overlap improves our sampling of the ambiguous MIR SED and will reduce the dependence of the SED fit on a single data point, which is important in the coarsely sampled wavelength ranges, e.g. around 24 μm. At the same time, this serves as a sanity check of the measurements of both instruments. We found no strong outliers between WISE and Spitzer fluxes.

Efforts to observe M31 in the NIR bands include the 2MASS survey (Skrutskie et al. 2006; Beaton et al. 2007) and the ongoing ANDROIDS project (Sick et al. 2014), all of them covering the J, H, and K bands. The main difficulty of NIR imaging is the brightness of the sky. At these wavelengths the brightness can vary significantly between pointings, making it extremely hard to produce a large–scale mosaic with a uniform background. To meet the goals of our investigation, it is important to have a reliable and consistent absolute flux calibration over the entire disk of M31. No JHK bands were included in our dataset for this reason. The NIR part of the SED is, however, sufficiently covered by the WISE, IRAC, and SDSS i and z bands.

3.2.2 UV/optical data

The Sloan Digital Sky Survey mapped M31 at superb resolution (FWHM $\sim$ 1.2 arcsec) in its optical u,g,r,i, and z filters. Background estimation for these observations proved difficult because of the great extent of the galaxy and the narrow field of view of the telescope. Tempel et al. (2011) created detailed mosaics from the separate SDSS tiles, taking special care of background subtraction and flux preservation. The resulting frames span a stunning $2.5^\circ \times 8^\circ$ field with a pixel scale of 3.96 arcseconds. The mosaics are contaminated by several artefacts around the brightest sources, especially in the u and z bands. They are most likely ghost projections as they are slightly smaller and appear on each of the four sides of brightest sources along the pixel grid. After masking (see Sect. 3.3.1), the images proved sufficiently reliable for SED fitting at SPIRE resolutions.

Unattenuated ultraviolet photons are the main tracers of very recent star formation. Most of the emitted UV light, however, is heavily attenuated by interstellar and circumstellar dust and consequently important to constrain the dust distribution in our spatially resolved SED. Thilker et al. (2005) created images using separate observations from the Galaxy Evolution Explorer (GALEX) in both near-UV (NUV) and far-UV (FUV) filters. The number of frames has recently been expanded to 80, almost fully covering a $5^\circ \times 5^\circ$ field around the centre of M31. Their mosaics have FWHM values around $5''$. Because of the co-adding of separate tiles, background variations were visible at the edges of each tile. Additionally, the UV sky around M31 is clouded with scattered light from Galactic cirrus structures. Both features will be taken into account as background variations in the uncertainty estimation for the fluxes.

3.3 Multi-wavelength data processing

In this section we present the road towards spatially resolved, panchromatic SED fitting. The data obtained from various sources and own *Herschel* observations are manipulated in order to make a consistent comparison over such a wide wavelength range (Sect. 3.3.1). These manipulations bring with them a complex uncertainty propagation which is addressed in Sect. 3.3.2.

3.3.1 Image manipulations

Background subtraction

The WISE and GALEX subsets had a non-zero average background value due to emission from unresolved sources. The *Herschel* images also come with a flat, non-zero background as a consequence of the data reduction process. The average background for the *Spitzer* and SDSS images was already zero, hence no background subtraction was performed for these frames.

While global background gradients were significant in the WISE frames, no clear gradients were identified in the GALEX or *Herschel* images. We therefore fit and subtract a second–order polynomial to the background in the WISE frames using standard `ESO-MIDAS` routines. In the other frames, we estimate the background as follows.

A set of regions was chosen far enough from visible emission from M31 to avoid contamination by the galaxy, but close enough to make a reliable estimation of the background near the M31. Inside these pre-defined regions, a number of aperture measurements was made. The number of measurements per region was set to be proportional to the number of pixels inside. For PACS and SPIRE, a total of 10000 measurements were spread over 8 regions. In the GALEX fields, 20000 measurements were divided over 23 regions. From the set of measured fluxes, a sigma clipped median was derived as a reliable estimate for the background flux. We used 3σ as a threshold and iterated until convergence. This median background value was consequently subtracted from the images.

Masking

Andromeda covers a large part of the sky for a single galaxy and lies close to the Galactic disk (with a Galactic latitude of $-21.6°$). It is consequently contaminated by the light of thousands of foreground stars, especially in the UV and optical part of the spectrum. At longer wavelengths, the infrared emission of background galaxies becomes the main source of contaminating sources. At *Herschel* wavelengths, however, most of the emission from non-M31 point sources is negligible even at scales of the SPIRE 500 μm beam. As mentioned before, the extended emission of the Milky Way Galactic Cirrus is prominently visible here. This dust emission can fortunately be associated with HI emission. Using the velocity information of HI maps, the Galactic cirrus can partly be disentangled from the emission of M31. HELGA I goes into more detail about this technique.

We made use of SExtractor v2.8.6 (Bertin & Arnouts 1996) to list the location of all point sources above a certain threshold (5 times the background noise level). The program simultaneously produces background maps that can be tweaked to represent the diffuse emission from

M31. In this way, we could replace the non-M31 point sources with the local M31 background value obtained from these maps.

For each source an optimal radius was derived by comparing the pixel flux with the local background at increasing distance from the peak location. Once the pixel-to-background flux ratio dropped below 2, the radius was cut off at that distance. Based on this radius, a total flux was extracted in order to make colour evaluations. We constructed point source masks for the GALEX, SDSS, WISE, and *Spitzer* subsets based on different colour criteria.

The GALEX and SDSS point sources were evaluated based on their UV colour. This technique was applied by Gil de Paz et al. (2007) for over 1000 galaxies and proved successful. In practice, we mask all sources with

$$| FUV - NUV | > 0.75 \tag{3.1}$$

if they are detected at the 1σ level in their particular wavelength band. SExtractor identified 58330 point sources in the UV fields, of which over 51000 were masked in the FUV and NUV. Many point sources from the UV catalogue were not detected at optical bands, hence only 25000 sources were masked in the SDSS bands. Around 7000 sources were identified as extragalactic. They were therefore assumed to belong to M31 and were not masked.

As an example, Fig. 3.1 shows the *u*–band image of M31 before and after the mask was applied. The contamination of the image has been significantly reduced using the above technique.

The point sources in the WISE and the *Spitzer* IRAC and MIPS frames were masked analogously, based on their IRAC colours (see below). At these wavelengths, however, the non-M31 point sources are a mix of foreground stars and background galaxies. Furthermore, some bright sources may be associated with HII regions in M31 and must not be masked. We designed a scheme based on the technique by Muñoz-Mateos et al. (2009b), which was successfully applied to the SINGS galaxies. Foreground stars have almost no PAH emission, while the diffuse ISM in galaxies shows a roughly constant $F_{5.8}/F_8$ ratio (Draine & Li 2007). Background galaxies are redshifted spirals or ellipticals and can consequently have a wide range in $F_{5.8}/F_8$. It is thus possible to construct a rough filter relying on the difference in MIR flux ratios. First, it was checked which point source extracted from the IRAC 3.6 μm had a non-detection at 8 μm. This criterion proved to be sufficient to select the foreground stars in the field. A second, colour-based, criterion disentangled the background galaxies from the HII regions:

$$0.29 < F_{5.8}/F_8 < 0.85 \tag{3.2}$$

$$F_{3.6}/F_{5.8} < 1.58. \tag{3.3}$$

Figure 3.2 shows the colour–colour diagram for these sources. The HII regions follow a more or less horizontal track at the lower–left part of the plot. The colour criteria for filtering out these HII regions were obtained empirically to ensure effective identification. Once identified,

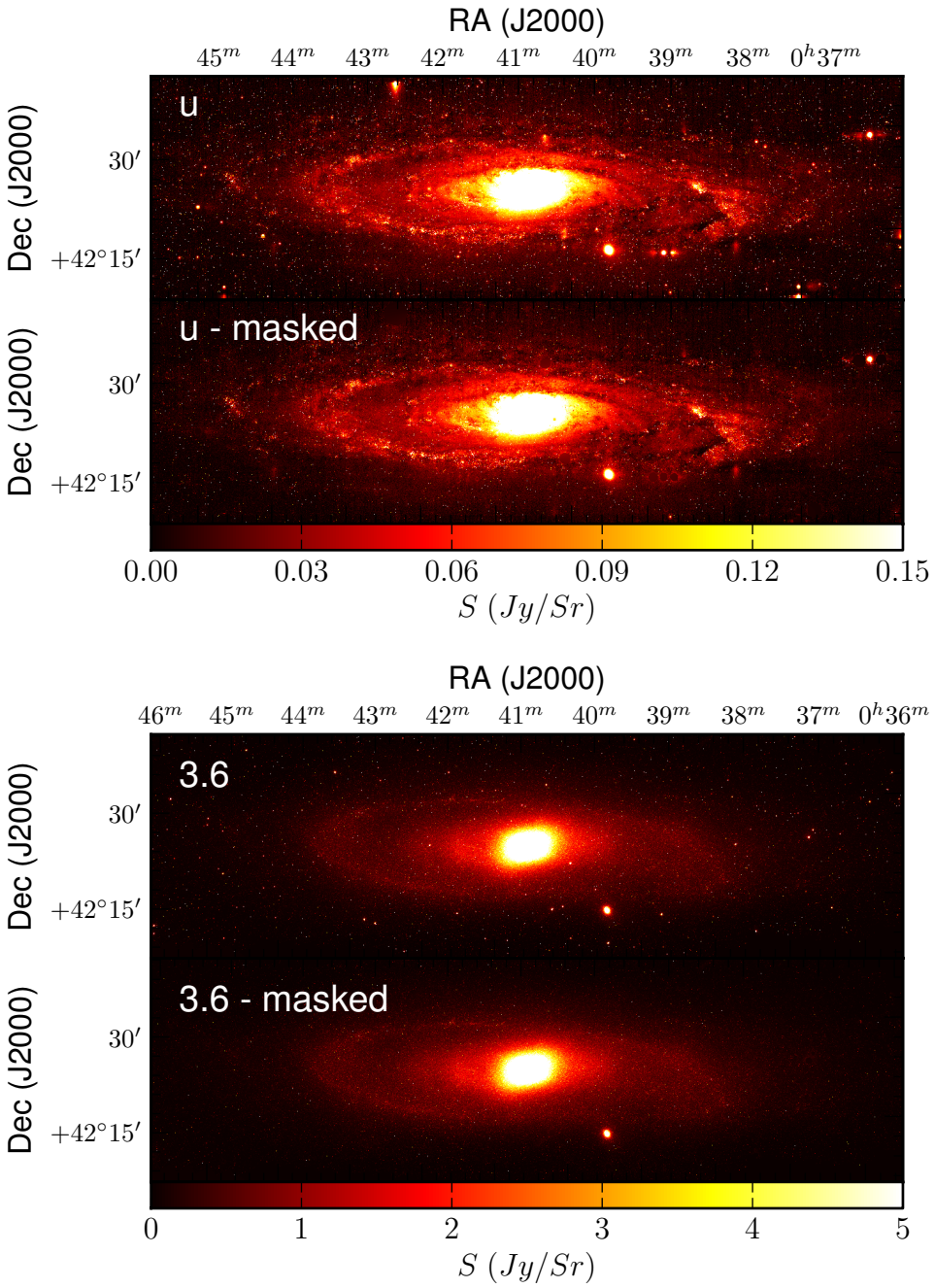

Figure 3.1: Masking of point sources that do not belong to M31: before and after view of the galaxy in the *u* band (top) and IRAC 3.6 μm band (bottom). The bright source that is still visible below Andromeda is its satellite M32.

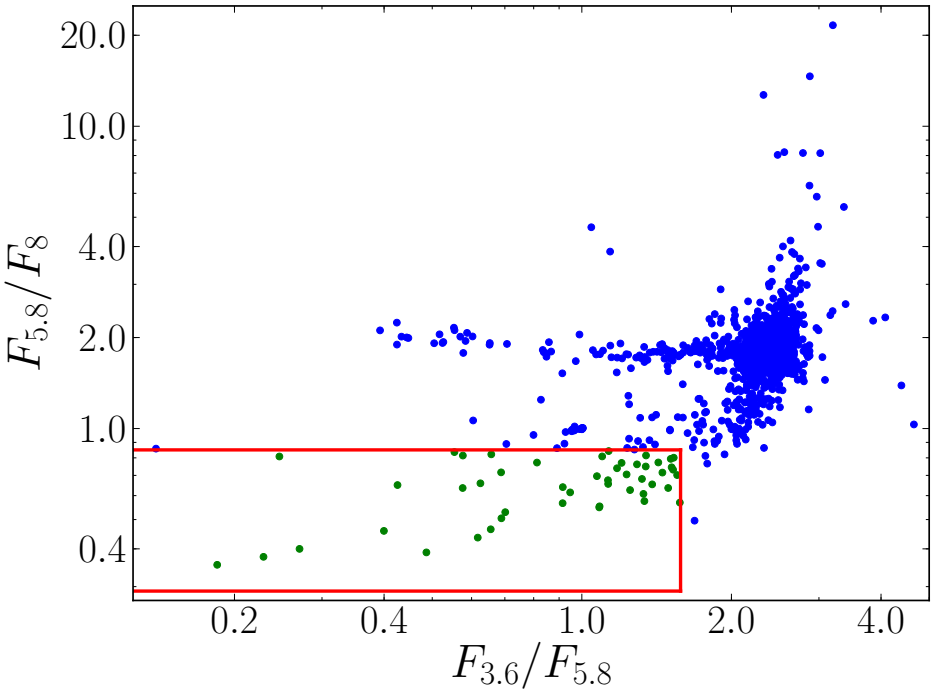

Figure 3.2: Colour-colour plot of the IRAC selected bright sources. The sources inside the red rectangle are identified as HII regions belonging to M31. They were consequently not masked.

these star forming regions were consequently not masked. The resulting mask was applied to all IRAC and MIPS bands. Sources that were not detected at longer wavelengths were obviously not masked. Figure 3.1 shows the IRAC 3.6 μm image of M31 before and after the mask was applied. SExtractor identified 1933 sources in the IRAC bands and 536 in MIPS. From these catalogues, around 1800 sources were masked in IRAC and 230 in MIPS. All masked sources in IRAC were also masked in the WISE frames as both instruments cover roughly the same wavelength range. No additional masking was necessary for the WISE data.

As a way to check the reliability of our masks, we compared the masked regions with the locations of known Andromeda sources, i.e. HII regions and planetary Nebula (Azimlu et al. 2011) and bright young clusters (Barmby et al. 2009). The overlap between our masked sources and actual M31 sources proved negligible; 0.3%, 0.1%, 0.4%, 0.4%, and 1.5% of the identified sources were incorrectly masked in the GALEX, SDSS, WISE, IRAC, and MIPS bands, respectively. The handful of sources that were incorrectly masked were manually restored.

Convolution and rescaling

The masked images were all brought to the same resolution before extracting the separate pixel values. By doing this, information is lost because of the significantly lower resolutions of the end products. It is, however, a critical step to make a consistent comparison of the fluxes over

this wide range of wavelengths. Our working resolution was limited by the SPIRE 500 μm point spread function, which is 36.0 arcseconds. As M31 is the nearest spiral galaxy, this still corresponds to an unprecedented physical scale of 136.8 pc. Aniano et al. (2011) conducted an in-depth study on convolution kernels for most known telescope PSFs. Additionally they wrote an efficient IDL routine `convolve_image.pro` which makes use of their designed kernels and takes NaN values into account when convolving. The kernels for the GALEX, WISE, IRAC, MIPS, PACS, and SPIRE instruments were readily available to make the convolution. For the SDSS images, we used a Gaussian-to-SPIRE 500 kernel which assumes an initial FWHM of 4″ for the SDSS images (see Sect. 3.2.2).

The SPIRE 500 μm beam is sampled with a pixel scale of 12″ for a FWHM of 36″. This means that over 95% of the light in the beam is captured by the 3x3 pixels of 12″ sampling the beam. It is common practice in pixel-by-pixel SED fitting of extended sources to bin these 9 pixels together and create pixels that are as independent as possible (see e.g. Aniano et al. 2012, for a detailed account). The convolved and rebinned frames were consequently rescaled to match the pixel grid of the SPIRE 500 μm rebinned image. Our data cube covers the electromagnetic spectrum from UV to submm wavelengths. Figure 3.3 gives an overview of all frames used for the fitting of a panchromatic SED to each pixel.

This series of steps results in sets of corresponding pixels which each represent a physical region of 136.8×632.0 pc along the major and minor axes (using an inclination of $i = 77.5°$). Off course, it must be noted that the third dimension, the direction along the line of sight, also contributes to the appearance of each pixel. Spiral galaxies are, however, known to have relatively thin disks compared to their lengths, so even along this axis, the resolution remains subgalactic. The attenuation effects of this larger dimension will, however, be treated during the modelling in terms of optical depth parameters (see Sect. 3.4.1).

3.3.2 Single–pixel uncertainties

Each pixel comes with several sources of uncertainty, which will have to be estimated and combined to a total error. Uncertainty propagation based on initial errors can become complex and hazardous after masking, convolutions, rebinning, and rescaling. In their Appendix D.1, Aniano et al. (2012) opted to start the uncertainty estimation after all these steps in their resolved analysis for NGC 628 and NGC 6946. They postulate two sources of uncertainties: background variations and calibration errors. Additionally, we add a third source for the UV and optical subsets: the Poisson error. This term is negligible for infrared and submm observations because of the large number of incoming photons.

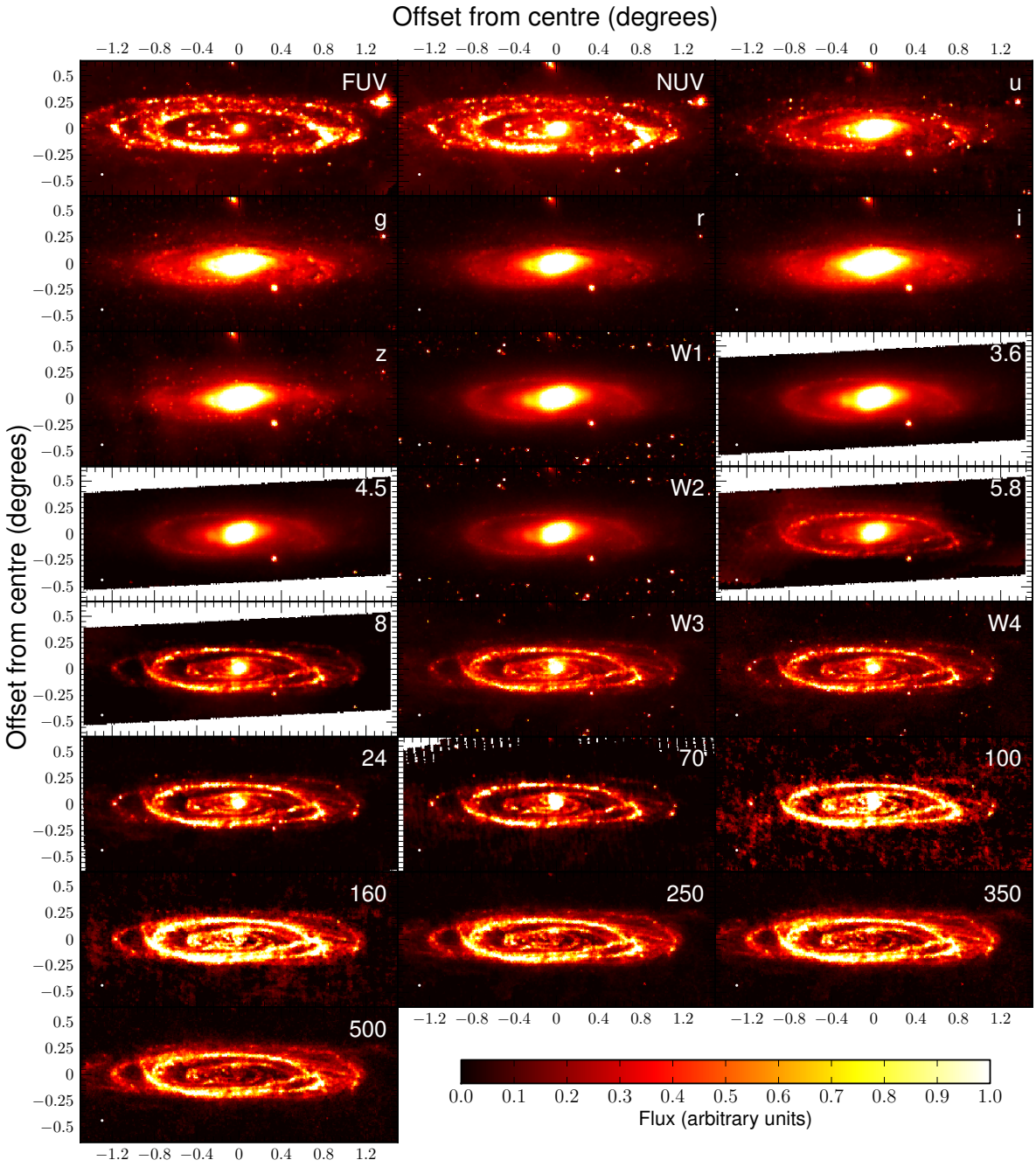

Figure 3.3: Overview of the FUV to submm dataset at SPIRE 500 resolution, rotated from a position angle of 38°.

Background variations

Variations of the background can give rise to errors in the flux measurements. To estimate the impact of this term, we select regions around M31 where the background is dominant. A sigma clipping filter is used on the pixels inside each region. Different methods of sigma clipping were evaluated. They proved not to affect the resulting variance by much as the evaluated regions were chosen to be free of point sources. In the end, a low–level clipping was done (10σ and only two iterations) to filter out any non-background emission. The variance of the remaining pixels from all of the regions will be a good representation of the background variation error $\sigma_{\text{background}}$, following Equation D2 from Aniano et al. (2012),

$$\sigma_{\text{background}} = \sqrt{\frac{1}{N_{\text{bg}} - 3} \sum_{(\text{x,y})} [I^{\text{obs}}(x, y)]^2}, \tag{3.4}$$

where N_{bg} is the number of background pixels used and I^{obs} the observed background subtracted flux of the pixel with coordinates x and y. For each telescope, a different set of background regions was used. This was needed because the background and Galactic Cirrus features change in morphology and brightness along the electromagnetic spectrum.

Poisson errors

Photon arrivals are considered a random event following a Poisson distribution; the variability of the counts scales with the square root of the number of photons. Infrared and submm observations deal with huge numbers of photons (all of which have low energy) and consequently have a negligible Poisson error compared to calibration uncertainties and background variations.

Optical and UV observations, however, do not collect as many photons and consequently their Poisson-like nature could start to play a more prominent role. In the cases of the GALEX and SDSS observations, the images were converted from flux to actual photon counts using the individual exposure time for each pixel and then converted to counts/Sr. This surface density unit was necessary to rebin and rescale the frames to the SPIRE 500 μm pixel grid without disrupting the exposure time information. We note that convolution did not take place here. The resulting images were converted back to counts using the new pixel scale and from here the Poisson errors could be computed for each individual pixel by taking the square root of the counts.

Table 3.1: Overview of the adopted relative calibration uncertainties for each pixel.

Filter	Error	Reference
GALEX-FUV	5%	a
GALEX-NUV	3%	a
SDSS	2%	b
WISE-W1	2.4%	c
WISE-W2	2.8%	c
WISE-W3	4.5%	c
WISE-W4	5.7%	c
IRAC-3.6	8.3%	d
IRAC-4.5	7.1%	d
IRAC-5.8	22.1%	d
IRAC-8	16.7%	d
MIPS 24	4%	e
MIPS 70	10%	f
PACS	10%	g
SPIRE	7%	h

References. (a) Morrissey et al. (2007); (b) Padmanabhan et al. (2008); (c) Jarrett et al. (2011); (d) Aniano et al. (2012); (e) Engelbracht et al. (2007); (f) Gordon et al. (2007); (g) HELGA I; (h) Herschel Space Observatory (2011).

Calibration errors

In higher signal-to-noise areas, the calibration of the instrumentation can become a dominant term. We therefore include a fixed percentage as calibration uncertainty for each filter (see Table 3.1) in addition to the previous error terms.

Finally, all error sources are added in quadrature for each pixel i and each wavelength band λ to obtain its total photometric uncertainty

$$\sigma^{\mathrm{Tot}}_{\lambda,i} = \sqrt{(\sigma^{\mathrm{bg}}_{\lambda,i})^2 + (\sigma^{\mathrm{cal}}_{\lambda,i})^2 + (\sigma^{\mathrm{Pois}}_{\lambda,i})^2}\,. \tag{3.5}$$

The above procedures yield a panchromatic SED for thousands of pixels, each corresponding to a sub-kpc region in Andromeda. A complete UV-to-submm spectral energy distribution will be fitted to each of these regions to investigate their underlying properties.

3.4.1 MAGPHYS

We again use MAGPHYS to perform the panchromatic SED modelling. The MAGPHYS SED libraries are derived from realistic, galaxy scale parameter values (da Cunha et al. 2008). The parameter space is thus optimised for objects that are orders of magnitude brighter than the sub-kpc regions to be modelled here. Pixel-by-pixel fitting makes no sense when the physical properties of a single pixel-region are out of the bounds of the MAGPHYS standard parameter space. We therefore adopted a flux scaling of 10^4 to obtain fluxes of the order of integrated nearby galaxies and feed these higher fluxes to the code for fitting. Most of the output parameters will remain unaffected because of their relative nature. Only four parameters scale with flux and do that linearly: M_*, $L_{\rm dust}$, $M_{\rm dust}$ and the SFR. These parameters were scaled back by the same factor to obtain their true fitted value.

As stated in appendix A.3, another limitation of the standard version of MAGPHYS is the range of cold dust temperatures, which is fixed between 15 K and 25 K. The boundaries of this interval are encountered in low (high) FIR surface brightness areas (see e.g. HELGA II). This causes the peak of the modified black body to be offset with respect to the observations and influences related parameters such as star formation and dust mass. We estimate that over 60% of the derived temperatures for cold dust lie outside of the standard 15 – 25 K interval (see upper panels of Fig. 3.4). The same is true for the temperature ranges of the warm dust. Here about 15% of all regions are estimated to lie outside the 30 – 60 K range. In order to execute reliable fits, it is thus mandatory to expand the temperature intervals and create a custom infrared library.

This is why we adopted a custom set of infrared SEDs (da Cunha, private communication). In the new library, cold dust temperatures $T_{\rm C}^{\rm ISM}$ range from 10 – 30 K and warm dust temperatures $T_{\rm W}^{\rm BC}$ from 30 – 70 K. With this extended library, the derived cold dust temperatures are more spread out over the parameter space, also populating the coldest ($<$ 15 K) regions (see the lower-left panel of Fig. 3.4). The distribution of the warm dust temperature is also considerably changed (lower–right panel), although the parameter space was only increased by 10 K. The peak is also not shifted towards higher temperatures as the distribution derived from the standard library would suggest. What we see here is a manifestation of the shift in cold dust temperature. As both dust components are not independent - the infrared SED is fitted entirely at the same

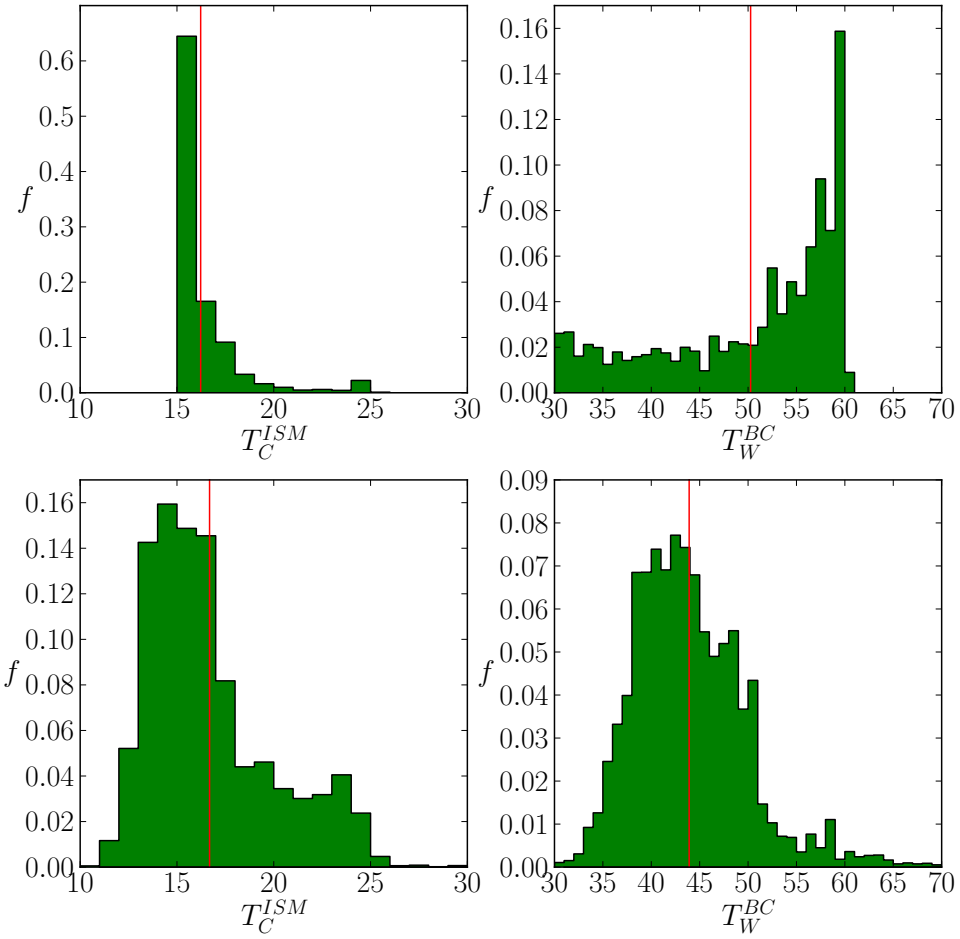

Figure 3.4: Distribution of the dust temperatures for the individual pixel fits. Top row; are the results from the standard MAGPHYS version. Bottom row; are the results from the modified version, using broader temperature ranges for the priors. The red lines indicate the average sample values.

time - the shift to lower cold dust temperatures will also cause a decrease in the warm dust temperature distribution in order to still match the flux in their overlapping area (FIR).

3.4.2 SED fits of sub-kpc regions

We perform panchromatic fits for a total of 22437 pixels within an ellipse with major axis of 22 kpc and an apparent eccentricity of 0.96, covering 2.24 square degrees on the sky. This area corresponds to the B-band D_{25} radius of M31 (de Vaucouleurs et al. 1991). The pixels are the same size as the FWHM of the 500 μm beam, making them statistically independent from each other. The choice of our aperture is limited to the field of view of the IRAC frames, which cover the main stellar disk of M31, but does not extend up to NGC 205 or to the faint outer dust structures as seen in the SPIRE maps. However, the field is large enough to cover over 95% of the total dust emission of the galaxy (Draine et al. 2014).

Quality of the fits

Instead of eliminating *a priori* those pixels with a non-optimal spectral coverage, we decided to exploit one of the characteristics of MAGPHYS, that is that the final results, i.e. the physical parameters we are looking for, are given as the peak values of a probability distribution function (PDF). When a pixel has a SED which is characterised by a poor spectral sampling, the parameters that are more influenced by the missing data points, whatever they are, will have a flatter PDF, showing the tendency to assume unrealistic values. For example, output parameters related to the stellar components (stellar mass, SFR, etc.) will be questionable for pixels in regions of Andromeda where the UV and optical background variations become dominant. Parameters related to interstellar or circumstellar dust turn unreliable when reaching very low flux density areas in the *Herschel* bands.

To decide which pixels are to be considered reliable for a given parameter and which ones should be not considered, we evaluate the mean relative error of each fit. Each PDF comes with a median value (50th percentile), a lower limit (16th percentile), and an upper limit (84th percentile). A way to quantify the uncertainty of the median value is to look at the shape of the PDF. Broadly speaking, if the peak is narrow, the difference between the 84th and 16th percentile will be small and the corresponding parameter will be well constrained. For a broad peak or a flat distribution, the opposite is true. We define this mean relative error as follows:

$$\sigma_{\rm rel} = 0.5 \cdot (p_{84} - p_{16}) / p_{50}, \tag{3.6}$$

where the p_x indicate the percentile levels of the PDF. This error only reflects the uncertainty on the modelling.

A double criterion was needed to filter out unreliable estimates for each of the parameters considered in Table A.1, because the average $\sigma_{\rm rel}$ is quite different in each parameter. Furthermore, it proved necessary to filter out most of the parameter estimates related to the outermost pixels in our aperture. These regions have FIR emission below the *Herschel* detection limits. A reliable detection at these wavelengths is crucial in constraining most of the dust-related parameters. Pixels with a non-detection at either PACS 100 μm or PACS 160 μm make up almost 40% of the sample. At the same time, these pixels generally have higher photometric uncertainties at shorter wavelengths as they correspond to the faint outskirts of the galaxy. Together with their poorly sampled FIR SEDs, their corresponding parameter estimates will have broad PDFs. We rank, for each parameter, all pixels according to increasing relative error for that particular parameter. Then, 40% of the parameter estimates (those with the highest mean relative errors) were removed from the sample. This corresponds to the exclusion of 8975 pixels per parameter.

Secondly, as several parameter estimates with broad PDFs were still present after the first filtering, an optimal cut was found which excludes these estimates. We chose to remove any parameter estimate with $\sigma_{\rm rel} > 0.32$. The combination of these filters excluded, for each parameter, all pixels with an unreliable estimate of this parameter. We note that the excluded pixels themselves might differ for each parameter set. For example, the dust mass of a particular pixel might be poorly constrained and thus removed. On the other hand, the stellar mass of that same pixel, will be kept in the sample if it meets our filter criteria. Most of the excluded pixels are associated with the outskirts of our field-of-view. However, there are certain pixels in the interring regions that do not meet our threshold for reliability. This is particularly the case for the SFR, sSFR, $T_W^{\rm BC}$,and τ_V parameters.

Several pixels (4384 in total) did not meet the requirements in any of the parameters and were thus completely removed from the sample (meaning they were not considered in the χ^2 distribution or in any further analysis). The distribution of the best–fit χ^2 values is shown in the upper–left panel of Fig. 3.5 and has an average value of 1.26. Here again, we find that the χ^2 values are generally too high then they should be from a theoretical point of view. Using the degrees of freedom (DOF) estimate of Smith et al. (2012a), we find (for 22 bands) that DOF=16. This means that 95% of our χ^2 values should lie below 1.20. For the distribution in Fig. 3.5, only 69% of our χ^2 values lie below this threshold. As we discussed in section 2.3, this most likely points towards an underestimate of the uncertainties. We note that this should be seen as a caveat, but it does not prohibit us from deriving basic galaxy properties and investigating their correlations. We do need to be careful in interpreting the uncertainty on these parameters.

Table 3.3 lists the number of reliable pixels for each parameter. In any further analysis, only these estimates will be used. Generally, $T_C^{\rm ISM}$ and $L_{\rm dust}$ are the best constrained parameters in the sample, with median uncertainties of 5% and 6%, respectively, and 13462 usable pixels. On the other hand, τ_V, $T_W^{\rm BC}$, and sSFR are the least constrained parameters. However, in the

case of sSFR, this quantity is computed from the SFR and stellar mass, the uncertainty on this parameter takes into account the uncertainty on both of its constituents, hence the relatively high median $\sigma_{\rm rel}$ of 0.18 for 6608 usable pixels. Quite differently, the high mean $\sigma_{\rm rel}$ (0.21 for 13462 usable pixels) on estimates for $T_W^{\rm BC}$ stems from the poor spectral coverage in the $30-70\,\mu$m regime. Other degeneracies in the fitting procedure will certainly reflect in the total number of reliable pixels per parameter, as well as in their median relative error. This is most obvious for τ_V, with a median $\sigma_{\rm rel}$ of 0.14 and only 3753 usable pixels. This parameter is not only influenced by the amount of dust, but also by its geometry with respect to the stars. This is impossible to take into account without complex radiative transfer modelling and falls beyond the goal of this work.

Consistency with previous parameter fits

We compare our results with previously derived values for each pixel, see Fig. 3.5. The MAGPHYS dust mass and cold dust temperature are compared to the modified black–body fits from HELGA II. Furthermore, our star formation rate is compared to the SFR derived from FUV+24 μm fluxes in HELGA III. Each pixel region of the HELGA II and HELGA III maps corresponds exactly to a pixel region in our sample, hence we are comparing parameter estimates for the exact same physical region.

In general, the different approaches yield consistent results. The dust mass shows the tightest relation ($rms = 0.08$), but also the largest offset $\Delta \log(\Sigma_{M_{\rm dust}}) = 0.22$. It is therefore important to understand what we are comparing here. For each dust component, the flux S_ν is modelled with a modified black–body function,

$$S_\nu = \frac{M_{\rm dust}}{D^2}\kappa_{\rm abs} B_\nu(T_{\rm dust}), \tag{3.7}$$

where D is the distance to the galaxy, $B_\nu(T_{\rm dust})$ the Planck function, and $\kappa_{\rm abs}$ is the dust mass absorption coefficient, modelled as

$$\kappa_{\rm abs} = \kappa_{\rm abs}(\lambda_0) \times \left(\frac{\lambda_0}{\lambda}\right)^\beta \tag{3.8}$$

with λ_0 the normalisation wavelength and β the emissivity index. MAGPHYS adopts the dust model from Dunne et al. (2000) (hereafter D00) who normalize the dust mass absorption coefficient at 850 μm: $\kappa_{850} = 0.077$ m^{2}kg^{-1}. At *Herschel* wavelengths this becomes $\kappa_{350} = 0.454$ m^{2}kg^{-1} assuming a fixed $\beta = 2$. In HELGA II, the Draine (2003a) (hereafter D03) absorption coefficient, which is $\kappa_{350} = 0.192$ m^{2}kg^{-1}, and a variable β were adopted. Lower $\kappa_{\rm abs}(\lambda_0)$ values are associated with more silicate-rich dust compositions (Karczewski et al. 2013). They will result in higher dust mass estimates, which is the case for HELGA II. On the other hand,

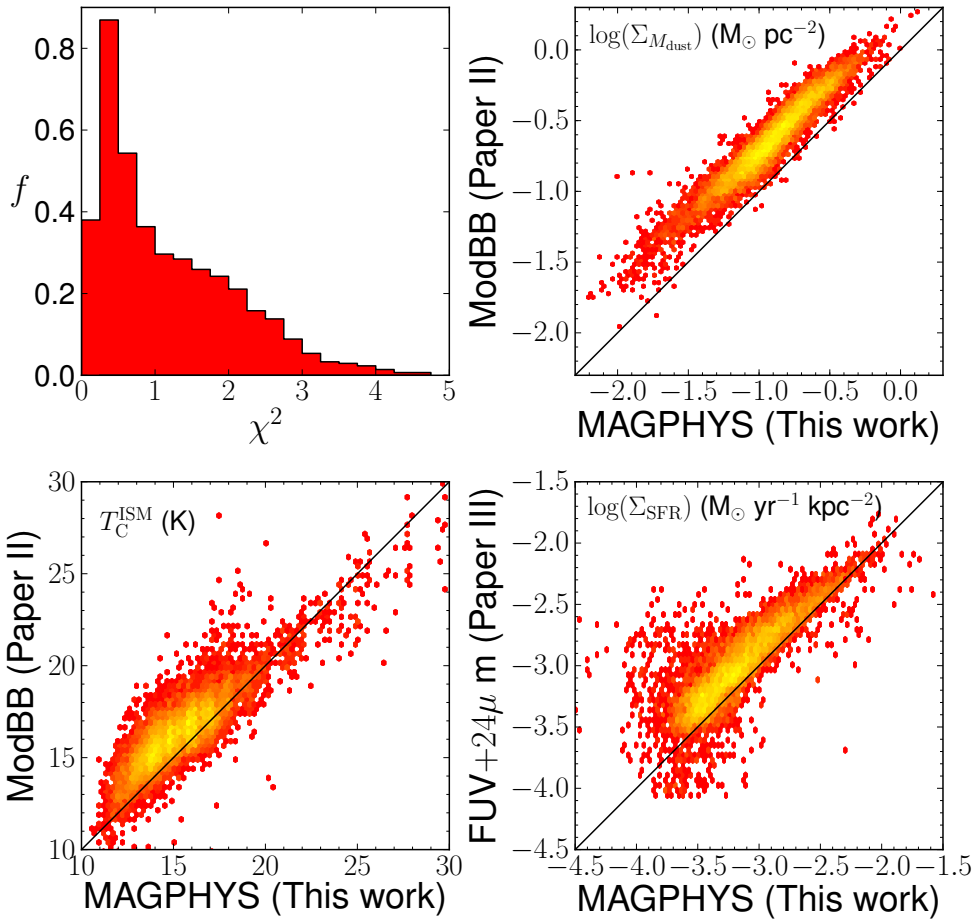

Figure 3.5: Upper–left: χ^2 distribution of the fits. Other panels: density plots comparing dust mass surface density, cold dust temperature, and star formation rate derived from MAGPHYS single pixel fits against modified black–body fits to *Herschel* bands (HELGA II) and FUV+24 μm SFR tracers (HELGA III). Red indicates a small number of data points, yellow a large number. The black line represents the 1 : 1 relation.

a variable β will generally result in higher dust temperatures. This will in turn yield lower dust masses. As MAGPHYS computes the total dust mass from components of various temperatures, grain sizes, and compositions, this should result in more realistic dust mass estimates.

A smaller offset ($\Delta T_d = 4.47$ K), but larger scatter ($rms = 0.93$) is seen in the temperature of the cold dust. The emissivity index β was fixed at 2 in this chapter, while left as a free parameter in HELGA II. As there is a known degeneracy between β and $T_{\rm dust}$ (see e.g. Hughes et al. 2014; Tabatabaei et al. 2014; Galametz et al. 2012; Smith et al. 2012c, and references therein), this could explain the scatter in the relation. Furthermore, most of the pixels in HELGA II had $\beta < 2$. Given this temperature-β degeneracy, smaller β values will yield higher dust temperatures. This probably explains the systematic offset from our sample.

The SFR shows a less clear deviation from the 1:1-relation. The rms of the scatter in the points is 0.28 and they have an offset of $\Delta \log(\Sigma_{SFR}) = -0.42$. We tend to find systematically lower SFR values compared to the FUV+24 μm tracer used in HELGA III. It must be noted that the SFR is derived in a different way in both approaches. The FUV+24 μm tracer is empirically derived from a sample of starforming galaxies (Leroy et al. 2008). Several regions in M31 exhibit only low star forming activity, far from the rates of starforming galaxies. Additionally, this formalism assumes a stationary star formation rate over timescales of 100 Myr. In M31, we resolve sub-kpc structures, where star formation may vary on timescales of a few Myr (Boselli et al. 2009). MAGPHYS does allow variations in SFR down to star formation timescales of 1 Myr.

Most of the outliers in the SFR plot of Fig. 3.5 correspond to pixels surrounding the bulge of M31. It is in these areas that the MIR emission from old stars is modelled quite differently. Overall, we expect that our SED fits give a more realistic estimate of the SFR because they take information from the full spectrum and are derived from local star formation histories.

Total dust and stellar mass

One of the most straightforward checks we can perform between our modelling technique and other techniques, is a comparison between the total number of stars and dust in M31. With respect to the first component, we find a value of $\log(M_\star / M_\odot) = 10.74$ from the fit to the integrated fluxes (see Sect. 3.4.2). This value, calculated by exploiting simple stellar population (SSP) models assuming a Chabrier (2003) IMF, lies a factor of 1.5–3 below dynamical stellar mass estimates for Andromeda (e.g. Chemin et al. 2009; Corbelli et al. 2010). This discrepancy can be easily accounted for if we consider that often in dynamical models the derived stellar M/L ratio are consistent with more heavyweight IMFs. Tamm et al. (2012) did exploit SSP models to calculate the stellar mass, and found values in the $\log(M_\star / M_\odot) = 11 - 11.48$ range, using the same IMF as we do. This discrepancy might arise from a number of possible causes: first of all, the aperture used to extract the total fluxes is slightly smaller in our case and

secondly, a different masking routine was applied to remove the foreground stars. The likely most effective difference, however, could be due to the fact that MAGPHYS considers an exponentially declining star formation history to which star formation bursts are added at different ages and with different intensities. This can cause the M/L to decrease, and might explain the difference in stellar mass.

Instead, when we compare the stellar mass in the inner 1 kpc with the value calculated with MAGPHYS by Groves et al. (2012), we find a remarkably good agreement ($\log(M_\star/M_\odot) = 10.01$ vs $\log(M_\star/M_\odot) = 9.91$ in our case).

The dwarf elliptical companion of Andromeda, M32, also falls in our field of view. We find a total stellar mass of $\log(M_\star/M_\odot) = 8.77$. Of course, as the light of M32 is highly contaminated by Andromeda itself, mass estimates of this galaxy are highly dependent on the aperture and on the estimation of the background flux of M31. Nevertheless, our estimate is only a factor of 2–3 lower then dynamical mass estimates (e.g. Richstone & Sargent 1972). This discrepancy is of the same order as the difference in total mass we find for M31.

As a total dust mass, we find $M_{\rm dust} = (2.9 \pm 0.7) \cdot 10^7 M_\odot$, for the sum of all pixel-derived dust masses, using the D00 dust model. This estimate is preferred over the dust mass from a fit to the integrated fluxes as the most recent dust mass estimates for M31 are derived from the sum of pixel masses. Furthermore, it is known that dust mass estimates from integrated fluxes underestimate the total dust mass (see also Sect. 3.4.2). We note that the uncertainly on this estimate appears very small. This is because of the very narrow PDF for $M_{\rm dust}$ from the global fit of M31. As previously stated, this error only reflects the uncertainty on the SED fitting. The absorption coefficient $\kappa_{\rm abs}(\lambda_0)$ from D03 was used in the next estimates.

In HELGA I we estimated the dust mass from a modified black-body fit to the global flux and found $M_{\rm dust} = (5.05 \pm 0.45) \cdot 10^7 M_\odot$. HELGA II derived a total dust mass from modified black-body fits to high signal-to-noise pixels (which cover about half of the area considered) and found $M_{\rm dust} = 2.9 \cdot 10^7 M_\odot$. Independent *Herschel* observations of M31 (Draine et al. 2014, Krause et al. in prep.) yield $M_{\rm dust} = (6.0 \pm 1.1) \cdot 10^7 M_\odot$ (corrected to the distance adopted in this work: $D_{M31} = 0.785$ Mpc) as the sum of the dust masses of each pixel.

We find a total dust mass of the same order as these previous estimations; however, our result is somewhat lower. The reason for this discrepancy is most likely the difference in dust model, as was already clear from Fig. 3.5. Determining the conversion factor q between dust models is rather difficult and requires the assumption of an average emissivity index:

$$q = \frac{\kappa_{D00}}{\kappa_{D03}} = \frac{\kappa_{D00}^{850}}{\kappa_{D03}^{350}} \cdot \left(\frac{350}{850}\right)^{-\beta}. \tag{3.9}$$

For M31, the mean β was found to be in the range $1.8 - 2.1$ (Smith et al. 2012c; Draine et al.

2014), yielding a conversion factor between 2.0 and 2.6, or dust masses in the range 5.70 – $7.44 \cdot 10^7 M_\odot$. The D00 dust model thus tends to produce dust masses that are about half of the D03 masses. Keeping this in mind, all dust mass estimates for Andromeda agree within their uncertainty ranges.

Local vs global

The MAGPHYS code was conceived for galaxy-scale SED fitting and it works well in that context (e.g. da Cunha et al. 2008, 2010; Clemens et al. 2013). At these large scales, a forced energy balance is justified because globally, most of the absorbed starlight is re-emitted by dust. When zooming in to sub-kpc regions, this assumption might not be valid any more. Light from neighbouring regions might be a significant influence on the thermal equilibrium of a star forming cloud, and if this is true, it may translate into an offset between the local parameters and the global value for that galaxy.

As a test for our extended library (see Sect. 3.4.1) we compare the mean values of the physical parameters to their global counterparts (upper part of Table 3.3). These parameters were derived from a MAGPHYS fit to the integrated fluxes of Andromeda. The fluxes are listed in Table 3.2. In the case of additive parameters (bottom part of Table 3.3), we compare their sum to the value derived from a global SED fit. It is important to note that we rely on our filtered set of pixels for each parameter. This means at least 40% of the pixels are excluded. Most of these badly constrained pixel values lie in the outskirts of M31. Nevertheless, their exclusion will surely affect the additive parameters.

Several parameters mimic their global counterparts quite well. This is the case for f_μ, $T_{\rm C}^{\rm ISM}$, τ_V, and $\tau_V^{\rm ISM}$, where the agreement lies within 1 standard deviation. The distribution of the pixel-derived sSFRs has a broad shape. In order to compare the sSFR of the pixels to the global value, we make use of the total SFR and stellar mass as derived from the pixels. We then find the pixel-sSFR by dividing the total SFR by the total $M_\star$. This value again lies close to its global counterpart, despite the wide range of sSFRs found on an individual pixel basis.

The temperature of the warm circumstellar dust differs significantly: the average pixel value is 43 K with a standard deviation of 7 K, while a fit to the global fluxes reveals $T_{\rm W}^{\rm BC} = 61^{+1}_{-9}$ K. Both values still overlap at a 2σ level, but the relative deviation is much larger than the other parameters. The peak of this dust component lies between 30 μm and 70 μm. The MIPS 70 μm band provides the only data point in this region, making it difficult to estimate this parameter accurately.

Additive parameters will also suffer because we exclude a significant number of pixels. Most of them do add up to the same order of magnitude as the global values: SFR, M_*, $L_{\rm dust}$, $L_{\rm PAH}^{\rm tot}$, and $L_{\rm C}^{\rm tot}$. All of them lie within 5 – 20% below the global value. This again indicates that the

Table 3.2: Overview of the obtained fluxes for the different regions of Andromeda. All measurements are in units of Jansky.

Band	Global	Bulge	Inner disk	Ring	Outer disk	M32
FUV	1.483 ± 0.074	0.042 ± 0.0021	0.1742 ± 0.0087	0.451 ± 0.023	0.811 ± 0.041	0.00587 ± 0.00029
NUV	2.67 ± 0.08	0.1403 ± 0.0042	0.447 ± 0.013	0.763 ± 0.023	1.304 ± 0.039	0.01807 ± 0.00054
u	18.71 ± 0.37	3.418 ± 0.068	5.59 ± 0.11	3.691 ± 0.074	5.77 ± 0.12	0.259 ± 0.0052
g	84.2 ± 1.7	17.55 ± 0.35	27.88 ± 0.56	15.34 ± 0.31	22.37 ± 0.45	1.17 ± 0.023
r	183.4 ± 3.7	38.88 ± 0.78	63.5 ± 1.3	33.73 ± 0.67	45.1 ± 0.9	2.394 ± 0.048
i	279.6 ± 5.6	60.7 ± 1.2	99 ± 2	51 ± 1	65 ± 1.3	3.596 ± 0.072
z	342 ± 6.8	80 ± 1.6	120.6 ± 2.4	56.3 ± 1.1	80.9 ± 1.6	4.52 ± 0.09
W1	287.3 ± 6.9	63.4 ± 1.5	103.2 ± 2.5	56.2 ± 1.3	61.4 ± 1.5	3.372 ± 0.081
IRAC 3.6	286 ± 24	63.1 ± 5.2	103.2 ± 8.6	56.1 ± 4.7	60 ± 5	3.37 ± 0.28
IRAC 4.5	161 ± 11	36.7 ± 2.6	58.9 ± 4.2	32.3 ± 2.3	31.5 ± 2.2	2.08 ± 0.15
W2	158.5 ± 4.4	33.7 ± 0.94	56.2 ± 1.6	32.1 ± 0.9	34.77 ± 0.97	1.855 ± 0.052
IRAC 5.8	222 ± 49	34.4 ± 7.6	68 ± 15	59 ± 13	59 ± 13	1.75 ± 0.39
IRAC 8	211 ± 35	21.2 ± 3.5	50 ± 8.3	94 ± 16	44.4 ± 7.4	1.53 ± 0.25
W3	209.3 ± 9.4	14.48 ± 0.65	48.4 ± 2.2	79.6 ± 3.6	66 ± 3	1.015 ± 0.046
W4	164.2 ± 9.4	9.51 ± 0.54	36 ± 2	69 ± 3.9	49.3 ± 2.8	0.671 ± 0.038
MIPS 24	119 ± 48	8 ± 3	26 ± 10	56 ± 22	29 ± 12	0.5 ± 0.2
MIPS 70	1051 ± 110	97.9 ± 9.8	228 ± 23	492 ± 49	233 ± 23	1.49 ± 0.15
PACS 100	3500 ± 350	195 ± 19	805 ± 81	1601 ± 160	893 ± 89	8.13 ± 0.82
PACS 160	7526 ± 750	199 ± 20	1630 ± 160	3588 ± 360	2094 ± 210	18.9 ± 1.9
SPIRE 250	5952 ± 420	87.4 ± 6.1	1126 ± 79	2736 ± 190	1992 ± 140	13.25 ± 0.93
SPIRE 350	3122 ± 220	33.8 ± 2.4	520 ± 36	1395 ± 98	1168 ± 82	7.29 ± 0.51
SPIRE 500	1350 ± 94	11.76 ± 0.82	201 ± 14	583 ± 41	551 ± 39	3.37 ± 0.24

Table 3.3: Comparison of the main properties for M31 as derived from the pixel-by-pixel fitting and from a fit to the global fluxes. N_{pix} denotes the number of reliable pixels used for the analysis and σ_{rel} the median relative uncertainty for this sample. The mean value of the relative parameters are given in the upper part of the table, along with the standard deviation on their distribution. The sum of the additive parameters are given in the bottom part of the table. Note that the uncertainties on the additive parameters are maximum errors, not 1σ uncertainties like the others.

parameter	N_{pix}	Median σ_{rel}	Mean local	std. dev	Global	Unit
f_μ	13462	0.10	0.85	0.08	$0.88^{+0.01}_{-0.02}$	–
$sSFR$	6608	0.18	3.45	0.02	3.38 ± 0.01	$10^{-12}\mathrm{yr}^{-1}$
T_W^{BC}	13462	0.21	43	7	61^{+1}_{-9}	K
T_C^{ISM}	13462	0.05	15.4	2.1	$16.2^{+0.3}_{-0.2}$	K
τ_V	3753	0.14	0.62	0.68	0.32 ± 0.01	–
τ_V^{ISM}	13212	0.11	0.20	0.13	0.16 ± 0.01	–
χ^2	18053	–	1.26	–	1.35	–

parameter	N_{pix}	Median σ_{rel}	Total local	Global	Unit
$M_\star$	12853	0.17	4.8 ± 0.6	5.5 ± 0.01	$10^{10} M_\odot$
M_{dust}	10496	0.18	2.9 ± 0.7	$2.7^{+0.4}_{-0.1}$	$10^7 M_\odot$
L_{dust}	13462	0.06	4.5 ± 0.3	$4.98^{+0.6}_{-0.01}$	$10^9 L_\odot$
SFR	8673	0.16	0.16 ± 0.05	$0.189^{+0.002}_{-0.01}$	$M_\odot \mathrm{yr}^{-1}$
L_{PAH}^{tot}	12563	0.12	0.9 ± 0.8	$1.11^{+0.03}_{-0.16}$	$10^9 L_\odot$
L_C^{tot}	10709	0.10	2.5 ± 2.2	$2.55^{+0.15}_{-0.01}$	$10^9 L_\odot$

excluded pixels do not contribute significantly to the light of M31. The dust mass, however, turns out to be $\sim$ 7% higher when summing all pixels. It is known that SED fitting is not a linear procedure and will depend on the employed resolution. Aniano et al. (2012) found that modelling on global fluxes yields dust masses that are up to 20% lower than resolved estimates. Galliano et al. (2011) found discrepancies of up to 50% depending on the applied resolution. Even taking into account another 10% in flux due to the excluded pixels, our difference in dust mass estimates lies within this range.

To compute the uncertainties on the summed parameters, it is not adequate to simply add the squares of the individual absolute errors on the pixels, and taking the square root of that number. This assumes no correlation between the uncertainties of the pixels. This is of course not true, but difficult to quantify. Instead, we compute the maximum error by linearly adding the absolute errors on the dust mass for each pixel. These maximum errors are given in the 4th column of the bottom part in Table 3.3. As an additional error measure, we also provide the median relative pixel uncertainty in the second part of Table 3.3. These numbers lie in the 10 – 20% range, which reflects the order of magnitude the correlated pixel error. We advise to use these uncertainties for the parameters that are summed from the individual pixels.

The fact that we reproduce the global properties of M31 from our local SEDs, boosts confidence that the procedure applied here is valid, even though MAGPHYS was conceived for galaxy-scale SED fitting.

3.4.3 Parameter maps

We construct detailed maps of the SED parameters from the collection of pixels with reliable parameter fits in Fig. 3.6 and briefly discuss the morphologies observed. The blanked pixels in these map did not meet the necessary reliability threshold (see Sect. 3.4.2).

The dust luminosity $L_{\rm dust}$ closely follows the morphology seen in the PACS images (see also Fig. 3.3). Dust emission in Andromeda is brightest in the bulge and in the 10 kpc ring. Some fainter emission regions are seen in the outer parts of the galaxy, coinciding with a ring at 15 kpc.

As expected, the dust mass $M_{\rm dust}$ map closely resembles the SPIRE images (see also Fig. 3.3). Compared to the $L_{\rm dust}$ map, some intriguing distinctions can be noted. There seems to be almost no dust in the centre of M31, while the bulge is actually the brightest in dust luminosity. We hereby confirm earlier statements (HELGA II; Tempel et al. 2010; Groves et al. 2012; Draine et al. 2014) that the bulge of Andromeda holds a small amount of relatively warm ($>$ 25 K) dust. The south-west side is also smoother than in the $L_{\rm dust}$ map, pointing out that the heating of ISM dust and not the mass is crucial to the observed luminosity.

The PAH luminosity $L_{\rm PAH}^{\rm tot}$ appears relatively weak when compared to the $L_{\rm dust}$ map. The general

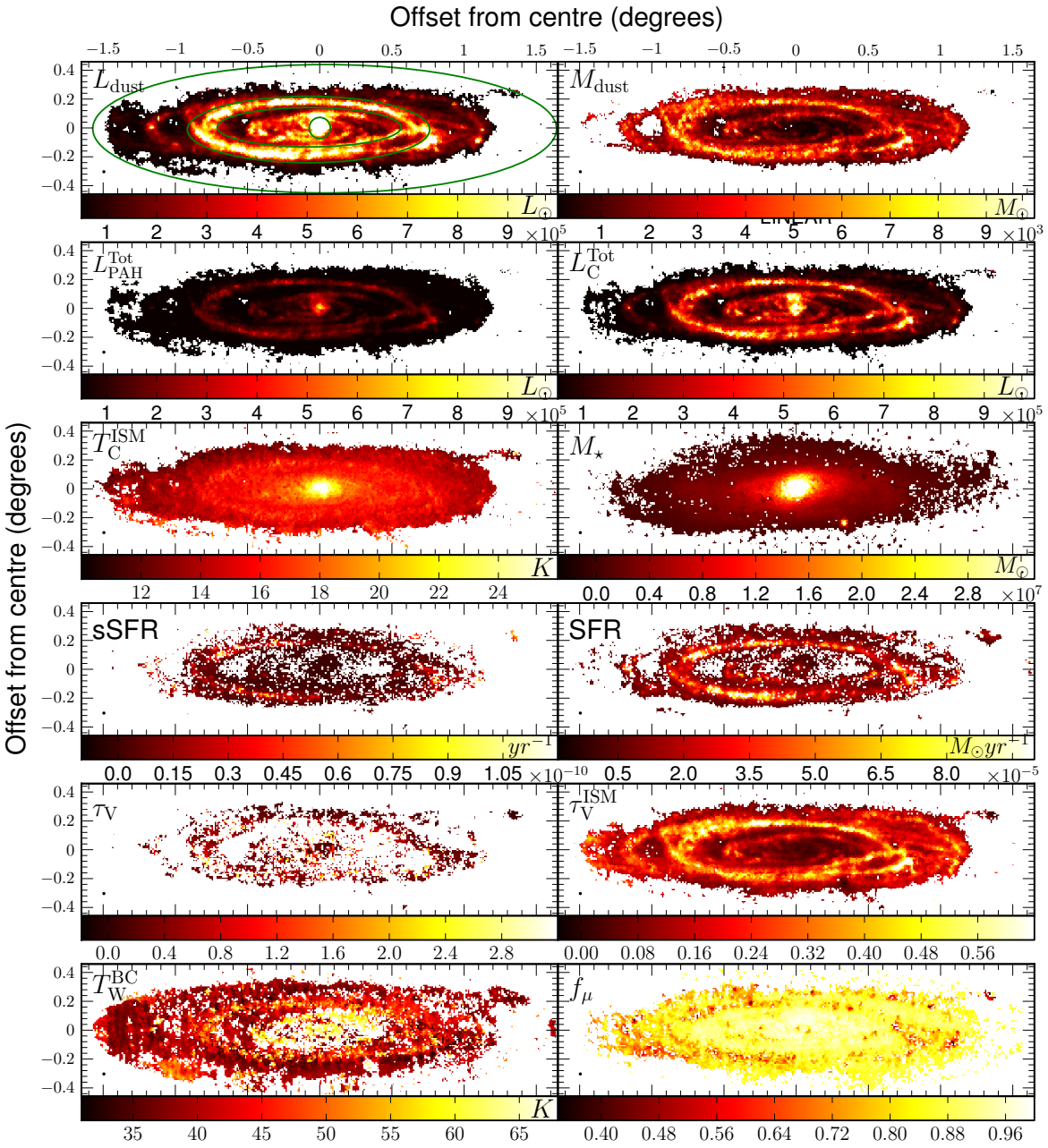

Figure 3.6: Parameter maps for M31, rotated from a position angle of 38°. See Table A.1 for the meaning of the parameters. Pixels with uncertainties that were considered too large (see Sect. 3.4.2) were blanked out. The green ellipses in the upper–left panel represent the apertures of the macro-regions of M31: the bulge, inner disk region, 10 kpc ring, and the outer disk.

morphology, however, is similar. The surface brightness at these wavelengths is the highest in the bulge of Andromeda. Furthermore, the emission is mostly concentrated in the 10 kpc ring and in the dusty parts of the inner disk. If reprocessed UV light of recent and ongoing star formation is the only energy source for MIR emission, no bright MIR and PAH features are expected in the bulge of M31. Emission from PAHs can, however, be enhanced by increases in the diffuse ISRF (Bendo et al. 2008). This again, suggests that the radiation field of older stars in the centre of M31 is quite strong.

A similar morphology is seen when looking at the contribution of the diffuse cold dust to the total dust emission, $L_{\mathrm{C}}^{\mathrm{tot}}$. The cold dust, only found in the diffuse ISM, appears significantly more luminous than the PAH emission (the L_{dust}, $L_{\mathrm{C}}^{\mathrm{tot}}$ and $L_{\mathrm{PAH}}^{\mathrm{tot}}$ maps in Fig. 3.6 have the same scale). Interestingly, the emission from this component is equally bright in the bulge and in the ring, in contrast with the PAH luminosity map.

Consequently, the temperature of the ISM dust $T_{\mathrm{C}}^{\mathrm{ISM}}$ peaks in the centre ($\sim$ 30 K). It follows a smooth radial decline until it reaches a plateau at 16 K in the ring. Higher values are reached in the brightest star forming regions. This suggests the cold ISM dust is partially heated by recent and ongoing star formation. On the other hand, older stars can also contribute to the heating of the dust. In the NIR wavebands, the surface brightness is slightly enhanced in the ring, indicating a higher concentration of older stars. Outside the star forming ring, the temperature quickly drops two degrees to 14 K.

For the warm dust temperature $T_{\mathrm{W}}^{\mathrm{BC}}$, the picture is far less clear. The map is crowded with blanked pixels due to their high uncertainties. As already mentioned in Sect. 3.4.2, the MIPS 70 μm data point is the only observation in this temperature regime. Additionally, the emission of the cold dust component overlaps greatly with the SED of the warm dust, making it difficult to disentangle both components. We do find significantly higher temperatures in the bulge, where the ISRF is highest, and in the 10 kpc ring, where most of the new stars are being formed. Outside these areas, the warm dust is relatively cold ($<$ 45 K).

The stellar mass $M_{\star}$ is one of the best constrained parameters thanks to the good coverage of the optical and infrared SED. It is highest in the bulge and the central regions around it and declines smoothly towards the outskirts of the galaxy. Interestingly, a small peak is seen where M32 resides. We do not detect this dwarf satellite in our *Herschel* maps. This is caused by the overlap of emission from M32 and M31's diffuse dust emission at this location on the sky. Nevertheless, it is evident that M32 does not contain much dust.

The star formation rate map of M31 largely coincides with the dust luminosity (except in the bulge), although the distribution is more peaked in the rings. Regions where the dust emission is lower (inter-ring regions and outskirts) are mostly blanked out because it is hard to constrain very low star formation rates. Some residual star formation is seen in the bulge. However it must be noted that the high dust luminosities in the central region might cause a degeneracy

between the SFR, which directly heats the dust, and $M_\star$, representing the number of older stars that have been proven to strongly contribute to dust heating.

The specific star formation rate is obtained by dividing the SFR over the last 100 Myr by the stellar mass and gives a measure of ongoing vs past star formation. This quantity combines the uncertainties of both parameters, hence the large number of blanked pixels. The 10 kpc and 15 kpc rings have the highest sSFR in M31. Interestingly, the inner ring has very low values of sSFR and the bulge has close to zero. In general, we can say that stars are nowadays formed most efficiently in the rings of the galaxy.

The V–band optical depth is the poorest constrained parameter of the sample. Accurately estimating this value requires detailed knowledge on the dust geometry. This is not available here, so assumptions must be made based on colour criteria and an extinction law. As we are not able to probe individual star formation regions, the optical depth must be seen as an average over each resolution element. Liu et al. (2013) showed that when averaged over scales of $\sim 100-200$ pc, the dust geometry can be approximated by a foreground dust screen. Individual stars or star forming regions are, however, likely to experience much greater optical depths than the averaged values. In Andromeda, this average varies from 0.2 to 2. Most of the higher optical depth regions coincide with the dusty rings of the galaxy.

The picture is more obvious for the contribution of cold ISM dust to the total optical depth $\tau_V^{\rm ISM}$. This parameter closely resembles the ring–like structure we also see in the $M_{\rm dust}$ and ranges from $0.1-1.1$. The ratio of those two parameters $\tau_V^{\rm ISM}/\tau_V = \mu$, measures the contribution of diffuse cold ISM dust to the extinction of starlight. We find a median $\mu = (54 \pm 22)\%$, but the contribution of ISM dust ranges from less than $\sim 25\%$ in the centre to over 70% in the 10 kpc ring. This suggests that diffuse dust is the main contributor to starlight extinction in the more active regions of a galaxy. This is consistent with the results of Keel et al. (2014), who find that a greater fraction of the UV extinction is caused by the diffuse dust component. Furthermore, detailed radiative transfer models of galaxies show the importance of this diffuse component in the FIR/submm emission, and thus absorption of starlight (see e.g. Tuffs et al. 2004; Bianchi 2008; Popescu et al. 2011).

The contribution of the ISM dust to the dust luminosity f_μ peaks ($\sim 90\%$) in the centre, where most of the dust is in the diffuse ISM. It linearly decreases along the disk, reaching $\sim 80\%$ in the star forming ring. Going beyond this ring, the ISM dust contribution declines more quickly to reach values around 50% at 15 kpc.

3.4.4 SED of the macro-regions

As a first step towards a spatially resolved analysis, we decompose Andromeda into macro–regions, located at different galactocentric distances: the bulge, the inner disk, the star forming

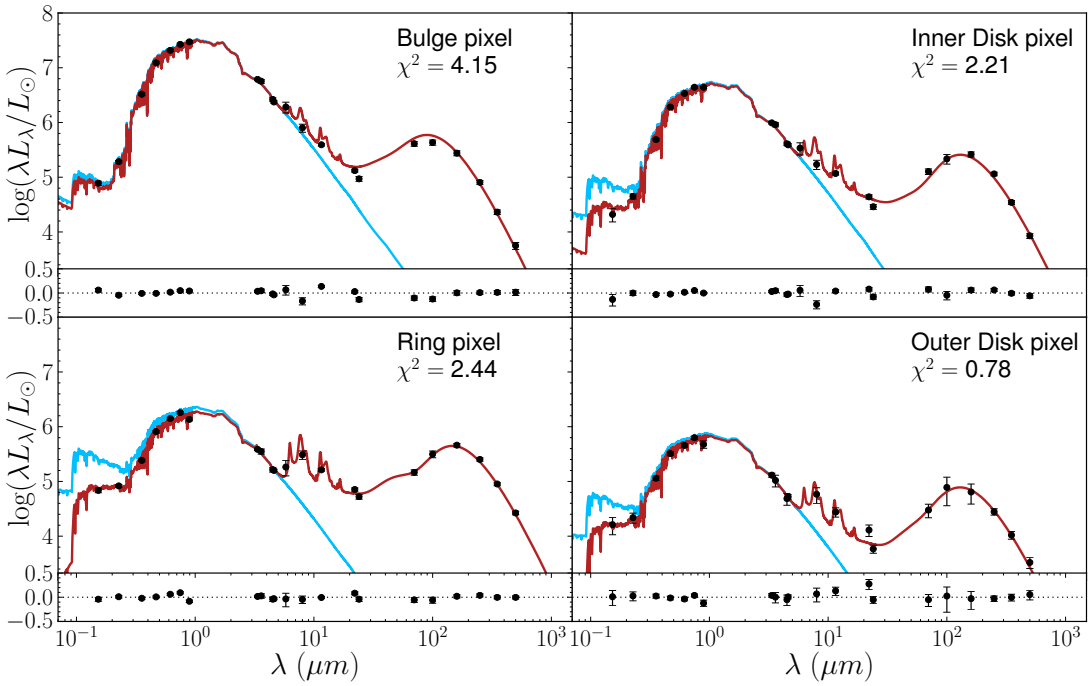

Figure 3.7: The panchromatic SED of four representative pixels in the bulge, inner disk, the 10 kpc ring, and the outer disk region. The blue line represents the unattenuated SED and the red line the best fit to the observations. Residuals are plotted below each graph.The χ^2 values are those for the best fitting template SED.

ring centred at a radius of 10 kpc, and the outer part of the disk. We choose to base our definition of these regions on the morphology of the $L_{\rm dust}$ map of Fig 3.6. The advantage is that, in the light of constructing dust scaling relations, each region corresponds to a separate regime in terms of SFR, radiation field, dust content, and composition. For example, the bulge is limited to the inner $1kpc$ region and is thus significantly smaller than the optical/NIR bulge, but it coincides with the zone with the hardest radiation field. The shapes of the borders between regions are apparent ellipses on the sky and do not necessarily coincide with projected circles matching the disk of M31 (see also Table 3.4 for their exact definition).

We choose a set of individual pixels, selected to represent the typical shape of an SED in these regions. They are shown in Fig. 3.7, together with the residual values for each wavelength band. Along with the single pixel SEDs, we also show SED fits to the integrated fluxes of these macro–regions in Fig. 3.8. Integrated fluxes for the separate regions can be found in Table 3.2. The goodness of fit is here expressed by the χ^2 value for the best fitting template SED. The parameter values from this SED will differ slightly from the peak values in the PDFs, which express their most likely values. Nevertheless, the template SED gives a good indication of how well the observed fluxes can be matched.

When comparing the fits in Figs. 3.7 and 3.8, it is clear that the macro-region fits have a systematically lower χ^2 than their respective single-pixel fits. This is not surprising as one might

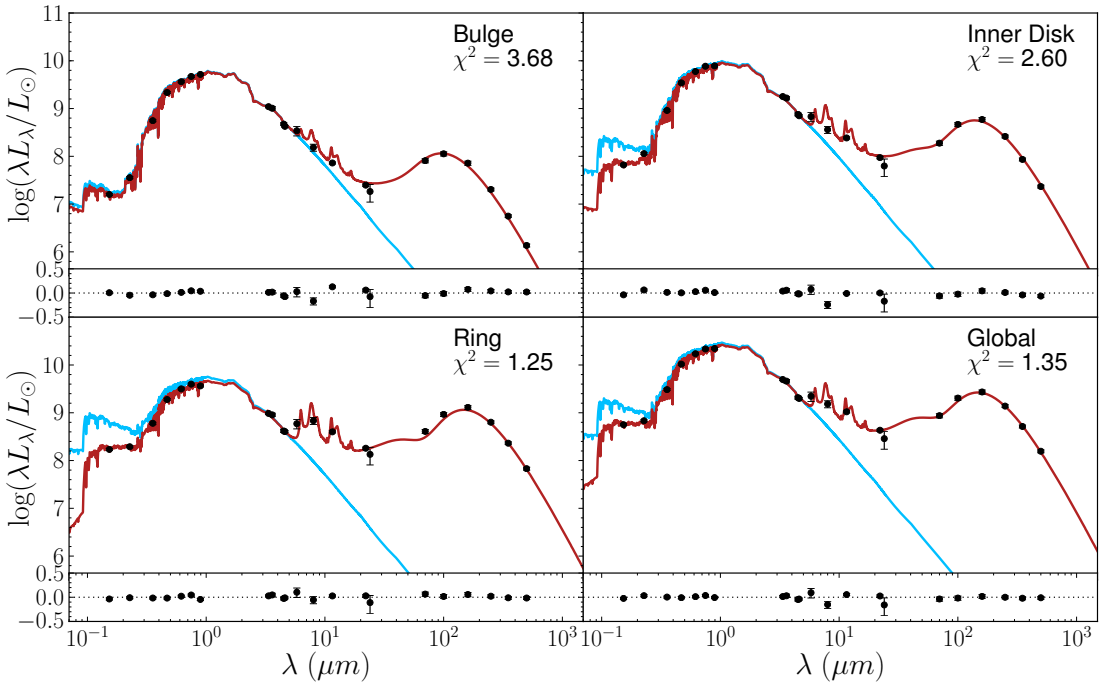

Figure 3.8: The panchromatic SED of four main apertures: the bulge, the inner disk region, the 10 kpc ring, and the integrated galaxy. The blue line represents the unattenuated SED and the red line the best fit to the observations. Residuals are plotted below each graph. The χ^2 values are those for the best fitting template SED.

expect greater signal-to-noise variations on smaller scales. In general, however, most of the observed fluxes are well reproduced by the best fit. Only the MIPS 24 μm point seems to be systematically below the theoretical SED. The MIPS 24 μm observations do come with large error bars, so that is accounted for in the determination of the parameter PDFs.

In the bulge, stars are completely dominant over the dust component in terms of mass and luminosity. This is visible in the ratio of the total dust luminosity to the g–band luminosity ($L_{\rm dust}/L_g = 0.48$), and in the small offset between the unattenuated (blue) and the attenuated (red) SED. The optical/NIR SED is much more luminous than the UV part of the spectrum, indicating a relatively low SFR and a strong interstellar radiation field (ISRF), dominated by older stars. Furthermore, the peak of the FIR SED lies at relatively short wavelengths caused by high temperatures of the cold dust. There are only weak PAH features visible in the centre of M31, although the MIR flux is relatively large compared to the other regions. Some residual star formation can be found in the bulge of M31, but the contribution to the total SFR is negligible.

The inner disk is forming stars at a slow pace ($2.30 \times 10^{-2} M_\odot {\rm yr}^{-1}$). This is confirmed by a visible offset between the unattenuated and attenuated SED in the UV regime. The FIR emission peaks at longer wavelengths than in the bulge, indicating a milder ISRF and lower dust temperatures. We consequently find a higher $L_{\rm dust}/L_g$ ratio of 1.50. This less harsh environment allows

PAHs to survive longer, giving rise to more prominent MIR features. The same conditions hold in the outer disk of M31, although the surface brightness is systematically lower there. The dust also gains in importance here ($L_{\rm dust}/L_g = 2.37$). The FIR peaks at even longer wavelengths, meaning the diffuse dust is colder in the outskirts of the galaxy.

The most active star forming region of M31 is unquestionably the ring at $\sim$ 10 kpc. This region contains only 20% of the stellar mass and almost half of the total dust mass of M31 at temperatures near the galaxy's average (see also Table 3.4). The luminosity difference between the UV and the optical/NIR SED is the smallest of all regions, indicating that new stars dominate the radiation field. This also translates in strong PAH features in the MIR. The offset between the attenuated and unattenuated SED is large in the UV and even visible in the optical-NIR regime, indicating significant dust heating. Consequently, we find the highest dust–to–g-band ratio $L_{\rm dust}/L_g = 4.84$.

Interestingly, several MAGPHYS models have a small secondary peak at wavelengths shortward of the main dust peak. This can again be related to the lack of data points in this area to constrain the SED. There is no physical reason for there to be a secondary bump of dust emission. As a result, this adds slightly to the dust luminosity and could bias the total dust mass towards higher values. However, the effect will be small since the cold dust is the main contributor to the dust mass.

3.5 Dust scaling relations

In the following we will investigate scaling relations of stellar and dust properties in Andromeda at different sizes: we first consider the galaxy as a whole, and we will then look at its main components as separate regions. Finally, we will push the analysis down to the smallest possible scale: the hundred–pc sized regions defined by the statistically independent pixels whose SED we have modelled as explained above.

Our results can then be compared to already known results for similar physical quantities. In this respect, the ideal sample for comparison is surely the one provided by the local dataset of the *Herschel* Reference Survey (HRS; Boselli et al. 2010b). The HRS is a volume–limited, K–band selected survey including more than 300 galaxies selected to cover both the whole range of Hubble types and different environments. Cortese et al. (2012b) have analysed in detail how the specific dust mass correlates to the stellar mass surface density ($\mu_\star$) and to NUV–r colour (see Fig. 3.9). Furthermore, da Cunha et al. (2010) also found links between the dust mass and SFR and between f_μ and the specific SFR using a sample of low-redshift star forming galaxies from the SDSS survey. We will check where Andromeda is located with respect to the above relations and, more importantly, we will address the issue regarding the physical scales at which the aforementioned relations start to build up.

3.5.1 Andromeda as a whole

Andromeda is classified as a SA(s)b galaxy (de Vaucouleurs et al. 1991) and has a prominent boxy bulge. The disk contains two conspicuous, concentric dusty rings and two spiral arms (see e.g. HELGA V; Gordon et al. 2006).

In Table 3.4 we report a summary of the main physical properties we have derived for Andromeda from integrated fluxes. The total stellar mass was found to be $5.5 \times 10^{10} M_{\odot}$, a typical value in local starforming galaxies (see e.g. Clemens et al. 2013). The total dust mass was found to be $2.70 \times 10^{7} M_{\odot}$, comparable to the amount of dust in our own Galaxy (e.g. Sodroski et al. 1997). The distribution of dust in the Andromeda galaxy is, however, atypical for an early–type spiral. The infrared emission from early-type galaxies is usually quite compact (e.g. Bendo et al. 2007; Muñoz-Mateos et al. 2009b). Extended ring structures, such as the ones in M31, appear rather infrequently.

As an early–type spiral, Andromeda has a low star formation rate of 0.19 $M_{\odot}\mathrm{yr}^{-1}$, about ten times smaller than the value measured in the Milky Way (Kennicutt & Evans 2012). In da Cunha et al. (2010) a relation was derived between the SFR of normal, low redshift ($z < 0.22$) SDSS galaxies and their dust content. Despite a total dust mass which is close to the sample average, the SFR in M31 is about one order of magnitude below the average relation at this dust content. Consequently, Andromeda's specific star formation rate (sSFR) of 3.38×10^{-12} yr^{-1} is at the lower end compared to the trend found by da Cunha et al. (2010).

If we compare the locus of M31 in the scaling relation plots presented in Cortese et al. (2012b), we find that Andromeda follows precisely the average trends defined by HRS galaxies (see the cyan dot in the two top panels in Fig. 3.9). In general, M31 has dust and stellar masses that are typical for early–type spiral galaxies. On the other hand, the star formation activity is unusually low. This is consistent with a more active star formation history, possibly related to an encounter with M32 (Block et al. 2006).

3.5.2 Scaling relations in the different regions

As outlined in Sect. 3.4.4, we have grouped our set of pixels in four macro-regions based on the morphology of the L_{dust} map. These macro-regions represent physically different components in the galaxy. It is well known, for example, that the bulges in spiral galaxies usually host the oldest stellar populations (e.g. Moorthy & Holtzman 2006). Bulges are usually devoid of ISM and have barely any star formation (e.g. Fisher et al. 2009), closely resembling elliptical galaxies in many respects. However, unlike stand-alone elliptical galaxies, galactic bulges are intersected by galactic disks. At this intersection, a significant amount of gas, dust, and many young stars are present. In this respect, Andromeda is again an atypical early-type spiral as none of these components are prominently visible at the bulge-disk intersection.

Table 3.4: Summary of the parameters characterising the main apertures of M31. The semi-major axis a and apparent eccentricity ϵ describe the annuli on the plane of the sky. The other parameters are physical properties derived from an SED fit to the integrated fluxes inside these apertures.

Region	RA centre	DEC centre	a	ϵ	$M_\star$	$\mu_\star$	$M_{\rm dust}$	SFR	sSFR	NUV–r
	hh:mm:ss	dd:mm:ss	kpc		$10^{10}M_\odot$	$10^8 M_\odot \mathrm{kpc}^{-2}$	$10^6 M_\odot$	$10^{-2} M_\odot \mathrm{yr}^{-1}$	$10^{-12}\mathrm{yr}^{-1}$	Mag
Global	10:39:52.6	41:14:30.1	22.0	0.96	5.50	3.11	27.0	18.9	3.38	4.59
Bulge	10:41:10.2	41:16:18.4	1.0	0.00	0.81	25.1	0.11	0.18	0.27	6.11
Inner Disk	10:44:22.8	41:20:00.2	8.7	0.98	2.00	4.23	3.95	2.30	1.20	5.38
10 kpc Ring	10:45:37.6	41:19:39.6	11.5	0.96	0.96	1.66	12.8	9.06	9.55	4.11
Outer Disk	10:39:52.6	41:14:30.1	22.0	0.96	1.07	1.58	12.5	1.18	1.07	3.85
M32	10:40:21.1	40:51:52.6	0.636	0.00	0.06	4.65	0.08	0.03	0.60	5.31

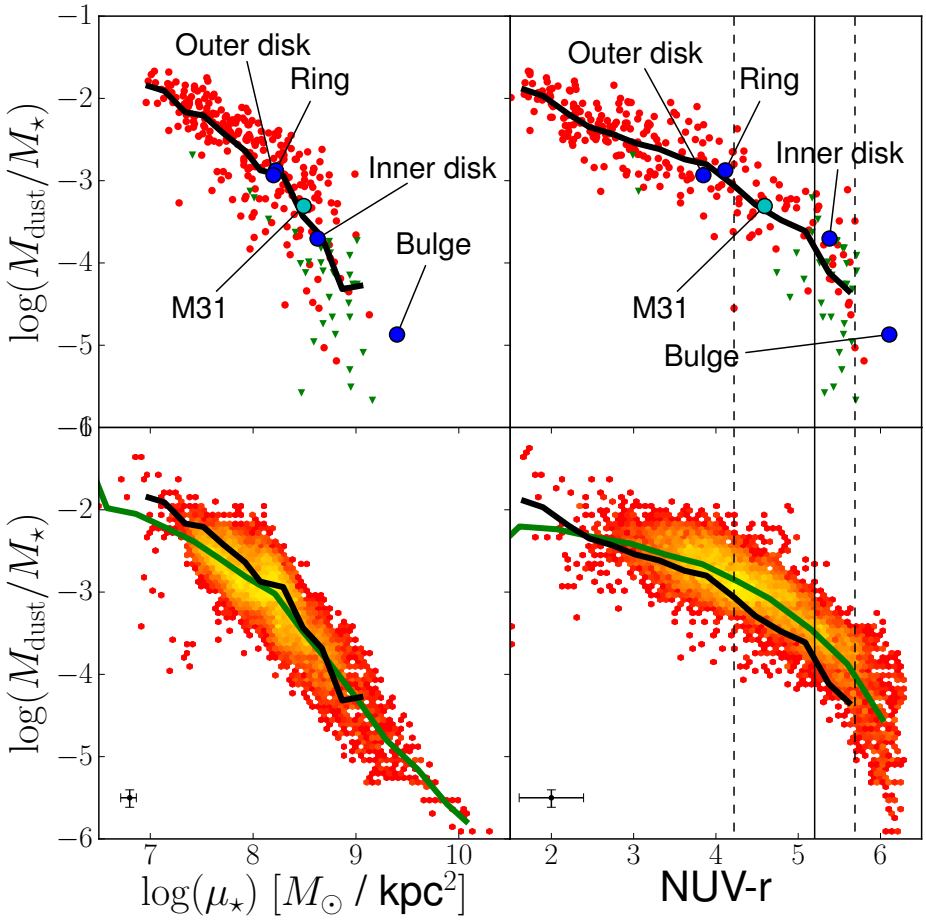

Figure 3.9: Top: dust scaling relations from the *Herschel* Reference Survey (Cortese et al. 2012b); the specific dust mass $M_{\rm dust}/M_\star$ as a function of the stellar mass surface density $\mu_\star$ (left) and NUV-r colour (right). NUV-r serves as an inverse tracer of the sSFR. Red are *Herschel* detected galaxies, green are upper limits for the undetected ones. The blue dots represent the macro-regions of M31 and the cyan dot indicates the position of the galaxy itself. The thick black line is the HRS mean trend. The vertical solid line indicates our division between late-type and early-type galaxies. The dashed vertical lines indicate the bluest early-type galaxy and the reddest late-type galaxy, respectively. Bottom: Same scaling relations, but now represented in a density plot using single pixel regions from M31. Yellow points indicate a higher density of points, red a lower density. The black line is the HRS mean trend, the green line is the M31 mean trend.

In the top panels of Fig. 3.9, we plot the physical quantities derived from fitting the integrated fluxes of Andromeda's four macro-regions (blue points), together with the relations for HRS galaxies (red dots) and their average trend (black line). Quite remarkably, they all fall on (or very close to) the average HRS relation, each of those components lying on a specific part of the plot which is typical for a given Hubble (morphological) type. On average, the outer parts of M31 closely resemble the physical properties of late–type HRS galaxies, while its bulge has, instead, characteristics similar to those of elliptical galaxies.

In the remainder of this chapter, we define objects as early-type when NUV–r > 5.2. This is the transition where most of the HRS objects are either E or S0 galaxies. Consequently, we define objects as late-type bluewards from this line. In Fig. 3.9, we also indicate the bluest S0 galaxy (NUV–r = 4.22) and the reddest Sa galaxy (NUV–r = 5.69) of the sample to indicate the spread of the transition zone.

In this respect, it is worth noting that Andromeda's bulge is significantly redder than any of the submm detected HRS galaxies because we are picking, by definition, only its very central, hence redder, regions. There is a known colour gradient in elliptical galaxies, which have bluer outskirts with respect to their inner parts, and this difference can be as high as $\sim$ 1 mag (see e.g. Petty et al. 2013). This can easily explain the offset in the bulge colour with respect to the HRS elliptical galaxies, whose colours are instead calculated from global apertures. For similar reasons, Andromeda's bulge is found at larger stellar mass surface densities values if compared to global elliptical galaxies, where also the outer, less dense parts are included in the measurements.

From a geometrical perspective, these regions follow a pattern that is determined by the average galactocentric distance: going from the centre outwards, we find the macro-regions at progressively bluer colours or, equivalently, lower stellar mass surface density. This reflects a typical inside-out formation of the bulge-disk geometry (White & Frenk 1991; Mo et al. 1998). This is consistent with the results from Pérez et al. (2013) and González Delgado et al. (2014), where they confirm an inside-out growth pattern for a sample of local starforming galaxies. Inside the disk, the situation might be more complex. An increasing sSFR for the macro-regions, from the inner disk to the 10 kpc ring supports this scenario. However, it does drop down significantly in the outer disk (see Table 3.4).

Muñoz-Mateos et al. (2007) have derived sSFR gradients for a sample of nearby galaxies. They found a slope that is, on average, positive and constant outwards of one scale length. When considering the very coarse sampling provided by the four macro-regions, Andromeda shows hints of a similar behaviour, with the sSFR declining in the outer disk with respect to the inner one. However, the 10 kpc ring exhibits a clear peak in SFR and sSFR.

This can also be seen from the top panel of Fig. 3.10, where the scaling relations of the individual pixels are separated in the different macro-regions, and the pixel-derived properties are

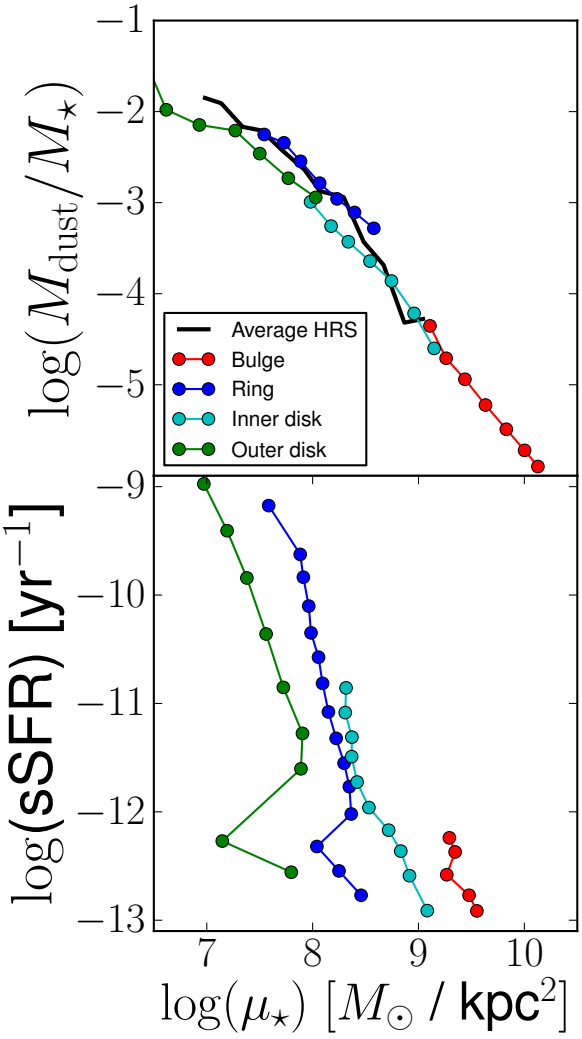

Figure 3.10: Average trends of the scaling relations for the stellar mass surface density $\mu_\star$, separated by the main morphological regions of M31: the bulge (red), the inner disk (cyan), the 10 kpc ring (blue), and the outer disk (green). Top: $\mu_\star$ vs $M_{\rm dust}/M_\star$. All pixel values are binned in $\mu_\star$; each point is the average of a bin. Bottom: $\mu_\star$ vs sSFR, where all pixels are binned in sSFR.

binned within each macro-region: the bulge (red), inner disk (cyan), ring (blue), and outer disk (green). In the $\log(\mu_\star)$ vs $\log(M_{\rm dust}/M_\star)$ plot, all regions but the ring follow a continuous relation which coincides with the HRS scaling relation. The ring is clearly offset in this relation, indicating a dustier environment compared to the average in the disk.

The specific dust mass was found to correlate with both the stellar mass surface density and NUV–r colour. It is important to verify whether both relations are not connected by a tighter correlation between $\mu_\star$ and NUV–r. In the bottom panel of Fig. 3.10, the relation between $\mu_\star$ and sSFR is displayed. We prefer sSFR over NUV–r as the former allows a direct comparison of physical quantities. We find that both quantities are tightly anti-correlated (see also Salim et al. 2005), so any evident link with one of them directly implies a link with the other. It must be noted, however, that sSFR values below 10^{-12} yr^{-1} should be interpreted with care, these values correspond to low star formation rates for any stellar mass and are subject to model degeneracies. It is immediately evident, as seen before, that the regions can be separated in stellar mass surface density. All of them lie within a small interval in $\mu_\star$ of about 1 order of magnitude. In sSFR, however, the spread within one region covers over three orders of magnitude, except for the bulge. This implies that, no matter the density of stars, a wide range of star formation rates are possible. The bulge, which is the region with the lowest SFR, is an obvious exception to this trend. Across the regions, the correlation sSFR and $\mu_\star$ is not particularly tight. In comparison, the link between both parameters and the specific dust mass is much more compact. The correlation between sSFR and $\mu_\star$ is therefore not likely to be the main driver of the other dust scaling relations.

3.5.3 Scaling relations at a sub-kpc level

We can now go a step further and see if and how the aforementioned scaling relations still hold at a sub-kpc level. We are not yet able to reach the resolution of the molecular clouds, the cradles of star formation, but we are instead sampling giant molecular cloud aggregates or complexes. Hence, we cannot yet say if the scaling relations will eventually break, and at which resolution.

In the lower panels of Fig. 3.9 we show the $M_{\rm dust}/M_\star$ ratio as a function of both the stellar mass surface density and NUV–r colour, for the statistically independent pixels. Regions with a higher number density of pixels in the plot are colour–coded in yellow. Displayed as a green line is the average relation for the pixels. The relations found between the dust–to–stellar mass ratio and NUV–r and $\mu_\star$ confirm, from a local perspective, the findings of Cortese et al. (2012b). As NUV–r traces sSFR very well, we also confirm the local nature of the results from da Cunha et al. (2010), who use the same spectral fitting tool as we do, and found a strong correlation between the sSFR and the specific dust content in galaxies.

As already mentioned in Sect. 3.5.1, M31 has a significantly lower SFR compared to the galax-

ies in the da Cunha et al. (2010) sample. In the relation between the dust mass and the SFR for each pixel, we recover an average displacement with respect to the extrapolation of the empirical law found by da Cunha et al. (2010). Nevertheless, the slope of the average relation defined by individual pixels is remarkably similar. This suggests that the intrinsic star formation relationship with dust (i.e. more dust equals more star formation, or vice versa) still holds, but is less efficient and hence scaled down to lower SFR in M31.

Following da Cunha et al. (2010) we can compare f_μ, the fraction of the total IR luminosity contributed by dust in the diffuse ISM, to the specific SFR for each pixel. In Fig. 3.11, we show how this relation, found for galaxies as a whole, is recovered on a local basis as well, with two main differences. First, the region corresponding to values of f_μ close to 1 is more densely populated. It turns out that these regions correspond to the very red bulge of M31. Secondly, systematically lower sSFR values are found for a given f_μ at these local scales. This is likely a manifestation of the low star formation activity of Andromeda with respect to the galaxies in the sample of da Cunha et al. (2010).

There are a few strong outliers on the top right of the main trend. Interestingly, this region of the parameter space is also occupied by outliers in the da Cunha et al. (2010) sample. These regions correspond to certain pixels in the main ring of M31. They are regions of relatively high star formation, but where most of the dust is in the diffuse ISM. We manually inspected the SEDs of these pixels and found no irregularities or bad fits. Nevertheless, it may be that we are fitting regions at in coarsely sampled part of the MAGPHYS parameter space. The discretization of each input parameter in MAGPHYS is not done in a uniform way. This is a limitation of the model we have to work with. Therefore, we only focus on the main trend in this plot and do not draw any second-order conclusions.

More specifically, these results combined together show that the interplay between the ISM, the radiation field and the stellar content (so the SFR as well) takes place on a sub-kpc scale. That the scaling relations were local in nature was already suggested in the previous section, when we subdivided M31 in morphologically distinct regions. We can now state that, globally, the main scaling relations are built up from the properties of the local galactic environment.

Furthermore, even on the smallest scales accessible with our data, the inside–out trend is, on average, preserved. The bulge is dominated by very red sub-kpc regions with very low sSFR values and high stellar densities. Pixels in the inner disk region are on average slightly bluer, but still have low sSFR values. Star forming pixels are mostly found in the 10 kpc ring and also have the highest specific star formation. In the outer part of M31 the star forming activity drops again.

It must be stressed that the above considerations are the average trends constructed from the large set of pixels within each macro-region. It is clear from the sub-kpc regions plotted in Fig. 3.9 and from the trends within each region in Fig. 3.10, that a wide range of physical

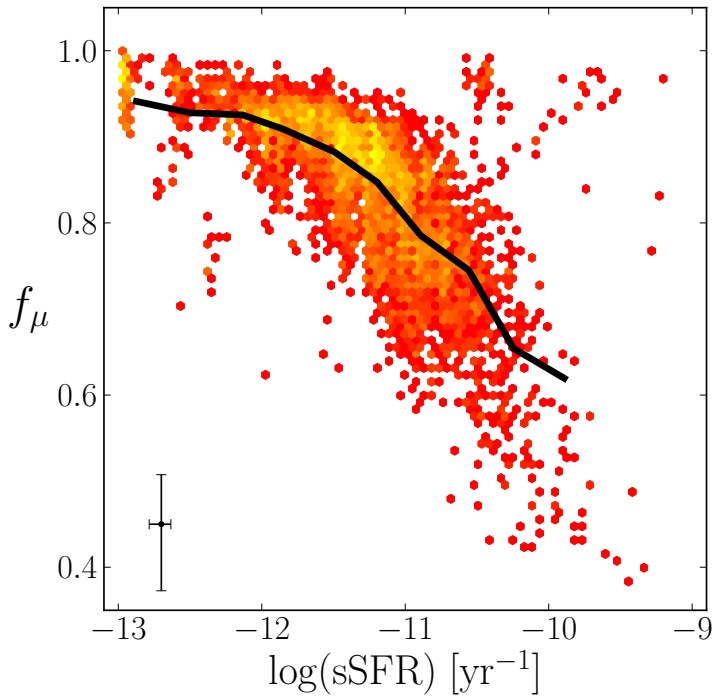

Figure 3.11: Density plot of the sSFR against f_μ, the luminosity fraction of ISM dust to the total dust. Yellow points indicate a higher density of points, red a lower density. The black line represents the mean trend of the points.

properties are present within each of the macro-regions. For example, the star forming ring does hold a small number of early-type pixels, while it is dominated by the starforming pixels. Vice versa, the inner disk of M31 holds a significant amount of late-type pixels, while the bulk of its sub-kpc regions are red and have low sSFR values. The exception to these findings is the bulge of M31, which consists purely of early-type regions with high stellar densities and only a minor SFR.

3.5.4 Radiation field and dust heating

We can now analyse the local characteristics of the radiation field in Andromeda and study the dependence of the dust temperature as a function of the stellar characteristics. This exercise has already been performed in Smith et al. (2012c), but we repeat it here using a physically consistent model, which simultaneously takes into account information from the whole spectral domain.

In Fig. 3.12 we plot the cold dust component temperature as a function of the stellar mass surface density, for each single independent pixel (upper panel) and for each of the macro-regions of M31 (lower panel). We observe a clear bimodality in this trend, which can be characterised by two slopes, with a break at $\log(T) \sim 1.25$ or T $\sim$ 18 K. The upper part of the relation, towards the higher temperature regime, is entirely and exclusively populated by pixels of the

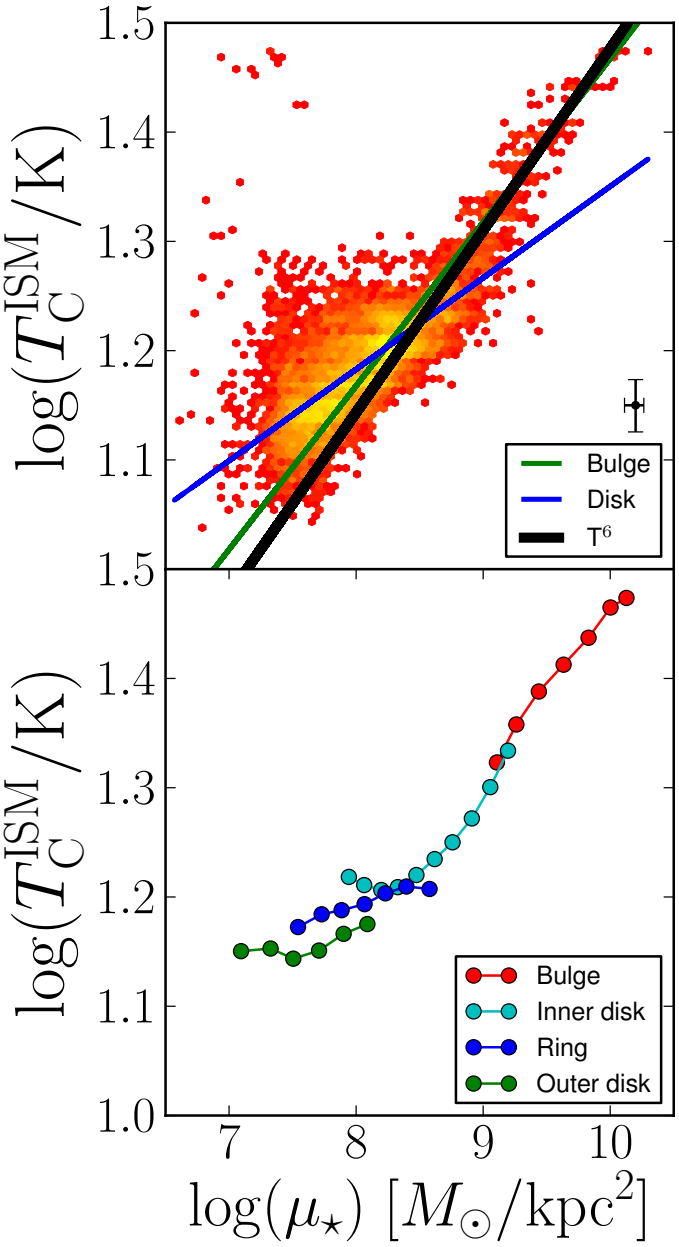

Figure 3.12: Top: Density plot of the stellar mass surface density $\mu_\star$ vs $T_{\rm C}^{\rm ISM}$ for the individual sub-kpc regions of M31. Yellow points indicate a higher density of points, red a lower density. A linear function was fit to the bulge (green line) and disk (blue line) regions. The black line is a theoretical function for pure heating by the old stellar populations. Bottom: Same relation, but separated in the macro-regions for M31: the bulge (red), the inner disk (cyan), the 10 kpc ring (blue), and the outer disk (green). All pixel values are binned in $\mu_\star$; each point is the average of a bin.

bulge. In the intermediate regime, the inner disk region dominates, while the ring and outer disk correspond to the lowest regime of temperatures and stellar densities. Interestingly, the transition takes place at stellar surface densities of $\log(\mu_\star) \sim 8.5$. In the case of integrated galaxies, this is exactly the value that indicates the transition from disk to bulge dominated systems (Schiminovich et al. 2007).

As described in Smith et al. (2012c), we expect a slope of 6^{-1} in a T_d vs $\mu_\star$ plot (as $\mu_\star \sim T^{4+2}$ from the Stefan–Boltzmann law, weighted with the dust emissivity index $\beta = 2$) if the heating of diffuse dust is purely due to the ISRF of the old stellar populations. The slope of the linear fit to the bulge pixels is 6.68^{-1}, which compares to the value of 4.61^{-1} that was calculated by Smith et al. (2012c), correlating the dust temperature from black–body fitting and the 3.6 μm surface density. Figure 3.12 visually shows how that our value is close to the expected one. The slope of the "low–temperature" regime is instead 11.95^{-1}.

The bimodal relation we find is clearly indicative of two different heating regimes. This duality lies in the line of previous investigations of dust heating sources on sub-kpc scales (e.g. Boquien et al. 2011; Bendo et al. 2012a). In the disk of Andromeda, the dust is heated by both old and new stars, giving rise to a rather flat slope and a significant amount of scatter. The bulge of M31 is instead dominated by the light of old stars, making them the dominant dust heaters. This further supports the results of Smith et al. (2012c), Groves et al. (2012), and Draine et al. (2014).

3.6 Discussion and conclusions

In the present work, we have performed SED fitting of a panchromatic dataset, collected for our neighbour galaxy M31. New *Herschel* observations were combined with GALEX, SDSS, WISE, and *Spitzer* data, covering UV to submm wavelengths and allowing us to derive, by exploiting a physically self–consistent model, some physical parameters both on a global and on a local scale. To create statistically independent regions, all the data were convolved to a resolution matching that of the SPIRE 500 μm waveband, the lowest in our dataset, which allowed us to probe physical scales of $\sim 137 \times 608$ pc in the plane of M31. In this chapter we concentrate on the analysis of the scaling relations linking the dust and stellar properties.

We have fitted a multi-component theoretical SED to each pixel which allowed us to estimate several physical properties of that region. Every physical parameter for every pixel was given an uncertainty estimation based on the broadness of its corresponding PDF. Physical quantities that could not be sufficiently constrained were removed from the sample. Furthermore, 2-D parameter maps are constructed for each physical quantity.

Additionally, we have decomposed Andromeda in four macro-regions: the bulge, the star forming ring (the so–called 10 kpc ring), and the inner and outer disk regions. The same fitting

routine was applied to the integrated fluxes of each of these main components, as well as to the global observed fluxes.

From the point of view of the dust scaling relations, M31 is an average galaxy when compared to the local galaxies in the HRS sample. On the other hand, it lies above the average $M_{\rm dust}$ vs SFR relation of da Cunha et al. (2010); despite a dust mass close to the sample average, Andromeda is forming stars significantly less efficiently than the other galaxies.

By investigating the properties of the distinct morphological components, we find strong hints for an inside–out star formation scenario. In this evolutionary model, the bulk of stars are being formed at early epochs in the bulge, and the more recent star formation happens at larger galactocentric distances (i.e. $\gtrsim$ 3 kpc). In particular, the bulk of star formation is currently taking place in the 10 kpc ring, the morphological structure that contains most of the dust in the galaxy. While the analysis presented in this chapter can give no strong clues regarding the past star formation history, we do find an enhancement of dust and star formation in the ring with respect to the galactic disk. This would be consistent with a triggering due to a close encounter with the dwarf satellite M32. Block et al. (2006) used numerical N-body simulations to model the effect of the passage of M32 through Andromeda's disk. Beginning with a model with two spiral arms, they end up with a morphological structure closely matching the 10 kpc ring and the "hole" which is easily visible in IR images towards the south. Similarly, Gordon et al. (2006) argued that a head–on encounter with M32, might have resulted in star forming waves propagating through the 10 kpc ring.

The bulge and inner disk region have red colours and high stellar mass surface density ($\mu_\star$). The star forming ring and outer disk region are bluer and have lower $\mu_\star$. Each of these regions lies on the average trend of the HRS scaling relations. In terms of NUV–r colour, the bulge of M31 is a remarkable exception, being redder than any of the submm detected HRS galaxies. The macro-regions thus have characteristics closely resembling those of global galaxies, where the bulge and inner disk may be seen as early-type while the ring and outer disk resemble late-type galaxies.

The results for M31 not only support an inside-out formation pattern for the bulge-disk morphology, but they also tell us something about the differences in the local environments. When looking at the dust–to–stellar mass ratio as a function of the stellar mass surface density (see Fig. 3.10), we observe a smooth transition from high stellar mass/low dust regions in the bulge, to the low stellar mass/high dust content of the outermost regions. Only the starforming ring, containing a significant fraction of the dust of the whole galaxy, is slightly displaced from this relation.

On the other hand, the four regions behave quite differently when the sSFR is plotted as a function of $\mu_\star$ (see Fig. 3.10). A tendency is found for regions of higher stellar mass surface density to host less star formation, in a way mimicking an internal downsizing process in star

formation, in which the regions of highest stellar density have already stopped forming stars. Within each region, the variation in $\mu_\star$ spans only about 1 order of magnitude, whereas the sSFR always varies by more than 3 (with the exception of the bulge, where there is barely any star formation).

These relations seem to suggest that downsizing relations break down when considering the smallest scales. Star formation at these scales has a weak dependence on the stellar mass: small-scale environments characterised by different stellar masses can be associated with very different levels of star formation, at least as far as a quiescent galaxy like M31 is concerned. What drives the general star formation mode, which determines where the galaxy as a whole places itself on the scaling relations, must instead be the total mass of all its constituents.

When considering the modelling of the observed SED on the smallest scales, our main conclusions are as follows.

1. The SED of sub-kpc regions can be successfully fitted using galaxy-based models, provided that the parameter space is adequately sampled.
2. When investigating the dust heating in the bulge, we recover the theoretical $(T_{\rm C}^{\rm ISM})^6 \sim \mu_\star$ relation. This indicates that old stars are the dominant heating source in this region. The dust heating source is more ambiguous in the disk, where both star formation and the diffuse ISRF irradiate the dust.
3. We find strong correlations, on a pixel–by–pixel scale, between $M_{\rm dust}/M_\star$ and NUV–r (or, equivalently, sSFR), and between $M_{\rm dust}/M_\star$ and $\mu_\star$. These scaling relations, involving the dusty component of the ISM, are remarkably similar to those found for entire local galaxies. This suggests that the dust scaling relations are built *in situ*, with underlying physical processes that must be local in nature.
4. As already found for other galaxies, M31 seems to have undergone an inside–out evolution in its star formation process, possibly influenced by interactions with its satellites.
5. When considering the smallest scales, a wide range in dust content, sSFR, and $M_{\rm dust}/M_\star$ is found within Andromeda illustrating the great diversity of sub-kpc regions. Even within the late-type ring and outer disk of M31, early-type micro-regions can be found. Vice versa, the inner part of M31 still holds a small number of late-type regions.

The fact that we are able to reproduce the dust scaling relations on a sub-kpc scale states that these relations are not only partially a manifestation of a galaxy-wide equilibrium, but they also arise from local scales.

We speculate that the local radiation field balance lies at the core of these relations. The local radiation field can be roughly separated in an energetic component arising from newly forming stars, and a more modest component associated with the general stellar population. A balance leaning towards new stellar populations, will yield bluer colours and higher specific dust masses

(star formation boosts dust production). This usually happens in galaxy disks, where the stellar mass surface density is lower. This regime occupies the left part of the panels in Fig. 3.9. Vice versa, the right part of the scaling relations are associated with regions of higher stellar density and lower star formation. Dust destruction happens faster than dust production here. The radiation field balance leans towards the general stellar population, yielding redder colours. This theory is of course difficult to prove, but the answer potentially lies in detailed chemical evolution models and radiative transfer simulations.

Still, the question remains why the scaling relations are valid on scales of GMCs. In fact, this relates to another question: at what scales does the balanced interplay between the evolutionary processes involving dust and stars break down? Answers to this may be found in similar studies of the Galactic ISM or by future, high–resolution FIR space missions. Zooming into the ISM of our own galaxy can unveil two very different results. If these scaling relations break down at the size of individual molecular clouds, it would indicate that non–local scattered light plays an important role in the dust energy balance. Alternatively, if the scaling relations stay intact, non–local light is negligible at each scale, which would call for a revision of the physical properties of interstellar dust.

Part III

Radiative Transfer Modelling

Inferring the dust content in nearby galaxies

4

Keep your eyes on the stars, and your feet on the ground.

Theodore Roosevelt

4.1 Introduction

To study the starlight-dust interaction in more detail, we must resort to the modelling of single galaxies. Ideally, Andromeda offers the most detail while still keeping the global view of the galaxy. The drawback of such detailed observations is that 1) analytical prescriptions fall short to mimic the observed geometrical structure, and 2) radiative transfer calculations will take long to run, making inverse radiative transfer practically impossible. As there is still much to learn through this unbiased modelling, we chose to apply it to another local galaxy. This galaxy should have a simple geometry for both stars and dust. Furthermore, it makes sense to look beyond the realm of edge-on spiral galaxies, because they have been extensively investigated in recent years (Xilouris et al. 1997, 1999; Popescu et al. 2000; Bianchi 2007; De Looze et al. 2012b,a; De Geyter et al. 2013, 2014).

Early-type galaxies (ETGs) usually have a smooth and regular shape. Moreover, ETGs are not red and dead as was once the common understanding. Deeper observations across the electromagnetic spectrum have revealed significant amounts of matter in the interstellar medium (ISM) and even star forming activity in these objects (see e.g. Rampazzo et al. 2005; Combes et al. 2007; Young et al. 2011; Smith et al. 2012d). They could thus be modelled in the same way as edge-on spirals, through inverse radiative transfer.

The likely mechanism to form early-type galaxies is found in major or minor mergers of spiral galaxies. During these events, interstellar matter of the progenitors is partly expelled and partly consumed in waves of fast star formation (see e.g. Barger et al. 1996; De Lucia et al.

Chapter based on Viaene et al. (2015).

2006). After a few Gyr, the galaxy relaxes to become a stable, non-star-forming object with a depleted ISM. Many ETGs, especially the more massive ones, are embedded in a halo of hot, X-ray-emitting gas (Forman et al. 1985; Sarzi et al. 2013), which is the remnant of the violent merger processes. Interstellar dust cannot survive in the harsh environment of the hot gas. Measurements of significant amounts of dust of various morphologies in over half of the ETGs (Goudfrooij et al. 1994b,a; van Dokkum & Franx 1995; Ferrari et al. 1999; Tran et al. 2001; Patil et al. 2007; Finkelman et al. 2008; Kaviraj et al. 2012; Kulkarni et al. 2014) then lead to the conclusion that the dust reservoir must be replenished in some way. Since internal production mechanisms seem to fall short, a merger origin of the dust seems the most likely option (see e.g. Finkelman et al. 2012, for an elaborate account).

The dust mass determination in ETGs is complicated by the discrepancy found between the different dust mass measurements. Numerous FIR observations of ETGs have been obtained using *IRAS*, *ISO,* and *Spitzer* (see e.g. Knapp et al. 1989; Leeuw et al. 2004; Temi et al. 2004, 2007; Xilouris et al. 2004). Temi et al. (2004) found that dust masses derived from *ISO* observations (2.5 – 240 μm) are more than an order of magnitude higher than *IRAS*-derived (12 – 100 μm) dust masses. They argue that *ISO* detects much more cold dust, which could explain the difference. Indeed, *IRAS* was only sensitive to wavelengths shorter than 100 μm, making it insensitive to the emission from cold ($<$ 25 K) dust (Devereux & Young 1990). Because cold dust is actually by far the most massive dust component in galaxies, *IRAS*-derived dust masses consequently yield lower limits (Gordon et al. 2010).

IRAS-derived dust masses are in turn an order of magnitude higher than those computed using extinction models (see e.g. Patil et al. 2007; Finkelman et al. 2012, and references therein). Deriving dust masses from ultraviolet (UV), optical, and near-infrared (NIR) data can be difficult due to the effects of scattering and the complicated star-dust distribution (see e.g. Witt et al. 1992; Baes & Dejonghe 2001). The estimated amount of dust is thus highly model dependent. Moreover, it requires a consistent dataset spanning a sufficient wavelength range to infer the wavelength-dependent extinction by dust. Up to now, the generally applied dust geometry was that of a dust screen in between the galaxy and the observer (see e.g. Goudfrooij et al. 1994a; Ferrarese et al. 2006; Patil et al. 2007; Finkelman et al. 2008, 2010). This naturally yields lower limits of the dust mass when derived from extinction. The dust mass discrepancy with far-IR (FIR) measurements may be explained by invoking a second dust component, which follows the stellar body and is diffuse (hence not detectable in the optical; Goudfrooij & de Jong 1995; Wise & Silva 1996).

The diffuse dust component in ETGs is not to be confused with the component of the same name found in spiral galaxies. The latter term was invoked to differentiate the dust that resides in clumps or filaments in the disks of spiral galaxies. The diffuse dust in ETGs does not refer to this low-scale height component, but to the dust components following the stellar distribution. Furthermore, in ETGs, it is heated solely by the old stellar populations, while in the discs of

spiral galaxies, young stars contribute significantly to the heating of the diffuse dust (see e.g. De Looze et al. 2014; Bendo et al. 2015, and references therein).

To explain the dust mass discrepancy found in ETGs, a diffuse dust component should be about 10-100 times as massive as the dust lane (based on *IRAS* and *ISO* mass estimates, respectively). Such a vast reservoir of cold dust should then be observable with *Herschel*. However, in most ETGs, the FIR and sub-mm emission is much more compact (see e.g. Smith et al. 2012d). As a result, dust emission is not spatially resolved in the vertical direction in Herschel observations. Therefore, a direct detection of a diffuse dust component following the stellar distribution has not yet been reported in ETGs.

We can now revisit these problems using high-quality data covering a broad range of wavelengths and advanced models. The dust content in ETGs has been studied intensely over the past few years. Dedicated investigations of individual targets (e.g. M87 Baes et al. 2010, M86 Gomez et al. 2010, and NGC 4125 Wilson et al. 2013) were supplemented with statistical studies. For example, from the *Herschel* Reference Survey (HRS, Boselli et al. 2010b): Smith et al. (2012d); Cortese et al. (2012b), from the *Herschel* Virgo Cluster Survey (HeViCS, Davies et al. 2010a): Clemens et al. (2010); di Serego Alighieri et al. (2013), and from the *Herschel* Astrophysical Terahertz Large Area Survey (H-ATLAS, Eales et al. 2010): Agius et al. (2013); Rowlands et al. (2012). As the SPIRE and PACS instruments on-board the *Herschel* spacecraft cover wavelengths from 70-500 μm, the peak of cold dust emission could be sufficiently sampled, and more reliable dust masses could be derived for all of these objects.

In this study, we re-evaluate the dust mass discrepancy in ETGs using new high-quality optical and FIR/submm data, and advanced models. NGC 4370 is an edge-on lenticular in the Virgo cluster at a distance of 23 Mpc (taken from the GoldMine archive; Gavazzi et al. 2003). It has been classified as a boxy S0 galaxy in several independent studies (Binggeli et al. 1985; Baillard et al. 2011; Buta et al. 2015). However, the edge-on view makes it difficult to classify because stellar discs or spiral arms may be hidden by the dust lane. A difference of more than a factor 3 between the dust mass obtained from the modelling of optical data and from IRAS fluxes was found for this galaxy (Finkelman et al. 2008). Since *IRAS* dust masses are usually underestimations, this discrepancy can only widen. Thanks to its smooth stellar profile and conspicuous, regular dust lane, the galaxy is suited to several (semi-)analytical modelling techniques. Excellent optical data are now available for this object, complemented by deep FIR/sub-mm observations from *Herschel*. We therefore choose NGC 4370 for this pilot study. This chapter is organised in the following way. The data is described in Sect. 4.2, and our modelling efforts are outlined in Sect. 4.3. We discuss the results in Sect. 4.4 and present our conclusions in Sect. 4.5.

4.2.1 Optical/NIR data

Optical imaging for NGC 4370 was obtained from the Next Generation Virgo Cluster Survey (NGVS, Ferrarese et al. 2012). This legacy survey was executed with the MegaCam wide-field optical imager at the Canadian-France-Hawaii-telescope over the 2009A-2013A cycles. All fields were observed in the *ugiz* filters, with some also covered in the *r* band. The survey consists of 117 separate MegaCam fields of ~1.0 deg^2 with a pixel scale of 0.187 arcsec. The fields overlap slightly, covering a total area of more than 104 deg^2 on the sky. The fields are centred on M87 and M49, and they map the Virgo cluster out to one virial radius. The NGVS data is photometrically calibrated using stars from the SDSS resulting in rms errors of 0.01 – 0.02 mag (Gwyn 2008). Through dedicated data processing, a point-source depth of $\approx$ 25.9 mag (10σ) is achieved in the g band. For extended sources, the surface brightness limit is $g = 29$ mag arcsec^{-2} for a 2σ detection above the sky.

NGC 4370 was imaged in the *ugi* and *z* bands. This dataset exposes the galaxy in great detail (seeing $< 1''$) and allows for an accurate study of the extinction effects (see Fig. 4.1). The fully reduced and calibrated images were first brought to the same point spread function (PSF). The full width half maximum (FWHM) of the PSF was determined for each band as an average of several brighter stars in the image. The resolution (FWHM) was measured to be 0.81, 0.87, 0.53, and 0.70 in the u, g, i, and z bands, respectively, and therefore all images were convolved to a common 0.87 arcsec seeing using a Gaussian convolution kernel. The frames were regridded to the pixel grid of the g band as well in order to work with a set of pixels that correspond to the exact same physical regions. After that, the images were rotated over 6° in such a way that the dust lane fell along the x-axis of the frame. Both steps required some interpolations that reduced our working resolution to $0.98''$. This corresponds to 97 parsecs at the distance adopted for NGC 4370 (23 Mpc).

In a final step, bright foreground stars were masked out in each band. The stars were identified based on their shape and offset to the galaxy's brightness profile and verified with the NOMAD catalogue (Zacharias et al. 2004). Background galaxies in the field of view were identified using NED [1]. All reported galaxies in the field lie near the edge of the image, and the brightest one has a g band magnitude of only 20.3. We therefore did not mask any background sources.

The dust in NGC 4370 greatly affects the appearance of the optical images, which we use to our advantage. However, it is also useful to gain more insight into the underlying stellar morphology. We therefore include the IRAC 3.6 μm image from the Spitzer Survey of Stellar Structure of Galaxies (S^{4}G, Sheth et al. 2010) which is shown in the top right-hand panel of

[1] http://ned.ipac.caltech.edu

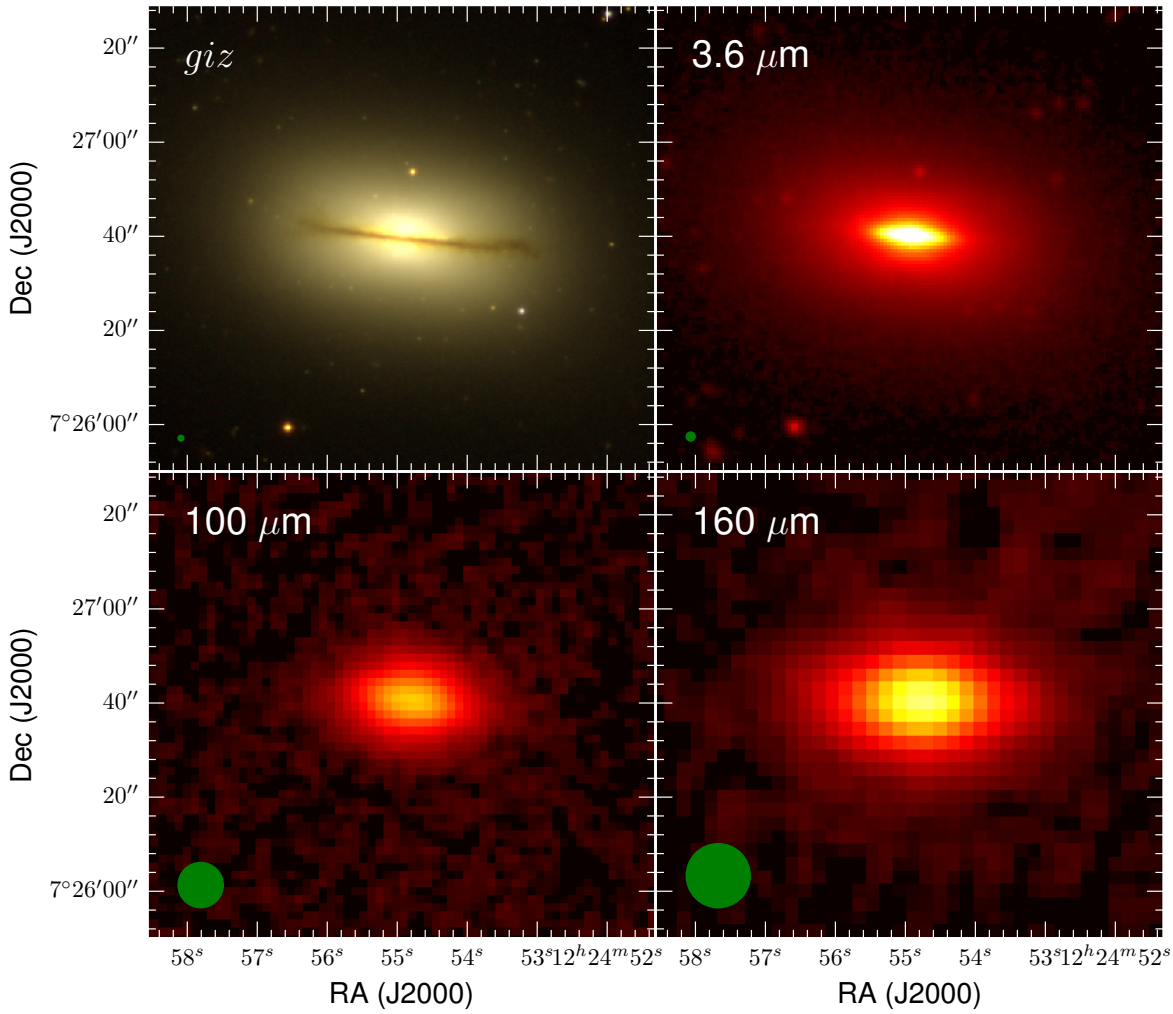

Figure 4.1: Overview of the dataset. Top left: RGB colour map of NGC 4370 based on the *giz* images of the NGVS. Top right: IRAC 3.6 μm image from the S^{4}G. Bottom: PACS 100 μm (left) and 160 μm (right) images. The beam size is indicated as a green circle in the lower left corner of each image.

Fig. 4.1. At these wavelengths, we expect minimal dust contamination and still benefit from a decent spatial resolution (FWHM ~1.7 arcsec).

4.2.2 FIR/sub-mm data

The *Herschel* Virgo Cluster Survey (HeViCS; Davies et al. 2010a) observed 84 deg^2 of the Virgo Cluster with both PACS (100, 160 μm) and SPIRE (250, 350, 500 μm). The observations were done in parallel fast-scan mode (60 arcsec s^{-1}). The area is subdivided into four areas, corresponding to the region around M87 (V2), and the clouds to the north-west (V1), west (V3), and south (V4) of V2. Each area was covered by a 4×4 sq. degree tile and observed four times in two orthogonal scan directions to reduce the $1/f$ noise. The PACS data were reduced using a combination of HIPE (v12.0, Ott 2010) and `Scanamorphos` (version 24, Roussel 2013). The

latter, in particular, corrects for a flatfield distortion that causes an offset of up to ~7% in the fluxes at 160 μm. In a subsequent observing run, 44 galaxies from the bright galaxy sample of HeViCS were observed with PACS in the 70 and 160 μm bands in map-making mode. NGC 4370 was one of them, and we use the 70 μm data from this run. These observations were reduced in a similar way to the parallel scan maps. The SPIRE observations were reduced using HIPE (v12.0) and the custom routine BriGAdE (Smith, in prep.) For more details on the data reduction, we refer the reader to Auld et al. (2013). The final maps have a beam size (FWHM) of 5.7, 9.4, 13.4, 18.2, 25.4, and 36.0 arcsecs for 70, 100, 160, 250, 350, and 500 μm, respectively, corresponding to a physical scale of 0.64, 1.05, 1.49, 2.03, 2.83, and 2.01 kpc at a distance of 23 Mpc for NGC 4370.

Because NGC 4370 lies on the intersection between two tiles (V3 and V4), it was observed –partially– by scans targeting the two different fields. It turns out that the galaxy was observed by a total of 13 scans, which were thus used to construct the maps at 100 and 160 μm. This is allowed by the option `cutout` in `Scanamorphos`, which forces the use of only those parts of the scanlegs that contain emission from the galaxy. This will enhance the signal-to-noise ratio (S/N), positively affecting the flux uncertainty determination, so we chose to redo the flux density measurement in the PACS 100 μm and 160 μm bands. We find new values of $F_{100\,\mu\mathrm{m}} = 3.03 \pm 0.18$ Jy and $F_{160\,\mu\mathrm{m}} = 3.65 \pm 0.24$ Jy. This is about 3% lower for $F_{100\,\mu\mathrm{m}}$ and 6% for $F_{160\,\mu\mathrm{m}}$ compared to the measurements of Cortese et al. (2014), who used the standard data products. These are, however, not corrected for the flatfield distortion in the PACS bands, while our measurements do include this correction. Figure 4.1 shows the newly reduced PACS maps. We also measure the integrated flux of the PACS 70 μm image and find $F_{70\,\mu\mathrm{m}} = 1.348 \pm 0.073$ Jy, which is fully consistent with the MIPS 70 μm flux measured by Bendo et al. (2012b). Since the SPIRE flux measurements from Ciesla et al. (2012) are already of good quality with just eight cross-scans, we take these for our further analysis. They are $F_{250\,\mu\mathrm{m}} = 1.95 \pm 0.05$, $F_{350\,\mu\mathrm{m}} = 0.77 \pm 0.04$, and $F_{500\,\mu\mathrm{m}} = 0.25 \pm 0.02$ Jy. Table 4.1 summarises the integrated fluxes for NGC 4370 used in this work.

4.3 Methods and results

We explore several methods of investigating the extinction properties and determine the dust mass of NGC 4370. Each model treats the dust geometry, hence the corresponding attenuation effects, in a different way. It is important to note that different dust mass estimates cannot be compared unless a common dust model is used. To achieve this consistency, we adopt the Draine & Li (2007) dust model throughout this chapter. The dust model is derived from observations in our own Galaxy and consists of carbonaceous grains, amorphous silicates, and polycyclic aromatic hydrocarbons (PAH).

4.3.1 Dust masses from FIR/sub-mm emission

The bulk of the dust in galaxies resides in the diffuse ISM at low equilibrium temperatures of 10 – 30 K. This component is directly measurable through its emission in the FIR/sub-mm. The emission is mostly optically thin and so guarantees that all the dust will be visible, unlike in the case of the UV/optical/NIR where some dust may be hard to trace. Although the SPIRE observations were confusion limited, it may still be that we miss faint emission at larger radii. From the stacking of HRS spiral galaxies, Smith et al *(in prep.)* find that ~2.4% of the dust resides outside the D_{25} radius. Assuming this is even less for ETGs, the missing dust will not contribute significantly to the sub-mm emission.

In the past, the dust mass and temperature of dusty ETGs were derived using a modified black body function (Hildebrand 1983) and *IRAS* fluxes (e.g. Young et al. 1989; Goudfrooij & de Jong 1995; Patil et al. 2007; Finkelman et al. 2008). For NGC 4370, in particular, a dust mass of $4.54^{+0.33}_{-0.31} 10^5\,M_\odot$ was found, scaled to the distance we assume in this work (23 Mpc). The dust temperature from the *IRAS* colours was found to be $T_d = 43.1 \pm 1.3$ K (Finkelman et al. 2008). It must be noted, however, that *IRAS* was unable to detect dust with temperatures colder than 25 K. The values thus only apply to the warm dust component.

Since the broad availability of *Herschel* observations, it has become common practice to estimate the dust mass from a modified black body fit to the FIR and sub-mm fluxes. Following the recommendations of Bianchi (2013), we only fit a modified black body model with a fixed $\beta = 2$. This allows us to determine the dust mass using the Draine & Li (2007) dust model, with an emissivity of $\kappa_{350\mu m} = 0.192$ m^2 kg^{-1} (see Fig. 4.2). We find a temperature $T_d = 21.8 \pm 0.3$ K and a total dust mass $M_d^{\rm modBB} = 6.17^{+0.38}_{-0.36} \times 10^6\,M_\odot$. This is in line with di Serego Alighieri et al. (2013), who used similar data and methodology. It is roughly an order of magnitude higher than the *IRAS*-derived dust mass. This is consistent with the results of Dunne & Eales (2001) and states again the importance of sampling the sub-mm emission of the cold dust component.

We also model the full UV-submm SED with MAGPHYS for comparison. Since this model uses more data points, and ensures an energy balance, it is considered to put better constraints on the galaxy's dust content. We sample the panchromatic SED of NGC 4370 using *GALEX* fluxes from Cortese et al. (2012a), the *ugiz* fluxes from the NGVS, *JHK* magnitudes from the GoldMine archive (Gavazzi et al. 2003), *WISE* fluxes from Agius et al. (2015), and MIPS fluxes from Bendo et al. (2012b). The *Herschel* data described above complete our dataset. Table 4.1 lists the fluxes that were used. The best-fitting SED is shown in Fig. 4.2, as is the intrinsic (stellar) SED without dust attenuation. The model is able to match the observed data remarkably well. If we use the same Draine & Li (2007) dust model, we find a total dust mass of $5.7^{+0.63}_{-0.07} \times 10^6\,M_\odot$ and a temperature of $22.4^{+0.1}_{-0.4}$ K for the cold dust. It is reassuring that we retrieve –within the error bars– a similar cold dust temperature and total dust mass to the

Table 4.1: Observed fluxes used for the SED fits for NGC 4370.

Band	Flux (mJy)	Source
FUV	0.0463 ± 0.0063	a
NUV	0.2166 ± 0.0059	a
u	6.1 ± 1.1	b
g	22.9 ± 1.8	b
i	62.3 ± 2.5	b
z	80.9 ± 3.2	b
J	107 ± 21	c
H	138 ± 21	c
K	121 ± 24	c
WISE 1	73.8 ± 1.9	d
WISE 2	39.8 ± 1.3	d
WISE 3	64.8 ± 3.1	d
WISE 4	56.4 ± 4.7	d
MIPS 24 μm	48.3 ± 2.1	e
MIPS 70 μm	1284 ± 132	e
PACS 70 μm	1348 ± 73	f
PACS 100 μm	3027 ± 172	f
PACS 160 μm	3647 ± 231	f
MIPS 160 μm	2880 ± 350	e
SPIRE 250 μm	1947 ± 53	f
SPIRE 350 μm	772 ± 38	f
SPIRE 500 μm	251 ± 19	f

References. (a) Cortese et al. (2012a), (b) NGVS, this work. (c) GoldMine (Gavazzi et al. 2003), (d) Agius et al. (2015), (e) Bendo et al. (2012b), (f) HeViCS, this work.

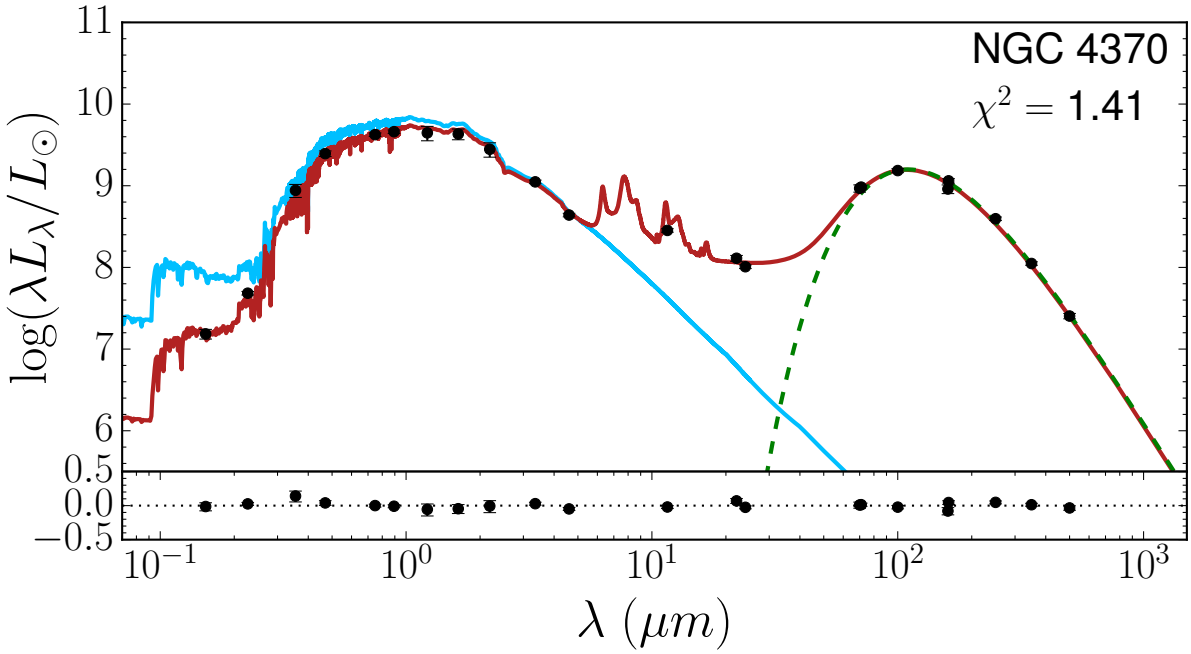

Figure 4.2: MAGPHYS fit of the panchromatic SED of NGC 4370. The black points are the observed fluxes, the blue line is the unattenuated (stellar) SED, and the red line the attenuated, best-fitting template SED. The residuals are plotted below. The dashed green line is the best-fitting modified black body function to the *Herschel* fluxes.

modified black body model.

We note that even these dust mass determinations are still only a best guess of the true dust mass. There are known caveats in the modified black body fitting method. First, a single temperature is assumed for the cold, diffuse dust. In reality, this is likely a continuous range of temperatures, heated by a combination of emission sources. The multiple thermal components of dust appear to blend in such a way that it can be fit by a single modified black body (Bendo et al. 2015). In this scenario, the resulting dust temperatures from a single modified black body may be higher than the actual dust temperatures, and the resulting dust masses may be biased to lower values. Second, it is assumed that the dust in NGC 4370 has the same mixture as in our own Galaxy and that this mixture is the same everywhere in the galaxy. This should not, however, affect relative dust mass differences such as those investigated in this chapter. Last, recent results from Planck Collaboration (2014) indicate that the Draine & Li (2007) dust model overestimates the dust mass by a factor 2-4. Throughout this work we nevertheless consider SED fitting to be the most objective and reliable way to estimate at least the order of the true dust mass in NGC 4370.

4.3.2 Dust masses from colour maps

Given the homogeneous dataset, colour maps are the simplest way to trace the extinction by dust. We can write the observed colour between two bands X and Y as

$$(X - Y) = (X_0 - Y_0) + (A_X - A_Y) \tag{4.1}$$

where $X_0 - Y_0$ is the intrinsic colour and $A_X - A_Y$ the difference in attenuation between the two wavelength bands, also called selective attenuation. The intrinsic colour $X_0 - Y_0$ is a manifestation of the wavelength-dependent luminosity of the stellar populations. The intrinsic colour was determined from the regions in the galaxy that do not show any obscuration by dust. Because we have four bands, *six* colour maps can be constructed: $u-g$, $u-i$, $u-z$, $g-i$, $g-z$, and $i-z$. Figure 4.3 shows radial profiles along the major and minor axes for each of the colours. The same profile is retrieved in all colours: along the major axis, reddening starts increasing around ~30 arcsec from the centre when dust reddening starts to be effective. It peaks in the centre where most dust is expected along the line of sight. Along the minor axis, a small gradient is present outside the dust lane. The reddening increases sharply when entering the dust lane at ~4 arcsecs and peaks in the centre. Not surprisingly, the highest reddening is found for the $u-z$ colour and the lowest reddening for $i-z$.

Interestingly, at the centre of the dust lane, a minor dip is observed in the colour profiles along the minor axis. This effect is most evident in the $u-g$ profile (dark green), but also visible in most of the other profiles. Figure 4.4 shows the maps of selective attenuation, i.e. colour maps minus intrinsic colour. Here, the central part of the dust lane also shows this dip in reddening as a dark line running along the major axis. This colour inversion effect has been observed by Bianchi (1999) in the B-I colour map of NGC 891, a massive edge-on spiral galaxy. It is suggested that saturation of the dust extinction occurs in these regions. At the same time, the number of stars between the dust and observer is expected to be largest here. As a result, the colour of the stars that lie in front of the dust becomes dominant over the reddening by dust. This makes the central part appear bluer than the dusty regions right above or below.

We must note that there are known colour gradients in ETGs, which possibly affect the measurement of the intrinsic colour. Petty et al. (2013) showed that the inner parts of ETGs are generally redder than the outskirts, and several spectroscopic studies have revealed age and metallicity gradients (e.g. Carollo et al. 1993; Kobayashi & Arimoto 1999; Baes et al. 2007; Koleva et al. 2011). As a result, when measuring the intrinsic colours of NGC 4370 outside the dust lane, it is possible that we pick up bluer colours than those behind the dust lane. This would result in slightly lower $A_X - A_Y$ values, hence lower dust masses. We confirm colour gradients along the minor axis of NGC 4370 (see Fig. 4.3), however they are small with respect to the reddening in the dust lane. We therefore assume that the above effect will only cause a limited decrease in dust mass. The resulting maps of selective attenuation are shown in the left-hand

column of Fig. 4.4.

On the other hand, since NGC 4370 is classified as an S0 type galaxy, a stellar disc may be present, concealed by the dust lane. The IRAC 3.6 μm image (see Fig. 4.1) indeed shows a disc-like feature in the centre of the galaxy. If this obscured disc contains some ongoing star formation, it will be bluer than the intrinsic colours we measure outside the dust lane. Consequently, this can lead to underestimating the dust mass. It is nearly impossible to determine the intrinsic colour of a potential stellar disc from the edge-on perspective, which immediately illustrates the limitations of this simple approach. Fortunately, the stellar disc is relatively small ($< 25''$ in diametre or $< 0.25 D_{25}$) and limited to the central regions of NGC 4370, so this effect may be relatively small. Nevertheless, this implies that resulting dust masses should be seen as lower limits to the true dust mass in NGC 4370.

The degree of the reddening is limited (1-4 magnitudes) because we only consider optical observations. The reason not to expand this set to UV or NIR observations is twofold: first is the superb resolution in the optical images. The FWHM of the IRAC maps is twice that of the g band, the largest optical beam size. For GALEX observations, the difference is more than a factor of 5. Second are the intrinsic colour gradients, which are much stronger when colour maps are created over these wide wavelength ranges. An accurate subtraction of the intrinsic colour is crucial for producing a reliable selective attenuation map. We therefore chose to proceed with the limited but fully consistent and high-quality optical dataset.

To convert (selective) attenuation maps to dust maps, we need to make assumptions about the star-dust geometry. Dust masses can be derived from the dust mass surface density in each pixel Σ_d. The total extinction coefficient κ_λ of the dust at a certain wavelength, relates the dust mass to the optical depth τ_λ:

$$\tau_\lambda = \kappa_\lambda \Sigma_{\rm d}. \tag{4.2}$$

To determine the optical depth from the attenuation maps, the geometry of the dust distribution needs to be taken into account. We consider two different dust geometries. The first one is a simple foreground dust screen between the stars and the observer:

$$A_\lambda = -2.5 \log(e^{-\tau_\lambda}) = 1.086 \tau_\lambda. \tag{4.3}$$

This geometry requires a minimal amount of dust to obtain the observed attenuation. The second model describes a layer of dust embedded in a layer of stars and is usually dubbed "the sandwich model" (Disney et al. 1989; Boselli et al. 2003; Cortese et al. 2008):

$$A_\lambda = -2.5 \log\left[\left(\frac{1-\zeta_\lambda}{2}\right)(1+e^{-\tau_\lambda}) + \left(\frac{\zeta_\lambda}{\tau_\lambda}\right)(1-e^{-\tau_\lambda})\right]. \tag{4.4}$$

The dimensions of the dust disc, relative to the stellar disc, are expressed by the parameter ζ_λ. We limit ourselves to the two extreme cases of this geometry, $\zeta_\lambda \to 1$ and $\zeta_\lambda \to 0$. The former

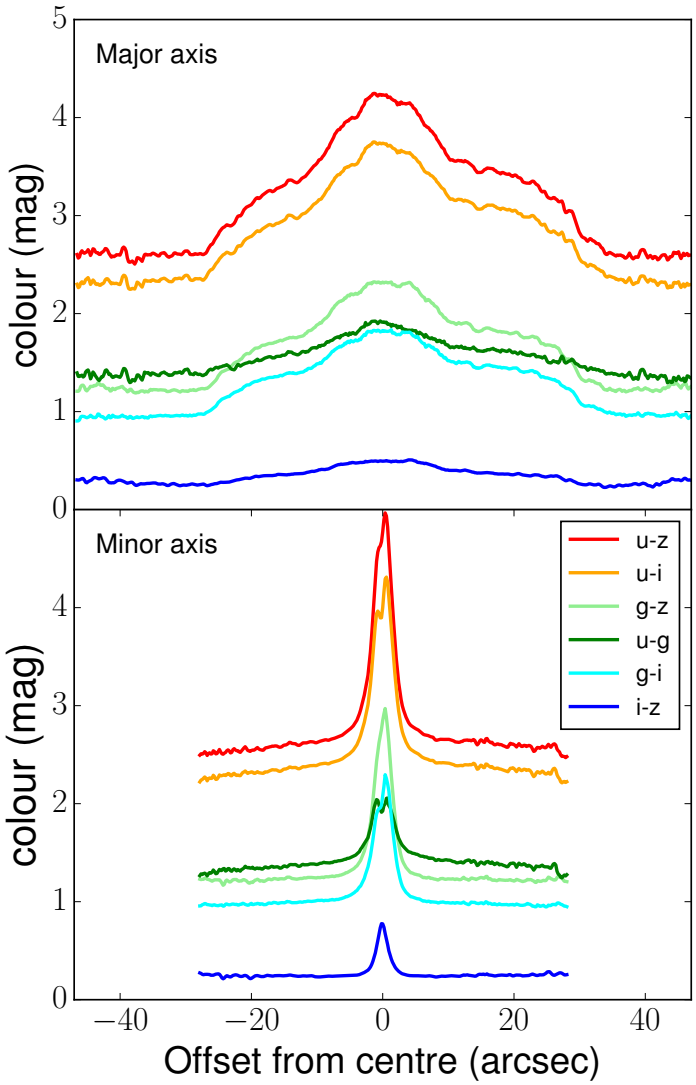

Figure 4.3: Colour profiles along the major and minor axes, derived from each colour map of NGC 4370.

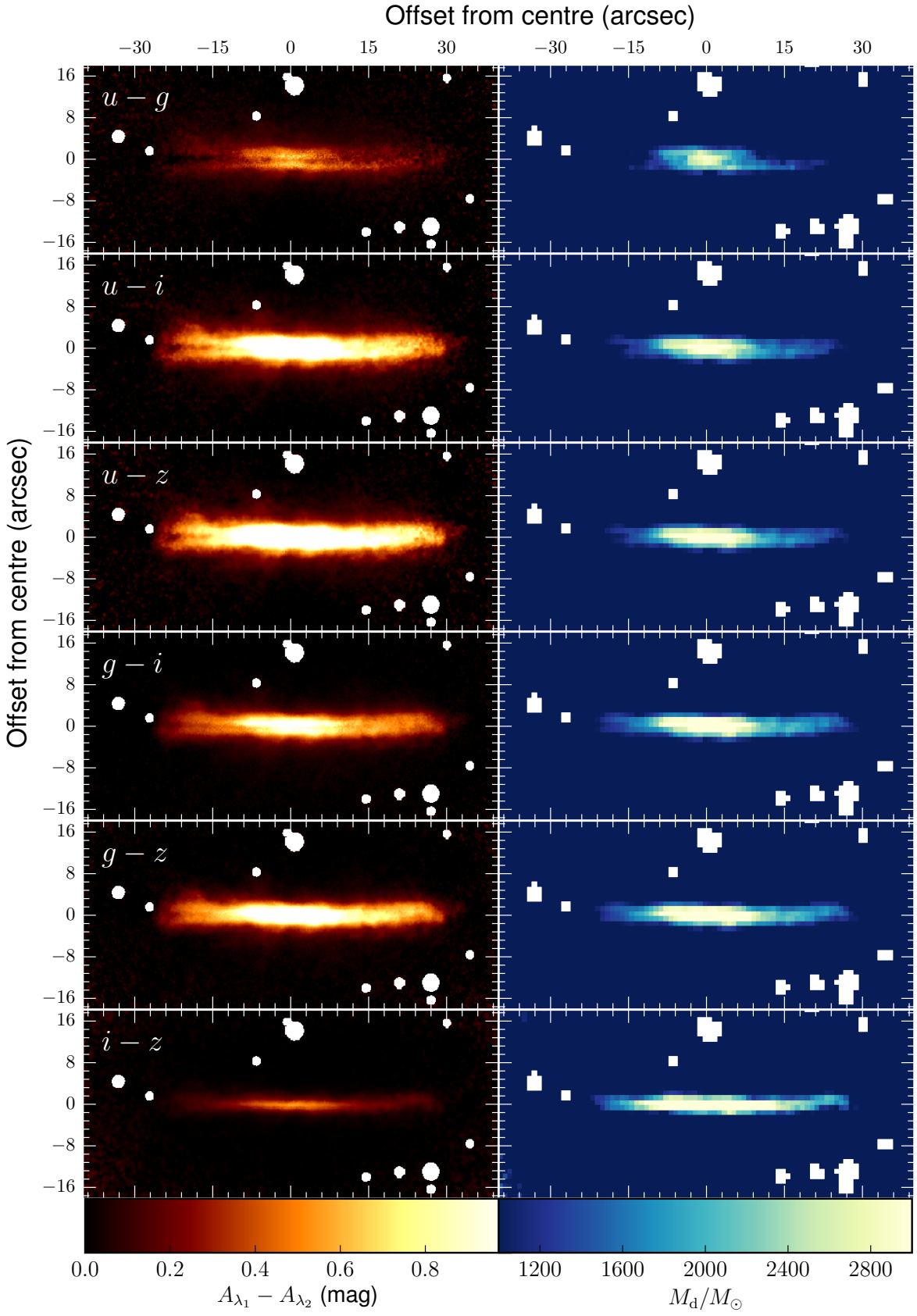

Figure 4.4: Left: Selective attenuation ($A_{\lambda_1} - A_{\lambda_2}$) for all optical colours of NGC 4370. Right: corresponding dust mass maps in the foreground screen geometry at the critical 1 arcsec resolution. The white dots indicate masked foreground stars.

limit corresponds to a dust layer of equal dimensions to the stellar layer. This boils down to a uniform mixing of dust and stars:

$$A_\lambda = -2.5 \log \left(\frac{1 - e^{-\tau_\lambda}}{\tau_\lambda} \right). \tag{4.5}$$

This formula can in principle be inverted analytically by means of the Lambert W function to recover the optical depth from an observed attenuation (see Boquien et al. 2013).

On the other hand, when $\zeta_\lambda \to 0$, an infinitely thin slab of dust is embedded in the stellar layer along the line of sight:

$$A_\lambda = -2.5 \log \left(\frac{1 + e^{-\tau_\lambda}}{2} \right). \tag{4.6}$$

Colour maps yield maps of selective attenuation $A_{\lambda_1} - A_{\lambda_2}$. This can be written as a combination of optical depth functions using equations (4.3) - (4.6): $A_{\lambda_1} - A_{\lambda_2} = f(\tau_{\lambda_1}) - f(\tau_{\lambda_2})$. Using the Draine & Li (2007) dust model, the optical depth at one wavelength can be converted into the equivalent optical depth at another wavelength:

$$\frac{\tau_{\lambda_1}}{\kappa_{\lambda_1}} = \frac{\tau_{\lambda_2}}{\kappa_{\lambda_2}} \tag{4.7}$$

These equations were then numerically solved to yield a value for a specific optical depth, which in turn yields a dust mass through Eq. 4.2.

Uncertainties on the attenuation and attenuation differences were derived following Goudfrooij et al. (1994a). Attenuation values were first derived on a pixel-by-pixel basis at the native pixel scale of 0.19″. This is roughly five times smaller than the PSF of the convolved images (0.98″). We therefore rebinned each attenuation image using a 5×5 pixel box and assigned to each (rebinned) pixel a value and uncertainty equal to the mean attenuation (or selective attenuation) and standard deviation calculated within each 5×5 pixel box. These uncertainties are propagated further through the standard bootstrapping method; we created 1000 randomly perturbed attenuation (or attenuation difference) maps based on the errors of the real attenuation maps. For each map, the resulting dust mass is then computed. The uncertainty on the dust mass is then taken to be three times the standard deviation of the random set of dust masses. The final dust masses and their errors are listed in Table 4.2.

Figure 4.4 shows the dust mass maps derived from the corresponding colour maps in the case of the foreground screen geometry. We only sum pixels inside the dust lane, because this is the only region where dust is directly visible. In the foreground dust screen geometry, the same morphology is retrieved for all dust mass maps. Although there are some local variations in the dust mass per pixel, the total dust masses lie close to each other and average out to $5.60^{+0.87}_{-1.3} \times 10^5 M_\odot$, which should be interpreted as a lower limit. This is a value that is comparable to the *IRAS*-derived dust mass, but still an order of magnitude below the dust mass estimates using

Herschel data.

In the case of the sandwich model, retrieving a real solution for the optical depth was not possible for many pixels. For the $u-z$ colour, for example, the maximal attainable selective attenuation based on eq. (4.5) is 1.2597. For eq. (4.6), this is only 0.3276. In contrast, the observed selective attenuation for the $u-z$ colour reached 2.49. Consequently, the pixels with the largest selective attenuation are incompatible both with an embedded thin slab of dust ($\zeta_\lambda \rightarrow 0$) and with a uniform mixing of dust and stars ($\zeta_\lambda \rightarrow 1$). Their mixed nature means that changing the properties of the dust distribution also changes the location of the stars relative to the dust. Because there will always be stars in front of and behind the dust, there are inherent limitations to the attenuation values along a line of sight. It appears that the sandwich model – in the limits we explore here – cannot achieve attenuation values that are high enough to explain the observed ones. We therefore chose not to pursue these geometries any further for the colour maps.

4.3.3 Dust masses from multi-Gaussian expansion models

As a third method, we compare the observations with a dust free model of the galaxy in each waveband to construct monochromatic attenuation maps. A dust-free model is constructed through multi-Gaussian expansion (MGE) fitting. This technique was first developed by Emsellem et al. (1994) and consists of the summing of multiple 2-D Gaussian functions to mimic the brightness profile of elliptical galaxies. Cappellari (2002) constructed a dedicated set of IDL routines to efficiently fit a set of Gaussians to an observed image. We prefer this method over the classic Sérsic profile fit because MGE is more general. This way it better captures the boxy nature of NGC 4370 than a Sérsic profile. The deprojection of the 2D Gaussian functions to 3D is also more straightforward.

It is crucial that the modelling is based on the dust-free part of the galaxy so that the dust lane is masked. We fixed the coordinates of the centre of the galaxy as determined from the z band image (which is assumed to have the least dust contamination) using the MGE-IDL routine `find_galaxy`. NGC 4370 has a boxy stellar distribution, not easily modelled by an elliptical profile. The MGE fitting software fortunately allows each Gaussian to have a different position angle, relative to the x-axis of the frame. A boxy brightness profile can be constructed by summing multiple 2-D Gaussian distributions with a slightly different angle.

MGE models were fitted to each of the four bands of our data set. A roughly equal effective area was used to constrain the free parameters. This corresponded to a S/N threshold of three in the u and g bands, and five in the i and z bands. The number of initial Gaussians is fixed for each MGE run. Allowing more Gaussians increases the number of free parameters, so that more complex brightness profiles can be constructed. On the other hand, if too many free parameters are available, peculiar and unphysical profiles may be found. To find a balance, we evaluated

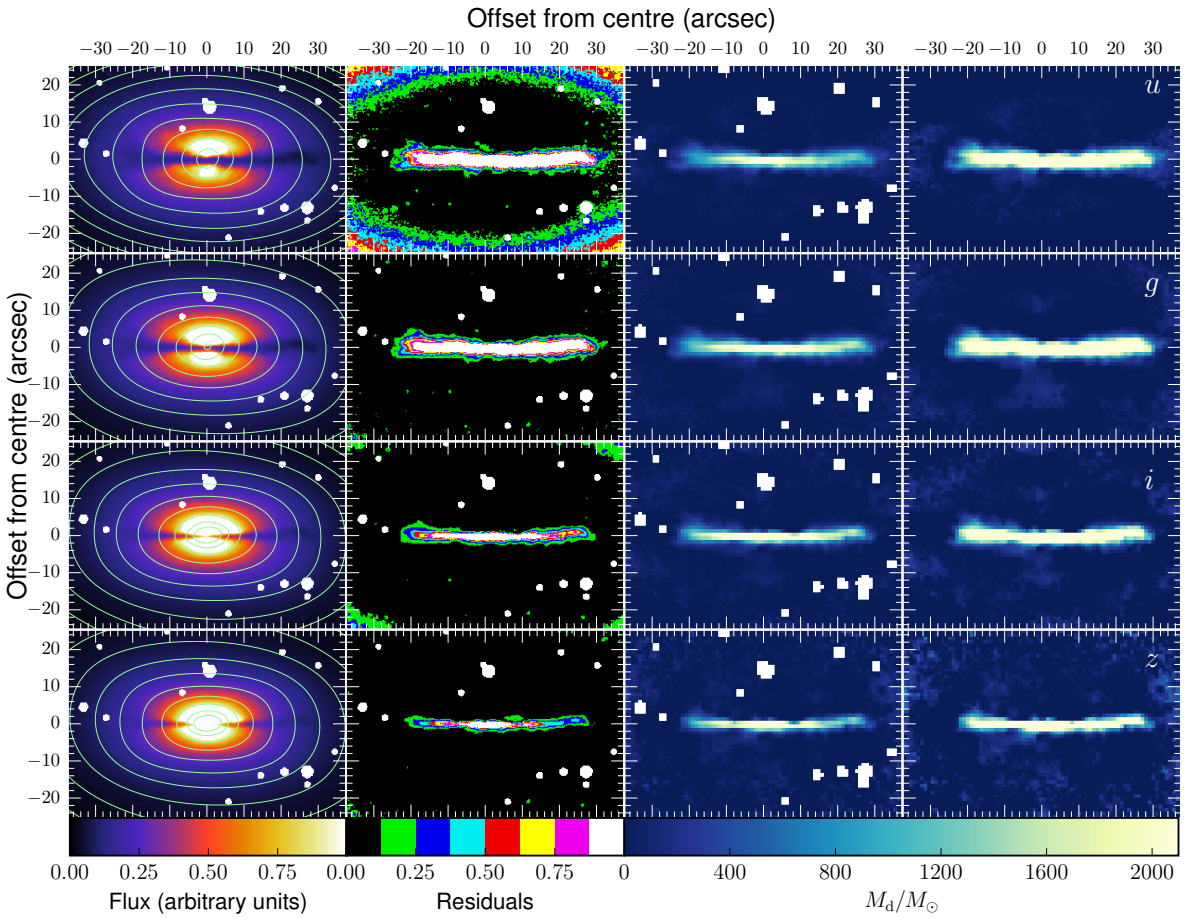

Figure 4.5: First column: Observed images of NGC 4370, overlaid with contours of the corresponding dust-free MGE model. The contour levels are the same for all bands. 2nd column: Residuals of the MGE models and the observed images. 3rd column: corresponding dust mass maps in the foreground screen geometry and at the critical 1 arcsec resolution. 4th column: corresponding dust maps in the uniform star-dust mix geometry. The white dots indicate masked foreground stars.

the non-reduced χ^2 and shape of the brightness profile as a function of the number of free parameters until the best fit was obtained.

The resulting set of Gaussians allows constructing a 2-D, dust-free model of the galaxy. We can now compute the attenuation A_λ for each of the bands by taking

$$A_\lambda = -2.5 \log\left(\frac{I_{\lambda,\mathrm{obs}}}{I_{\lambda,\mathrm{model}}}\right), \tag{4.8}$$

where $I_{\lambda,\mathrm{model}}$ and $I_{\lambda,\mathrm{image}}$ are the model and reference frames, respectively. The attenuation values can then be converted to optical depths using equations (4.3), (4.5), and (4.6). Equation (4.2) then allows the computation of the dust mass maps.

Figure 4.5 shows the results of the MGE modelling for the *ugiz* bands. In the first column, the observations are overlaid on the contours of the dust-free MGE model. In all bands, the contours

closely follow the stellar emission in the observed images. Generally, the model is elliptical in the centre and becomes boxier in the outer part of the galaxy. Owing to the obscuration of the dust lane, some small differences in the central contour shapes are visible across the wavebands. The second column shows the residuals of the MGE model and the observations. Obviously, the dust lane sticks out here because no dust was included in the MGE model. Apart from that, the residual levels are usually below 12.5% and only increase in the outer, low S/N regions. Using this formalism, it is thus possible to reproduce the stellar emission of NGC 4370, and we can now construct attenuation maps. These are shown in Fig. 4.8 and discussed in Sect. 4.3.4.

In the last two columns of Fig. 4.5, the resulting dust mass maps are displayed for the screen, along with uniform-mix geometries. In the case of the embedded thin slab (eq. (4.6)), again no real solutions were found for many of the pixels. This particular geometry can only generate moderate attenuation values up to $2.5 \log 2 = 0.753$, which are lower than most pixels in the dust lane. We therefore do not pursue this geometry any further. For the other two geometries, the dust mass maps have similar morphology and pixel values. A slight decrease in pixel dust-mass values is observed in the z band. This is not entirely surprising since the z band is the longest in wavelength, hence least sensitive to attenuation by dust. Comparing both the dust screen (3rd column) and uniform dust mix (4th column) geometries, the latter clearly has higher dust masses in each pixel. Owing to the mixing of dust and stars, more dust is needed to obtain the same level of attenuation as for the foreground screen of dust. The obtained dust masses are consistent with this view. The total masses are listed in Table 4.2 and were obtained by summing the pixel values in the dust lane. As already visible from the maps, the dust masses in the u, g, and i bands lie close to each other, within each geometry. The z band total dust masses are significantly lower.

On average, the foreground screen yields a total dust mass of $3.35^{+0.64}_{-0.90} \times 10^5 M_\odot$ and the uniform mix geometry $7.9^{+1.9}_{-2.5} \times 10^5 M_\odot$. These values are comparable to the average total dust mass from the colour maps and consistent with the *IRAS*-based dust mass for this galaxy. In the end, with this high-quality data, we are already able to alleviate the previously found dust mass discrepancy between optical and *IRAS*-based dust masses. Of course, *IRAS* masses are still insensitive to cold dust. Indeed, as for the colour maps, the masses are still about an order of magnitude lower than the ones obtained using the *Herschel* observations, which do observe emission from cold dust.

4.3.4 Dust masses from radiative transfer modelling

The most advanced way of treating the extinction of starlight through a dusty medium is through radiative transfer (RT) simulations. It allows us to test realistic dust distributions (e.g. embedded discs or rings) and takes the 3-D geometry of the problem into account. The main advantage over the previous techniques is the self-consistent treatment of dust extinction along the line of

Table 4.2: Dust masses for NGC 4370 as derived from the various methods, in units of $10^5 M_\odot$. The embedded slab geometry did not yield real solutions for either the colour or the MGE method and are therefore not included in the table. We note that the FitSKIRT uncertainties are rms values from fits with different random seeds and are not centred around the best fit value.

Colour maps	Screen	Mix
$u-g$	4.48 ± 0.15	no solution
$u-i$	5.37 ± 0.15	no solution
$u-z$	5.48 ± 0.14	no solution
$g-i$	6.03 ± 0.17	no solution
$g-z$	6.06 ± 0.17	no solution
$i-z$	6.20 ± 0.27	no solution
Average	$5.60^{+0.87}_{-1.3}$	no solution
MGE fits	Screen	Mix
u	3.25 ± 0.12	8.20 ± 0.31
g	3.83 ± 0.15	9.36 ± 0.37
i	3.58 ± 0.24	8.14 ± 0.55
z	2.72 ± 0.27	5.93 ± 0.49
Average	$3.35^{+0.64}_{-0.90}$	$7.9^{+1.9}_{-2.5}$
	FIR/sub-mm	
IRAS [a]	$4.54^{+0.33}_{-0.31}$	
ModBB	$61.7^{+3.8}_{-3.6}$	
MAGPHYS	57^{+6}_{-1}	
	FitSKIRT	
Exponential disc	50 ± 24	
Ring	33 ± 27	
IRAC Ring	70 ± 18	

References. (a) Finkelman et al. (2008)

sight. This provides a more realistic determination of the amount of dust needed to produce the observed dust lane. We make use of FitSKIRT to solve the inverse RT problem.

We start with an initial population of 150 different parameter sets and let them evolve for 100 generations. The code was originally designed and tested to fit the complex geometries of edge-on spiral galaxies. These objects are successfully modelled with up to 19 free parameters. Several of those describe the complex bulge-disc geometry of the stars. In our model, however, we keep the stellar geometry fixed, which drastically reduces the number of free parameters to fit, thereby increasing our confidence in the results of the fits. We explore RT models with two different geometries for the dust distribution in NGC 4370: an exponential disc geometry and a ring geometry. Their best-fitting parameters are determined using FitSKIRT. We simultaneously fit each RT model to the four images (u, g, i, and z bands). Note that we do not make any assumptions on the underlying stellar populations (mass, age, metallicity) in the galaxy. FitSKIRT only fits the flux in each band, without a forced connection or colour between the bands.

The stellar distribution for each model is the same and derived from the z-band image. The longest waveband was chosen to limit contamination by the dust. We construct a dust-free MGE model similar to the one obtained in section 4.3.3. In this case, however, we force each Gaussian to have the same position angle $\theta = 90°$. Allowing different position angles for each Gaussian would severely increase the difficulty of deprojecting the 2-D model to a 3-D stellar distribution. We have chosen to work with only one position angle. The inclination angle for deprojection is left as a free parameter within the $88° < i < 90°$ interval.

Both geometries are fitted five times[1], each time with a different random seed for the genetic algorithms, hence leading to a different solution. The variation in the resulting parameters of each individual fit is used as an indication of the uncertainty and the ability of FitSKIRT to constrain them. The difference between the models lies in the adopted dust distribution, which we discuss below. The results of the fitting are summarised in Table 4.3, which lists the parameters of the dust geometries, and Table 4.2, which lists the corresponding dust masses.

Model A

The first geometry consists of a classic exponential dust disc, generally applied in the RT models of edge-on spiral galaxies (Xilouris et al. 1999; Popescu et al. 2000; Bianchi 2007; Baes et al. 2010; Popescu et al. 2011; De Looze et al. 2012a; De Geyter et al. 2013, 2014) and also derived from several FIR observations (see e.g. Muñoz-Mateos et al. 2009b; Verstappen et al. 2013). The geometry is determined by three free parameters: the radial scale length h_R, the axial scale

[1] A full FitSKIRT run takes about 1000 CPU hours, which limits the number of models we can fit.

height h_z, and the central dust density ρ_0. The dust density ρ_d, is then described by

$$\rho_d(R,z) = \rho_0 \exp\left[-\frac{R}{h_R} - \frac{|z|}{h_z}\right], \tag{4.9}$$

from which the total dust mass can be derived.

The observed images are reproduced relatively well (see Fig. 4.6), with residuals (right column) generally staying below 30%. The noise in the residual images is a combination of observational noise and the Monte Carlo noise from the RT simulations. This is also why the models (middle column) appear noisier than the observations (left column). The dust lane in the model does seem to extend up to larger distances, while it falls off more abruptly in the observed images. In the central part, there is a difference of up to a factor of 2 in luminosity. The model slightly overestimates the luminosity in the nucleus of the galaxy in favour of a better fit to the outer regions. Since the S/N in the centre is highest, these pixels will have the most weight in the fitting algorithm. A sufficient number of well-fitting pixels with lower S/N are needed to compensate for a deviation in the model from the observations in these high-S/N pixels to still yield a lower χ^2. NGC 4370 is not perfectly symmetric, as is already evident from Fig. 4.1.

The western side of the galaxy shows a thicker dust lane with stronger extinction than the eastern side. On the other hand, the exponential dust disc is an axially symmetric analytical geometry. Therefore, it is not surprising that some asymmetry can be spotted in the residuals. It appears that the FitSKIRT optimal solution favours fitting the western part of the dust lane. As a result, the model overestimates the extinction in the eastern part by about 50% in the u band and 20% in the z band. The spread on the five independent fit results is not more that 10% except for the dust scale height and the dust mass, where it amounts to 50%. We find a total dust mass of $5.0 \times 10^6 M_\odot$ for the best-of-five outcome fit. The dust masses of the five best-fit models range from $(5.0 - 8.0) \times 10^6 M_\odot$. A truncated exponential disc could potentially produce better fits. However, it would not change the total dust mass significantly because the mass in the outer parts is low due to the exponential fall off. Furthermore, the central over-density will persist. We therefore chose not to pursue a fit with these additional free parameters, but explored the possibility of a ring geometry.

Model B

Dust could be distributed in a ring-like geometry. This has been observed for several ETGs (Goudfrooij et al. 1994a; Bendo et al. 2006; Patil et al. 2007; Finkelman et al. 2008), but is difficult to confirm through observations alone when seen edge-on. We explored a modified ring distribution, which has a Gaussian profile in the radial direction and an exponential fall-off in the vertical direction. It is characterised by four free parameters: the radius R_0 at which the highest density occurs, the radial width W of density peak, the vertical scale height H, and again

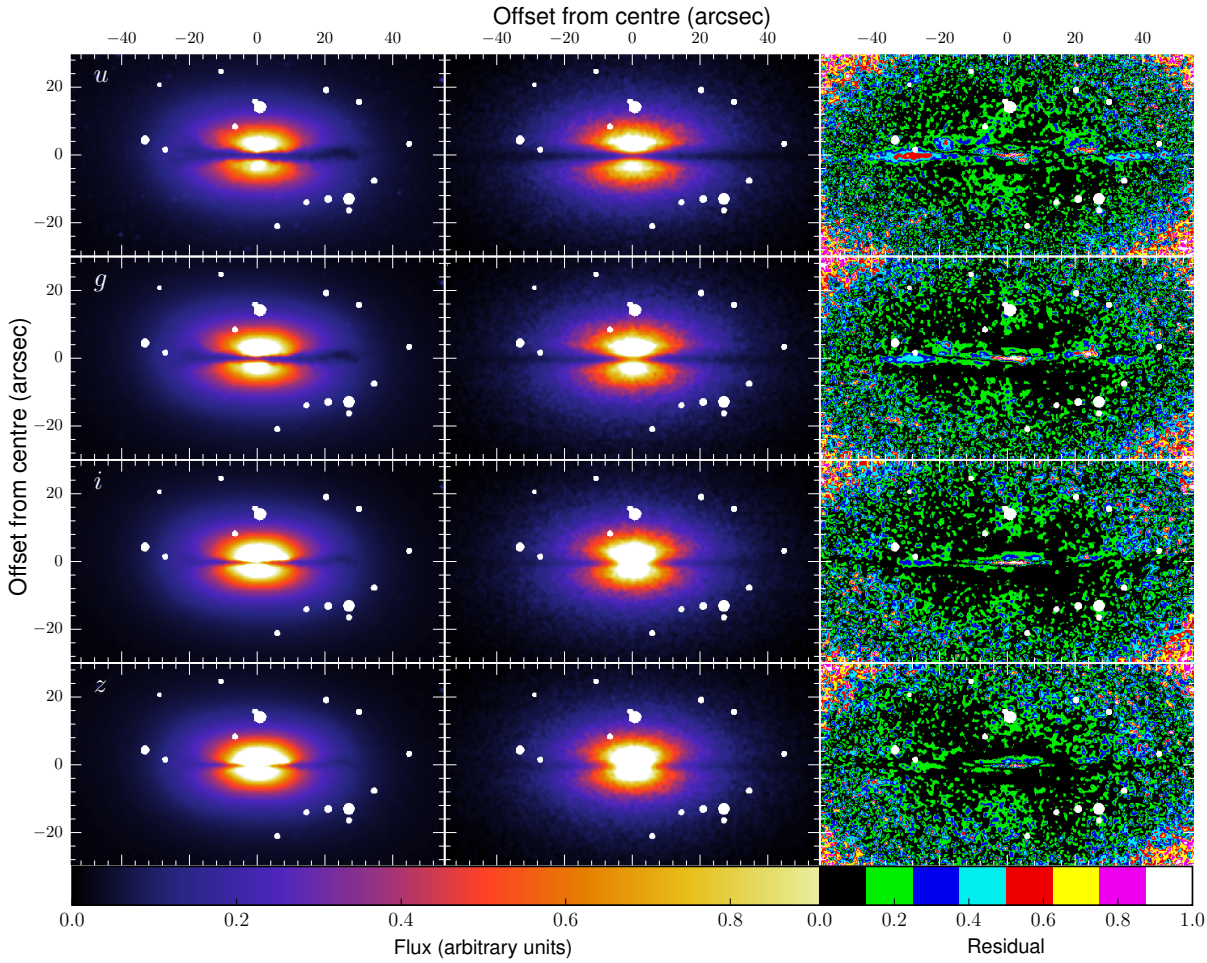

Figure 4.6: FitSKIRT model results for the exponential dust disc geometry. Left column are the observations, with masked-out foreground stars. Middle column shows the corresponding model images. The residuals are shown in the right column.

the dust density in the centre ρ_0. The density in the dust ring is described by

$$\rho_d(R,z) = \rho_0 \exp\left[-\frac{(R-R_0)^2}{2W^2}\right] \exp\left(-\frac{|z|}{H}\right). \tag{4.10}$$

The observed images are also accurately reproduced by the dust ring geometry (see Fig. 4.7). The spread on the five independent fit results is slightly greater than for the disc geometry. Especially the width W and dust mass have large variations (up to a factor of 2.5). Nevertheless, the five independent fits yield residual maps that show very similar morphology. There is still a slight enhancement visible in the centre of the residuals, which is, however, less prominent than in Model A, and the discrepancy is not more than 50% in most pixels. This is also an axisymmetric geometry, and again the extinction in the eastern part of the galaxy is overestimated, while the western part is reproduced better. Judging from the low residual values in the outer parts of the dust lane (30 – 50%), Model B is more accurate than Model A in these regions. This is also visible in the model images, where the dust lane is more compact than Model A and corresponds better to the observations. Based on these considerations, a dust ring seems more likely than an exponential dust disc in NGC 4370, although the results lie close to each other. The total dust mass is $3.3 \times 10^6 M_\odot$ for the best-of-five outcome fit. The dust masses of the five best-fit models range from $(3.3 - 6.4) \times 10^6 M_\odot$ which is lower than, but consistent with Model A.

Attenuation maps

To investigate the validity of the FitSKIRT modelling further, we produced the attenuation maps for the *ugiz* bands. SKIRT offers the option of also outputting a transparent model (i.e. only stellar emission), which serves a dust-free model. These were then convolved to the same PSF as the observed images and compared to the FitSKIRT best-fitting images using eq. (4.8). Figure 4.8 shows the resulting attenuation maps, together with the ones obtained from the MGE fitting in section 4.3.3. Attenuation maps offset the dusty and dust-free images and consequently enhance deviations from a smooth dust distribution. In the case of the FitSKIRT attenuation maps, which have smooth distributions as an input, this is limited to the Monte Carlo noise inherent to the RT simulations. For the MGE modelling, which works with the observed images as input, observational noise is added on top of the intrinsic deviations of a smooth dust distribution. With this in mind, we limit ourselves to a qualitative comparison of the attenuation maps.

The MGE attenuation maps appear thin, but with constant thickness. At the edges, the attenuation seems to be slightly puffed up in the vertical direction. There is also a clear decrease in attenuation going from u to z, which is inherent to the extinction properties of dust. The FitSKIRT attenuation maps exhibit the same decrease with increasing wavelength. There are

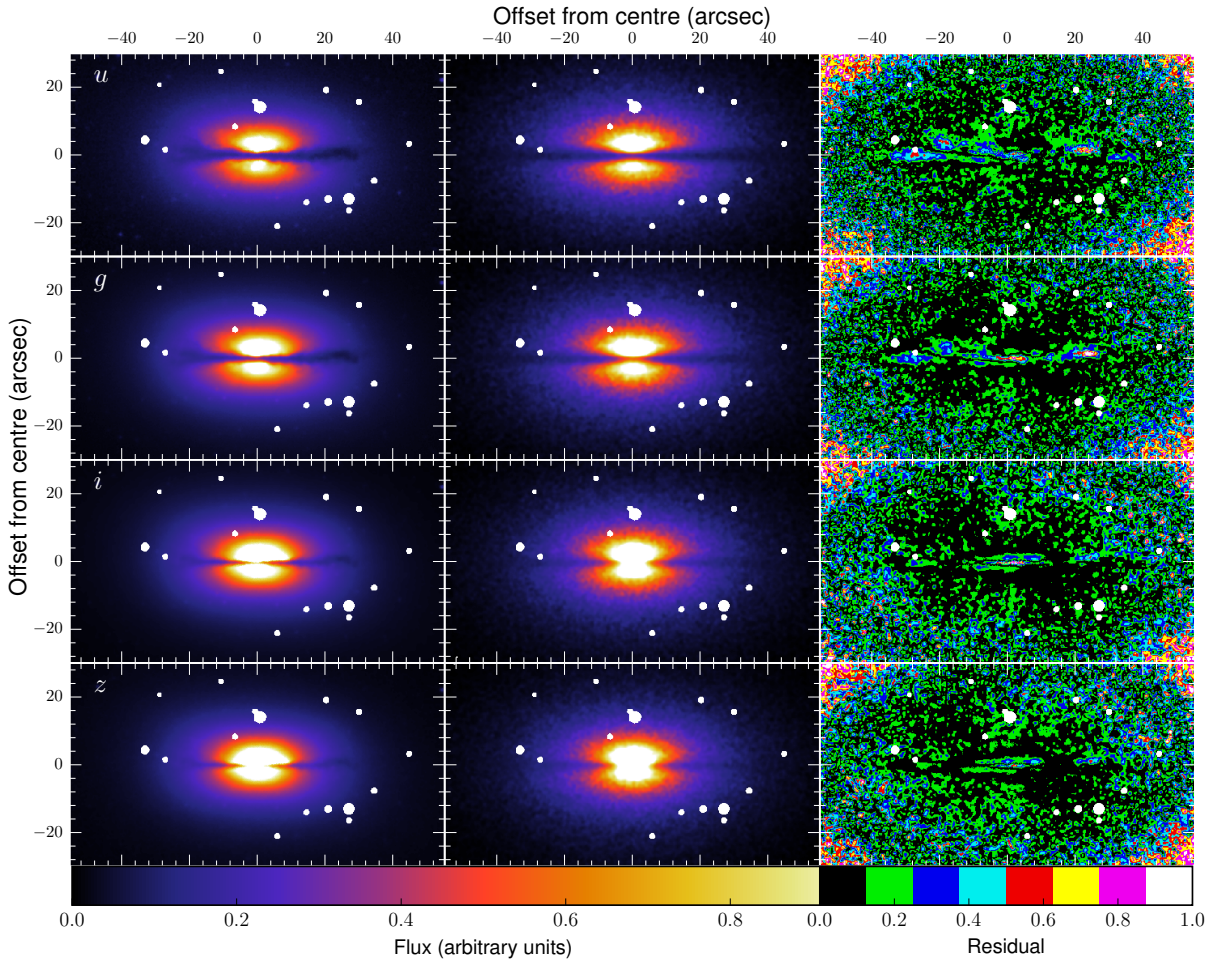

Figure 4.7: FitSKIRT model results for the ring dust geometry. Left column are the observations with masked-out foreground stars. Middle column are the corresponding model images. The residuals are shown in the right column.

some evident differences between the MGE maps and the FitSKIRT maps. In the case of the exponential disc geometry, the attenuation features are more elongated and are thicker in the middle than at the edges (as is inherent to the analytical distribution). As a result, they overestimate attenuation values in the centre and outskirts of the galaxy. The attenuation maps from the ring geometry lie closer to the ones from the MGE models. They are more compact in scale length and less peaked in the centre. Still, the ring geometry yields higher attenuation values in the centre and fails to reproduce the puffed-up morphology in the outer parts.

In general, the radiative transfer models yield an attenuation map that has higher values (by an average factor of 2), but that resembles the observed map. This can partially contribute to the discrepancy in dust mass with the MGE-based estimates. However, all models produce roughly the same thin and elongated morphology. SKIRT treats the extinction of dust in a self-consistent way, so it is reassuring that the attenuation maps are reproduced this well. This boosts confidence in the applied method and the resulting dust mass parameters. It also underlines the importance of the dust geometry and a proper treatment of absorption and multiple scattering to convert these attenuation values to more reliable dust masses.

Effect of a stellar disc

As already mentioned in section 4.3.2, NGC 4370 may have a nuclear stellar disc. This is obscured by the dust lane in the optical images, but visible in the IRAC 3.6 μm image (see Fig. 4.1). Such a component is not explicitly included in the RT models when deriving the stellar distribution from the z band. We explored the possibility of deriving the stellar distribution from the IRAC 3.6 μm image using an MGE model, similar to the one derived from the z band image. The drawback to this method is the difference in spatial resolution between IRAC and the NGVS data. We only explored the ring geometry and ran the FitSKIRT simulation five times to get a grip on the uncertainties.

Figure 4.9 shows the results of the FitSKIRT simulation. At first sight, the observations are reproduced quite well. The dust lane is rather compact, and the outer stellar halo is retrieved. The inner stellar distribution, however, is much brighter above the dust lane in the model. Below the dust lane, it is fainter. The larger beam size of the IRAC image also leaves its mark: the stellar component is generally more stretched along the major and minor axes. The quality of the fit is easier to judge from the residuals, as shown in the right-hand column of Fig. 4.9. There is a large residual feature above the dust lane due to the overestimation of the stellar emission. The residuals at the location of the dust lane itself again show the features that are present for the other models (offsets in the centre and asymmetry in the outer part), but they are more prominent here. Just above and below the dust lane, the residuals of the nuclear stellar disc are also visible. This means the brightness profile of the stellar disc in the *ugiz* bands does not scale linearly with the shape it has at 3.6 μm. It is less prominent in the optical bands. This

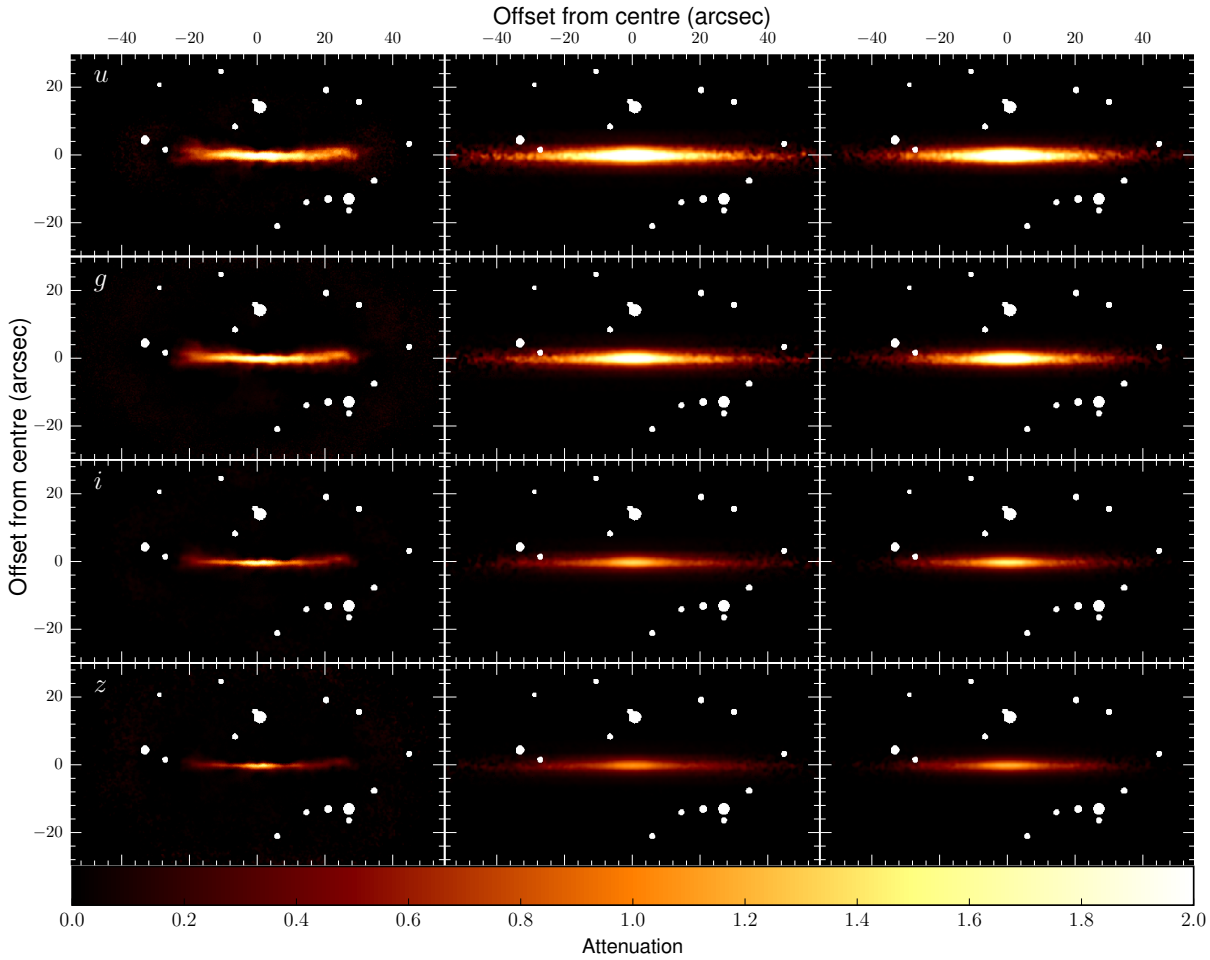

Figure 4.8: Attenuation maps for the various models of NGC 4370. Left: Attenuation maps from the MGE models. Middle: maps from the FitSKIRT exponential dust disc model. Right: maps from the FitSKIRT dust ring model. All images are convolved to the same beam size.

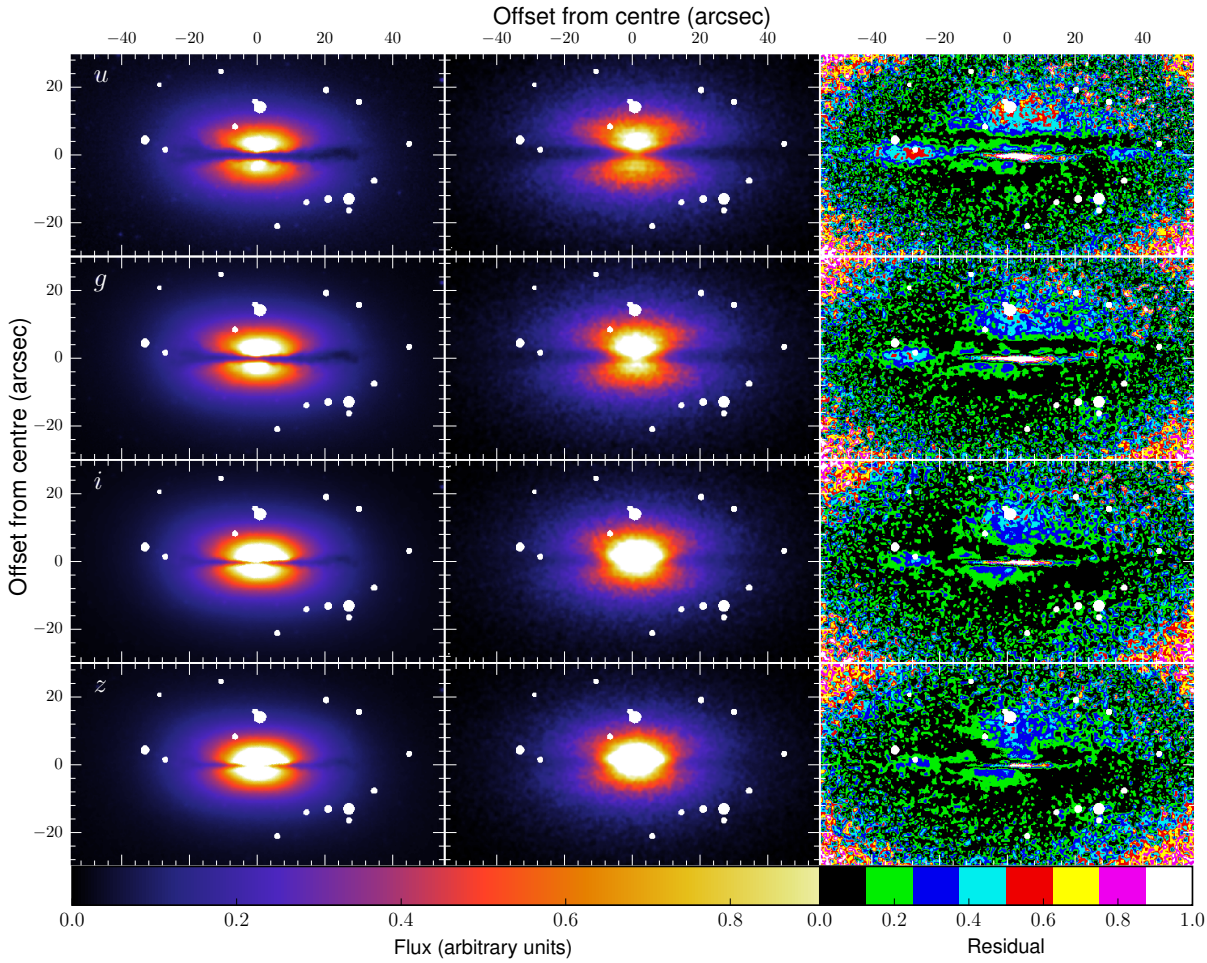

Figure 4.9: FitSKIRT model results for the ring dust geometry, but with the stellar geometry derived from the IRAC 3.6 μm image. Left column shows the observations with masked-out foreground stars. The middle column gives the corresponding model images. The residuals are shown in the right column.

Table 4.3: Overview of the resulting dust geometry parameters and their variation from the FitSKIRT modelling of NGC 4370. The obtained dust masses are listed in Table 4.2.

Parameter	Unit	$ugiz \pm$ rms
Exponential disc		
Scale length h_R	pc	3966 ± 1953
Scale height h_z	pc	155 ± 17
Inclination i_{disc}	deg	89.27 ± 0.10
Ring (z band)		
Radius R_0	pc	1969 ± 498
Width W	pc	2130 ± 3346
Height H	pc	146 ± 14
Inclination i_{Ring}	deg	88.83 ± 0.59
Ring (IRAC 3.6 μm)		
Radius R_0	pc	1094 ± 2085
Width W	pc	4199 ± 1195
Height H	pc	299 ± 93
Inclination i_{Ring}	deg	89.08 ± 0.04

suggests a colour gradient in the disc, which is stronger than the general stellar distribution. Consequently, if the disc is relatively red, the embedded star formation will be low. This would mean that the caveat we described at the end of section 4.3.2 will have a relatively low impact on the dust mass estimate from the colour maps or the MGE fits. Thanks to the inclusion of a stellar disc, we retrieved a higher total dust mass of $7.0 \times 10^6 M_\odot$ for the best-of-five model fit. The dust masses of the five best-fit models range from $(7.0 - 10.2) \times 10^6 M_\odot$, which is slightly higher than the other FitSKIRT models. The dust masses of all FitSKIRT models are consistent with each other within 1 rms (see Table 4.2). This again suggests that the effects of the nuclear stellar disc on the estimate of the dust mass are relatively small.

4.4 Discussion

The existence of a diffuse dust component in dust-lane ETGs was first proposed by Goudfrooij & de Jong (1995) to explain the dust mass discrepancy between optically derived dust masses and *IRAS*-based masses. The foreground dust screen geometry they adopted naturally yields lower limits to the optical dust mass. In a similar two-component modelling, Kaviraj et al. (2012) computed the dust mass in clumpy or filamentary structures in dusty ETGs. The dust mass in clumps was found to be on average five times lower than the *IRAS*-derived total dust masses, again favouring a diffuse dust component, invisible in the UV/optical/NIR. A similar

discrepancy in optical and IRAS-derived dust mass was found for NGC 4370 (Finkelman et al. 2008). In this work, we re-evaluate this discrepancy using data of higher quality at optical and FIR/sub-mm wavelengths. Using colour maps, we find an average dust mass of $5.6^{+0.9}_{-1.3} \times 10^5 M_\odot$ for a foreground screen geometry, which should be seen as a lower limit. From MGE modelling, we find $M_d = 3.4^{+0.7}_{-0.9} \times 10^5 M_\odot$ for the same geometry, and $M_d = 7.9^{+1.9}_{-2.5} \times 10^5 M_\odot$ for a uniform dust-star mix. On the other hand, modelling of the FIR/sub-mm SED yields $M_d = (6.2 \pm 0.4) \times 10^6 M_\odot$, and a panchromatic MAGPHYS fit yields $M_d = 5.7^{+0.46}_{-0.1} \times 10^6 M_\odot$. This quantifies the dust mass discrepancy at a factor between 7 – 18. From the optical data, we only found dust inside the dust lane. The spatial resolution of the FIR/sub-mm data was not high enough to disentangle any potential dust at higher scale heights.

Wise & Silva (1996) argue that a diffusely distributed dust component, invisible in single-band optical images, can be traced by means of broadband optical colour gradients. Using a diffuse dust model, they show that the gradients expected from *IRAS*-based dust masses are compatible with the observed gradients. More precisely, if the observed colour gradients were completely due to dust attenuation, the resulting dust masses would be significantly higher than the *IRAS* dust masses. They note that age and metallicity gradients may also contribute. Therefore, their dust masses may be considered as upper limits. In the case of NGC 4370, we found that the colour gradients outside the dust lane are relatively flat, suggesting only minor dust reddening.

On the other hand, a diffuse dust component is somewhat at odds with colour gradients derived by (Michard 2005); models with significant amounts of diffuse dust have colour gradients that contradict the observed ones. In fact, such objects would completely remove the correlation they find between B-R and B-V colours. Additionally, Vanderbeke et al. (2011) find a one-to-one correspondence in stellar velocity dispersions in the optical and near-infrared. Comparing this to theoretical models (Baes & Dejonghe 2000, 2002) suggests there is little effect of diffuse dust on the stellar kinematics. They conclude that ETGs are virtually optically thin in the V band.

Thanks to the new possibilities offered by FitSKIRT, we are able to simulate the dust-starlight interaction properly. The automated inverse RT fitting makes it possible to determine the best parameters in an unbiased way. The only assumption that is being made is the choice of dust geometry. We fit two axisymmetric dust geometries to mimic the dust distribution in the dust lane: an exponential disc and a ring. We do not add a second, diffuse component to the model. The exponential disc geometry yields a total dust mass of $(5.0 \pm 2.4) \times 10^6\ M_\odot$, and the ring geometry yields $(3.3 \pm 2.7) \times 10^6\ M_\odot$. While the disc produces slightly higher dust masses than the ring, both values are close and fall within their respective error bars. The uncertainties on these masses are in fact the rms of the dust masses of five equivalent simulations, run for each geometry. We found that the χ^2 values for each of the simulations lie very close together, but the resulting dust masses vary significantly, hence the relatively high rms values. Most simulations

actually yield a dust mass that is higher than the one with the lowest χ^2, so the uncertainties on the dust masses should be seen as possible fluctuations towards the high end. With this in mind, we can say that the total dust masses from the RT fits are fully consistent with the FIR/sub-mm and panchromatic SED fit estimates.

Additionally, we tested an alternative stellar distribution derived from the IRAC 3.6 μm image to minimize the effects of dust obscuration and include the nuclear stellar disc. We only explore a ring geometry. The global model quality from this set-up is lower than the previous set-ups. The main issue seems to be the resolution, which causes a slightly different inclination angle and a stretched-out stellar profile. The residual features at the location of the dust lane are similar to the ones from the previous methods, but are generally larger. We find a total dust mass of $(7.0 \pm 1.8) \times 10^6\ M_\odot$, which is slightly larger, but consistent with the other RT methods. In this manner, it seems that the effect of a nuclear disc on the dust mass determination is minor. The dust mass from this model is also fully consistent with the FIR/sub-mm and panchromatic SED fit estimates. However, given the strong residual features, we do not prefer this model to the other RT fits.

We must point out that the dust mass derived from FitSKIRT may be overestimated. An exponential disk has its highest density in the centre, which is unlikely for the case of NGC 4370. Second, the density in this geometry only falls to zero at infinite radii. Dust extinction is visible in the outskirts of the galaxy in the disc model, while this does not seem to be the case in the observed images. These two arguments may lead to an overestimation of the dust mass. The ring geometry does not suffer from the above problems. Inherent to the analytical description of the geometry, there is less dust in the centre and almost none at large radii. One can therefore assume that the representation of the dust geometry by a ring is better. A final argument, applicable to both geometries, is a line-of-sight effect. NGC 4370 is an edge-on galaxy, meaning we only see one side of the dust lane. It is possible that the dust distribution does not extend to the other side of the galaxy. These so-called "arcs" or incomplete dust structures have been observed in several dusty ETGs with different inclinations (Goudfrooij et al. 1994a; Patil et al. 2007; Finkelman et al. 2008). In the extreme case that the other side of the galaxy is completely free of dust, this can cause an overestimation of the total dust mass by a factor of 2. This underlines the importance of a realistic dust geometry and the proper treatment of absorption and multiple, anisotropic scattering to derive dust masses from optical data.

Our models do not assume anything about the emission of the dust in NGC 4370. Such energy balance studies have been conducted for several spiral galaxies (e.g. Baes et al. 2010; Popescu et al. 2011; De Looze et al. 2012a; De Geyter et al. 2015) and for the Sombrero galaxy (M104, De Looze et al. 2012b). However, this requires assumptions on the dust emissivity, sub-resolution physics (clumps and filaments) and a thorough knowledge of the dust-heating mechanisms: old and young stars, cosmic rays, and potentially external X-ray heating (NGC 4370 lies close to massive ellipticals in the Virgo cluster). All this requires further investigation

and falls beyond the scope of this work.

Foreground screen and uniform mix models fall short of representing the 3D intrinsic dust geometry. They should be seen as lower limits. Specifically in NGC 4370, RT simulations show that the dust is modelled best with an exponential disc or ring geometry. The latter produces lower residuals and images that are more similar to the observations. The total mass of the dust in these geometries is slightly lower, but consistent with *Herschel*-derived dust masses within 1 rms. Our results suggest that it is premature to invoke a diffuse dust component to explain the amount of dust that is observed in NGC 4370. In fact, the RT models suggest that the upper limit for the dust mass of such a component would be at most 50% of the total FIR-derived dust mass.

Our model can be improved in the future in two obvious ways. First is the fixed position angle for all components of the MGE stellar geometry. A variable position angle for each component would give a better representation of the boxiness of the galaxy. Second is the inclusion of a diffuse dust component in the fit, together with a ring or disk of dust. Both options, however, require significant changes to the design of the FitSKIRT and SKIRT code. Given the complexity of the problem, each of those changes should be rigorously tested on mock galaxies to assess whether the parameters can be accurately constrained in the fit. In particular, one can expect degeneracies to pop up when including multiple dust geometries. These adjustments fall beyond the scope of this thesis.

4.5 Conclusions

In this chapter, we explored several methods of deriving the total dust mass in the dust-lane ETG NGC 4370. Table 4.2 gives an overview of the total dust mass for all methods. We briefly summarize our findings here.

- Exploiting the sensitivity and wavelength range of *Herschel*, we were able to constrain the dust mass very well within the limits of the dust model. We find a dust mass that is an order of magnitude higher than previous estimates derived from IRAS fluxes.

- We constructed colour maps based on high-quality *ugiz* data and found a lower limit to the dust mass, which lies an order of magnitude below the FIR/sub-mm-based estimate.

- We find a dust mass comparable to the colour-derived mass through MGE fits to the stellar distribution of NGC 4370. These dust-free MGE models allow the creation of attenuation maps when compared to observations. Assuming a simple foreground screen geometry for the dust, this yields dust masses comparable to the average colour-derived mass. For a uniform mixing of dust and stars, we found dust masses that are two to three times higher.

- Since neither of these relatively simple methods yields a dust mass that is high enough to

match the FIR/sub-mm dust mass, we resorted to the more advanced method of radiative transfer simulations. Using FitSKIRT, an inverse radiative transfer optimizer around the radiative transfer code SKIRT, we could evaluate more realistic dust geometries: an exponential disc and a ring. Both geometries resulted in a decent fit, however the ring geometry is preferred. The dust masses of both models are slightly lower, but fully consistent with the FIR/sub-mm dust masses within 1 rms.

- We checked the influence of a nuclear stellar disc by adopting the stellar distribution from the IRAC 3.6 μm image instead of the z band image. We only explored the ring geometry, but found a best fit model of lower quality than the previous FitSKIRT models. The dust mass is a fraction higher, but consistent with these models and with the FIR/sub-mm dust masses. This suggests that the influence of a nuclear stellar disc is limited when determining the dust mass in NGC 4370.

- Within the current models, there is no need to invoke a diffuse dust component for NGC 4370. Instead, we suspect that radiative transfer simulations can reproduce the true dust mass with only dust in the dust lane, provided an accurate approximation of the intrinsic dust geometry is made.

These findings do not imply that the more empirical methods (colour maps and MGE fits) in itself are incorrect. If one adopted a proper description of a ring geometry and constructed the attenuation - optical depth formula as in equations (4.3) or (4.4), these methods would yield more reliable dust masses. We therefore caution against over-interpreting dust masses and optical depths based on optical data alone, when using overly simplistic star-dust geometries. In fact, for NGC 4370, the difference in total dust mass between the simple screen geometry and the 3D radiative transfer fits is a factor of $\sim$10.

We aim to expand this effort to a set of ten early-type galaxies with prominent dust lanes. The objects in this sample have all been observed with *Herschel* as part of the Far-infraRed Investigation of Early-type galaxies with Dust Lanes (FRIEDL). This will allow us to check the conclusions of this work against similar objects.

A full radiative transfer model of Andromeda

5

If we knew what we were doing, it wouldn't be called research, would it?

Albert Einstein

5.1 Introduction

On average, about one third of starlight in normal spiral galaxies is attenuated by dust, as shown in chapter 2. Young stellar populations emit mostly UV radiation, which is highly susceptible for extinction and scattering by dust. Stellar populations of intermediate age dominate the optical light, which is still significantly attenuated by the dust, but less dramatically than the UV. From all stellar emission, the near-IR (NIR) emission suffers least from dust attenuation. All the energy that is absorbed by the dust is reprocessed and emitted at longer wavelengths.

It is only the question how much energy each of the above stellar populations contribute to this dust heating. Such knowledge is important since far-IR (FIR) and sub-millimeter (submm) emission is a useful tool to study galaxies both near and far; the amount of dust obscuration roughly follows the star formation rate density in cosmic time (see e.g. Daddi et al. 2005; Gruppioni et al. 2013; Madau & Dickinson 2014). A correct understanding of dust heating allows the separation of dust in multiple temperature components. This in turn results in better dust mass estimates. An accurate dust mass can then be used estimate the total ISM content in distant objects for which HI or H_2 content cannot be observed (see e.g. Corbelli et al. 2012; Eales et al. 2012; Scoville et al. 2014; Groves et al. 2015).

Nearby galaxies are good test laboratories for such dust heating studies. The dust heating mechanisms in nearby galaxies have been studied through various techniques such as correlations with SFR indicators and stellar mass tracers (Galametz et al. 2010; Boquien et al. 2011; Foyle et al. 2013; Hughes et al. 2014; Bendo et al. 2015) or through panchromatic SED modelling (Groves et al. 2012; Aniano et al. 2012; Dale et al. 2012; Mentuch Cooper et al. 2012; Ciesla

et al. 2014). The current understanding is that the dust heating in some galaxies is dominated by the evolved stellar populations, feeding the general interstellar radiation field (ISRF), while in others it is dominated by the young and new stars, through strong UV radiation. In certain cases, even active galactic nuclei (AGN) can contribute to the dust heating (see e.g. Wu et al. 2007; Kirkpatrick et al. 2012; Schneider et al. 2015).

Usually, these investigations provide a qualitative view on the dominant heating source. In starbursts and galaxies with active star formation, the dust is predominantly heated by the young stellar populations. For early-type galaxies, little research has been conducted to estimate the dust heating sources. Based on their low star formation rates, one would expect that the evolved populations are dominant in these systems. But other heating sources are possible, for example X-rays (Natale et al. 2010). However, most galaxies fall in the ambiguous intermediate regime, where both evolved and young stellar populations contribute to the dust heating (Bendo et al. 2015). It is dangerous to infer properties like dust mass and SFR from FIR/submm data alone in these systems. In fact, the relative contribution of evolved and younger stars to the dust heating depends heavily on infrared wavelength (e.g. Boquien et al. 2011; Bendo et al. 2015), further complicating the matter.

A powerful method to investigate dust heating processes is through dust continuum radiative transfer (RT) simulations. Because these simulations treat the dust-starlight interaction in 3D, it allows more realistic geometries and non-local heating. The most common application is in models of edge-on spiral galaxies (see e.g. Bianchi 2008; Baes et al. 2010; Popescu et al. 2011; De Looze et al. 2012a; De Geyter et al. 2015, and references therein) or early-type galaxies (see e.g. De Looze et al. 2012b and chapter 4). Through consistent treatment of primary emission, scattering, absorption and thermal re-emission, dust heating mechanisms can be investigated. A general result of these studies is that evolved stars only usually fail to heat the dust to sufficient levels to match the observed FIR/submm emission. Often, obscured star formation is necessary to balance the energy between UV/optical (absorption) and FIR/submm (emission).

In a recent attempt to actually quantify the dust heating mechanisms, De Looze et al. (2014, hereafter DL14) performed a detailed radiative transfer simulation of M51. Their choice to model a face-on spiral galaxy proved a challenge, but allowed them to include more realistic geometries. Based on observed images, they closely mimic the distribution for both stars and dust, and then perform an accurate treatment of the dust-starlight interaction. They find that the contribution of evolved stars to the dust heating is not only significant, but also heavily wavelength and location dependent. In the MIR, the evolved stellar populations contribute about 10% to the total dust heating, while young stars consequently contribute 90%. This changes at submm wavelengths, where the contribution of evolved stars is $\sim 40\%$. There is also a significant enhancement of the contribution by young stars in the spiral arms ($> 80\%$) with respect to the inter-arm regions ($< 60\%$).

In this chapter, we want to push this novel technique a step further and apply it to the Andromeda galaxy. Looking at M31 as it is projected on the sky inevitably leads to parameters which are summed or averaged along the line of sight. A 3D model of the sources and sinks for radiation in M31 can help the understanding of our closest neighbour beyond the standard line-of-sight quantities. It grants us the opportunity to investigate the morphology from different viewing angles and its influence on the spectral energy distribution (SED), the attenuation law and the processes of scattering, absorption and re-emission by dust.

This endeavour sets new challenges to the radiative transfer modelling as M31 is much larger and has a higher inclination angle than M51 (in this work, we will use $i = 77.5°$, in line with McConnachie et al. 2005; Corbelli et al. 2010). On the other hand, it is the obvious choice to study dust heating mechanisms in great detail. Even for the observations at the sparsest resolution, the spatial resolution is still < 140 pc along the major axis. Dust heating mechanisms in M31 have been investigated previously using UV-FIR SED modelling (Montalto et al. 2009; Groves et al. 2012), using FIR/submm SED modelling by Smith et al. (2012d, HELGA II) and Draine et al. (2014), and through FIR colours (Planck Collaboration 2015). All of these methods show that the evolved stellar populations are the main contributor to the dust heating, especially at wavelengths beyond 160 μm. However, quantifying the contributions of the different heating sources and their wavelength dependency remains difficult.

In Section 5.2 of this chapter we describe the panchromatic dataset we use and core data products we derive from it. Our model and all its components are outlined in Section 5.3 and validated in Section 5.4. We present a 3D view of Andromeda in Section 5.5 and a dust heating analysis in Section 5.6. We present our main conclusions in Section 5.7.

5.2 A panchromatic dataset of M31

The data used in this work is the same as for our previous study, in chapter 3 (hereafter referred to as V14). We briefly recall the different data sources: The UV part of M31 was observed by GALEX in the FUV and NUV bands (Thilker et al. 2005). Optical data are acquired from SDSS and mosaicked by Tempel et al. (2011), taking special care of the background variations. The result is a stunning, large (2.5° x 8°) field of view in the *ugriz* bands. In the near and mid-infrared, we rely on observations from Spitzer using the IRAC instrument and WISE. Andromeda was imaged in all four IRAC bands and is described in Barmby et al. (2006). High-quality mosaics of the WISE observations were created in all four bands by the WISE Nearby Galaxy Atlas team (Jarrett et al. 2013). In the FIR regime, we use observations from the MIPS instrument aboard Spitzer. Due to resolution and sensitivity restrictions, we only use the maps at 24 and 70 μm from Gordon et al. (2006). FIR/submm imaging from the *Herschel* completes the dataset. The *Herschel* Exploitation of Local Galaxy Andromeda (HELGA) observed the

galaxy with PACS at 100 and 160 μm and with SPIRE at 250, 350 and 500 μm.

We work within a limited field of view to ensure good coverage at all wavelengths. Our field of view is limited by an ellipse with center at α = 00:43:06.28 and δ = +41:21:12.22, semi-major axis of 1.425°, semi-minor axis of 0.400° and a position angle of 38.1°. The corresponding physical scale is about 19.5 kpc along the major axis. This is larger than the optical disk and encloses almost all emission from UV to submm including the star-forming ring and the brightest outer dust features.

Although foreground stars and background galaxies were masked out in these images, M32 and NGC 205 were not. Both dwarf galaxies are satellites of Andromeda and M32 in particular lies in our area of interest. This object is thought to have played an important role in the recent history of Andromeda due to a head-on collision (see e.g. Block et al. 2006; Gordon et al. 2006). M32 is currently not part of the disk of Andromeda and its emission will only dilute our measurements of the main galaxy itself. We therefore mask out its dwarf companion where it is detected (from the FUV to the 24 μm band). To do that, we fit a 2nd order 2D polynomial to the pixels surrounding M32 and replace the emission from M32 by the interpolated local background.

Finally, we use integrated fluxes from IRAS (Neugebauer et al. 1984) and Planck (Planck Collaboration 2011) as additional constraints on the global SED of M31. IRAS fluxes at 12, 25, 60 and 100 μm were taken from Miville-Deschênes & Lagache (2005). We use the Planck 350, 550 and 850 μm fluxes derived by Planck Collaboration (2015). Most of the images described above will serve as observational constraints on the model. However, we use a handful of images as an input for our model construction. They are assumed to trace different components of M31 and are discussion in section 5.3.2.

5.3 Constructing a 3D model

5.3.1 Radiative transfer simulations

We make use of SKIRT[1] (Baes et al. 2011; Camps & Baes 2015), an advanced dust continuum RT code that uses the Monte Carlo approach. The code allows panchromatic RT simulations using efficient dust grids (Camps et al. 2013; Saftly et al. 2014), a vast suite of possible geometries and geometry decorators (Baes & Camps 2015) and was recently updated with a user-friendly interface.

A key feature for this investigation is the input of a 2D FITS image as a possible geometry as first demonstrated by DL14. It treats the relative surface brightness in the image pixels to

[1] SKIRT is freely available at `http://skirt.ugent.be` and can be redistributed and/or modified under the terms of the GNU Affero General Public License v3.

set up a 2D density distribution in the virtual 3D space. This density distribution can then be deprojected using a simple $\cos(i)$ factor, with i the inclination angle. To give the deprojected 2D geometry a 3D nature, the density is smeared out in the vertical direction according to an exponential profile with a vertical scale height chosen by the user. This powerful technique allows more realistic stellar geometries such as asymmetric features or clumpy and filamentary structures. For M31 in particular, with its highly disturbed and clumpy rings (Fritz et al. 2012), this is a big step forward. Of course, the deprojection of a highly inclined galaxy such as M31 ($i = 77.5°$) is always degenerate. Brighter spots in the disk will be smeared out in the direction of deprojection and the assumption of an exponential vertical profile will again smear the bright spots in the vertical direction. This technique ensures, however, flux conservation and the deprojection is consistently applied to all input geometries.

5.3.2 Model components

For our aim to investigate dust heating properties, we simplify the galaxy to a handful of 'average' galaxy components. They are listed in Table 5.1 and we discuss them below.

Evolved stellar populations

The 3D structure of the evolved stellar populations ($>$ 100 Myr [1]) is a necessary input for our model. We simplify this distribution to two components: a disk and a bulge. For M31, we derive the distribution of the evolved stellar populations from the IRAC 3.6 μm image. The derived geometries must be deprojected to construct their 3D equivalent. Deprojecting an image assumes all features reside in the same (flat) disk. The bulge, however, has a large vertical dimension, so it will be smeared out into a bar-like structure in the deprojected image. This issue is avoided by subtracting the bulge from the IRAC 3.6 μm image before deprojection. Our goal is to find an accurate representation of the bulge of M31 in 2D - to subtract from the 3.6 μm image - but also in 3D, to implement it in our RT model. We thus require an analytical model that can be fitted to the 2D image, but can be deprojected in a realistic way. The big issue here is the boxiness of Andromeda's bulge (Beaton et al. 2007).

Several analytical bulge-disk decompositions are available for M31 (e.g., Courteau et al. 2011; Tamm et al. 2012), but they all produce elliptical isophotes. Using N-body simulations, Athanassoula & Beaton (2006) managed to construct a 3D model that approximately reproduced the boxy bulge of M31. They argue that a bar is responsible for the observed boxiness. Unfortunately, they do not provide an analytical prescription. The fitting of 2D analytical boxy bulges is possible using e.g. GALFIT (Peng et al. 2010). Unfortunately, to our knowledge there is no 3D

[1] In this study, we consider stellar populations to be evolved when their UV radiation is not significant any more and they mainly produce optical/NIR emission.

analytical prescription to mimic a boxy bulge. Deriving such a prescription quickly becomes complex and falls beyond the scope of this chapter. We therefore resort to the next best 3D representation of Andromeda's bulge: the flattened Einasto profile derived by Tamm et al. (2012). The bulge is parametrized by a central radius of $a_c = 1.155$ kpc, a structure parameter $N = 2.7$ and a flattening of $q = 0.72$. We also tested the flattened Sérsic bulge derived by Courteau et al. (2011), but the resulting disk (subtracting the bulge from the IRAC 3.6 μm image) showed stronger artefacts.

Another important detail is the difference in position angle of the bulge and the disk. We find a difference of 13.8° between the major axis of the bulge and the major axis of the disk. Tamm et al. (2012) found a bulge-to-disk ratio (B/D) of 0.54 from SDSS-i band imaging and we found this ratio also works well at 3.6 μm. Upon subtraction of the bulge model from the 3.6 μm image, some pixels showed a slight over- or under subtraction caused by the small deviation of the bulge in M31 from the smooth Einasto profile. To ensure no negative emission in the center of the disk, we replace the inner 685 pc (5 pixels) by the local disk background just like we have masked M32 (see Sect. 5.2). This correction is unlikely to affect the radiation field in the nucleus of M31 as the bulge is dominant here.

We use the corrected, bulge-subtracted 3.6 μm image as our input geometry for the evolved stellar disk. The deprojected image of this geometry only yields a 2-D distribution. This could be a decent approximation if all components have the same vertical extent. This is unfortunately not the case. A proper investigation of the dust-starlight interactions requires a 3-D geometry. Following DL14, we assume an exponential vertical profile for the disk. In practice, this introduces an extra parameter: the vertical scale height. We rely on the modelling efforts of Tempel et al. (2010), who derive radial scale lengths and flattening parameters for Einasto profile fits to M31. They take the 3-D nature of the galaxy into account by concurrently modelling the extinction by dust. Their results are equivalent to a vertical scale height of 538 pc for the evolved stellar disc. This value also matches the average scale height found by De Geyter et al. (2014) for a sample of 12 edge-on galaxies.

The analytical Einasto profile is already 3-dimensional and is used as the bulge geometry for the evolved stellar component.

A panchromatic approach requires each model component to have a luminosity at every UV to submm wavelength. In practice this is achieved by selecting a suitable template SED for each component. The luminosity is then scaled to match a certain value at a representative wavelength. For the evolved stars we make use of the Bruzual & Charlot (2003) simple stellar populations (SSPs). For the bulge, we assume an average age of 12 Gyr and solar metallicity ($Z = 0.02$). In the disc, we assume the same metallicity and an average age of 8 Gyr for the stars. The estimates for age and metallicity are taken from Saglia et al. (2010), who analysed several long-slit spectra across the bulge and inner disc of M31. We normalize this SED for

both bulge and disc to the total IRAC 3.6 μm luminosity and use $B/D = 0.54$. This is the only stellar SED we can unambiguously normalize as the IRAC 3.6 μm band is a "pure" band, i.e. it traces only one component (evolved stars) and suffers least from attenuation by dust.

Young stellar populations

Following the general picture of large galaxies, we assume that the young stellar populations reside in a disc that is thinner than the evolved stellar disc. These stars should have had the time to migrate from or dissolve their dusty birth clouds, which is typically 10^6-10^7 yr (Hartmann et al. 2001; Murray 2011; Bailey & Basu 2014). Their emission is therefore only obscured by dust in the diffuse ISM. We assume that the surface brightness in the FUV band gives a good approximation of the distribution of these stars, even though the intrinsic flux may differ from the observed one. One important issue is that evolved stars can also contribute significantly to the FUV flux (e.g. Kennicutt et al. 2009). We correct for this using the formula derived by Ford et al. (2013):

$$F_{\rm young} = F_{FUV} - \alpha_{FUV} F_{\rm IRAC\,3.6}. \tag{5.1}$$

They find $\alpha_{FUV} = 8.0 \times 10^{-4}$ based on the same FUV and IRAC 3.6 μm observations of M31 as used in this work. The corrected FUV image is used as the 2D input geometry for the young stellar populations. Similar to the disk of evolved stellar populations in the previous section, we add an exponential profile in the third dimension. We set the scale height to be 190 pc, following Tempel et al. (2010).

A Bruzual & Charlot (2003) SED template was also used for the young, non-ionizing stars. There is a known metallicity gradient in M31 (e.g., Mattsson et al. 2014), but it is shallow within the optical disc. As we are working with average stellar components, we keep the metallicity at the solar value. We set a mean age of 100 Myr for this component as this is the timescale for most star formation tracers (see Sect. 5.4.1). This SED is normalized to its intrinsic FUV luminosity. Dust extinction hampers the measurement of the total energy emitted in the FUV band and thus we leave this as a free parameter in our model. We can, however, make an educated guess. Using Eq. (5.1) we find that the contribution of young stars to the total FUV flux is about 84%. The extinction in the FUV band of the global SED model of V14 is 45%. When we correct the observed FUV flux with these two factors, we obtain an estimate of the intrinsic FUV flux due to young stars.

Ionizing stellar populations

Recent efforts in RT modelling have revealed that embedded star formation is crucial to mitigate the dust energy balance problem (Baes et al. 2010; De Looze et al. 2012b,a, 2014). The new stars (10 Myr) are still embedded in their birth clouds and produce a hard, ionizing radiation.

Due to the dust in these clouds it is near impossible to trace their emission directly. New stars ionize their surrounding gas, creating photo-dissociation regions (PDRs). The ionized H II gas can be traced through its Hα emission. Devereux et al. (1994) mapped a large part of Andromeda in Hα. Unfortunately their map does not cover the entire disk and there are several artefacts present after continuum subtraction. We therefore choose another, more suitable map as a tracer for the embedded star formation. Another indirect tracer is the warm dust surrounding the stellar birth clouds. Ford et al. (2013) already derived the emission of warm dust using the MIPS 24 μm image of M31. This waveband can hold a significant contribution of warm dust residing in the atmospheres of evolved stars, Ford et al. (2013) therefore derive the following correction:

$$F_{\text{Ionizedgas}} = F_{24} - \alpha_{24} \times F_{\text{IRAC 3.6}}, \tag{5.2}$$

with $\alpha_{24} = 0.1$, in line with Leroy et al. (2008). In the third dimension, we again use an exponential profile, as for the young and evolved stellar disks. The vertical scale height is set to 190 pc, similar as for the young stellar disk.

For the SED of the ionizing stars we follow the approach of DL14 and use the template SEDs for obscured star formation from Groves et al. (2008). These SEDs are 1-D representations of the H II regions around massive clusters of young stars. We adopt the same values for metallicity ($Z = 0.02$), compactness ($\log C = 6$), pressure of the surrounding ISM ($P_0 = 10^{12}$ K/m^3) and cloud covering factor ($f = 0.2$) as in DL14 and refer the reader to this work for more specifics about the use of these templates in SKIRT. As for the young stellar component, we also normalize this SED to the total intrinsic FUV emission of the ionizing stars. For the same reason (extinction by dust) we leave this as a free parameter. We can again make an initial guess for this parameter: the Groves et al. (2008) templates are normalized to a SFR of 1 $M_\odot$ yr^{-1}. We take the template luminosity in the FUV band and scale this to 0.2 $M_\odot$ yr^{-1}, which is a good approximation of the SFR in M31 (Tabatabaei & Berkhuijsen 2010; Ford et al. 2013; Rahmani et al. 2015, chapter 3). We use this value as initial guess for the intrinsic FUV luminosity of the ionizing stars.

Interstellar dust

To map the dust in a galaxy one can resort to one of the FIR/submm bands. However, as dust emission peaks at different wavelengths depending on its temperature, choosing a single band is not straightforward. At submm wavelengths, the morphology traces the cold dust component, which is the most massive one. In the FIR, the hot and warm dust is the strongest emitter. Although not so massive, it can still yield a significant contribution to the total dust mass. Alternatively a map of the UV attenuation A_{FUV} can be created (Cortese et al. 2008; Montalto et al. 2009; De Looze et al. 2014). This method takes into account multiple FIR/submm wavebands and links this to the FUV morphology, where dust can be seen in extinction. Consequently, it

should produce a tighter constraint on the dust morphology. A drawbacks of this method is that it relies on theoretical recipes derived from simple geometries.

For M31 in particular, Draine et al. (2014) constructed a dust mass map based on pixel-by-pixel SED fits from MIR to submm wavelengths. Independently, V14 performed a panchromatic pixel-by-pixel fit of M31. Their dust map is also consistent - within their model - with the attenuation of UV and optical light. They found that their map was consistent with the one from Draine et al. (2014), within the model uncertainties. We will use the V14 dust mass map for our diffuse dust model. To this 2D geometry we again add an exponential profile in the third dimension. Tempel et al. (2010) find a dust scale height of 238 pc, which yields a dust-to-stellar scale height $\lesssim 0.5$. This is consistent with RT models of edge-on galaxies (Xilouris et al. 1999; Bianchi 2007; De Geyter et al. 2014).

We use the THEMIS dust model compiled by Jones et al. (2013). The model consists of amorphous hydrocarbons and silicates and we use their parametrization for diffuse dust. It is able to naturally produce the dust emission features in the FIR and is consistent in explaining both extinction and emission by the same dust mixture for diffuse dust in the Milky Way (Jones et al. 2013; Ysard et al. 2015). The dust component in our RT model is normalized by the total dust mass. This quantity is accurately determined from the dust mass map from V14. However, a correction for dust in local star forming clouds is necessary. Indeed, the SED of the obscured ionizing stars holds a certain amount of dust (see Sect. 5.3.2). This is heated by the ionizing stars and results in emission in the FIR. The total amount of dust in these clouds has to be subtracted from the total dust mass in M31. What remains is the mass of dust in the diffuse ISM, associated with the dust geometry described above. This introduces no extra free parameters, but couples the normalization of the dust component to the normalization of the SED of the ionizing stars. We do leave the total dust mass as a free parameter. As an initial guess for this value we take the total dust mass given from the MAGPHYS dust map, which is normalized using the Dunne et al. (2000) dust extinction coefficient $\kappa_{350\,\mu\mathrm{m}} = 0.454$ m^2/kg. In the Jones et al. (2013) model, the average $\kappa_{350\,\mu\mathrm{m}}$ is 0.305 m^2/kg. This increases the total dust mass with a factor of 1.5. However, we note that this average $\kappa_{350\,\mu\mathrm{m}}$ should in general not be used to convert dust emission into dust masses. The value for the extinction coefficient varies strongly with dust mixture and is still an average factor, with large variance. Still, for our back-of-the-envelope initial guess, it is sufficient.

Table 5.1: Overview of the parameters in our model. We used an inclination angle of 77.5° to deproject the input images. Most parameters remain fixed during the SED fitting. For our 3 variable parameters we give the range of our parameter grid.

Description	Parameter	Initial Guess	Range	Best fit
Evolved stars bulge (> 100 Myr)				
Total luminosity at 3.6 μm	$\lambda L_{\lambda}^{\mathrm{bulge}}$ $[L_{\odot}]$	1.53×10^{9}	fixed	
Central radius of the Einasto profile	a_{c} [kpc]	1.155	fixed	
Einasto structure parameter	N	2.7	fixed	
Flattening factor	q	0.72	fixed	
Evolved stars disk (> 100 Myr)				
Total luminosity at 3.6 μm	$\lambda L_{\lambda}^{\mathrm{evolved}}$ $[L_{\odot}]$	2.86×10^{9}	fixed	
2D geometry of the evolved stars	2-D image	IRAC 3.6 μm[a]	fixed	
Vertical scale height	h_{z} [pc]	538	fixed	
Young stars (100 Myr)				
Total intrinsic FUV luminosity	$\lambda L_{\lambda}^{\mathrm{young}}$ $[L_{\odot}]$	0.93×10^{9}	$(0.7 - 1.9) \times 10^{9}$	0.96×10^{9}
2D geometry of the young stars	2-D image	GALEX FUV[b]	fixed	
Vertical scale height	h_{z} [pc]	190	fixed	

Table 5.1 – *Continued.*

Description	Parameter	Initial Guess	Range	Best fit
Ionizing stars (10 Myr)				
Star formation rate	SFR $[M_\odot \mathrm{yr}^{-1}]$	0.2	0.1 – 1.3	1.0
2D geometry of the ionizing stars	2-D image	MIPS 24 μm[b]	fixed	
Vertical scale height	h_z [pc]	190	fixed	
Interstellar Dust				
Total dust mass	M_{dust} $[M_\odot]$	4.3×10^7	$(3.2 - 5.4) \times 10^7$	4.7×10^7
2D geometry for the interstellar dust	2-D image	MAGPHYS map[c]	fixed	
Vertical scale height	h_z [pc]	238	fixed	

Notes. [(a)] The Einasto bulge was first subtracted from the image, see Sect. 5.3.2. [(b)] The contribution from the evolved stars was first subtracted from the image, see Sect. 5.3.2. [(c)] The dust mass map derived from the pixel-by-pixel MAGPHYS modelling by Viaene et al. (2014).

5.3.3 Model optimization

In the end, the initial guess-values for our model parameters are well-motivated and we test this setup by running a full panchromatic RT simulation. We compute the stellar emission and the effects of dust at 128 wavelengths betwee 0.05 and 1000 μm. The wavelength grid is logarithmicly spaced over this range, but has a finer spacing in the MIR range (1-30 μm) to capture the aromatic peaks. Figure 5.1 (top panel) shows the global SED for this set of parameters. Our model SED follows the observed data points relatively close. Still, some important discrepancies are visible. First, the UV luminosity is underestimated, especially in the NUV band. This could point at an underestimation of the emission by young and new stellar populations, or at too much dust extinction. Second, the MIR and FIR luminosity is too low, suggesting more dust is needed or the warm dust should emit more (i.e. the warm dust component needs more energy by absorbing more UV photons).

Our goal is to quantify the dust heating mechanisms, so it is of vital importance to properly fit the SED in these regions. It is not straightforward to do this since UV emission is very sensitive to dust extinction. Vice versa, dust emission is related to the input UV/optical emission and the total dust mass. Due to this interaction, there is no determined recipe to find the best model parameters. An additional difficulty is the large computational cost of panchromatic RT simulations, which seriously hampers the efficient optimization of the problem. Therefore, to find a set of parameters that provide a good working model, we fix all but three parameters: the intrinsic FUV luminosity of the young stars, the SFR (or FUV flux of ionizing stars), and the total dust mass. For each of those parameters we choose a limited set of possible values, chosen within a narrow but realistic range. For the dust, mass, we take 7 values around our initial guess, within a ±25% range. The intrinsic FUV radiation of the young stars range from $0.75 - 2.0$ times the initial guess value, equally spaced in 10 grid points. We choose 15 values for the SFR ranging from 0.1 to 1.3 $M_{\odot}\mathrm{yr}^{-1}$. This was found necessary to prevent the best fitting model to be at the edge of the parameter space. The upper limit for the SFR is much higher than conventional SFRs measured for M31 (Tabatabaei & Berkhuijsen 2010; Ford et al. 2013; Rahmani et al. 2015, chapter 3), but note that this is the SFR of stellar population up to 10 Myr, whereas conventional tracers probe the average SFR over the last 100 Myr.

Using this parameter grid, we run a panchromatic RT simulation for each of the 1050 possible combinations of the free parameters. The best fitting model SED is determined by a simple χ^2 calculation between observed and model fluxes. However, when each observed data point has an equal weight in the χ^2 value, we find a best fitting model that represents the MIR observations very well, but is off in the UV and FIR/submm. For our goals, it is important to have a good fit in these regimes. We therefore introduce a weighing so that each wavelength regime has a roughly equal weight in the χ^2 determination, regardless of the number of data points. The 10 best fitting models are then visually inspected to confirm that the lowest χ^2 does correspond to

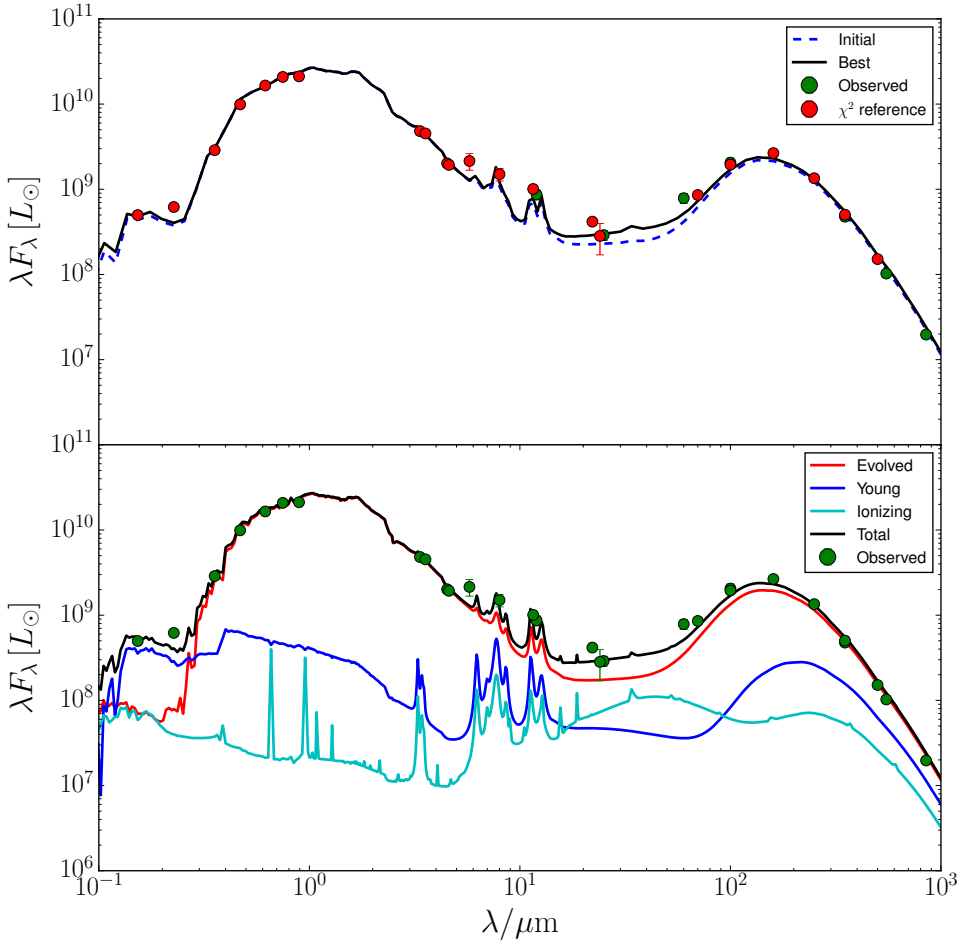

Figure 5.1: Top: Panchromatic SED of Andromeda. Blue dashed line is the RT model with our initial guess parameters. Black line is the best fitting RT model. The green data points are integrated luminosities not used to determine the χ^2. The red data points were used to compute the χ^2. Bottom: Model SEDs at higher spectral resolution, compared to the observed data points in green. The black line is the full model, including all stellar components and the diffuse dust component. The red line is the SED when only the evolved stellar component and the diffuse dust component are included. With only the young stellar component and the diffuse dust, we obtain the blue curve. The cyan curve represents the total emission from the ionizing stellar component, including diffuse dust and the dust in its birth clouds.

the best fitting model.

5.4 Model validation

5.4.1 Global SED

Before investigating the 3D structure of M31 and the dust heating mechanisms in this galaxy, we perform a series of quality checks on the best fitting model. We found that the reduced $\chi^2 = 2.16$ was lowest for the model with dust mass $M_{\rm dust} = 4.7 \times 10^7 M_\odot$, intrinsic FUV luminosity by the young stars of $\lambda L_\lambda^{\rm young} = 9.6 \times 10^8 L_\odot$ and with a SFR for the ionizing stars of 1.0 $M_\odot$ yr^{-1}. This model SED is shown in the top panel of Fig. 5.1, together with the observed fluxes and our initial guess SED. The best fit model has $\sim$ 9% more dust than our initial guess, $\sim$ 3% more FUV luminosity for the young stellar component and a 5 times higher SFR for the ionizing component. The result is a slightly higher luminosity in the UV region and in the submm and a significantly higher FIR luminosity. Interestingly, the optical/NIR regime remains unchanged, indicating that the young and ionizing stellar component are not strong enough to affect the optical SED. There is still room for higher MIR/FIR luminosities to fit the observations in this area. However, that requires more FUV emission and/or more dust mass, which will affect the UV part of the SED. Since we tried these options in our fitting routine and did not get a lower χ^2, we assume this situation is not preferable.

The dust mass is on the high end of previous dust mass estimates (Fritz et al. 2012; Smith et al. 2012c; Draine et al. 2014, chapter 3), but still consistent. One must note that a different dust model is assumed here, which can easily lead to a difference of a factor 2-3 (Jones et al. 2013; Planck Collaboration 2014; Rémy-Ruyer et al. 2015). The SFR is more difficult to compare with literature values since most of them trace SFR averaged over the last 100 Myr. The ionizing stellar component has a constant SFR of $1.0\,M_\odot/$yr over 10 Myr. This number is derived from the MAPPINGS III formalism used here to model the ionizing stars. It corresponds to an intrinsic FUV luminosity of $\lambda L_\lambda^{\rm new} = 2.0 \times 10^8 L_\odot$. We also have to count the contribution of the young stellar component before we compare with empirical SFRs. The young stellar component has an intrinsic FUV luminosity of $\lambda L_\lambda^{\rm young} = 9.6 \times 10^8 L_\odot$.

We use the recipe from Salim et al. (2007) who derive the intrinsic FUV luminosity from the Bruzual & Charlot (2003) stellar population models (which are the ones we also use to construct the stellar SEDs). They find a relation equivalent to

$$\mathrm{SFR} = 1.34 \times 10^{-10} L^0(FUV), \tag{5.3}$$

where $L^0(FUV)$ is the intrinsic luminosity in the FUV band in solar luminosities. For our best fitting model, this corresponds to SFR $= 0.16 M_\odot/$yr averaged over 100 Myr (i.e. including the

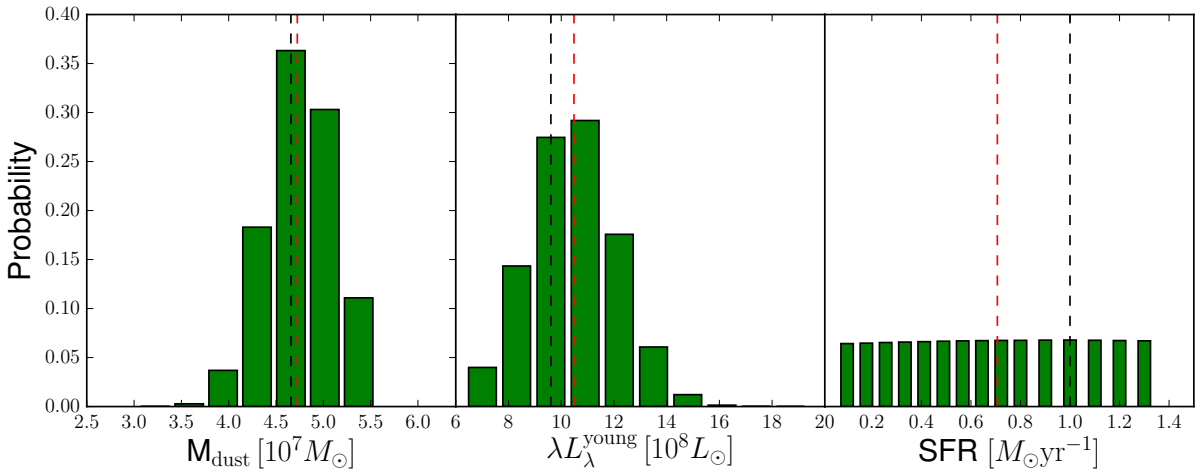

Figure 5.2: PDFs of the three free parameters in our model optimization: the total dust mass $M_{\rm dust}$, the intrinsic FUV luminosity from the young stars $L^{FUV}_{\rm young}$ and the SFR for the ionizing stars. Black dashed lines are the parameter values for the best fitting model. Red dashed lines are the median (50th percentile) values from the PDFs.

luminosity of both young stellar populations). This value is slightly below, but in agreement with previous estimates (see e.g. Tabatabaei & Berkhuijsen 2010; Ford et al. 2013; Rahmani et al. 2015, chapter 3).

To estimate the uncertainty on the free parameters, we construct probability distribution functions (PDFs). For each of the tested models, we compute the probability as proportional to $\exp(-\chi^2/2)$. For each parameter value we then add the probabilities and plot the PDFs in Fig. 5.2. We find that dust mass and FUV luminosity are reasonably well constrained (the PDFs resemble a normal distribution). The SFR, on the other hand, has a more or less flat probability distribution and thus is poorly constrained. The median (50th percentile) values that come from these PDFs are $M_{\rm dust} = 4.72^{+0.36}_{-0.39} \times 10^7 M_\odot$, $\lambda L_\lambda^{\rm young} = 10.5^{+1.7}_{-1.6} \times 10^8 L_\odot$ and ${\rm SFR} = 0.71^{+0.41}_{-0.42} M_\odot {\rm yr}^{-1}$. Here the upper and lower errors correspond to the 84th and 16th percentile of the PDFs, respectively.

The best fitting model is re-simulated at higher resolution[1] to extract images of higher signal-to-noise. The wavelength sampling was increased by a factor 4 to 512 wavelengths between 0.05 and 1000 μm. Additionally, we use 20 times more photon packages per wavelength to accurately sample extinction, scattering, and emission. The resulting high-resolution model is shown in the bottom panel of Fig. 5.1. In this plot, we also show the influence of the separate stellar components. To this end, we re-run the simulation, but each time two stellar components are switched off and only one remains. The total SED of M31 is clearly dominated by the evolved stellar populations. They produce nearly all of the optical and NIR light, and are the strongest source in the MIR. They are also - indirectly - responsible for the bulk of the dust emission.

[1] The high-resolution model required about 4000 CPU hours to run. This shows why we limited our resolution when determining the best-fit model.

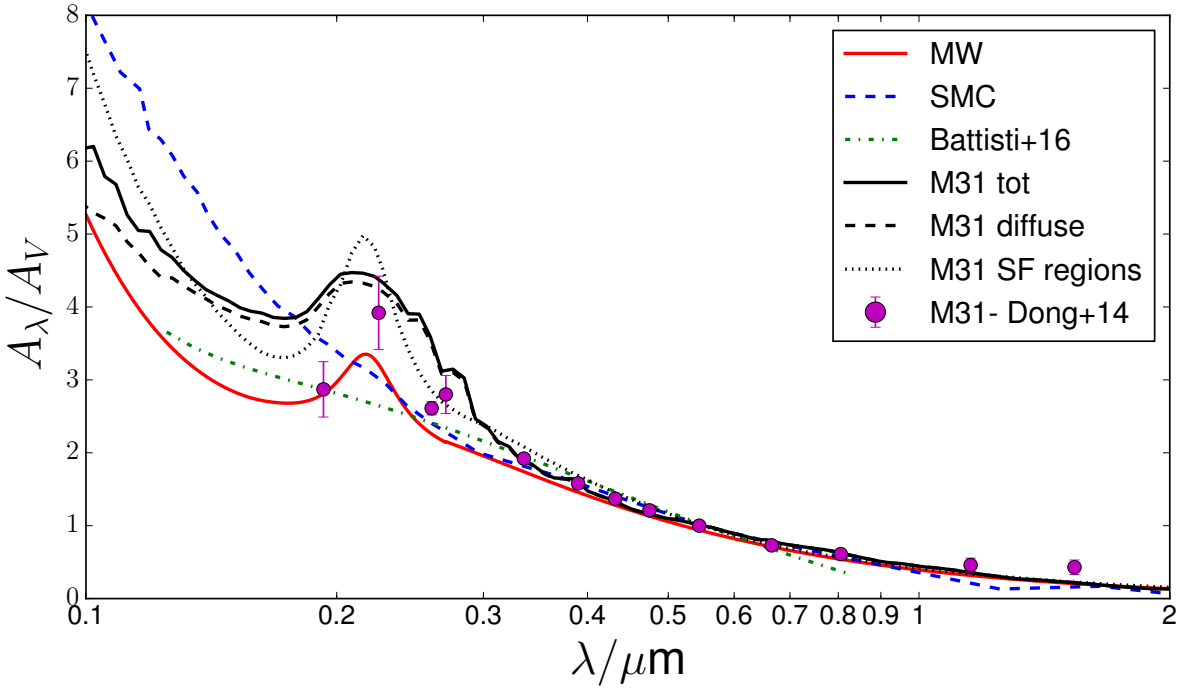

Figure 5.3: Attenuation laws from our model. The black solid line is the global law. The dashed line reflects the attenuation law for the diffuse dust and the dash-dotted black line for the dust in star-forming regions. Several literature measurements are shown; red curve: MW curve for $R(V) = 3$ from Fitzpatrick & Massa (2007), blue dashed line: SMC bar region (Gordon et al. 2003), and green dash-dotted line: attenuation curve from Battisti et al. (2016).

We come back to this in section 5.6. Only in the UV domain, the contribution of the young (non-ionizing) stellar component is higher than that of the evolved stellar populations. The emission of the ionizing stellar populations is comparable to the evolved stellar populations in this domain. However, this is still about 5 times lower than the young, non-ionzing component. The ionizing stars affect the total SED most profoundly in the MIR, because their associated dust emission peaks there. This peak is due to hot dust in the molecular clouds around the ionizing stars. The secondary dust emission peak of this component is due to thermal re-emission by the diffuse dust (heated by radiation escaping the star forming regions).

5.4.2 Attenuation law

We can accurately reconstruct the attenuation law in our model since we know the sources and sinks of the starlight. The attenuation curve for the best fit model is given in Fig. 5.3. We find a steadily increasing attenuation with decreasing wavelength, with on top of that a broad bump that peaks around 0.22 μm. This curve is a combination of attenuation by diffuse dust as modelled by the dust mass map described in Sect. 5.3.2, and attenuation by dust in star forming clouds. The latter is incorporated in the MAPPINGS III SED templates, which were used for

the ionizing stellar component. The attenuation laws for both components are also shown in Fig. 5.3. The dust around new, ionizing stars contributes less than 0.1% of the absorbed energy in the V band. At shorter wavelengths, however, this ratio increases to 5% in the UV bands. The total attenuation curve is thus mainly shaped by the diffuse dust. The effect of the MAPPINGS III attenuation curve is visible in a slightly higher NUV bump, and in a sharper increase at the shortest wavelengths. In Fig. 5.3, we also show several empirical attenuation laws: the Milky Way average curve from Fitzpatrick & Massa (2007), the SMC bar region from Gordon et al. (2003), and the average attenuation law for 10000 local ($z \lesssim 0.1$) star-forming galaxies from Battisti et al. (2016). We also plot the average attenuation measurements from Dong et al. (2014) for the central 1' of M31.

At optical and NIR wavelengths ($\lambda > 0.4\,\mu$m) our attenuation curve follows the others almost perfectly. At shorter wavelengths, the curves start to diverge. The UV bump in our model curve is much broader than that of the MW. Interestingly, on the long wavelength side of the bump, our model is consistent with the empirical measurements of Dong et al. (2014). Their UV bump does seem to be less pronounced. Unfortunately, they have no measurements shortward of 0.193 μm. The broad UV bump can explain why our model has difficulties in reproducing the observed NUV flux (see Fig. 5.1) as much of the light is absorbed at these wavelengths. The broadness of the bump of this dust model is discussed in Jones et al. (2013). They related the feature to the grain size distributions and their band gap properties. Beyond the UV bump, our model curve steadily increases and falls somewhere between the MW and SMC attenuation laws. In general, our model naturally produces an attenuation law that is broadly in line with observations, indicating that our treatment of extinction and scattering yields realistic results.

5.4.3 Images vs. observations

Fitting the global fluxes is an important first check for our model, but we can go a step further, comparing also model and observations at a spatially resolved scale. Figure 5.4 shows a selection of important bands across the spectrum. We only show pixels with an observational SNR above 2. The easiest way to visualize the difference between observation (left column) and model (middle column) is through the residual image (right column):

$$\text{residual} = \frac{\text{observation} - \text{model}}{\text{observation}}. \tag{5.4}$$

In the residual images, a negative (positive) fraction means the model overestimates (underestimates) the observed flux.

The residuals are reasonably good given the complexity of the problem. Most of the model pixels fall within 50% of their observed counterpart. Some bands (g, 3.6 μm and 250 μm) have

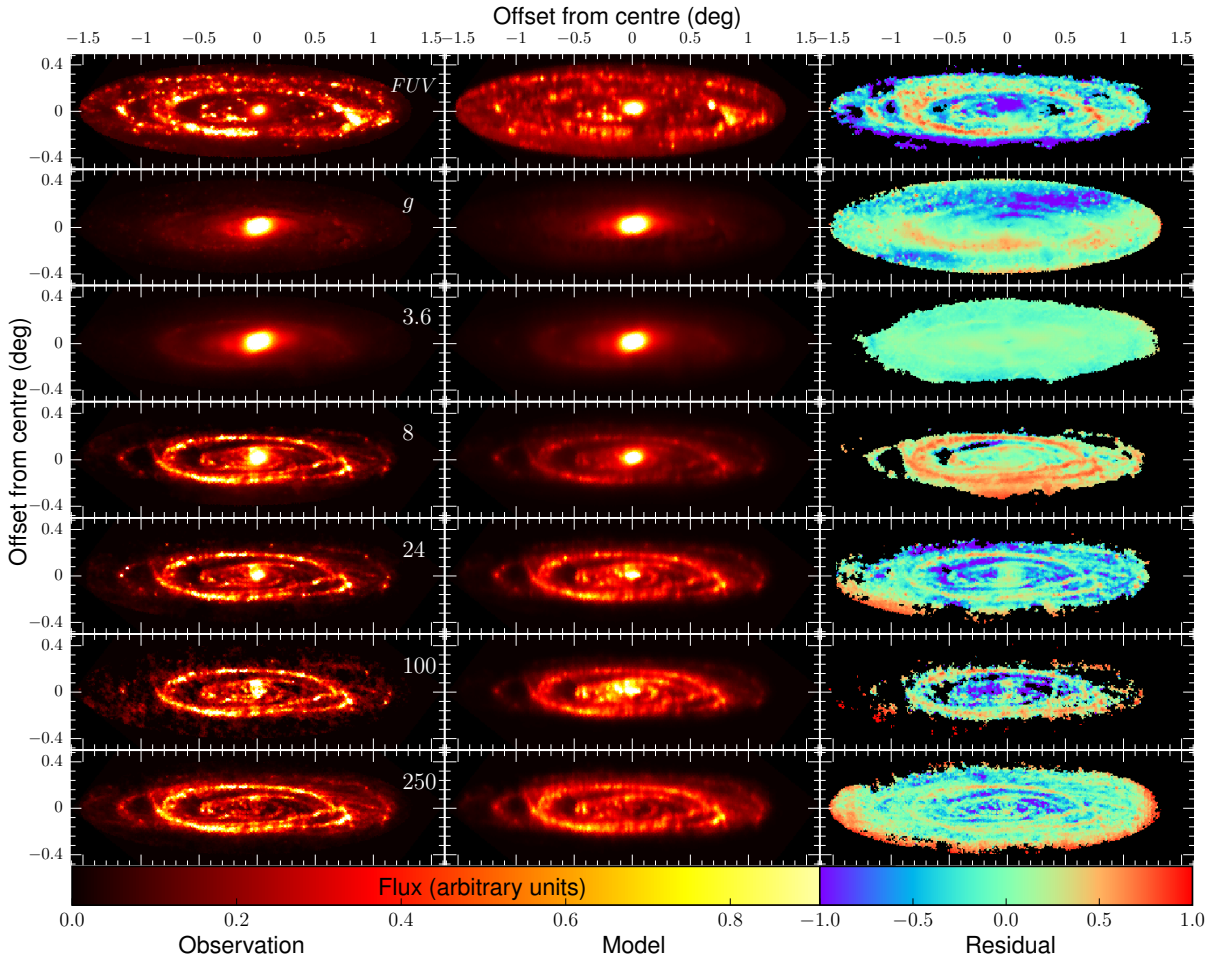

Figure 5.4: Comparison of the model with observations in selected wavebands. First column show the observed images, second column the model images. The 3rd column shows the residuals. From top to bottom row: FUV, g, 3.6 μm, 8 μm, 24 μm, 100 μm and 250 μm.

much smoother residuals, while others (FUV, 8 μm, 24 μm, 100 μm) display clear structure. The duality appears to be related to the appearance of M31 across wavelengths. In the NIR, Andromeda is a smooth galaxy without much structure. The residuals in this regime are particularly regular. Bands in the ambiguous MIR regime, with contributions of evolved stars, hot dust and aromatic features, show a very clumpy and ring-like Andromeda. A slight deviation between model and observation will be highlighted in the residual maps. Accordingly, the residuals in these bands exhibit strong features.

A first explanation for the non-flat residuals is the vertical dimension that was added to the model. Upon deprojecting the images, bright regions tend to be smeared out in the direction of deprojection. After that, the light is again smeared out in the vertical direction. As a result, when viewing the model galaxy at its original inclination, bright regions appear less bright and vice versa. Consequently, the model underestimates the flux in the rings of M31 and overestimates the flux in the diffuse inter-ring regions.

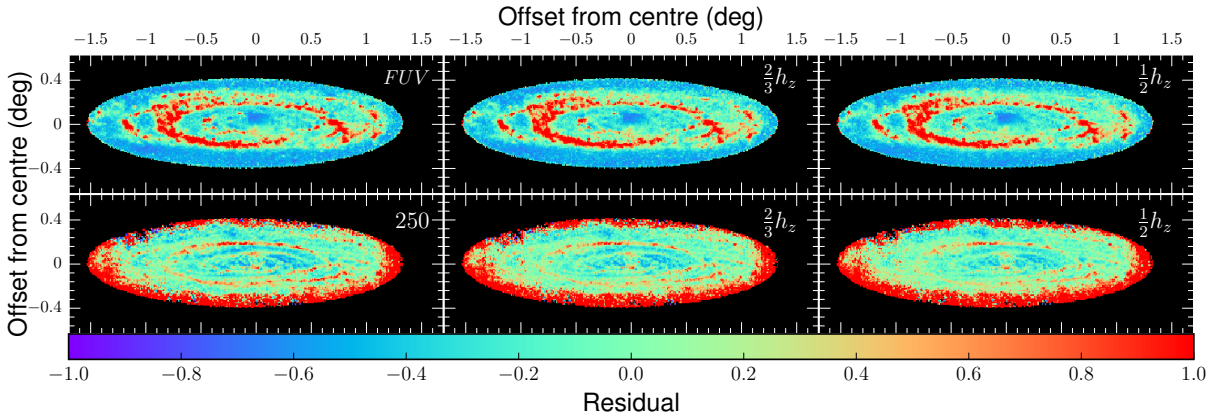

Figure 5.5: Effect of galaxy thickness on residuals in the FUV band (top row) and at 250 μm (bottom row). The left panels show residuals for the original thickness, middle and right panel for 2/3 and 1/2 of that thickness, respectively.

To test this, we ran the best-fitting model with smaller scale heights for stars and dust. We show the effect on the FUV and 250 μm band in Fig. 5.5. If the galaxy model is 1/3 thinner, we observe little effect on the residuals. The median deviation from observations decreases from 36.2% to 35.0% in the FUV and from 27.3% to 25.5% at 250 μm. Running the model at only 1/2 of the original thickness does yield observable differences, although still small. The median deviation from observation now becomes 34.3% in the FUV and 24.8% at 250 μm. So, Even with a lower scale length, the model still overestimates the flux in the inter ring regions and underestimates the flux in the rings. We therefore choose not to change our initial assumptions about the scale height of the individual components as these are compatible with the empirical optical depth study of Tamm et al. (2012).

A second aspect that is responsible for at least a fraction of the discrepancy between observations and model is the limited resolution, and in particular the fact that we are not capable of modelling the star forming regions in detail. Instead, we use a subgrid approach and model the ionizing stellar populations and their associated birth clouds by means of the MAPPINGS III models. Due to their intrinsic spherical shell geometry, these models emit isotropically and have a higher average attenuation per unit dust mass than models with a more asymmetric or clumpy distribution (Witt & Gordon 1996, 2000; Városi & Dwek 1999; Indebetouw et al. 2006; Whelan et al. 2011). This effect is particularly relevant in the UV, where the ionizing stellar populations are dominant and attenuation effects are pronounced.

However, the strong residual features point at a third effect contributing to the discrepancy. DL14 also observed residual features that could be associated with the spiral arms in their M51 model. They argue that there is a difference in both stellar populations and dust properties between arm and inter-arm region. Smith et al. (2012d, HELGA II) argued that such variations caused differences in the dust emissivity index β in their pixel-by-pixel modified black body fits of M31. While we allow for 3 stellar components in our model, we take the first order

assumption of just one type of dust mixture for the entire galaxy. Grain size distributions may vary significantly depending on radiation field and ISM phase (see e.g., Ysard et al. 2013, 2015). However, it falls beyond the scope of this work to investigate the changing size distributions and grain properties in the different regions of M31. Furthermore, this would multiply the number of parameters in our model. We therefore choose to stay at the current level of complexity, while being aware of the caveats.

5.4.4 FIR colours

As a final check for our model, we investigate commonly used FIR colours. In particular, we look at the 160/250 and 250/350 surface brightness ratios, which cover the wavelength range where the transition of dust heating sources occurs. Consequently, they have been used in the past to identify the dominant dust heating sources (see e.g. Bendo et al. 2010a; Boquien et al. 2011; Boselli et al. 2012; Bendo et al. 2015; Planck Collaboration 2015, and references therein). Figure 5.6 displays the observed colours and our model colour images. To construct the observational colour map, we only considered pixels with S/N > 3 as the PACS maps can have large uncertainties at low surface brightness.

There is a reasonable agreement in the morphology, with higher flux ratios (or bluer colours) in the center than in the outskirts. The models maps are smoother than the observed colour maps, but show some noise in the outskirts, where the Monte Carlo noise becomes significant. In Fig. 5.1, we find that our model falls below the observation at 160 μm, while it agrees with the 250 μm flux. The model thus underestimates the 160/250 colour on the global scale. The resolved colour map indicates that this underestimation comes from the star-forming ring. The colours are higher for the observed image. This is partially compensated by the center and outskirts, where the model produces slightly redder colours than observed. The 250/350 colour is also underestimated and the offset is more general. The observed colour is bluer than the model in most of the pixels. Taken together, the observed colours are relatively well reproduced by our model. This points at an adequate treatment of the dust physics, which is reassuring.

5.5 A 3D view of M31

The 3D RT simulations of Andromeda allow us to view the galaxy from different angles. Most inspiring is the face-on view shown in Fig. 5.7 in six bands. The images highlight the diversity and complexity of the galaxy across the spectrum. In the FUV band, the clumpy star formation regions are structured in several rings and arcs. The bulge is only small here, but still the brightest region. Most of the bright spots are elongated in the direction of the deprojection. This effect is inherent to the method and can not be corrected for.

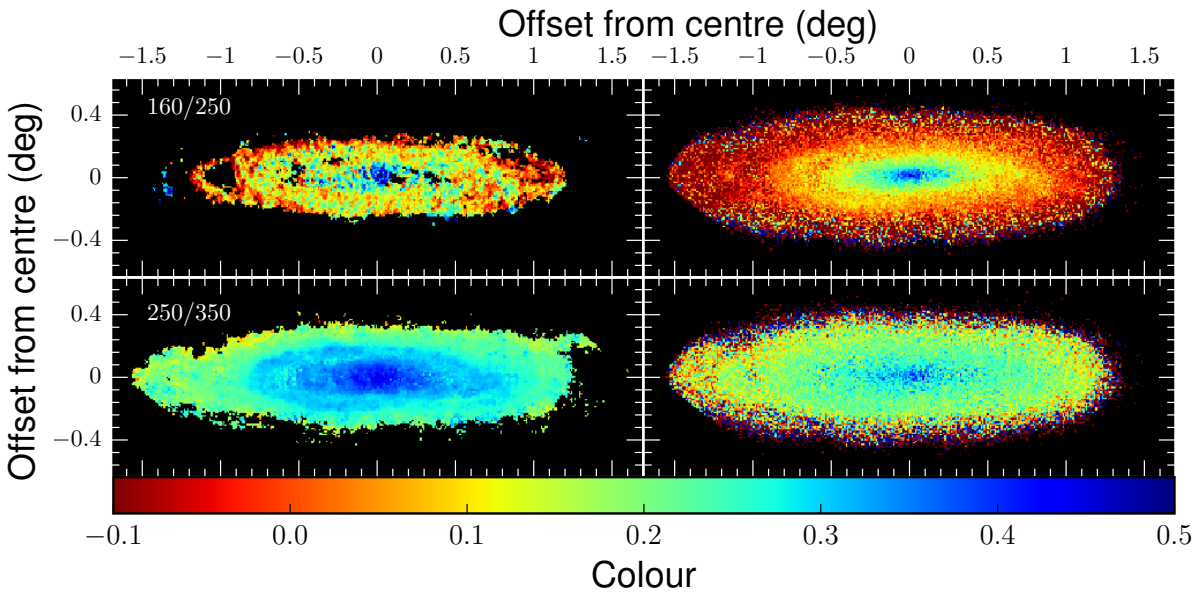

Figure 5.6: Observed (left) and model (right) FIR colours. First row corresponds to the 160/250 colour and second row to the 250/350 colour. Blue colours indicate a high flux ratio, red colours a low ratio.

At 3.6 μm the galaxy has a smooth disk with only the ring at 10 kpc as the reminder of the complex ring-arc morphology visible at 0.153 μm. The bulge is large and dominates the NIR emission. A small gap can be observed in middle of the image, along the vertical direction. This feature is an artefact of the bulge subtraction from the disc. Because we approximate the observed boxy bulge with an Einasto profile, some residual sidelobes remain in the disk. These sidelobes are smeared out in the direction of deprojection. This creates the two brighter features on the upper right and lower left of the vertical 'gap' in the model 3.6 μm image.

Going toward longer wavelengths the face-on view of M31 first appears morphologically similar to the UV, with prominent rings and bright star-forming regions. The bulge is still the brightest feature at 8 μm. Through the MIR and submm (24, 100 and 250 μm images) the appearance of Andromeda gradually evolves. The bulge becomes less dominant and the inner and outer rings turn brighter. The rings also exhibit a clear broadening going toward the submm. While the bulge is still visible at 100 μm, there is no sign of it at 250 μm and M31 consists only of clumpy rings.

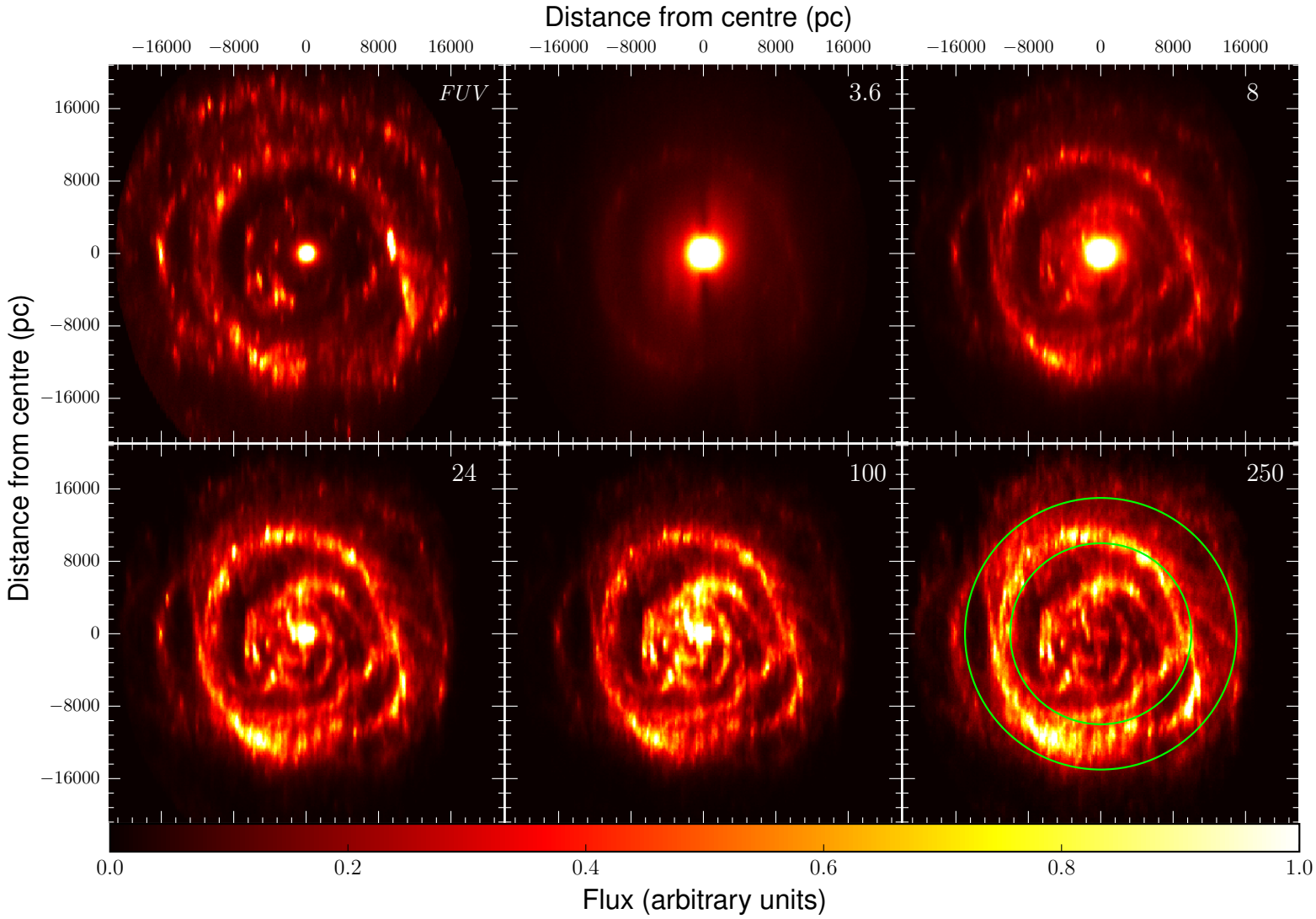

Figure 5.7: Face-on model images of M31 in the *FUV*, 3.6, 8.0, 24, 100 and 250 μm. Colour scale is different for each image for clarity. The green circles on the 250 μm image (bottom right) correspond to radii of 10 kpc and 15 kpc from the center.

In our model, we have included multiple sources of stellar radiation and two kinds of dust as sinks of radiation. These components are distributed in realistic, 3D geometries and their interaction (absorption, scattering) is simulated in a self-consistent way. We thus possess a powerful model to quantify the dust heating. We will first look at the intrinsic 3D radiation field and link that to the heating of dust (Sect. 5.6.1). Then, we define and compute the dust heating parameters for the projected model on the sky (section 5.6.2). This way, we can link them to observational properties (section 5.6.3).

5.6.1 3D analysis

We can consider each dust cell[1] in the model as a 3D pixel that processes stellar radiation. During the simulation, the absorbed luminosity $L_\lambda^{\rm abs}$ is stored in every cell and at every wavelength. Integrating over wavelength gives the total absorption rate $L^{\rm abs}$ in each cell.

Such an approach does require a good sampling of the radiation field in each dust cell during the simulation. If only a few photon packages pass through a dust cell, the Monte Carlo noise will be high. This issue is not relevant when looking at the line-of-sight projected pixels, since many photon packages travel through the line-of-sight and provide sufficient sampling. To investigate the ISRF for the dust cell, we run a separate set of simulations with more photon packages (10^8 per wavelength). The number of wavelengths is limited to 25, sampled logarithmically between 0.1 and 10 μm, to compensate the computational cost that comes with shooting more photon packages. This range is sufficient since the absorption comes mainly form stellar photons, and we integrate along the wavelength axis to compute $L^{\rm abs}$. The coarser sampling of the wavelength grid is compensated by the gain in signal-to-noise due to the integration.

We perform this simulation 4 times: including all stellar components yields $L_{\rm tot}^{\rm abs}$. Including only evolved, young or new stellar populations yields $L_{\rm evolved}^{\rm abs}$, $L_{\rm young}^{\rm abs}$ and $L_{\rm new}^{\rm abs}$, respectively. It is important to note that $L_{\rm new}^{\rm abs}$ is the luminosity that comes from the MAPPINGS template SED, and is absorbed by the diffuse dust component. There is also an internal absorption rate in the subgrid implementation of the MAPPINGS model for each dust cell. This can be seen as the absorbed energy from new stars by dust in star-forming clouds $L_{\rm new,SF}^{\rm abs}$. To test the sampling of the radiation field in our simulations, we plot the sum of $L_{\rm evolved}^{\rm abs}$, $L_{\rm young}^{\rm abs}$ and $L_{\rm new}^{\rm abs}$ against the total absorption by the diffuse dust in Fig. 5.8. It is not necessary to count the internal

[1] The dust grid in our simulations is constructed using a hierarchical binary tree. The cells are built by splitting the parent cell in turns in the x, y and z direction. Cells are not further split when reaching the dust mass fraction limit of 10^{-6}. For more information about this dust grid, we refer the reader to Saftly et al. (2014). The grid is automatically constructed and has 1.45 million dust cells for the full M31 model. Note that these cells are not equal in size.

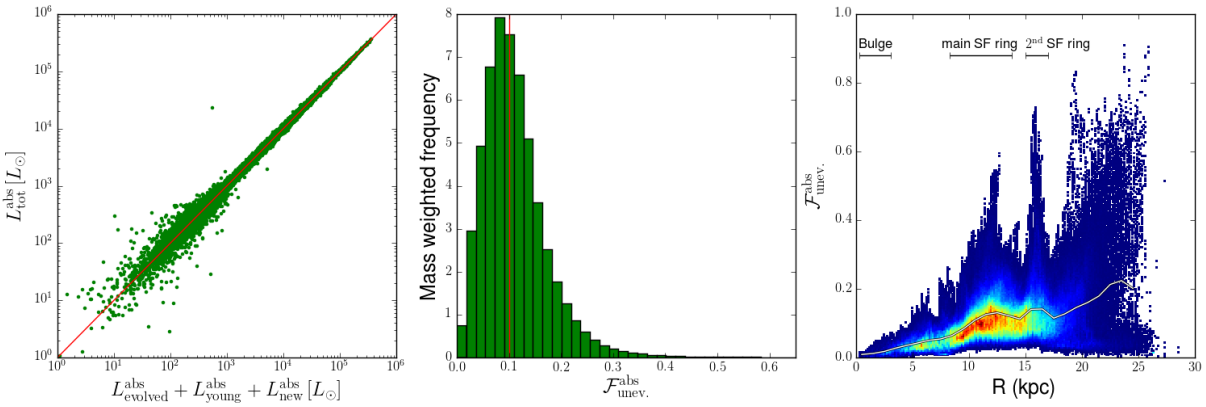

Figure 5.8: Left: Comparison of the integrated absorbed luminosity per dust cell including all stellar components $L^{\rm abs}_{\rm tot}$ with the same quantity, but as the sum of separate simulations including only evolved, young and new stellar populations. Middle: Distribution of the bolometric absorption fraction of young stellar emission per dust cell; $\mathcal{F}^{\rm abs}_{\rm unev.}$. The histogram is weighted by mass fraction of each dust cell and normalized. The red line indicates the median $\mathcal{F}^{\rm abs}_{\rm unev.} = 0.10$. Right: 2D histogram, showing the radial distribution of $\mathcal{F}^{\rm abs}_{\rm unev.}$. The bins are weighted by the mass fraction of the dust cells. Red indicates a high number of data points, blue a low number. The spread at a fixed radius is a combination of dust cells at the same radius and with different vertical location in the disk. The white line is the weighted mean heating fraction per radius.

absorption in the star-forming clouds here because the energy balance is internally secured in the subgrid model. The 1:1 line is plotted in red and shows a good correspondence between the three quantities. Only at low absorption rates, the variance starts to increase. This indicates that the radiation field in each dust cell is well sampled and we can separate the contribution from evolved, young and new stellar populations to the total absorbed luminosity. We then define the contribution of young and new stellar populations to the absorbed energy per dust cell as

$$\mathcal{F}^{\rm abs}_{\rm unev.} \equiv \frac{L^{\rm abs}_{\rm young} + L^{\rm abs}_{\rm new} + L^{\rm abs}_{\rm new,SF}}{L^{\rm abs}_{\rm evolved} + L^{\rm abs}_{\rm young} + L^{\rm abs}_{\rm new} + L^{\rm abs}_{\rm new,SF}}. \tag{5.5}$$

where we consider the contributions of the young and new stellar populations together under the umbrella of 'unevolved stellar populations'.

Summing the radiation of respectively unevolved and evolved stellar populations in each dust cell, we can estimate their relative contribution. The total fraction of absorbed energy that comes from the evolved stellar populations was found to be 91%. This is a particularly high number and most likely dominated by strong radiation field of the bulge.

We take a closer look at the dust heating of the individual dust cells in the middle and right panel of Fig. 5.8. The middle panel shows the distribution of $\mathcal{F}^{\rm abs}_{\rm unev.}$ for the dust cells. We weighted each dust cell with its mass fraction to account for the difference in size and dust content between the individual dust cells. Cells with higher dust masses are given more weight. The distribution peaks near the median value of 0.10 and is skewed towards higher fractions.

However, the contribution of unevolved stellar populations to the absorbed energy hardly exceeds 50%. This indicates that, even at the level of individual dust cells, the heating by evolved stellar populations dominates.

The radial variation of the dust heating fraction can be investigated by plotting $\mathcal{F}^{\rm abs}_{\rm unev.}$ as a function of radius for each dust cell. In the right panel of Fig. 5.8, this is shown for each dust cell, irrespective of its vertical coordinate. The 2D histogram is weighted by the mass fraction (cells with more dust have a bigger weight), and the weighted mean $\mathcal{F}^{\rm abs}_{\rm unev.}$ for each 1 kpc bin is shown as a white line. The contribution of the unevolved stellar populations is only a few percent in the inner few kpc, where the bulge is dominant. There is a gradual increase when moving to larger galactocentric radii. However, there is a large variation in $\mathcal{F}^{\rm abs}_{\rm unev.}$ for a fixed radius, especially at larger radii. Each radius contains dust cells from all around the galaxy, and from different vertical coordinates. The spread here points towards quite different environments for these dust cells, even though they reside at the same galactocentric distance.

Most interestingly are the prominent spikes in the radial distribution. They point towards radii with an enhanced contribution of unevolved stellar populations to the absorbed energy (see also the circles in the bottom right panel of Fig. 5.7). Two moderate spikes are visible at roughly 6 and 8 kpc. They can be associated with the filamentary structures it the inner disk of M31. A broad peak occurs between 10 and 15 kpc which corresponds to the dust cells in the main star-forming ring. Just outside the 15 kpc radius, a second sharp peak occurs, which is linked to the second large ring of Andromeda. Beyond this radius, there is an overall increase in $\mathcal{F}^{\rm abs}_{\rm unev.}$, but without any distinct features. At these radii, the overall flux from the galaxy becomes very faint, and the dust grid contains fewer cells. The Monte Carlo noise starts to dominate, which makes it too speculative to interpret the structures that are still visible here.

5.6.2 Projected dust heating in M31

We now look at the dust heating in 2D pixels, projected on the sky. This exercise is useful to connect the 3D model to 2D observations. To this end, we define the fraction of the total dust emission caused by absorbed radiation from the evolved stellar populations as $F_{\rm evolved}$. As in the previous section, we treat the contributions of the other components as one. This includes absorbed energy from young and new stellar populations, plus the internally absorbed energy from the subgrid implementation of star-forming regions. We define this fraction of total dust heating by the unevolved populations as $F_{\rm unev.}$. Naturally, $F_{\rm evolved}$ and $F_{\rm unev.}$ add up to unity.

It is not straightforward to split these quantities into separate wavelengths because dust heating is non-local in wavelength. Dust emission at a particular wavelength is caused by the total radiation field and not stellar radiation of a single wavelength. Therefore, while $F_{\rm unev.} + F_{\rm evolved} = 1$ on a global scale, this is not true for individual wavelengths: $F_{\lambda,\rm evolved} + F_{\lambda,\rm unev.} \neq 1$. Yet again

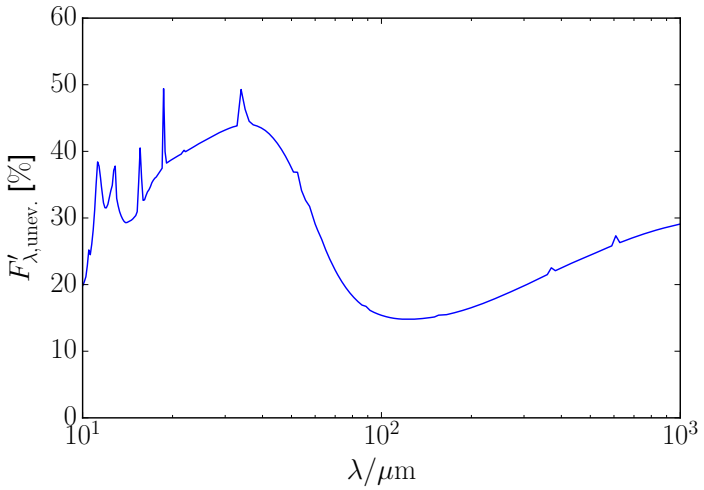

Figure 5.9: Dust heating fraction as a function of wavelength for the unevolved stellar populations.

it is useful to investigate whether warm dust (emitting in the MIR) is heated differently than cold dust (emitting in the submm). DL14 proposed a way to approximate $F_{\lambda,\mathrm{evolved}}$ and $F_{\lambda,\mathrm{unev.}}$, while maintaining energy conservation within a single waveband. This involves running the full radiative transfer simulation with different combinations of stellar populations (see again Fig. 5.1, bottom panel), and recording the FIR/submm flux at every wavelength, S_λ. DL14 then define:

$$F'_{\lambda,\mathrm{unev.}} \equiv \frac{1}{2}\frac{S_{\lambda,\mathrm{unev.}} + (S_{\lambda,\mathrm{total}} - S_{\lambda,\mathrm{evolved}})}{S_{\lambda,\mathrm{total}}} \tag{5.6}$$

and

$$F'_{\lambda,\mathrm{evolved}} \equiv \frac{1}{2}\frac{S_{\lambda,\mathrm{evolved}} + (S_{\lambda,\mathrm{total}} - S_{\lambda,\mathrm{unev.}})}{S_{\lambda,\mathrm{total}}}, \tag{5.7}$$

Where $S_{\lambda,\mathrm{tot}}$ is the dust emission heated by evolved, young and new stellar populations. $S_{\lambda,\mathrm{evolved}}$ is the dust emission when only the evolved stellar components are included in the simulations, and $S_{\lambda,\mathrm{unev.}}$ when only the young and new components are included. Note that there is no need to consider any missing subgrid contribution from the star-forming clouds here. Since we are dealing with emission, this is already included in the total SED of the new stellar component (the ionizing stellar populations discussed in section 5.3.2). In the above definitions, $F'_{\lambda,\mathrm{unev.}}$ and $F'_{\lambda,\mathrm{evolved}}$ are the approximate heating fractions by unevolved and evolved stellar populations. They now add up to unity by definition.

In Fig. 5.9 $F'_{\lambda,\mathrm{unev.}}$ is shown as a function of wavelength. At all wavelengths the unevolved stellar populations are under-represented in the dust heating in M31. There are, however, significant variations between the wavelengths. From 10 - 35 μm, there is a gradual increase in the contribution of unevolved stellar populations to a point where both components are almost equal in contribution. Beyond that, a strong dip is visible, with a minimal contribution of 15% from unevolved stellar populations at around 100 μm. Interestingly, $F'_{\lambda,\mathrm{unev.}}$ rises again when

it comes to heating the colder dust at submm wavelengths. This does not correspond to the classical view of dust heating, where unevolved stellar populations have their peak contribution at short wavelengths (10-100 μm), but fall off after that, leaving the evolved stellar populations to heat the diffuse dust that emits at submm wavelengths (see e.g. Bendo et al. 2015; De Looze et al. 2014).

It seems counter-intuitive that the contribution of the unevolved stellar populations starts to increase again beyond 100 μm. However, it must be noted that M31 is not the typical late-type galaxy for which most of these studies have been conducted. Andromeda is heavily bulge-dominated and has a low SFR. When we look at spatial heating maps at different wavelengths, shown in Fig. 5.10, we find the classical morphological segregation between disk and bulge, with the influence of the bulge almost stretching out to the 10 kpc ring. The heating of dust in M31 occurs in two regimes. In the rings the unevolved stellar populations are dominant at short wavelengths (up to 90% at 24 μm). Their contribution slowly declines in favour of the evolved stellar populations when moving to longer wavelengths. This evolution is largely seen in the dust heating of spiral galaxies. In the large bulge of M31, the contribution of evolved stellar populations is always high, but peaks at 100 μm. The radiation field caused by the evolved stellar population seems to be most effective at heating dust to the temperatures associated with FIR emission. So, after a closer look, we find large variations in the heating fraction at shorter wavelengths. The heating fraction changes differently with wavelength in the rings and bulge. The result is a more uniform heating fraction at submm wavelengths. The rise at submm wavelengths of the unevolved stellar contribution in Fig. 5.9 is not so much linked to an increase in $F'_{\lambda,\mathrm{unev.}}$ in the disk of M31. More correct would be to say that the evolved population in the bulge becomes so dominant in the FIR, that it causes a bump at 100 μm in Fig. 5.9. The 'rise' at submm wavelengths should thus be seen as a return to more uniform levels of dust heating fractions for unevolved and evolved stellar populations.

Going back to the global heating fractions (not the approximate quantities), we find that $F_{\mathrm{unev.}} = 21\%$. In other words, almost 80% of the total dust emission in Andromeda is due to heating by the evolved stellar populations. This is somewhat lower than the 91% found in the previous section. This underlines an important difference between the 3D and 2D determination of the dust heating sources. In the projected view, it is possible that the full magnitude of the bulge radiation field is not captured adequately. This results in a lower contribution of the evolved stellar populations to the dust heating. Nevertheless, the evolved stellar populations dominate the global dust heating in both scenario's. Our findings are broadly in line with the dust heating analysis based on Planck colours (Planck Collaboration 2015). These authors report that M31's cold dust is mainly heated by the evolved stellar populations as traced by the IRAC 3.6 μm emission. They do find that their 70/100 μm colour correlates better with the unevolved stellar populations (traced by the 24 μm emission). While we do see a rise in $F'_{\lambda,\mathrm{unev.}}$ at wavelengths $< 100\,\mu$m, we do not find that the unevolved stellar populations become the dominant

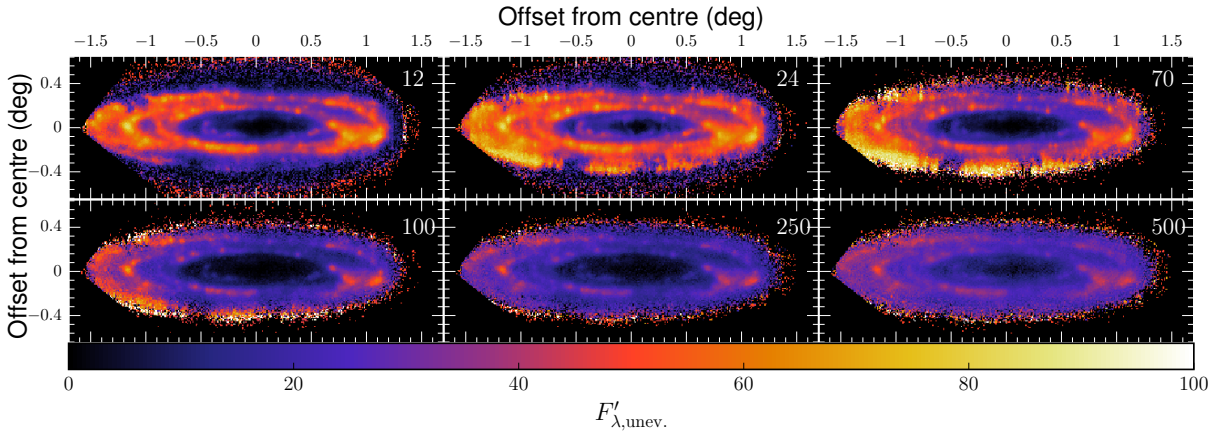

Figure 5.10: Maps of the dust heating fraction by unevolved stellar populations $F'_{\lambda,\mathrm{unev.}}$ for a selection of wavebands. Top row (left to right): 12, 24 and 70 μm. Bottom row (left to right): 100, 250 and 500 μm.

energy source. We come back to the point of FIR colours as dust heating tracers in the next section.

5.6.3 Tracers of dust heating

The analysis we have made so far, involving a full, self-consistent radiative transfer model, is a suitable way to explore the details of dust heating. On the other side, it is very demanding -both in terms of time and data- to construct a full RT model for any galaxy one would like to study. Hence, we have tried to look for possible correlations, in M31, between the total heating fraction, and some other physical properties. Here we use the global heating fraction per pixel (i.e. derived by integrating the dust SED) $F_{\mathrm{unev.}}$. In Fig. 5.11, we plot $F_{\mathrm{unev.}}$ against $NUV - r$ colour, commonly used in the context of galaxy evolution as an indirect tracer of the specific SFR (see e.g. da Cunha et al. 2010; Cortese et al. 2012b, chapters 2 and 3). There is a positive trend, but the variance for a fixed $NUV - r$ colour is significant. Nevertheless, it is the most prominent correlation between an observed colour and the total dust heating fraction.

In the middle and right panel of Fig. 5.11, $F_{\mathrm{unev.}}$ is plotted against two commonly used FIR colours to trace dust heating: the 160/250 and 250/350 flux ratios. In both cases $F_{\mathrm{unev.}}$ there is no clear trend. The global heating fraction does not seem to correlate with the shape of the FIR SED.

It is surprising that the heating fraction does not correlate well with the 160/250 and 250/350 colours, which are often used to map dust heating in galaxies (see e.g. Bendo et al. 2015; Planck Collaboration 2015, and references therein). One possible reason for this is non-local heating. Studies that correlate colours to check dust heating are based on the underlying assumption that the dust heating is local, i.e. photons are absorbed close to where they are emitted. In general, this does not need to be the case. Radiative transfer simulations do take this non-locality into

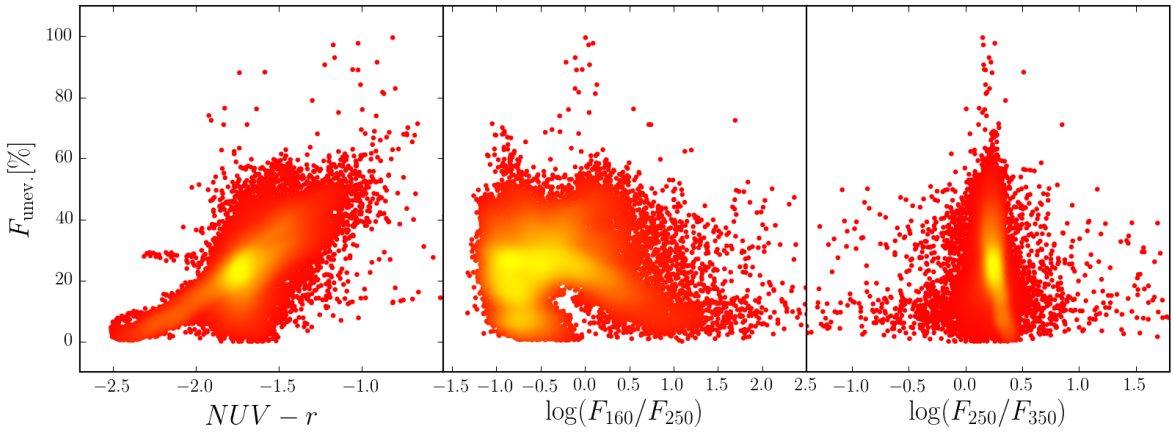

Figure 5.11: Density plots of the dust heating fraction from unevolved stellar populations $F_{\mathrm{unev.}}$ vs $NUV - r$ and two commonly used FIR colours. A red colour points at a small number of data points in that area of the plot, yellow at a large number.

account. For M31 in particular, the effect may be significant due to the bright bulge. The radiation field is strong in the center, where relatively little dust resides. Photons may thus travel through the galaxy without being absorbed. Once they reach the dusty ring at 10 kpc, their chance of being absorbed increases strongly. This explains why the dust heating in the star forming rings of M31 is still dominated by the evolved stellar populations.

We now look for possible correlations between the dust heating and physical properties. Our previous investigation of M31 (V14) offers a large dataset of physical parameters for each pixel. In Fig. 5.12, the most commonly used physical parameters are plotted against $F_{\mathrm{unev.}}$. There is a weak positive trend with M_{dust}. This could be interpreted in the context of star formation, where dusty regions are often associated with star-forming regions. Consequently, these regions are dominated by the radiation field of unevolved stellar populations. This is in accordance with a positive trend with SFR. However, the scatter in this correlation is large, suggesting other elements are in play as well. Interestingly, no clear trend with the total dust luminosity, L_{dust}, was found either. Infrared luminous galaxies often point at high levels of star formation, and so one would naively expect a higher contribution of unevolved stellar populations to the heating fraction. However, for the individual pixel-regions in M31, this is clearly not the case.

We find a negative correlation with stellar mass ($M_\star$). If one assumes that the bulk of stellar mass is in evolved stars, then it is no surprise that the pixels with high stellar mass correspond to low $F_{\mathrm{unev.}}$. But here as well, the trend is ambiguous and suggests the influence of a third parameter. We further investigate this by looking at the specific dust mass ($M_{\mathrm{dust}}/M_\star$). This quantity gives an idea of the dust content, relative to the stellar mass. High $M_{\mathrm{dust}}/M_\star$ values point at dusty regions and those can indeed be associated with high $F_{\mathrm{unev.}}$. The heating fraction of unevolved stellar populations approaches zero for the lowest specific dust masses. This suggests that at low dust content, there is also no significant radiation field from young or new

stellar populations.

The strongest correlation is with sSFR. This correlation is likely to be intrinsic as the trends with SFR or $M_\star$ separately show much more scatter. This trend is not completely unexpected, since we already found a positive link between $F_{\rm unev.}$ and $NUV - r$ colour, and V14 found that this colour correlates with sSFR in M31. However, the observed correlation with sSFR is much stronger that with $NUV - r$. DL14 also found a tight link between the dust heating fraction of unevolved stellar populations and sSFR for M51. We overplot their data points and best fit curve in the central, bottom-row panel of Fig. 5.12. In M51, higher fractions of $F_{\rm unev.}$ can be achieved compared to Andromeda. The regions of M31 follow the average relation for the M51 regions closely for all but the lower sSFR values. In fact, both datasets seem to lie in the continuation of one another. This is quite surprising, since the physical size along the major axis of the M31 pixels is about 3.5 times lower than for the M51 pixels. On top of that is the difference in inclination of both galaxies, where a far greater distance is probed along the line of sight in M31.

The bottom line is that extensive galaxy parameters such as $M_{\rm dust}$, $L_{\rm dust}$, $M_{\rm star}$ or SFR are not suitable to disentangle the dominant dust heating sources. A better option is to resort to intensive parameters that somehow express the ratio of evolved and unevolved stellar populations, e.g. $M_{\rm dust}/M_\star$ or sSFR. While there is still some variance in the correlation with sSFR, it is small enough to identify the dominant heating source. Of course, a more thorough investigation involving multiple galaxies is desirable to quantify this relation.

5.7 Conclusions

We have constructed a highly detailed model for the Andromeda galaxy to investigate the dust heating mechanisms in this galaxy. Our model is based on observed morphologies and uses 3-D panchromatic radiative transfer to self-consistently simulate the dust-starlight interactions. Our main conclusions are:

- The model is able to reproduce the observed morphologies relatively well from far-UV to submm wavelengths. The high inclination angle of M31 does induce certain elongated structures due to the deprojection.
- The integrated SED of M31 is well fitted and the resulting attenuation curve is consistent with observations. It has a strong UV bump, and falls somewhat between the SMC and Milky Way attenuation curves. We are able to constrain 2 of our 3 free parameters: the dust mass and the luminosity of the young stellar component. The star formation rate in obscured clouds is more difficult to constrain.
- On a resolved scale, the model underestimates the flux in the rings, and overestimates the flux in the inter-ring regions. Adjusting the vertical scale height of the galaxy somewhat

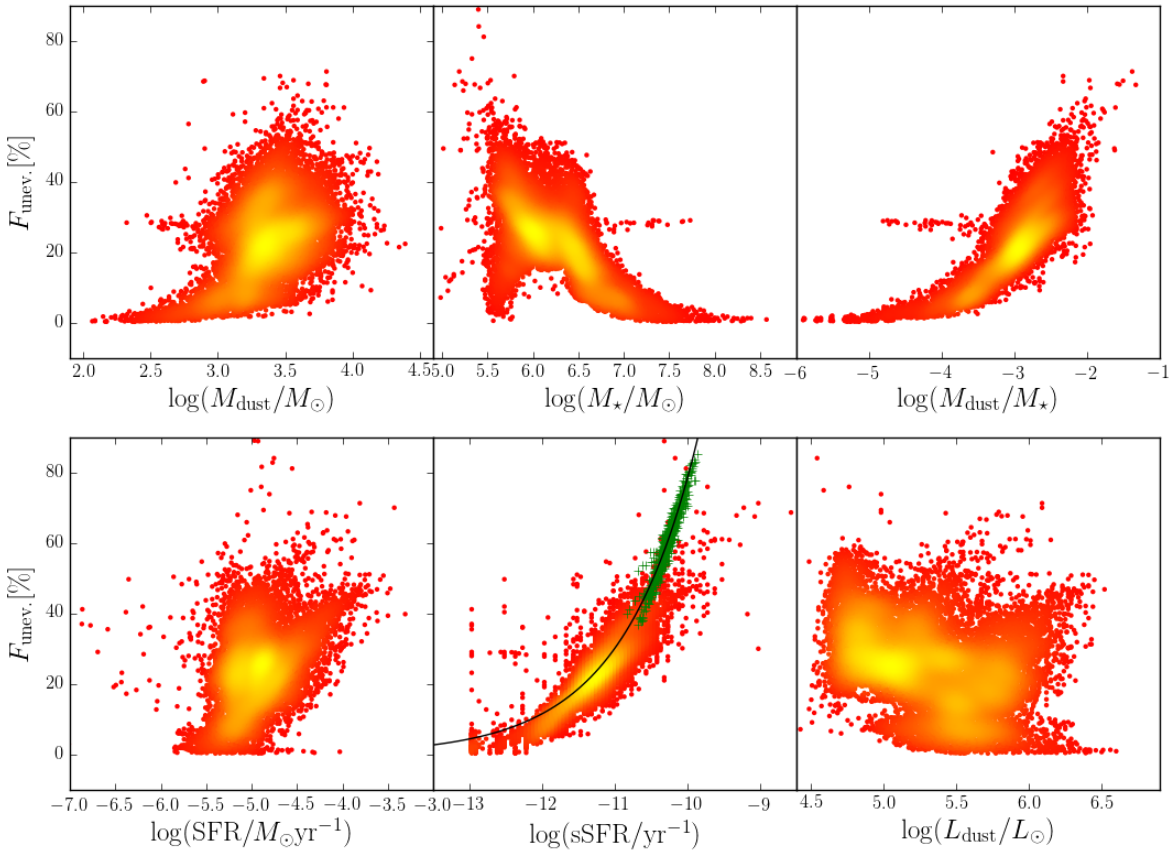

Figure 5.12: Density plots of the dust heating fraction from unevolved stellar populations $F_{\rm unev.}$ vs a number of physical parameters, obtained by V14. A red colour points at a small number of data points in that area of the plot, yellow at a large number. First row: dust mass, stellar mass, dust-to-stellar mass ratio. Second row: Star formation rate, specific SFR, temperature of the cold dust in the ISM. The black line is a best fit linear model, the green line is the relation found by DL14. Third row: Dust luminosity, PAH luminosity and temperature of the warm dust in stellar birth clouds. Parameters are derived according to the MAGPHYS SED model.

mitigates this effect, but cannot resolve it. Variations in the nature and size distribution of the dust grains, and the subgrid treatment of the star forming regions can contribute to the deviations between model and observation.

- The dust in Andromeda is mainly heated by the evolved stellar populations. From a 3D analysis of the radiation field, we find that 91% of absorbed stellar radiation comes from the evolved stellar populations. This strikingly high number is mainly due to the bright bulge, which dominates the radiation field out to the main star-forming ring at 10 kpc. Inside and beyond the star-forming ring, the contribution of unevolved stellar populations to the radiation field increases, but usually remains in the 10 – 30% range per dust cell.
- We also analyse the dust heating from a projected point of view, to mimic the observation of our model on the plane of the sky. This way, we still find that the dust is mainly heated by the evolved stellar populations, but the fraction drops to 79%. The contribution of the unevolved stellar populations changes significantly with radius and wavelength. Again, this fraction is lowest in the central regions, and peaks in the rings. It ranges between 20% and 45% across the infrared spectrum, but dips significantly around 100 μm. These results again indicate the dominance of the bulge.
- We find no correlation between the heating fraction of the unevolved stellar populations, and the 160/250 and 250/350 FIR colour ratios. These ratios are, however, commonly used to trace the dust heating in star forming galaxies. The bright bulge of M31 may explain the non-correlation. Due to the strong radiation arising from the center of M31, there is a significant non-local heating effect. Dust up to the 10 kpc ring is heated by photons from the inner parts of M31. This can not be captured by the line-of-sight colour ratios in the FIR.
- The most promising tracer for the dust heating is the sSFR. We find a tight correlation, which matches the best fit relation derived from M51 pixels. In fact, the two datasets make a rather smooth and continuous sequence. More research is required to assess whether sSFR is a general tracer of dust heating in galaxies at a local scale.

  This study allows us to couple back to the investigation of dust scaling relation in M31 in chapter 3. The pixel-by-pixel SED fitting method assumes that each pixel is an independent region. Our radiative transfer model on the other hand, suggests that non-local heating is significant in M31. We speculate that part of the scatter in the observed dust scaling relations can be attributed to this effect. Nevertheless, it is useful to apply both methods in parallel. The SED fitting yields many valuable parameters, which can be used for statistical studies to probe the correlations between dust and stars inside a galaxy. This method is however unfit for attenuation and energy balance studies on a local scale. Radiative transfer is the preferred method here. However, this technique makes several assumptions on the stellar and dust content. Radiative transfer models are thus not ideal

to derive independent galaxy properties for dust scaling relations. A true understanding of the internal working of galaxies should therefore come from a combination of statistical analysis and detailed simulations.

Part IV

Conclusions and outlook

Conclusions

6

All models are wrong, but some are useful.

George Box

We have set out, in this investigation, to better understand the influence of dust and stellar radiation on each other. Our research was focussed on Andromeda and galaxies in the Local Universe and rests on a combination of observation, theory, and simulation. We deliberately chose to work in a framework of physically motivated models to derive the main properties of stars and dust in our sample. In four chapters, we apply different astrophysical tools and address several manifestations of the dust-starlight interplay: attenuation, scaling relations, relative star-dust geometry, and dust heating. We summarize the main conclusions of our work for each chapter.

In chapter 2, we have performed panchromatic (UV-submm) SED modelling of the *Herschel* Reference Survey (HRS) late-type galaxies. We modelled the attenuation in these systems and derive three key parameters; the bolometric dust attenuation fraction $f_{\rm dust}$, the UV heating fraction $\xi_{\rm UV}$, and the FUV attenuation A_{FUV}. We find that the mean bolometric attenuation is 32%. In other words, for local, star forming galaxies about one third of the stellar radiation is attenuated by dust (see also Table 2.1 and Fig. 2.3). The mean UV heating fraction is 56%, which indicates that more than half of the attenuated stellar radiation is absorbed in the UV domain. There is a clear trend between $\xi_{\rm UV}$ and the morphological type of a galaxy (shown in Fig. 2.4), where high UV heating is more important in late-type galaxies. We also found a strong correlation with specific star formation rate (sSFR) and provide a power-law fit. These results suggest that dust attenuation and consequently, dust heating can be related to galaxy evolution. Galaxies in the early stage of their evolution (type Sc and Sd) will have higher levels of dust attenuation. This is in part because they are more dusty, but also because their dust distribution is more compact (e.g. in disks, rings or spiral arms).

The IRX vs. A_{FUV} relation is constructed for our sample, within the framework of our panchromatic SED model. We calibrated this relation for different values of $NUV - r$ (see Fig. 2.6), which allows us to estimate A_{FUV} based on quantities that are relatively easy to obtain and to

determine the FIR properties of galaxies lacking observations in this regime. As our sample was selected to be representative for local spiral galaxies, our relations can be applied to such systems.

Chapter 3 digs deeper in the panchromatic SED fitting method and explores its limits towards small regions. A dedicated pixel-by-pixel SED fit for the panchromatic dataset of the Andromeda galaxy is performed. At the resolution of $\sim$ 140 pc along the major axis of M31, the pixels are treated as independent sub-galactic environments. The SED of sub-kpc regions can be successfully fitted using galaxy-based models, provided that the parameter space is adequately sampled. We present 2-D parameter maps for a series of important galaxy properties derived from our model (see Fig. 3.6). These parameters are subsequently linked to each other in a set of dust-scaling relations. Our results indicate that the more recent star formation occurs beyond $\sim$ 3 kpc and peaks in the ring at 10 kpc. This is summarized in Table 3.4.

On a pixel–by–pixel basis, the cold dust temperature follows a power-law relation with the stellar mass surface density ($\mu_\star$) for bulge pixels, but this is more ambiguous in the disk (see Fig. 3.12). This suggests that dust in the bulge is mainly heated by the evolved stellar populations, while in the disk it is more likely that a mix of stellar populates is heating the dust. We also see strong correlations between the specific dust mass ($M_{\rm dust}\,/\,M_\star$) and the $NUV-r$ colour, and between the specific dust mass and the stellar mass surface density (shown in Fig. 3.9). These scaling relations are remarkably similar to those found for HRS galaxies, which suggests that the dust scaling relations are built *in situ*, with underlying physical processes that must be local in nature. The scale of the analysed pixels correspond to aggregates of giant molecular clouds in M31. The local evolutionary processes involving dust creation and destruction in these complexed should then lie at the base of the dust scaling relations.

We continued our exploration of the applicability of panchromatic SED fitting in chapter 4, where we performed a critical investigations on different dust mass estimates in the dust-lane early-type galaxy NGC 4370. The panchromatic SED fit and a modified black body fit yield consistent values for the total dust mass. We treat them as the gold standard for other methods, even though they are subject to some uncertainty due to limitations in our knowledge of the dust emissivity in the FIR. Colour maps, based on high-quality optical *ugiz* data, could only set a lower limit to the total dust mass. Even so, this is already consistent with previous FIR dust mass estimates based on IRAS observations. Table 4.2 summarizes all dust mass estimates obtained in this study. The lower limits are still an order of magnitude below our gold standard. A comparable lower-limit dust mass was found through the independent method of multi-Gaussian expansion fitting. This method did allow us to produce maps of the dust attenuation for different wavelengths. A conversion from attenuation to dust mass using analytical prescriptions falls short to explain the dust masses obtained from SED fitting.

The most advanced method we test is inverse radiative transfer. The dust content in NGC

4370 is automatically fitted using radiative transfer simulations. Two geometries are tested: an exponential disk and a ring, shown in Fig 4.6 and Fig. 4.7, respectively. Both geometries yield a total dust mass that is consistent with the values derived from SED fitting. There is a slight indication that the dust is distributed in a ring, rather than an exponential disk. We further assess the influence of a potential nuclear stellar disk, but find that it only slightly increases the total dust mass. Based on our analysis, we cannot exclude any diffuse dust component, but it is not necessary to explain the dust attenuation and emission in NGC 4370. Our results indicate that one should be careful in interpreting optical depths and dust masses derived using overly simplistic star-dust geometries, and ignoring scattering by dust.

In chapter 5, we explore the full potential of inverse radiative transfer with the goal to quantify the dust heating fractions in Andromeda. To this end, a detailed 3-D model for the galaxy is constructed with the observed morphology as input geometry for the different components. The model is able to fit the panchromatic SED of M31, and produce a realistic attenuation curve. The dust mass and the luminosity of the young stellar component are well constrained by our modelling. A third free parameter, the star formation rate in obscured clouds, is more difficult to constrain. Table 5.1 gives an overview of the parameters for the full model. The resolved images of M31 are in line with observations across the UV-submm regime (shown in Fig. 5.4). There are, however, some deprojection effects in the form of elongated structures. Our model underestimates the flux in the rings, and overestimates the flux in the inter-ring regions. Potential explanations for this systematic effect are a too high vertical scale length, an improper treatment of the sub-grid physics of obscured star formation, or different dust mixtures outside the rings compared to inside.

A 3-D analysis of the dust absorption levels clearly demonstrates the dominance of the evolved stellar populations. We find that 91% of absorbed stellar radiation comes from this component. The contribution of unevolved stellar populations is almost zero in the central regions of M31 (Fig. 5.8), indicating the major influence of the bulge here. From 10 kpc on, where most of the star formation occurs, the unevolved populations contribute more to the dust heating, but remain within the 10 – 30% range per dust cell. In search for tracers of dust heating sources, we also perform a 2-D analysis on the sky-projected model images. The evolved stellar populations are still the major source (79%) of dust heating in M31. The contribution of the unevolved stellar populations is lowest in the central regions, and peaks in the rings (see Fig. 5.10). Surprisingly, there is no correlation between the heating fraction of the unevolved stellar populations, and the 160/250 and 250/350 FIR colour ratios. These ratios are, however, commonly used to trace the dust heating in star forming galaxies. We suggest that the strong radiation in the bulge causes a significant non-local heating effect. Essentially, dust up to the 10 kpc ring is (partially) heated from the center of the galaxy, an effect which blurs out any link between FIR colours and the dust heating. We do find a tight correlation between the heating fraction of unevolved stellar populations and the specific star formation rate, shown in Fig. 5.12. Our results are remarkably

compatible with a similar analysis done for M51. Further research is necessary to test the wider applicability of this relation towards other galaxies or galactic environments.

In general, we are able to set solid constrains on the energy balance in galaxies on a global and local scale. On the global scale, we measured the bolometric attenuation and UV heating. The numbers we obtain are for the first time derived from a large and statistically representative sample. They can be used as the reference for studies in the Local Universe. On local scales, we have shown that the dust scaling relations are still hold in M31, despite strong effects of non-local heating. These insights challenge the current interpretation of energy reprocessing in galaxies. They should be the basis for new models and further observational studies.

Our results furthermore underline the importance of the relative star-dust geometry in galaxy models. All too often, the simplistic assumption is made that dust is distributed in a thin screen between the observer and the source of emission. In reality, the sources and sinks of radiation are a complex mix in galaxies. This thesis highlights several ways to model this more accurately, preferably using radiative transfer simulations. A realistic star-dust geometry naturally leads to more accurate attenuation properties in galaxies, which in turn open the path to more reliable estimates of the intrinsic stellar properties. Additionally, it provides valuable insights in the heating mechanisms for the dust.

7 Outlook

Somewhere, something incredible
is waiting to be known.

Carl Sagan

In this thesis, we have addresses a series of questions about the interplay of dust and starlight. Several of these questions are now answered, but some are not or only in part. Additionally, many new questions have popped up during the investigation. We have also demonstrated several innovative techniques that require further refinement and that should be applied to other astrophysical environments to test their validity. In this chapter, we briefly outline the prospects in the field and possible follow-up research that could be executed.

The HRS is to date one of the largest samples of galaxies in the Local Universe. Our results in chapter 2 are therefore representative for nearby galaxies. However, for the trends we find between attenuation properties and morphological type, the number of galaxies per bin is still limited. This study also focusses on late-type galaxies only, while it would be most interesting to study the trends for early-type and dwarf galaxies as well. Fortunately, a suitable dataset for this is in the making. DustPedia[1], an EU-FP7 project, has selected the largest sample of local galaxies with panchromatic coverage, from the UV to submm data. They will offer uniformly reduced and calibrated photometry for over 900 galaxies. This would be an ideal starting point for a follow-up study of the global dust attenuation properties in galaxies.

Additionally, as our technique does not rely on resolved images it is easily applicable to galaxies at higher redshift. A similar analysis of such galaxies should highlight differences and similarities in dust attenuation across cosmic time. This will shed light on the evolution of galaxies as a whole. However, one must know the caveats that come with the MAGPHYS code as outlined in Sect. 2.5. We therefore advocate for more testing of the reliability of non-standard properties such as attenuation and star formation history that come from these models. In fact, it would be helpful to expand the MAGPHYS SED library with new templates that cover alternative star formation histories and dust models.

[1] www.DustPedia.com

Further research is also needed in the dust scaling relations that we found on a local scale in M31 (see chapter 3). The main question here is what local processes drive these correlations, and how can they persist over many orders of magnitude, from an individual pixel to global scales. Solutions can be found by applying chemical evolution models to mimic the dust scaling relations, but also by probing the spatial scales at which they break down. For that, similar studies at higher spatial resolution would be particularly useful, for example for the Magellanic clouds or for giant molecular clouds in our own Galaxy. It is also not known how general the dust scaling relations are, in particular on local galaxy scales. Do they follow the same slope, are there systematic offsets in other galaxies? To this end, our method could be applied to other local galaxies, both on a resolved and global scale. Suitable targets would be the face-on spirals M33, M51, M81 and M101, but also the large sample provided by DustPedia.

In the modelling of early-type galaxies, the pilot study on NGC 4370 (chapter 4) could be expanded towards similar objects. In fact NGC 4370 is one of the 10 dust lane early-type galaxies in the FRIEDL sample (Far-infraRed Investigation of Early-type galaxies with Dust Lanes). These systems are surprisingly dusty, but little is known beyond their total dust mass. Using inverse radiative transfer on high-quality optical data, we could not clearly discriminate between an exponential disk or a ring geometry of the dust. However, with the ever growing number of high-resolution optical data, more of such systems are being observed. It would be particularly interesting to model those which deviate slightly form the perfect edge-on case of NGC 4370. It should allow a better determination of the dust geometry in dust-lane early-type galaxies. The FRIEDL project is a good starting point, and can be expanded towards dusty Virgo Cluster ETGs, which also have suitable data coverage thanks to the NGVS and *Herschel*.

In chapter 5 we further refine the radiative transfer modelling of resolved galaxies beyond the edge-on view. The technique is promising, but there are several caveats that need further investigation. In particular, the treatment of obscured star formation is highly uncertain. The MAPPINGS-recipes are still isotropic approximations of real star-forming regions. It would be useful to explore their validity and compare them to anisotropic models. Furthermore, it is critical to increase the sample size of resolved panchromatic models for a systematic investigation of the dust heating sources. Andromeda is only the second galaxy (after M51) to be modelled in such a way. A promising follow-up can again be found in the DustPedia consortium, who started the endeavour of modelling up to 100 nearby face-on spiral galaxies.

However, such highly-detailed radiative transfer models remain time-consuming. It is not realistic to model a sample larger than $\sim$ 100 in this way. In fact, the most important galaxy properties are encoded in their SED. For a larger, statistical studies, the only feasible approach is to extract galaxy properties through SED fitting, without going into the details of a resolved study for each galaxy. The way forward here lies in the combination of radiative transfer simulations and Bayesian panchromatic SED fitting. In this method, the library of SED templates in the current generation of SED fitters is replaced by simulated radiative transfer SEDs. The

construction of such a library requires a systematic sampling of the parameter space. Stellar population properties should be varied in mass, age, metallicity and star formation history. Dust can be parametrized by mass and grain composition. But the most important aspect would be the set-up of realistic and anisotropic distributions for both stars and dust. The treatment of dust as an active, local part of the ISM (in contrast with a simple foreground screen) would provide more accurate attenuation laws and ensure a local and global energy balance in the model. This would be a major improvement on the current generation of galaxy modelling tools.

Samenvatting

8

In deze thesis zijn we vertrokken vanuit de vraag hoe de wisselwerking tussen stof en het licht van sterren zich manifesteert in sterrenstelsels. Ons onderzoek is toegespitst op het Andromeda stelsel (zie figuur 8.1) en sterrenstelsels in het Lokale Universum. Het steunt op de drie pijlers van de moderne astrofysica: observatie, theorie en simulatie. We kozen er bewust voor om te werken in een kader van fysisch gemotiveerde modellen om de belangrijkste eigenschappen van sterren en stof te bepalen voor de stelsels in onze steekproef. In hoofdstuk 1 geven we een algemeen overzicht van de opbouw van sterrenstelsels en hoe deze gemodelleerd kunnen worden. In de vier volgende hoofdstukken passen we verscheidene methodes toe en bekijken we verschillende manifestaties van de wisselwerking tussen stof en sterren: de verduistering (attenuatie) van sterlicht door stof, relaties tussen globale eigenschappen van sterrenstelsels, het belang van de geometrie van het stof en de sterren, en de voornaamste bronnen voor de opwarming van het stof. We vatten ons werk hier samen voor elk hoofdstuk.

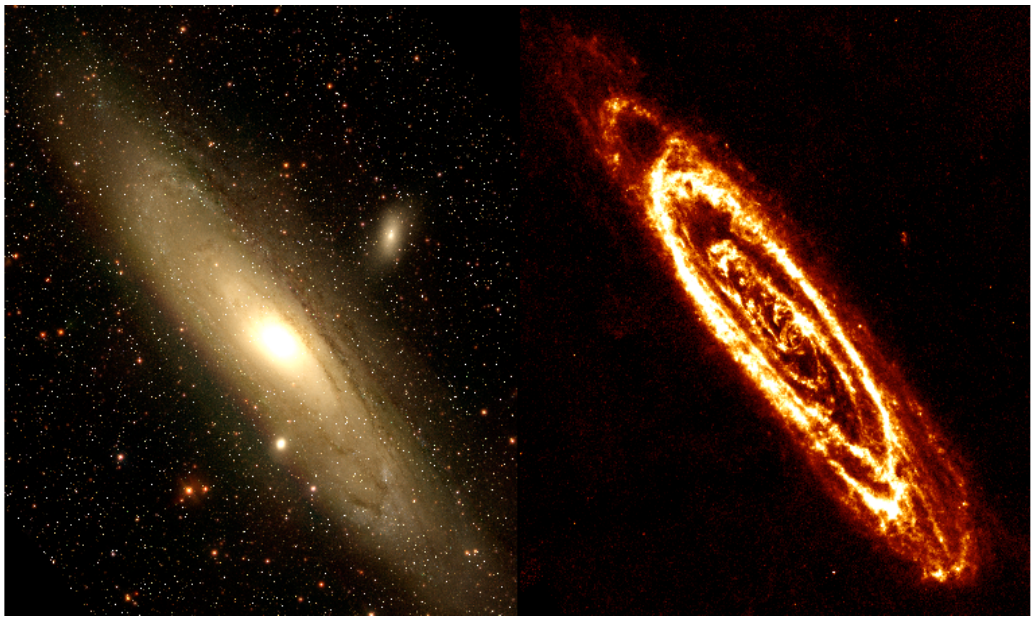

Figure 8.1: Twee sterk verschillende gezichten van het Andromeda stelsel (M31). Links is een optisch kleurenbeeld gemaakt uit de *g*, *r* en *i* band van de *Sloan Digital Sky Survey*. Het stof in M31 is zichtbaar als donkere lijnen tegen de gele achtergrond van sterren. Rechts toont hoe Andromeda er uit ziet op lange golflengte (250 μm). Dit beeld is waargenomen door de *Herschel* ruimtetelescoop en toont het licht uitgezonden door koud stof.

In hoofdstuk 2 hebben we de spectrale energieverdeling (SED) van sterrenstelsels gemodelleerd. Het ging hierbij om laat-type stelsels uit de *Herschel Reference Survey* (HRS) data set waarvoor waarnemingen van het UV tot sub-millimeter beschikbaar waren. Uit deze panchromatische modellen bepaalden we de attenuatie voor elk sterrenstelsel en leidden we drie parameters af: de bolometrische attenuatie fractie $f_{\rm dust}$, the UV opwarmingsfractie $\xi_{\rm UV}$, en de attenuatie in de FUV band A_{FUV}.

We vinden dat de gemiddelde bolometrische attenuatie 32% bedraagt. Anders gezegd, voor lokale, ster-vormende galaxieën wordt ongeveer een derde van de straling van sterren geabsorbeerd door stof. De gemiddelde UV opwarmingsfractie bedraagt 56%, wat aangeeft dat meer dan de helft van de attenuatie van straling plaatsvindt in het UV gebied. Er is een duidelijke trend tussen $\xi_{\rm UV}$ en het morfologisch type van een sterrenstelsel. Een hoge UV opwarming vindt namelijk vaker plaats bij laat-type stelsels. We zien ook een sterke correlatie met de specifieke stervormingsgraad (sSFR). Deze resultaten suggereren dat stof-attenuatie, en dus ook stof-opwarming, kan gelinkt worden aan de evolutie van galaxieën. Sterrenstelsels in een vroeg stadium van hun evolutie (type Sc en Sd) zullen hogere waarden voor stof-attenuatie hebben. Dit is deels omdat ze meer stof bevatten, maar ook omdat het stof compacter verdeeld is (vb. in schijven, ringen of spiraalarmen).

In figuur 8.2 tonen we A_{FUV} in functie van de verhouding tussen de totale lichtkracht in het infrarood en de lichtkracht in het verre UV. We kleuren de galaxieën uit onze steekproef op basis van hun $NUV - r$ kleur. Wanneer we de sterrenstelsels opdelen volgens $NUV - r$ kleur, zien we dat er verschillende parallelle trends zichtbaar worden. We stellen voor elke groep van gelijkaardige $NUV - r$ kleur een aparte relatie op. Dit stelt ons in staat om A_{FUV} te schatten op basis van eigenschappen die makkelijk te bepalen zijn voor de meeste sterrenstelsels. Omgekeerd kan dit ook gebruikt worden om de ver-infrarood eigenschappen van galaxieën te bepalen wanneer er geen observaties in dit gebied voorhanden zijn. Gezien onze steekproef representatief is voor het Lokale Universum, kunnen onze relaties voor dit soort objecten gebruikt worden.

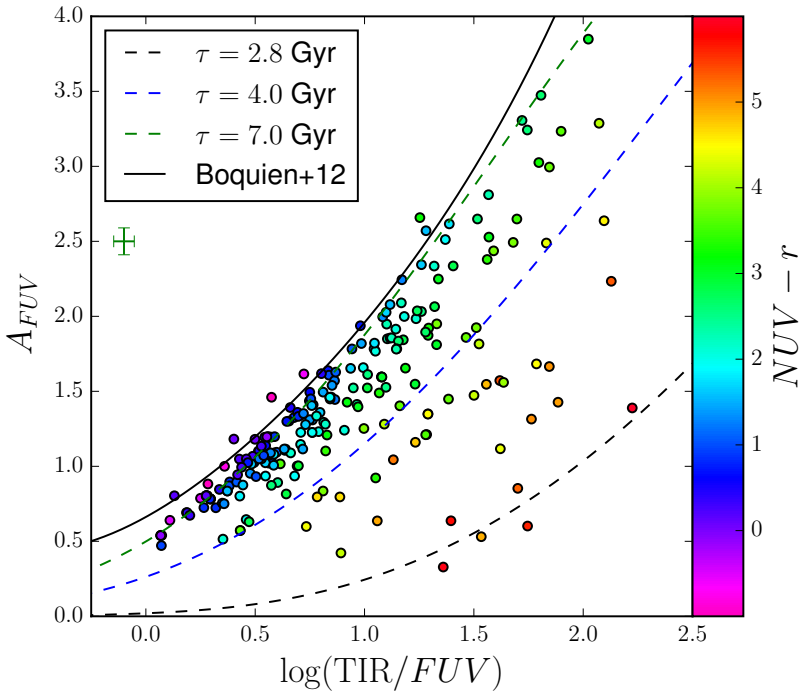

Figure 8.2: A_{FUV} in functie van $\log(\mathrm{TIR}/FUV)$ voor de laat-type galaxieën van de HRS. De kleur van de data punten geeft is volgens hun $NUV - r$ kleur. Enkele theoretische lijnen geven de trend weer voor verschillende evolutiescenarios.

Hoofdstuk 3 gaat dieper in op de methode van panchromatisch SED modelleren en verkent de limieten van deze toepassing in kleinere gebieden. Hiervoor werd de SED van elke afzonderlijke pixel in Andromeda gemodelleerd aan de hand van panchromatische observaties. Met een fysische resolutie van $\sim$ 140 pc langs de grote as kunnen de pixels als onafhankelijke galactische regio's beschouwd worden. De SED's van deze regio's konden met succes gemodelleerd worden. Hierbij werd gebruik gemaakt van dezelfde methode als voor het modelleren van sterrenstelsels op zijn geheel, mits een kleine uitbreiding van de parameter ruimte.

We presenteren de 2-D verdeling van een reeks belangrijke galactische parameters die we uit ons model halen. Deze parameters werden daarna gelinkt aan elkaar in zogenaamde stofschalingsrelaties. Voor de pixels van M31 zien we dat, in de bult van het sterrenstelsel, de temperatuur van de koude stofcomponent een machtswet volgt met betrekking tot de oppervlaktedichtheid van de stellaire massa, $\mu_\star$. Dit suggereert dat het stof in de bult vooral door oudere sterpopulaties wordt opgewarmd. Deze relatie is echter minder duidelijk buiten de bult, zodat het stof hier waarschijnlijk door zowel jonge als oude sterpopulaties wordt opgewarmd.

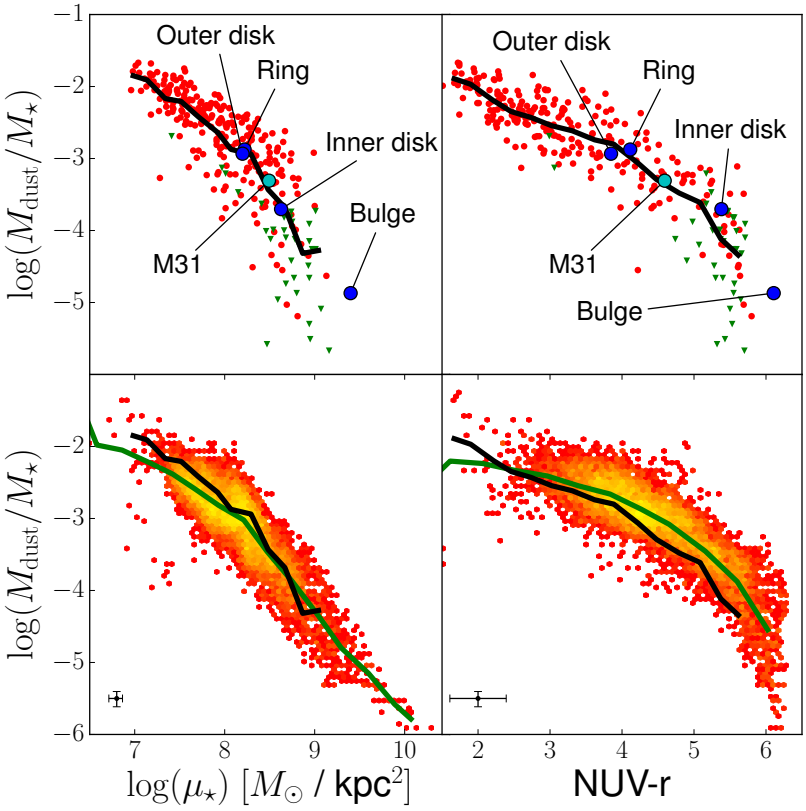

Figure 8.3: Boven: stof schalingsrelaties voor de HRS. $M_{\rm dust}/M_\star$ in functie van de oppervlaktedichtheid van de stellaire massa, $\mu_\star$, en $NUV-r$. De galaxieën in het rood zijn gedetecteerd door *Herschel*, degene in het groen zijn bovenlimieten voor ongedetecteerde stelsels. De blauwe punten geven de positie van de belangrijkste regio's en M31 zelf aan. De zwarte lijn is een gemiddelde trendlijn. Onder: Dezelfde schalingsrelaties, maar voor de individuele pixels in M31. In deze dichtheidsgrafiek geeft een gele kleur een hoge dichtheid aan data punten aan. Rood een lage dichtheid. De zwarte lijn is opnieuw de gemiddelde trend voor de HRS sterrenstelsels. De groene lijn geeft de gemiddelde trend weer voor de pixels in M31.

We zien ook een sterke correlaties tussen de $NUV-r$ kleur en de verhouding tussen de stofmassa en de stellaire massa (ook wel specifieke stofmassa genoemd; $M_{\rm dust}/M_\star$). De specifieke stofmassa is ook nauw verbonden aan de oppervlaktedichtheid van de stellaire massa ($\mu_\star$). Beide relaties zijn te zien in figuur 8.3. Deze schalingsrelaties zijn opmerkelijk gelijkaardig aan diegene gevonden voor de HRS galaxieën. Dit suggereert dat de stof-schalingsrelaties vanuit kleine gebieden opgebouwd worden. De wisselwerking tussen stof en de straling van sterren is dan vergelijkbaar op lokale als op globale schaal. De schaal die overeenkomt met de geanalyseerde pixels is die van groepen van grote stervormingsgebieden in M31. De lokale evolutionaire processen voor de aanmaak en vernietiging van stof in deze groepen zouden dan aan de basis liggen van de stof-schalingsrelaties.

In een verdere verdiepende studie (hoofdstuk 4) gaan we na hoe goed we het stof in NGC 4370 in kaart kunnen brengen. Dit is een vroeg-type sterrenstelsel met een duidelijk zicht-

bare stoflijn en verder een regelmatige structuur, zonder opvallende elementen (zie figuur 8.4). Hiervoor modelleren we de panchromatische SED en vergelijken we die met een SED model gebaseerd op enkel ver-infrarode data. Beide modellen geven een vergelijkbare stofmassa. We beschouwen deze dan als de standaard massa, omdat ze rechtstreeks bepaald is, aan de hand van de emissie van het stof. Deze standaard kunnen we dan vergelijken met andere methodes, die de stofmassa afleiden uit waarnemingen in het optische gebied. We maken gebruik van diepe *ugiz* data om kleurkaarten te maken. Hiermee kunnen we een ondergrens zetten op de stofmassa. Deze is op zich consistent met vroegere schattingen van de stofmassa op basis van IRAS data. De ondergrenzen zijn echter nog steeds een grootteorde lager dan onze standaard waarde. We vinden een vergelijkbare ondergrens via een onafhankelijke methode, gebaseerd op multi-Gaussische expansie modellen. Deze methode stelt ons wel in staat om de attenuatie in kaart te brengen voor verschillende golflengtes. Een omzetting van attenuatie naar stofmassa gebaseerd op analytische voorschriften schiet dus te kort om de standaard waarde te verklaren.

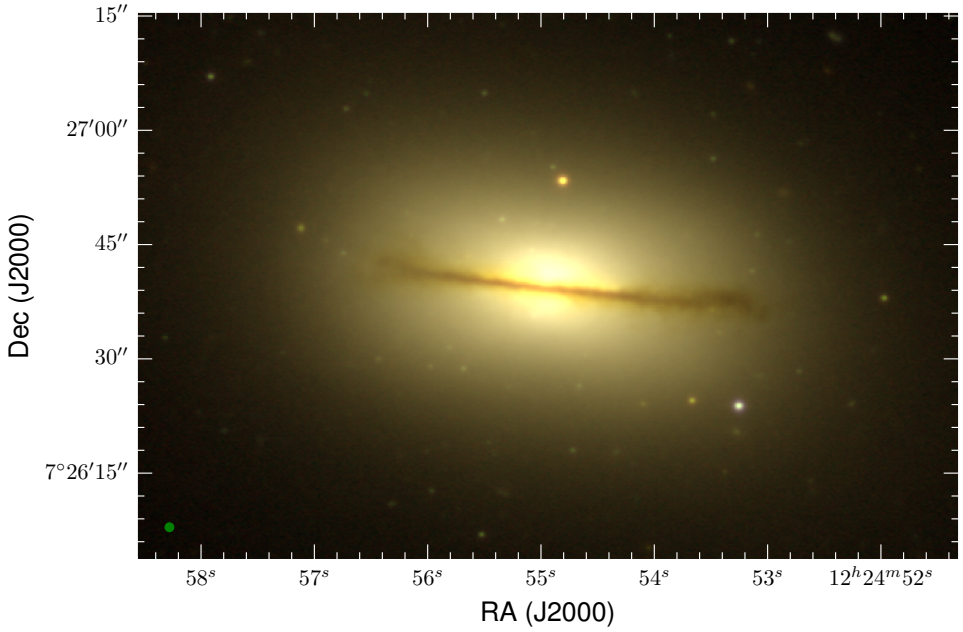

Figure 8.4: Kleurbeeld van het lensvormige stelsel NGC 4370, gemaakt van *g*, *i* en *z* band waarnemingen uit de *Next Generation Virgo cluster Survey*. De stoflijn is duidelijk zichtbaar tegen de gele achtergrond van sterren.

De meest geavanceerde methode die we testen is die van inverse stralingsoverdracht simulaties. Via deze computerberekeningen wordt de verdeling en massa van het stof in NGC 4370 automatisch bepaald. We testen twee soorten verdelingen: een exponentiële schijf en een ring. Figuur 8.5 toont de resultaten voor de ring, die net iets beter past dan de exponentiële schijf. Beide geometrieën geven echter een stofmassa die vergelijkbaar is met onze standaard. We testen ook de invloed van een mogelijke schijf van sterren in de kern, maar de stofmassa komt

voor dezeconfiguratie niet veel hoger uit. Met onze analyse kunnen we niet uitsluiten dat er een diffuse stofcomponent aanwezig is in NGC 4370. We hebben deze echter niet nodig om de attenuatie en emissie van stof in dit systeem te verklaren. Onze resultaten geven aan dat men voorzichtig moet zijn bij de interpretatie van optische diepte en stofmassa wanneer deze bepaald is aan de hand van te simpele geometrieën en de effecten van verstrooiing genegeerd worden.

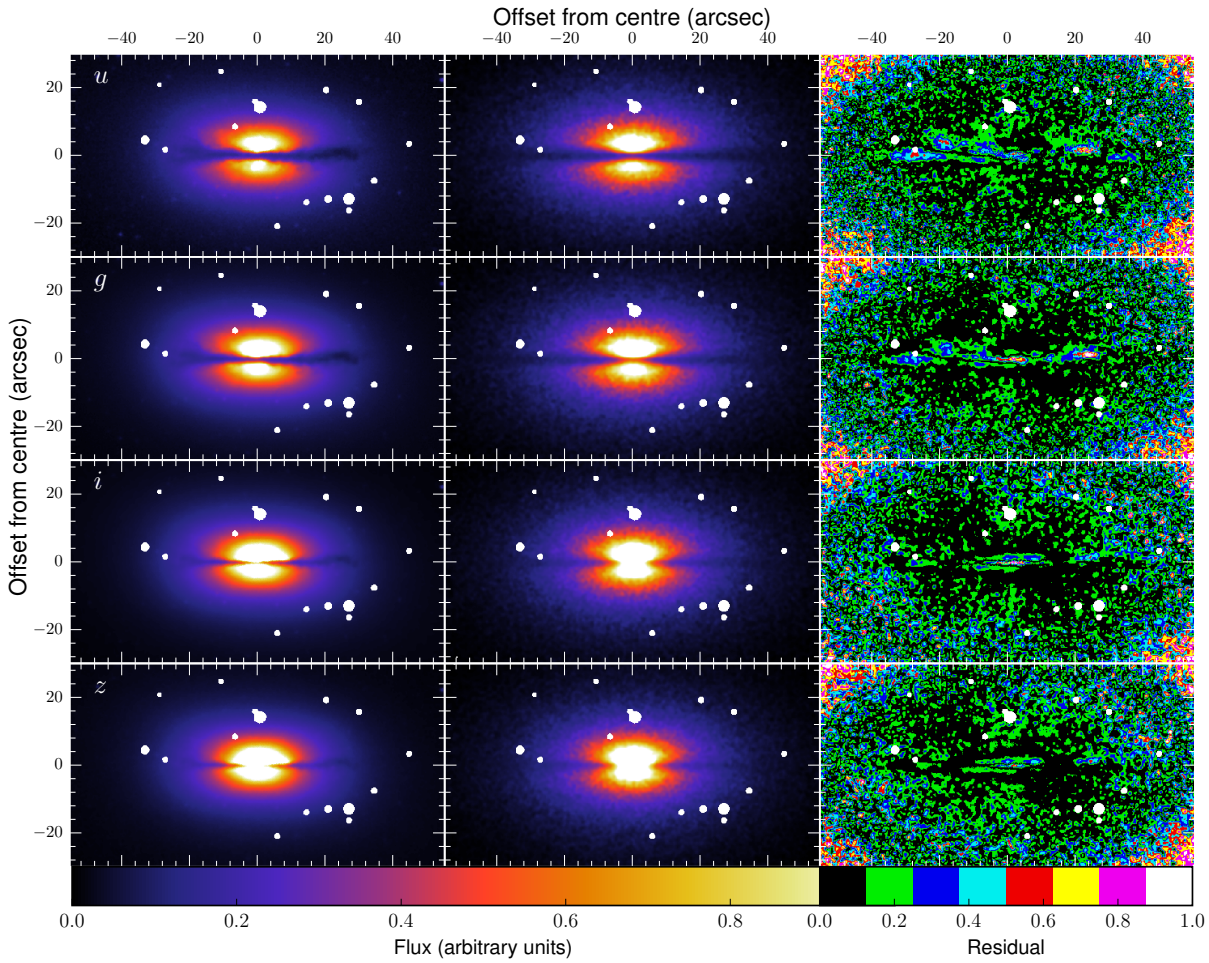

Figure 8.5: Best passend model voor een stofring in NGC 4370, voor vier optische banden (*ugiz*). Linker kolom toont de observaties waarbij de voorgrondsterren gemaskeerd zijn. Middenste kolom toont de overeenkomstige model beelden. Het relatieve verschil tussen beide beelden is te zien in de derde kolom.

In hoofdstuk 5 verkennen we het volle potentieel van inverse stralingsoverdracht simulaties met als doel de mechanismen voor de opwarming van stof in Andromeda te kwantificeren. Hiervoor wordt een gedetailleerd 3-D model van het sterrenstelsel opgezet. Als basis voor de geometrieën voor de verschillende componenten wordt gebruik gemaakt van geobserveerde beelden. Het model is in staat de panchromatische SED van Andromeda te reproduceren. We bekomen een realistische attenuatiecurve, die in lijn ligt met waarnemingen voor M31. De

stofmassa en de lichtkracht van de jonge sterren zijn goed bepaald door onze methode. Een derde vrije parameter, de stervormingsgraad in moleculaire wolken, is moeilijker te bepalen. De 2-D beelden van het model komen vrij goed overeen met de observaties in het UV tot submillimeter gebied. Wel zijn er enkele projectie-effecten zichtbaar in de vorm van uitgerekte structuren. Het model onderschat de flux in de ringen en overschat de flux tussen de ringen in de schijf van M31.

Een 3-D analyse van de absorptie in Andromeda demonstreert duidelijk de dominantie van de oudere sterpopulaties. We vinden dat ongeveer 91% van de geabsorbeerde stellaire energie afkomstig is van deze oudere component. Figuur 8.6 (linker paneel) toont de bijdrage van jongere sterpopulaties tot de geabsorbeerde energie per stofcel in functie van de afstand tot het centrum. Deze contributie is bijna nihil in de centrale regio's, wat de enorme invloed van de bult hier aangeeft. Vanaf 10 kpc, waar het meeste van de stervorming plaatsvindt, zien we een toename in de invloed van de jongere sterpopulaties. Zij blijven echter binnen het $10 - 30\%$ interval. We voeren ook een 2-D analyse uit, gebaseerd op projecties van het model op het vlak van de hemel. Hiermee gaan we op zoek naar observationele indicatoren voor de bronnen die stof opwarmen. De oudere sterpopulaties blijken ook uit deze analyse de grootste bron te zijn, met 79%. De bijdrage van jongere sterpopulaties is opnieuw laagst in de centrale gebieden, en piekt in de ringen. Het is verrassend dat we geen correlatie zien tussen de contributie van jongere sterpopulaties en verhoudingen in ver-infrarode flux in de *Herschel*-banden ($160/250$ en $250/350$), omdat deze verhoudingen populair zijn als indicatoren voor stof opwarming in stervormende systemen. We suggereren dat de sterke straling uit de bult voor significante niet-lokale opwarming zorgt. In essentie wordt het stof tot aan de ring op 10 kpc voor een groot deel opgewarmd vanuit het centrum van Andromeda. Dit effect wist iedere link uit tussen de ver-infrarode kleuren en stof-opwarming in een 2-D projectie. Wel vinden we een sterke correlatie tussen de stof opwarming door jongere sterpopulaties en specifieke stervormingsgraad (sSFR), te zien in het rechter paneel van figuur 8.6. Deze resultaten zijn opmerkelijk consistent met een gelijkaardige analyse voor M51. Er is verder onderzoek nodig om te verifiëren of deze relatie met sSFR geldig is in andere sterrenstelsels of galactische omgevingen.

In het algemeen onderlijnt dit onderzoek het belang van de relatieve geometrie van sterren en stof in modellen voor galaxieën. Nog te vaak wordt de simplistische aanname gemaakt dat stof zich bevindt in een dun scherm tussen de waarnemer en de bron van emissie. In de realiteit zijn de bronnen en plaatsen van absorptie een complexe mix in sterrenstelsels. Onze resultaten tonen verschillende manieren om dit op een meer accurate manier te modelleren. Hierbij gaat de voorkeur uit naar stralingsoverdracht simulaties. Een realistische verdeling van stof en sterren leidt op natuurlijke wijze tot nauwkeuriger attenuatie-eigenschappen in sterrenstelsels. Op zijn beurt effent dit het pad naar meer betrouwbare bepalingen van de intrinsieke stellaire eigenschappen. Tegelijkertijd biedt het waardevolle inzichten in de mechanismen die stof kunnen opwarmen.

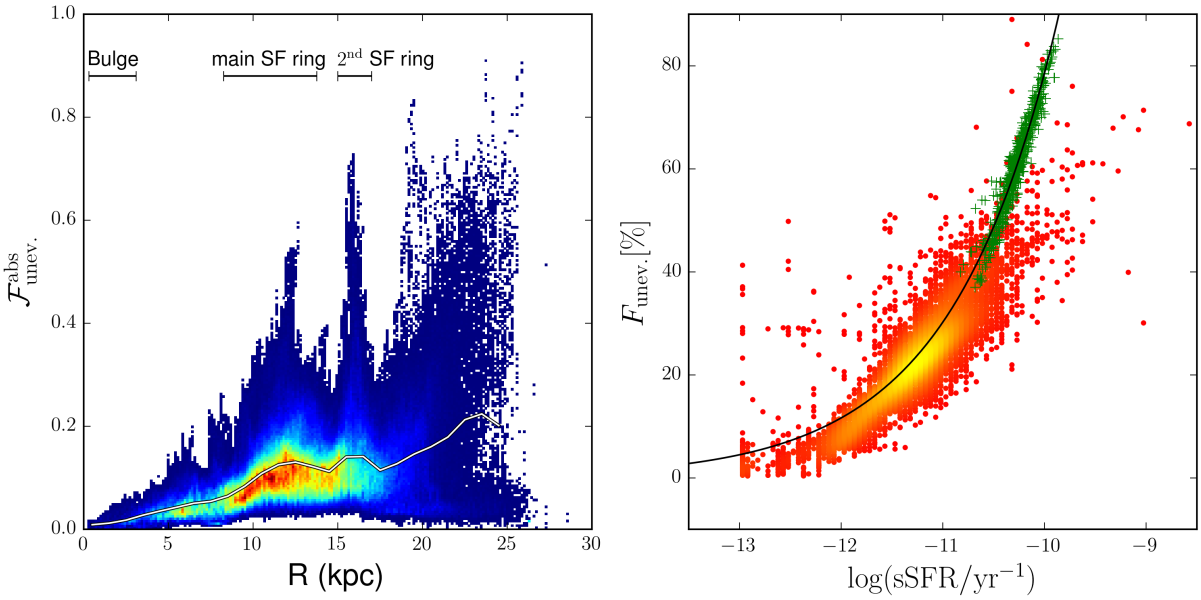

Figure 8.6: Links: Radiale distributie van de bolometrische absorptie fractie voor jongere sterpopulaties, $\mathcal{F}^{\rm abs}_{\rm unev.}$. De grafiek is een 2D histogram waarbij de punten gewogen zijn met de massafractie van de stofcellen. Hierbij duidt rood op een hoog aantal cellen en blauw op een laag aantal. Rechts: Dichtheidsgrafiek voor de geprojecteerde fractie van jongere sterpopulaties tot de stof opwarming, $F_{\rm unev.}$, in functie van sSFR. Gele kleur betekend een hoge densiteit aan data punten, rood een lagere densiteit. De groene plus-tekens zijn data punten van een soortgelijke analyse voor M51. Hiervan is ook de zwarte lijn afgeleid.

Part V

Appendix

Astrophysical methods and tools

A

A.1 Principles of dust continuum radiative transfer

The most advanced way of treating the interaction of starlight with dust is by simulating it. In these radiative transfer simulations, starlight is propagated through a dusty medium. The photons get absorbed or scatter on dust grains. In this work, we limit ourselves to continuum emission. Fortunately, line emission is - to first order - not important when studying general effects such as attenuation and dust heating. As previously mentioned (see Sect. 1.5), the emission of AGN is not considered either. The treatment of AGN light is analogous, but an AGN environment requires dust distributions with much higher optical depths. In this section, we will highlight the concepts of radiative transfer relevant to our needs. For a concise review of dust continuum radiative transfer, we refer the reader to Steinacker et al. (2013).

The principle of radiative transfer simulations is that the trajectory of photons is simulated through space. Photons originate from a *sources* and disappear in *sinks*. They can also leave the system or they are detected by a virtual detector. Once an initial set-up (e.g. a galaxy with stars and dust) is constructed, an observer must be defined. This means a line of sight and field of view must be set. It is evident that the radiation which is detected will depend on the viewing angle of the galaxy, and size of the virtual detector. Along this line of sight, there will be several sources and sinks of radiation. Obviously, stars act as sources, but starlight is also scattered by dust into the line of sight. Furthermore, dust emission is the main source at longer wavelengths. Sinks of radiation are absorption by dust, and scattering out of the line of sight. All these processes amount to a very complex and non-local radiative transfer equation, which is challenging to solve.

The most common way to tackle this problem is not to solve the radiative transfer equation, but to actually mimic the separate processes of emission, absorption, and scattering as light travels through the dusty medium. This can be done by tracing rays of light from source to detector. A method called ray-tracing. The intensity of the ray is decreased based on the dust content of the crossed cells. Ray tracing directly links source of emission to the detector, which limits the noise levels and is often computationally beneficial. On the other hand, the treatment of scattering is less obvious, especially at higher optical depths. Hence, only a handful of codes

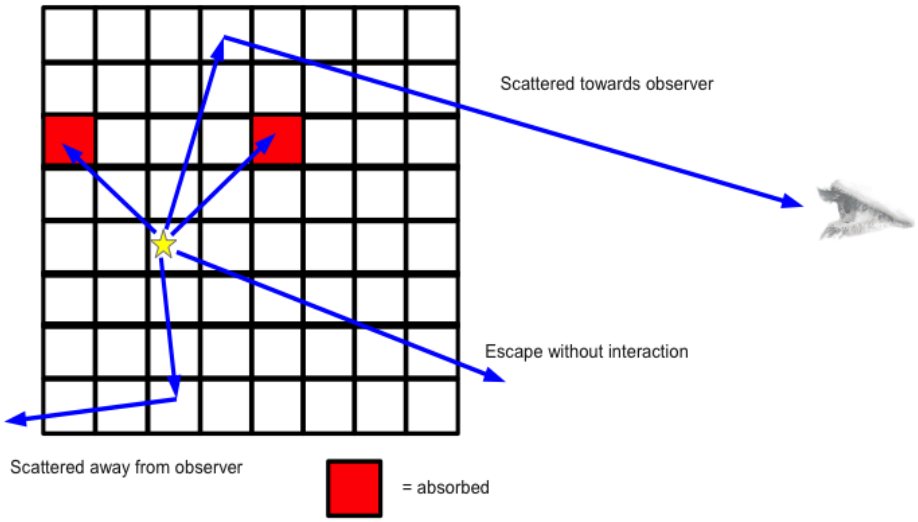

Figure A.1: Basic processes of Monte Carlo radiative transfer. The schematic shows a 2D dust grid with a stellar source. Radiation is absorbed in certain cells (coloured red), and scattered in others. The detector only records the photons that end up in its direction. *Image Courtesy: Steinacker et al. (2013)*

adopt the ray tracing formalism when modelling galaxies (Steinacker et al. 2006; Pinte et al. 2009; Natale et al. 2015).

Alternatively, the different radiative transfer processes can be treated in a more probabilistic way. This is done by following photon packages (i.e. a group of photons) as they propagate from the source of emission. Events such as absorption and scattering are then simulated using random numbers, sampled from probability distributions. This approach is called Monte Carlo radiative transfer. Using the Monte Carlo sampling, complex distributions of dust and stars are efficiently probed across space, direction and wavelength. The main drawback is that random sampling gives rise to high random noise levels when not enough photon packages are simulated. A sufficient amount of photon packages is required for a reliable flux at the end. Nevertheless, in the context of galaxy modelling, Monte Carlo radiative transfer is more efficient and intuitive than ray-tracing. It is therefore by far the most popular technique (see Steinacker et al. 2013 for an overview of available radiative transfer codes). The radiative transfer simulations in this work are also based on the Monte Carlo method (see App. A.2).

Monte Carlo radiative transfer requires a discrete dust grid through which light can travel. In practice, this is achieved by subdividing the dust geometry in 3D dust cells. In this framework, a photon package is created at a random position according to the density profile of the stellar geometry (see fig. A.1). The photon package travels through the galaxy until it crosses a grid cell with a non-zero quantity of dust. A random generator determines whether the photon package is scattered or absorbed, and by how much of its initial energy. This loop continues until the photon package leaves the galaxy or is detected by the virtual detector. In the cells where photon packages are (partially) absorbed, the dust gets heated.

Once all stellar photons are simulated, the radiation field in each grid cell can be computed based on the total absorbed energy in the cells. The energy will heat the dust and cause it to emit (as discussed in Sect. 1.3). Now, the dust cells act as a source of radiation, and the same loop as for the stellar sources is initiated. However, dust emits at longer wavelengths, significantly reducing the probability of absorption or scattering. In fact, to first order, dust self-absorption and scattering are negligible and often not simulated. The longer wavelength photons eventually reach the detector as well, forming the FIR peak in the SED.

A.2 SKIRT and FitSKIRT

The radiative transfer simulations presented in this work are executed with SKIRT[1] (Baes et al. 2011; Camps & Baes 2015). Although there are several state-of-the-art dust radiative transfer codes available, SKIRT (Stellar Kinematics Including Radiative Transfer) offers a unique combination of features and user-friendliness. It is an advanced dust radiative transfer code based on the Monte Carlo approach. The code allows panchromatic radiative transfer simulations using efficient hierarchical grids such as k-d trees (Saftly et al. 2014) and Voronoi grids (Camps et al. 2013), and several optimization techniques (smart detectors, peel-off, biassing, forced scattering, ...). For more in-depth information on these optimization techniques, we refer the reader to Baes et al. (2011) and Steinacker et al. (2013). SKIRT offers a parallel computing framework for shared and distributed memory systems (Verstocken et al. in prep). This powerful addition paves the way for more computationally demanding simulations. The code was recently updated with a user-friendly interface, increasing its applicability.

A vast suite of possible geometries is present, with on top of that several geometry decorators (Baes & Camps 2015). Decorators are a set of classes that allow the modification of any existing geometry, i.e. add clumps, spiral arms, offsets, rotations,... For the construction of realistic galaxy models, SKIRT offers three main types of geometries: purely analytical, semi-analytical, or derived from the output of 3-D numerical simulations (see Fig A.2). They can serve as static 3D distributions for both stars and dust.

Analytical distributions describe the 3-D density profile of matter (stars or dust). Their main advantage is that their 3-D distribution is analytically known, and that it is often relatively easy to generate random positions from these 3-D distributions (Baes & Camps 2015). This makes them computationally cheap. They can be applied to mimic the global structure of galaxies. For example, elliptical galaxies can be approximated by a Sérsic profile, spirals by an exponential disk plus a Sérsic bulge. Until recently, smooth analytical density profiles were the most common way to construct a galaxy model in 3D radiative transfer (Xilouris et al. 1999;

[1] SKIRT is freely available at `http://skirt.ugent.be` and can be redistributed and/or modified under the terms of the GNU Affero General Public License v3.

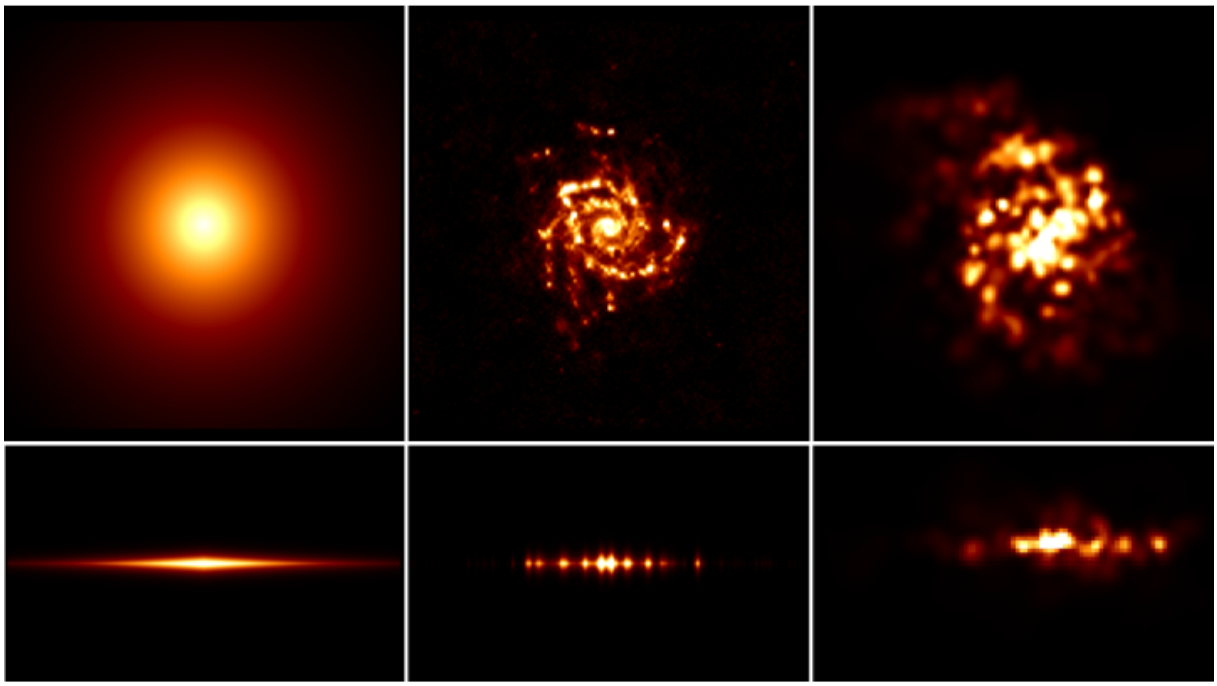

Figure A.2: Different classes of input geometries for radiative transfer simulations. They all represent the dust distribution in a galaxy's disk. Top row shows the face-on view, bottom row the edge-on view. Left column: the classic analytical exponential disk. Middle column: dust distribution derived from the surface brightness profile of NGC 628 at 100 μm. The density in this face-on galaxy was distributed vertically according to an exponential profile. Right column: Conversion of gas particles from an SPH simulation of a spiral galaxy.

Popescu et al. 2000; Dasyra et al. 2005; Bianchi 2007; MacLachlan et al. 2011; De Looze et al. 2012b; De Geyter et al. 2014; Shinn & Seon 2015). The main drawback here is that the level of complexity is limited.

Semi-analytical geometries are derived from observations. They require some conversion algorithm to the third dimension. As all observations of the sky are in two spatial dimensions, they must be deprojected. This requires some interpolation of the data, which is based on simple analytical prescriptions. The most notable example for this case is the recent work by De Looze et al. (2014). They construct a 3-D model of M51, the Whirlpool Galaxy based on observations in several wavebands. Their conversion to 3-D geometries is done by first deprojecting the observed images to a face-on view using a simple $\cos(i)$ factor. Hereby, the assumption is made that the galaxy's disk is relatively flat, and axisymmetric. Secondly, a vertical dimension is added by stretching the emission along the vertical axis according to an exponential profile. This powerful technique allows more realistic stellar geometries such as asymmetric features or clumpy and filamentary structures.

A last method to construct 3-D density profiles for stars and dust is through direct import from numerical simulations. Contemporary numerical simulations of galaxy dynamics have inherent 3-D information. Whether these simulations are particle-based (e.g. Smooth Particle Hydro-

dynamics; SPH), or grid based (e.g. Adaptive Mesh Refinement; AMR), they can provide a discrete density profile of the 3-D space. Recent advances have made it possible to post-process these simulations using radiative transfer (see e.g. Saftly et al. 2015; Hayward & Smith 2015; Guidi et al. 2015; Natale et al. 2015, Camps et al. in prep.). An important caveat in these studies is that dynamical simulations usually work with gas particles of certain metallicity. A key uncertainty here is the conversion from gas to dust. Generally, a metallicity-dependent gas to dust ratio is assumed, but these factors come with an uncertainty (see also Schaye et al. 2015; Saftly et al. 2015, Camps et al. in prep.).

The inverse radiative transfer problems in this work are solved with FitSKIRT (De Geyter et al. 2013, 2014), an optimization code built around SKIRT. The code is able to probe the parameter space efficiently and find the best-fitting model to a set of observations. It simultaneously fits to images in multiple wavebands, which is a unique feature and drastically improves the reliability of the resulting parameters. FitSKIRT's optimization technique is based on genetic algorithms, which start with an initial population of different parameter sets. For each set, a RT simulation is run and the simulated images are compared to the observed images. Then, a second generation of parameter sets is constructed from the best-fitting sets. Again, a RT simulation is run for each parameter set. Convergence towards the best fitting parameter set is usually reached within 100-150 generations. The code was originally designed and tested to fit edge-on spiral galaxies. These objects are successfully modelled with up to 19 free parameters.

A.3 MAGPHYS

We make use of the Bayesian SED fitting code MAGPHYS - Multi-wavelength Analysis of Galaxy Physical Properties (da Cunha et al. 2008) to perform the strenuous task of modelling panchromatic SEDs. The program determines the best fit from a library of optical and infrared SEDs, taking special care of the dust-energy balance when combining the optical and infrared part of the spectrum. This library is derived from one general multi-component galaxy-SED model, characterised by a number of parameters.

The stellar emission is computed by assuming a Chabrier (2003) initial mass function (IMF) and evolved in time using the latest version of the stellar population synthesis (SPS) model of Bruzual & Charlot (2003). The obscuring effects of interstellar and circumstellar dust are computed using the age-dependent extinction model of Charlot & Fall (2000). In this formalism, the radiation of young stars < 10 Myr is extinct by circumstellar dust clouds and by dust in the diffuse ISM. Stars older than that are extinct only by the diffuse ISM dust.

A multi-component dust model is used to calculate the infrared and submm emission from the reprocessed starlight. The model consists of five modified black bodies to construct the dust continuum. Three of them have fixed temperatures (850 K, 250 K, and 130 K) and a β of 1.

They represent the hot dust continuum. The other two have variable temperatures and embody the warm and cold dust components that dominate the emission at longer wavelengths. The warm dust component has $\beta = 1.5$, while the cold dust temperature has a steeper $\beta = 2$. The aromatic emission peaks in the MIR are modelled using a fixed template based on MIR spectra of the star-forming region M17 (Madden et al. 2006). Although MAGPHYS keeps the emissivity index of the modified black body, β, fixed at 2 for the coldest dust component, this is partially compensated by allowing the temperature of warm dust to vary, broadening the FIR-submm peak in function of the observations.

The mass associated with the warm and cold component is computed using the formula for modified black body dust mass (Hildebrand 1983):

$$M_{\rm dust}(T_{\rm dust}) = \frac{L_{\rm dust}}{4\pi\kappa_\lambda B_\lambda(T_{\rm dust})}. \tag{A.1}$$

Where κ_λ is the dust emissivity index normalized at a particular wavelength λ. The emissivity index depends strongly on the assumed dust mix. In the MAGPHYS model, κ_λ is normalized at 850 μm, based on Dunne et al. (2000). They found that $\kappa_{850\mu{\rm m}} = 0.077$ m^2 kg^{-1}. This lies close to the recent dust model of Jones et al. (2013), which yields $\kappa_{850\mu{\rm m}} = 0.071$ m^2 kg^{-1}. However, it is significantly higher than other dust models. For example, Weingartner & Draine (2001) find $\kappa_{850\mu{\rm m}} = 0.052$ m^2 kg^{-1} for Milky Way dust. This is similar to Zubko et al. (2004), who find $\kappa_{850\mu{\rm m}} = 0.057$ m^2 kg^{-1}. These numbers alone indicate that care should be taken in the comparison of dust masses across different dust models. The absolute value of the dust mass has a model uncertainty which is a factor 1.5 or more.

A limitation of the standard version of MAGPHYS is the range of cold dust temperatures, which is fixed between 15 K and 25 K. This can cause unphysical fits to those SEDs with cold dust temperatures which are warmer or colder than the given interval. An improper determination of the cold dust temperature will influence the value of the warm dust temperature and the dust mass. Therefore, a custom set of infrared SEDs was constructed (da Cunha, private communication), incorporating a wider range in cold and warm dust temperatures. The new library features cold dust temperatures $T_{\rm C}^{\rm ISM}$ ranging from 10 – 30 K and warm dust temperatures $T_{\rm W}^{\rm BC}$ from 30 – 70 K. With this extended library, a broader physical range can be explored, which proved necessary, especially on sub-galactic scales (see Chapter 3 for more details).

The library of template SEDs is derived from this multi-parameter model for the FUV–submm SED. Each free parameter comes with a physically motivated probability distribution. From these distributions, a random parameter set is drawn to create a template SED. The standard MAGPHYS library consists of 25000 UV–optical templates and 50000 IR–submm templates. The expanded version used here has 75000 IR–submm templates.

The UV-to-submm SED is then fitted by comparing this library of physically motivated SED

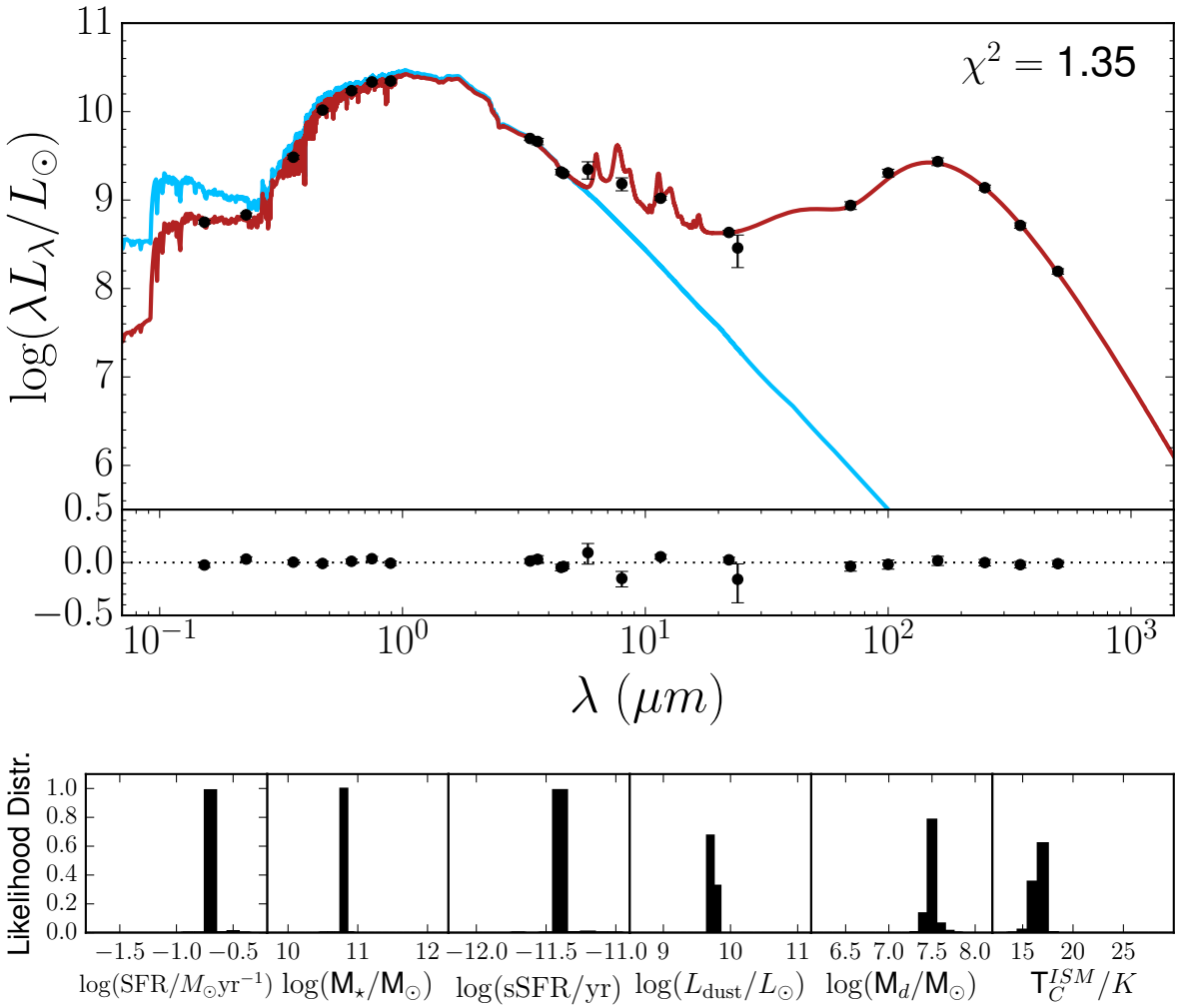

Figure A.3: Example MAGPHYS model for the SED of Andromeda. Top panel shows the best fit template (red) and the corresponding unattenuated SED (blue). The black points are observations. The residuals are plotted below the SED. Bottom row: PDFs of several key parameters of the galaxy. They are described in Table A.1.

templates to the observed data points. The parameter values used to build each template are weighted by the corresponding χ^2, creating probability density functions (PDF). As a result, we know the most probable value for each model parameter. Fig. A.3 shows an example of a MAGPHYS model for Andromeda. The PDFs for a selection of parameters are shown in the bottom row. The χ^2 goodness of fit in MAGPHYS differs conceptually from a classic reduced χ^2. The Bayesian approach of MAGPHYS does not actively vary a set of free parameters. Instead, a series of model templates are created a priori, and then one-by-one evaluated with the observations. The weighted χ^2 formalism described in da Cunha et al. (2008) reflects the difference between model and observations, taking the observational uncertainty into account. It is set up in such a way that a χ^2 around unity indicates a good fit.

The result is that, given a discrete set of observed fluxes, we can decode the SED and extract a wide range of physical parameters with a good determination of their uncertainty. The different output parameters of MAGPHYS are summarised in Table A.1 and are briefly discussed below.

- The contribution of the dust component in the diffuse ISM to the total infrared luminosity $f_\mu = L_{\rm dust}^{\rm ISM}/L_{\rm dust}^{\rm Tot}$ is derived from both the absorption of starlight and from infrared emission.
- The total stellar mass M_* is derived from the population synthesis models and is proportional to the flux in the UV to NIR wavebands.
- The standard star formation rate (SFR) expresses the number of stars formed per year, averaged over the last 100 Myr. The process of star formation is modelled with an exponentially declining SFR law starting from the birth of the galaxy. Superimposed are bursts with a random chance of occurring throughout its lifetime.
- The specific star formation rate (sSFR) is then simply the ratio of the SFR and the stellar mass and compares the number of stars formed during the last 100 Myr with the total number of stars formed throughout the lifetime of the galaxy.
- Dust attenuation is expressed by the optical depth parameter, which is evaluated in the V band: $\tau_V = \tau_V^{\rm BC} + \tau_V^{\rm ISM}$. Starlight of young stars in their birth clouds (BC) experiences extinction from circumstellar dust and from the diffuse interstellar dust. This is parametrised by $\tau_V^{\rm BC}$. Most of the stars however, only irradiate the interstellar dust, modelled by $\tau_V^{\rm ISM}$.
- The bulk of the dust mass is contributed by warm and cold dust in the diffuse ISM and by warm circumstellar dust. A factor of 1.1 takes into account the contributions of hot dust and PAHs to the total dust mass:

$$M_{\rm dust} = 1.1(M_{\rm W}^{\rm BC} + M_{\rm W}^{\rm ISM} + M_{\rm C}^{\rm ISM}). \tag{A.2}$$

- The equilibrium temperature for the warm circumstellar dust and cold ISM dust is left free for the FIR/submm modified black–body components. They are represented in $T_{\mathrm{W}}^{\mathrm{BC}}$ and $T_{\mathrm{C}}^{\mathrm{ISM}}$, respectively.
- Each dust component produces infrared emission, which is summed in the total dust luminosity L_{dust}. The relative contributions of the dust components are quantified in fractions to the total BC or ISM dust luminosity. We refer the reader to Sect. 2.2.1 of da Cunha et al. (2008) for a detailed explanation of the infrared emission parameters. Two important components will be discussed in this work: $L_{\mathrm{C}}^{\mathrm{Tot}}$, the total luminosity of the cold dust in the diffuse ISM and $L_{\mathrm{PAH}}^{\mathrm{Tot}}$, the total luminosity from PAHs in the ISM and around young stars.

Table A.1: Overview of the output parameters from a MAGPHYS SED fit.

Symbol	Unit	Description
f_{μ}		ISM dust to total dust luminosity
τ_V		Total V band optical depth
τ_V^{ISM}		ISM dust contribution to τ_V
SFR	$M_{\odot}\mathrm{yr}^{-1}$	Star formation rate
sSFR	yr^{-1}	Specific star formation rate
M_*	$M_{\odot}$	Total stellar mass
L_{dust}	$L_{\odot}$	Total luminosity of emitting dust
M_{dust}	$M_{\odot}$	Total dust mass
$T_{\mathrm{W}}^{\mathrm{BC}}$	K	Dust temperature in birth clouds
$T_{\mathrm{C}}^{\mathrm{ISM}}$	K	Dust temperature in ISM
$L_{\mathrm{C}}^{\mathrm{Tot}}$	$L_{\odot}$	Total cold dust luminosity
$L_{\mathrm{PAH}}^{\mathrm{Tot}}$	$L_{\odot}$	Total PAH luminosity

Bibliography

Agius, N. K., di Serego Alighieri, S., Viaene, S., et al. 2015, MNRAS, 451, 3815

Agius, N. K., Sansom, A. E., Popescu, C. C., et al. 2013, MNRAS, 431, 1929

Aniano, G., Draine, B. T., Calzetti, D., et al. 2012, ApJ, 756, 138

Aniano, G., Draine, B. T., Gordon, K. D., & Sandstrom, K. 2011, PASP, 123, 1218

Athanassoula, E. & Beaton, R. L. 2006, MNRAS, 370, 1499

Auld, R., Bianchi, S., Smith, M. W. L., et al. 2013, MNRAS, 428, 1880

Azimlu, M., Marciniak, R., & Barmby, P. 2011, AJ, 142, 139

Baes, M. & Camps, P. 2015, A&C, 12, 33

Baes, M., Clemens, M., Xilouris, E. M., et al. 2010, A&A, 518, L53

Baes, M. & Dejonghe, H. 2000, MNRAS, 313, 153

Baes, M. & Dejonghe, H. 2001, MNRAS, 326, 733

Baes, M. & Dejonghe, H. 2002, MNRAS, 335, 441

Baes, M., Sil'chenko, O. K., Moiseev, A. V., & Manakova, E. A. 2007, A&A, 467, 991

Baes, M., Verstappen, J., De Looze, I., et al. 2011, ApJS, 196, 22

Bailey, N. D. & Basu, S. 2014, ApJ, 780, 40

Baillard, A., Bertin, E., de Lapparent, V., et al. 2011, A&A, 532, A74

Barger, A. J., Aragon-Salamanca, A., Ellis, R. S., et al. 1996, MNRAS, 279, 1

Barmby, P., Ashby, M. L. N., Bianchi, L., et al. 2006, ApJ, 650, L45

Barmby, P., Perina, S., Bellazzini, M., et al. 2009, AJ, 138, 1667

Battisti, A. J., Calzetti, D., & Chary, R.-R. 2016, ArXiv: 1601.00208

Beaton, R. L., Majewski, S. R., Guhathakurta, P., et al. 2007, ApJ, 658, L91

Bendo, G. J., Baes, M., Bianchi, S., et al. 2015, MNRAS, 448, 135

Bendo, G. J., Boselli, A., Dariush, A., et al. 2012a, MNRAS, 419, 1833

Bendo, G. J., Buckalew, B. A., Dale, D. A., et al. 2006, ApJ, 645, 134

Bendo, G. J., Calzetti, D., Engelbracht, C. W., et al. 2007, MNRAS, 380, 1313

Bendo, G. J., Draine, B. T., Engelbracht, C. W., et al. 2008, MNRAS, 389, 629

Bendo, G. J., Galliano, F., & Madden, S. C. 2012b, MNRAS, 423, 197

Bendo, G. J., Wilson, C. D., Pohlen, M., et al. 2010a, A&A, 518, L65

Bendo, G. J., Wilson, C. D., Warren, B. E., et al. 2010b, MNRAS, 402, 1409

Bertin, E. & Arnouts, S. 1996, A&AS, 117, 393

Bianchi, S. 1999, PhD thesis, PhD Thesis, 1999

Bianchi, S. 2007, A&A, 471, 765

Bianchi, S. 2008, A&A, 490, 461

Bianchi, S. 2013, A&A, 552, A89

Bianchi, S., Davies, J. I., & Alton, P. B. 2000, A&A, 359, 65

Binggeli, B., Sandage, A., & Tammann, G. A. 1985, AJ, 90, 1681

Block, D. L., Bournaud, F., Combes, F., et al. 2006, Nature, 443, 832

Bocchio, M., Jones, A. P., & Slavin, J. D. 2014, A&A, 570, A32

Bocchio, M., Micelotta, E. R., Gautier, A.-L., & Jones, A. P. 2012, A&A, 545, A124

Boquien, M., Boselli, A., Buat, V., et al. 2013, A&A, 554, A14

Boquien, M., Buat, V., Boselli, A., et al. 2012, A&A, 539, A145

Boquien, M., Calzetti, D., Combes, F., et al. 2011, AJ, 142, 111

Boselli, A., Boissier, S., Cortese, L., et al. 2009, ApJ, 706, 1527

Boselli, A., Ciesla, L., Buat, V., et al. 2010a, A&A, 518, L61

Boselli, A., Ciesla, L., Cortese, L., et al. 2012, A&A, 540, A54

Boselli, A., Cortese, L., & Boquien, M. 2014a, A&A, 564, A65

Boselli, A., Eales, S., Cortese, L., et al. 2010b, PASP, 122, 261

Boselli, A., Fossati, M., Gavazzi, G., et al. 2015, A&A, 579, A102

Boselli, A. & Gavazzi, G. 2006, PASP, 118, 517

Boselli, A. & Gavazzi, G. 2009, A&A, 508, 201

Boselli, A., Gavazzi, G., & Sanvito, G. 2003, A&A, 402, 37

Boselli, A., Hughes, T. M., Cortese, L., Gavazzi, G., & Buat, V. 2013, A&A, 550, A114

Boselli, A., Voyer, E., Boissier, S., et al. 2014b, A&A, 570, A69

Brinchmann, J., Charlot, S., White, S. D. M., et al. 2004, MNRAS, 351, 1151

Bron, E., Le Bourlot, J., & Le Petit, F. 2014, A&A, 569, A100

Bruzual, G. & Charlot, S. 2003, MNRAS, 344, 1000

Buat, V., Giovannoli, E., Heinis, S., et al. 2011, A&A, 533, A93

Buat, V., Heinis, S., Boquien, M., et al. 2014, A&A, 561, A39

Buat, V. & Xu, C. 1996, A&A, 306, 61

Burgarella, D., Buat, V., & Iglesias-Páramo, J. 2005, MNRAS, 360, 1413

Buta, R. J., Sheth, K., Athanassoula, E., et al. 2015, ApJS, 217, 32

Byun, Y. I., Freeman, K. C., & Kylafis, N. D. 1994, ApJ, 432, 114

Calzetti, D., Kinney, A. L., & Storchi-Bergmann, T. 1994, ApJ, 429, 582

Camps, P. & Baes, M. 2015, A&C, 9, 20

Camps, P., Baes, M., & Saftly, W. 2013, A&A, 560, A35

Camps, P., Misselt, K., Bianchi, S., et al. 2015, A&A, 580, A87

Cappellari, M. 2002, MNRAS, 333, 400

Cappellari, M., Emsellem, E., Krajnović, D., et al. 2011, MNRAS, 416, 1680

Carollo, C. M., Danziger, I. J., & Buson, L. 1993, MNRAS, 265, 553

Chabrier, G. 2003, PASP, 115, 763

Chang, Y.-Y., van der Wel, A., da Cunha, E., & Rix, H.-W. 2015, ApJS, 219, 8

Charlot, S. & Fall, S. M. 2000, ApJ, 539, 718

Chemin, L., Carignan, C., & Foster, T. 2009, ApJ, 705, 1395

Ciesla, L., Boquien, M., Boselli, A., et al. 2014, A&A, 565, A128

Ciesla, L., Boselli, A., Smith, M. W. L., et al. 2012, A&A, 543, A161

Clark, C. J. R., Dunne, L., Gomez, H. L., et al. 2015, MNRAS, 452, 397

Clayton, D. D. & Nittler, L. R. 2004, ARA&A, 42, 39

Clemens, M. S., Jones, A. P., Bressan, A., et al. 2010, A&A, 518, L50

Clemens, M. S., Negrello, M., De Zotti, G., et al. 2013, MNRAS

Combes, F., Young, L. M., & Bureau, M. 2007, MNRAS, 377, 1795

Conroy, C. 2013, ARA&A, 51, 393

Corbelli, E., Bianchi, S., Cortese, L., et al. 2012, A&A, 542, A32

Corbelli, E., Lorenzoni, S., Walterbos, R., Braun, R., & Thilker, D. 2010, A&A, 511, A89

Cortese, L., Bendo, G. J., Boselli, A., et al. 2010a, A&A, 518, L63

Cortese, L., Boissier, S., Boselli, A., et al. 2012a, A&A, 544, A101

Cortese, L., Boselli, A., Franzetti, P., et al. 2008, MNRAS, 386, 1157

Cortese, L., Ciesla, L., Boselli, A., et al. 2012b, A&A, 540, A52

Cortese, L., Davies, J. I., Pohlen, M., et al. 2010b, A&A, 518, L49

Cortese, L., Fritz, J., Bianchi, S., et al. 2014, MNRAS, 440, 942

Courteau, S., Widrow, L. M., McDonald, M., et al. 2011, ApJ, 739, 20

Croxall, K. V., Smith, J. D., Wolfire, M. G., et al. 2012, ApJ, 747, 81

da Cunha, E., Charlot, S., & Elbaz, D. 2008, MNRAS, 388, 1595

da Cunha, E., Eminian, C., Charlot, S., & Blaizot, J. 2010, MNRAS, 403, 1894

Daddi, E., Dickinson, M., Chary, R., et al. 2005, ApJ, 631, L13

Dalcanton, J. J., Williams, B. F., Lang, D., et al. 2012, ApJS, 200, 18

Dale, D. A., Aniano, G., Engelbracht, C. W., et al. 2012, ApJ, 745, 95

Dale, D. A., Helou, G., Contursi, A., Silbermann, N. A., & Kolhatkar, S. 2001, ApJ, 549, 215

Dasyra, K. M., Xilouris, E. M., Misiriotis, A., & Kylafis, N. D. 2005, A&A, 437, 447

Davies, J. I., Baes, M., Bendo, G. J., et al. 2010a, A&A, 518, L48

Davies, J. I., Wilson, C. D., Auld, R., et al. 2010b, MNRAS, 409, 102

Davies, R. D. & Lewis, B. M. 1973, MNRAS, 165, 231

De Geyter, G., Baes, M., Camps, P., et al. 2014, MNRAS, 441, 869

De Geyter, G., Baes, M., De Looze, I., et al. 2015, MNRAS, 451, 1728

De Geyter, G., Baes, M., Fritz, J., & Camps, P. 2013, A&A, 550, A74

De Looze, I., Baes, M., Bendo, G. J., et al. 2012a, MNRAS, 427, 2797

De Looze, I., Baes, M., Fritz, J., & Verstappen, J. 2012b, MNRAS, 419, 895

De Looze, I., Fritz, J., Baes, M., et al. 2014, A&A, 571, A69

De Lucia, G., Springel, V., White, S. D. M., Croton, D., & Kauffmann, G. 2006, MNRAS, 366, 499

de Vaucouleurs, G., de Vaucouleurs, A., Corwin, Jr., H. G., et al. 1991, Third Reference Catalogue of Bright Galaxies. (Springer)

Devereux, N. A., Price, R., Wells, L. A., & Duric, N. 1994, AJ, 108, 1667

Devereux, N. A. & Young, J. S. 1990, ApJ, 359, 42

di Serego Alighieri, S., Bianchi, S., Pappalardo, C., et al. 2013, A&A, 552, A8

Dierickx, M., Blecha, L., & Loeb, A. 2014, ApJ, 788, L38

Disney, M., Davies, J., & Phillipps, S. 1989, MNRAS, 239, 939

Domínguez-Tenreiro, R., Obreja, A., Granato, G. L., et al. 2014, MNRAS, 439, 3868

Dong, H., Li, Z., Wang, Q. D., et al. 2014, ApJ, 785, 136

Draine, B. T. 2003a, ARA&A, 41, 241

Draine, B. T. 2003b, ApJ, 598, 1017

Draine, B. T., Aniano, G., Krause, O., et al. 2014, ApJ, 780, 172

Draine, B. T., Dale, D. A., Bendo, G., et al. 2007, ApJ, 663, 866

Draine, B. T. & Li, A. 2007, ApJ, 657, 810

Driver, S. P., Wright, A. H., Andrews, S. K., et al. 2016, MNRAS, 455, 3911

Dunne, L., Eales, S., Edmunds, M., et al. 2000, MNRAS, 315, 115

Dunne, L. & Eales, S. A. 2001, MNRAS, 327, 697

Dunne, L., Gomez, H. L., da Cunha, E., et al. 2011, MNRAS, 417, 1510

Eales, S., Dunne, L., Clements, D., et al. 2010, PASP, 122, 499

Eales, S., Smith, M. W. L., Auld, R., et al. 2012, ApJ, 761, 168

Emsellem, E., Monnet, G., & Bacon, R. 1994, A&A, 285, 723

Engelbracht, C. W., Blaylock, M., Su, K. Y. L., et al. 2007, PASP, 119, 994

Fazio, G. G., Hora, J. L., Allen, L. E., et al. 2004, ApJS, 154, 10

Ferrarese, L., Côté, P., Cuillandre, J.-C., et al. 2012, ApJS, 200, 4

Ferrarese, L., Côté, P., Jordán, A., et al. 2006, ApJS, 164, 334

Ferrari, F., Pastoriza, M. G., Macchetto, F., & Caon, N. 1999, A&AS, 136, 269

Finkelman, I., Brosch, N., Funes, J. G., et al. 2012, MNRAS, 422, 1384

Finkelman, I., Brosch, N., Kniazev, A. Y., et al. 2008, MNRAS, 390, 969

Finkelman, I., Brosch, N., Kniazev, A. Y., et al. 2010, MNRAS, 409, 727

Fisher, D. B., Drory, N., & Fabricius, M. H. 2009, ApJ, 697, 630

Fitzpatrick, E. L. & Massa, D. 2007, ApJ, 663, 320

Ford, G. P., Gear, W. K., Smith, M. W. L., et al. 2013, ApJ, 769, 55

Forman, W., Jones, C., & Tucker, W. 1985, ApJ, 293, 102

Foyle, K., Natale, G., Wilson, C. D., et al. 2013, MNRAS, 432, 2182

Fritz, J., Franceschini, A., & Hatziminaoglou, E. 2006, MNRAS, 366, 767

Fritz, J., Gentile, G., Smith, M. W. L., et al. 2012, A&A, 546, A34

Gadotti, D. A., Baes, M., & Falony, S. 2010, MNRAS, 403, 2053

Gail, H.-P., Zhukovska, S. V., Hoppe, P., & Trieloff, M. 2009, ApJ, 698, 1136

Galametz, M., Kennicutt, R. C., Albrecht, M., et al. 2012, MNRAS, 425, 763

Galametz, M., Kennicutt, R. C., Calzetti, D., et al. 2013, MNRAS, 431, 1956

Galametz, M., Madden, S. C., Galliano, F., et al. 2011, A&A, 532, A56

Galametz, M., Madden, S. C., Galliano, F., et al. 2010, A&A, 518, L55

Galliano, F., Hony, S., Bernard, J.-P., et al. 2011, A&A, 536, A88

Gavazzi, G., Bonfanti, C., Sanvito, G., Boselli, A., & Scodeggio, M. 2002, ApJ, 576, 135

Gavazzi, G., Boselli, A., Donati, A., Franzetti, P., & Scodeggio, M. 2003, A&A, 400, 451

Gil de Paz, A., Boissier, S., Madore, B. F., et al. 2007, ApJS, 173, 185

Giovanelli, R. & Haynes, M. P. 1983, AJ, 88, 881

Gomez, H. & Matsuura, M. 2012, Astronomy and Geophysics, 53, 19

Gomez, H. L., Baes, M., Cortese, L., et al. 2010, A&A, 518, L45

Gomez, H. L., Clark, C. J. R., Nozawa, T., et al. 2012, MNRAS, 420, 3557

González Delgado, R. M., Pérez, E., Cid Fernandes, R., et al. 2014, A&A, 562, A47

Goosmann, R. W. & Gaskell, C. M. 2007, A&A, 465, 129

Gordon, K. D., Bailin, J., Engelbracht, C. W., et al. 2006, ApJ, 638, L87

Gordon, K. D., Clayton, G. C., Misselt, K. A., Landolt, A. U., & Wolff, M. J. 2003, ApJ, 594, 279

Gordon, K. D., Clayton, G. C., Witt, A. N., & Misselt, K. A. 2000, ApJ, 533, 236

Gordon, K. D., Engelbracht, C. W., Fadda, D., et al. 2007, PASP, 119, 1019

Gordon, K. D., Galliano, F., Hony, S., et al. 2010, A&A, 518, L89

Goudfrooij, P. & de Jong, T. 1995, A&A, 298, 784

Goudfrooij, P., de Jong, T., Hansen, L., & Norgaard-Nielsen, H. U. 1994a, MNRAS, 271, 833

Goudfrooij, P., Hansen, L., Jorgensen, H. E., & Norgaard-Nielsen, H. U. 1994b, A&AS, 105, 341

Gould, R. J. & Salpeter, E. E. 1963, ApJ, 138, 393

Groves, B., Dopita, M. A., Sutherland, R. S., et al. 2008, ApJS, 176, 438

Groves, B., Krause, O., Sandstrom, K., et al. 2012, MNRAS, 426, 892

Groves, B. A., Schinnerer, E., Leroy, A., et al. 2015, ApJ, 799, 96

Gruppioni, C., Pozzi, F., Rodighiero, G., et al. 2013, MNRAS, 432, 23

Guidi, G., Scannapieco, C., & Walcher, C. J. 2015, MNRAS, 454, 2381

Gwyn, S. D. J. 2008, PASP, 120, 212

Hao, C.-N., Kennicutt, R. C., Johnson, B. D., et al. 2011, ApJ, 741, 124

Hartmann, L., Ballesteros-Paredes, J., & Bergin, E. A. 2001, ApJ, 562, 852

Häußler, B., Bamford, S. P., Vika, M., et al. 2013, MNRAS, 430, 330

Haynes, M. P. & Giovanelli, R. 1984, AJ, 89, 758

Hayward, C. C. & Smith, D. J. B. 2015, MNRAS, 446, 1512

Hermelo, I., Lisenfeld, U., Relaño, M., et al. 2013, A&A, 549, A70

Herschel Space Observatory. 2011, SPIRE Observer's Manual, http://herschel.esac.esa.int/Docs/SPIRE/html/spire_om.html

Hildebrand, R. H. 1983, QJRAS, 24, 267

Hirashita, H. & Kuo, T.-M. 2011, MNRAS, 416, 1340

Hubble, E. P. 1936, Realm of the Nebulae (New Haven: Yale University Press)

Hughes, T. M., Baes, M., Fritz, J., et al. 2014, A&A, 565, A4

Hughes, T. M., Cortese, L., Boselli, A., Gavazzi, G., & Davies, J. I. 2013, A&A, 550, A115

Hughes, T. M., Foyle, K., Schirm, M. R. P., et al. 2015, A&A, 575, A17

Indebetouw, R., Whitney, B. A., Johnson, K. E., & Wood, K. 2006, ApJ, 636, 362

Issa, M. R., MacLaren, I., & Wolfendale, A. W. 1990, A&A, 236, 237

Jarrett, T. H., Cohen, M., Masci, F., et al. 2011, ApJ, 735, 112

Jarrett, T. H., Masci, F., Tsai, C. W., et al. 2013, AJ, 145, 6

Jones, A. P. 2004, in Astronomical Society of the Pacific Conference Series, Vol. 309, Astrophysics of Dust, ed. A. N. Witt, G. C. Clayton, & B. T. Draine, 347

Jones, A. P., Fanciullo, L., Köhler, M., et al. 2013, A&A, 558, A62

Jonsson, P. 2006, MNRAS, 372, 2

Karczewski, O. Ł., Barlow, M. J., Page, M. J., et al. 2013, MNRAS, 431, 2493

Kaviraj, S., Ting, Y.-S., Bureau, M., et al. 2012, MNRAS, 423, 49

Keel, W. C., Manning, A. M., Holwerda, B. W., Lintott, C. J., & Schawinski, K. 2014, AJ, 147, 44

Kendall, M. & Gibbons, J. 1990, Rank correlation methods, A Charles Griffin Book (E. Arnold)

Kendall, M. G. 1938, Biometrika, 30, pp. 81

Kennicutt, R. C., Calzetti, D., Aniano, G., et al. 2011, PASP, 123, 1347

Kennicutt, R. C. & Evans, N. J. 2012, ARA&A, 50, 531

Kennicutt, Jr., R. C. 1998, ApJ, 498, 541

Kennicutt, Jr., R. C., Hao, C.-N., Calzetti, D., et al. 2009, ApJ, 703, 1672

Kirk, J. M., Gear, W. K., Fritz, J., et al. 2015, ApJ, 798, 58

Kirkpatrick, A., Pope, A., Alexander, D. M., et al. 2012, ApJ, 759, 139

Knapp, G. R., Guhathakurta, P., Kim, D.-W., & Jura, M. A. 1989, ApJS, 70, 329

Kobayashi, C. & Arimoto, N. 1999, ApJ, 527, 573

Köhler, M., Stepnik, B., Jones, A. P., et al. 2012, A&A, 548, A61

Koleva, M., Prugniel, P., de Rijcke, S., & Zeilinger, W. W. 2011, MNRAS, 417, 1643

Kong, X., Charlot, S., Brinchmann, J., & Fall, S. M. 2004, MNRAS, 349, 769

Koribalski, B. & Jerjen, H. 2008, Galaxies in the Local Volume, Astrophysics and Space Science Proceedings (Springer Netherlands)

Kroupa, P. 2001, MNRAS, 322, 231

Kulkarni, S., Sahu, D. K., Chaware, L., Chakradhari, N. K., & Pandey, S. K. 2014, New A, 30, 51

Kwok, S. & Zhang, Y. 2011, Nature, 479, 80

Kwok, S. & Zhang, Y. 2013, ApJ, 771, 5

Kylafis, N. D. & Bahcall, J. N. 1987, ApJ, 317, 637

Ladjal, D., Justtanont, K., Groenewegen, M. A. T., et al. 2010, A&A, 513, A53

Leeuw, L. L., Sansom, A. E., Robson, E. I., Haas, M., & Kuno, N. 2004, ApJ, 612, 837

Leroy, A. K., Walter, F., Brinks, E., et al. 2008, AJ, 136, 2782

Lewis, A. R., Dolphin, A. E., Dalcanton, J. J., et al. 2015, ApJ, 805, 183

Lisenfeld, U. & Ferrara, A. 1998, ApJ, 496, 145

Liu, G., Calzetti, D., Hong, S., et al. 2013, ApJ, 778, L41

Lutz, D. 2010, PACS photometer PSF, http://herschel.esac.esa.int/twiki/pub/Public/PacsCalibrationWeb/bolopsfv1.01.pdf

MacLachlan, J. M., Matthews, L. D., Wood, K., & Gallagher, J. S. 2011, ApJ, 741, 6

Madau, P. & Dickinson, M. 2014, ARA&A, 52, 415

Madden, S. C., Galliano, F., Jones, A. P., & Sauvage, M. 2006, A&A, 446, 877

Magrini, L., Bianchi, S., Corbelli, E., et al. 2011, A&A, 535, A13

Maraston, C. 2005, MNRAS, 362, 799

Martin, D. C., Fanson, J., Schiminovich, D., et al. 2005, ApJ, 619, L1

Matsuura, M., Dwek, E., Barlow, M. J., et al. 2015, ApJ, 800, 50

Mattsson, L., Gomez, H. L., Andersen, A. C., et al. 2014, MNRAS, 444, 797

McConnachie, A. W., Irwin, M. J., Ferguson, A. M. N., et al. 2005, MNRAS, 356, 979

Mentuch Cooper, E., Wilson, C. D., Foyle, K., et al. 2012, ApJ, 755, 165

Meurer, G. R., Heckman, T. M., & Calzetti, D. 1999, ApJ, 521, 64

Michałowski, M. J., Hayward, C. C., Dunlop, J. S., et al. 2014, A&A, 571, A75

Michard, R. 2005, A&A, 441, 451

Misiriotis, A. & Bianchi, S. 2002, A&A, 384, 866

Miville-Deschênes, M.-A. & Lagache, G. 2005, ApJS, 157, 302

Mo, H. J., Mao, S., & White, S. D. M. 1998, MNRAS, 295, 319

Möllenhoff, C., Popescu, C. C., & Tuffs, R. J. 2006, A&A, 456, 941

Montalto, M., Seitz, S., Riffeser, A., et al. 2009, A&A, 507, 283

Moorthy, B. K. & Holtzman, J. A. 2006, MNRAS, 371, 583

Morgan, H. L. & Edmunds, M. G. 2003, MNRAS, 343, 427

Morrissey, P., Conrow, T., Barlow, T. A., et al. 2007, ApJS, 173, 682

Muñoz-Mateos, J. C., Gil de Paz, A., Boissier, S., et al. 2009a, ApJ, 701, 1965

Muñoz-Mateos, J. C., Gil de Paz, A., Boissier, S., et al. 2007, ApJ, 658, 1006

Muñoz-Mateos, J. C., Gil de Paz, A., Zamorano, J., et al. 2009b, ApJ, 703, 1569

Murakami, H., Baba, H., Barthel, P., et al. 2007, PASJ, 59, 369

Murray, N. 2011, ApJ, 729, 133

Natale, G., Popescu, C. C., Tuffs, R. J., et al. 2015, MNRAS, 449, 243

Natale, G., Tuffs, R. J., Xu, C. K., et al. 2010, ApJ, 725, 955

Neugebauer, G., Habing, H. J., van Duinen, R., et al. 1984, ApJ, 278, L1

Noll, S., Burgarella, D., Giovannoli, E., et al. 2009, A&A, 507, 1793

Ormel, C. W., Paszun, D., Dominik, C., & Tielens, A. G. G. M. 2009, A&A, 502, 845

Ossenkopf, V. 1993, A&A, 280, 617

Ott, S. 2010, in ASP Conference Series, Vol. 434, Astronomical Data Analysis Software and Systems XIX, ed. Y. Mizumoto, K.-I. Morita, & M. Ohishi, 139

Pacifici, C., da Cunha, E., Charlot, S., et al. 2015, MNRAS, 447, 786

Padmanabhan, N., Schlegel, D. J., Finkbeiner, D. P., et al. 2008, ApJ, 674, 1217

Parkin, T. J., Wilson, C. D., Foyle, K., et al. 2012, MNRAS, 422, 2291

Pastrav, B. A., Popescu, C. C., Tuffs, R. J., & Sansom, A. E. 2013a, A&A, 553, A80

Pastrav, B. A., Popescu, C. C., Tuffs, R. J., & Sansom, A. E. 2013b, A&A, 557, A137

Patil, M. K., Pandey, S. K., Sahu, D. K., & Kembhavi, A. 2007, A&A, 461, 103

Peng, C. Y., Ho, L. C., Impey, C. D., & Rix, H.-W. 2010, AJ, 139, 2097

Pérez, E., Cid Fernandes, R., González Delgado, R. M., et al. 2013, ApJ, 764, L1

Petty, S. M., Neill, J. D., Jarrett, T. H., et al. 2013, AJ, 146, 77

Pierini, D., Gordon, K. D., Witt, A. N., & Madsen, G. J. 2004, ApJ, 617, 1022

Pilbratt, G. L., Riedinger, J. R., Passvogel, T., et al. 2010, A&A, 518, L1

Pinte, C., Harries, T. J., Min, M., et al. 2009, A&A, 498, 967

Planck Collaboration. 2011, A&A, 536, A1

Planck Collaboration. 2014, ArXiv: 1409.2495

Planck Collaboration. 2015, A&A, 582, A28

Pohlen, M., Cortese, L., Smith, M. W. L., et al. 2010, A&A, 518, L72

Popescu, C. C., Misiriotis, A., Kylafis, N. D., Tuffs, R. J., & Fischera, J. 2000, A&A, 362, 138

Popescu, C. C. & Tuffs, R. J. 2002, MNRAS, 335, L41

Popescu, C. C., Tuffs, R. J., Dopita, M. A., et al. 2011, A&A, 527, A109

Popescu, C. C., Tuffs, R. J., Völk, H. J., Pierini, D., & Madore, B. F. 2002, ApJ, 567, 221

Rahmani, S., Lianou, S., & Barmby, P. 2015, ArXiv: 1512.06675

Rampazzo, R., Annibali, F., Bressan, A., et al. 2005, A&A, 433, 497

Rémy-Ruyer, A., Madden, S. C., Galliano, F., et al. 2015, A&A, 582, A121

Richstone, D. & Sargent, W. L. W. 1972, ApJ, 176, 91

Rieke, G. H., Young, E. T., Engelbracht, C. W., et al. 2004, ApJS, 154, 25

Roussel, H. 2013, PASP, 125, 1126

Roussel, H., Wilson, C. D., Vigroux, L., et al. 2010, A&A, 518, L66

Rowan-Robinson, M., Roseboom, I. G., Vaccari, M., et al. 2010, MNRAS, 409, 2

Rowlands, K., Dunne, L., Dye, S., et al. 2014, MNRAS, 441, 1017

Rowlands, K., Dunne, L., Maddox, S., et al. 2012, MNRAS, 419, 2545

Saftly, W., Baes, M., & Camps, P. 2014, A&A, 561, A77

Saftly, W., Baes, M., De Geyter, G., et al. 2015, A&A, 576, A31

Saglia, R. P., Fabricius, M., Bender, R., et al. 2010, A&A, 509, A61

Salim, S., Charlot, S., Rich, R. M., et al. 2005, ApJ, 619, L39

Salim, S., Rich, R. M., Charlot, S., et al. 2007, ApJS, 173, 267

Salpeter, E. E. 1955, ApJ, 121, 161

Sandstrom, K. M., Leroy, A. K., Walter, F., et al. 2013, ApJ, 777, 5

Sarzi, M., Alatalo, K., Blitz, L., et al. 2013, MNRAS, 432, 1845

Schaye, J., Crain, R. A., Bower, R. G., et al. 2015, MNRAS, 446, 521

Schechtman-Rook, A., Bershady, M. A., & Wood, K. 2012, ApJ, 746, 70

Schiminovich, D., Wyder, T. K., Martin, D. C., et al. 2007, ApJS, 173, 315

Schmidt, M. 1959, ApJ, 129, 243

Schneider, R., Bianchi, S., Valiante, R., Risaliti, G., & Salvadori, S. 2015, A&A, 579, A60

Scoville, N., Aussel, H., Sheth, K., et al. 2014, ApJ, 783, 84

Serra, P., Amblard, A., Temi, P., et al. 2011, ApJ, 740, 22

Serra Díaz-Cano, L. & Jones, A. P. 2008, A&A, 492, 127

Sérsic, J. L. 1963, Boletin de la Asociacion Argentina de Astronomia La Plata Argentina, 6, 41

Sheth, K., Regan, M., Hinz, J. L., et al. 2010, PASP, 122, 1397

Shinn, J.-H. & Seon, K.-I. 2015, ApJ, 815, 133

Sick, J., Courteau, S., Cuillandre, J.-C., et al. 2014, AJ, 147, 109

Silva, L., Schurer, A., Granato, G. L., et al. 2011, MNRAS, 410, 2043

Skibba, R. A., Engelbracht, C. W., Dale, D., et al. 2011, ApJ, 738, 89

Skrutskie, M. F., Cutri, R. M., Stiening, R., et al. 2006, AJ, 131, 1163

Smith, D. J. B., Dunne, L., da Cunha, E., et al. 2012a, MNRAS, 427, 703

Smith, D. J. B., Dunne, L., da Cunha, E., et al. 2012b, MNRAS, 427, 703

Smith, D. J. B. & Hayward, C. C. 2015, MNRAS, 453, 1597

Smith, J. D. T., Draine, B. T., Dale, D. A., et al. 2007, ApJ, 656, 770

Smith, M. W. L., Eales, S. A., Gomez, H. L., et al. 2012c, ApJ, 756, 40

Smith, M. W. L., Gomez, H. L., Eales, S. A., et al. 2012d, ApJ, 748, 123

Sodroski, T. J., Odegard, N., Arendt, R. G., et al. 1997, ApJ, 480, 173

Soifer, B. T. & Neugebauer, G. 1991, AJ, 101, 354

Soifer, B. T., Sanders, D. B., Madore, B. F., et al. 1987, ApJ, 320, 238

Speagle, J. S., Steinhardt, C. L., Capak, P. L., & Silverman, J. D. 2014, ApJS, 214, 15

Steinacker, J., Bacmann, A., & Henning, T. 2006, ApJ, 645, 920

Steinacker, J., Baes, M., & Gordon, K. D. 2013, ARA&A, 51, 63

Stepnik, B., Abergel, A., Bernard, J.-P., et al. 2003, A&A, 398, 551

Tabatabaei, F. S. & Berkhuijsen, E. M. 2010, A&A, 517, A77

Tabatabaei, F. S., Braine, J., Xilouris, E. M., et al. 2014, A&A, 561, A95

Tamm, A., Tempel, E., Tenjes, P., Tihhonova, O., & Tuvikene, T. 2012, A&A, 546, A4

Temi, P., Brighenti, F., & Mathews, W. G. 2007, ApJ, 660, 1215

Temi, P., Brighenti, F., Mathews, W. G., & Bregman, J. D. 2004, ApJS, 151, 237

Tempel, E., Tamm, A., & Tenjes, P. 2010, A&A, 509, A91

Tempel, E., Tuvikene, T., Tamm, A., & Tenjes, P. 2011, A&A, 526, A155

Thilker, D. A., Hoopes, C. G., Bianchi, L., et al. 2005, ApJ, 619, L67

Tielens, A. G. G. M. 2008, ARA&A, 46, 289

Tielens, A. G. G. M., Waters, L. B. F. M., & Bernatowicz, T. J. 2005, in ASP Conference Series, Vol. 341, Chondrites and the Protoplanetary Disk, ed. A. N. Krot, E. R. D. Scott, & B. Reipurth, 605

Todini, P. & Ferrara, A. 2001, MNRAS, 325, 726

Tran, H. D., Tsvetanov, Z., Ford, H. C., et al. 2001, AJ, 121, 2928

Tuffs, R. J., Popescu, C. C., Völk, H. J., Kylafis, N. D., & Dopita, M. A. 2004, A&A, 419, 821

van Dokkum, P. G. & Franx, M. 1995, AJ, 110, 2027

Vanderbeke, J., Baes, M., Romanowsky, A. J., & Schmidtobreick, L. 2011, MNRAS, 412, 2017

Városi, F. & Dwek, E. 1999, ApJ, 523, 265

Verstappen, J., Fritz, J., Baes, M., et al. 2013, A&A, 556, A54

Viaene, S., Baes, M., Bendo, G., et al. 2016, A&A, 586, A13

Viaene, S., De Geyter, G., Baes, M., et al. 2015, A&A, 579, A103

Viaene, S., Fritz, J., Baes, M., et al. 2014, A&A, 567, A71

Vidali, G., Roser, J. E., Manicò, G., & Pirronello, V. 2004, Advances in Space Research, 33, 6

Vika, M., Bamford, S. P., Häußler, B., et al. 2013, MNRAS, 435, 623

Walcher, J., Groves, B., Budavári, T., & Dale, D. 2011, Ap&SS, 331, 1

Walterbos, R. A. M. & Schwering, P. B. W. 1987, A&A, 180, 27

Wang, B. & Heckman, T. M. 1996, ApJ, 457, 645

Watson, W. D. 1972, ApJ, 176, 103

Weingartner, J. C. & Draine, B. T. 2001, ApJ, 548, 296

Werner, M. W., Roellig, T. L., Low, F. J., et al. 2004, ApJS, 154, 1

Whelan, D. G., Johnson, K. E., Whitney, B. A., Indebetouw, R., & Wood, K. 2011, ApJ, 729, 111

White, S. D. M. & Frenk, C. S. 1991, ApJ, 379, 52

Wild, V., Charlot, S., Brinchmann, J., et al. 2011, MNRAS, 417, 1760

Wilson, C. D., Cridland, A., Foyle, K., et al. 2013, ApJ, 776, L30

Wise, M. W. & Silva, D. R. 1996, ApJ, 461, 155

Witt, A. N. & Gordon, K. D. 1996, ApJ, 463, 681

Witt, A. N. & Gordon, K. D. 2000, ApJ, 528, 799

Witt, A. N., Thronson, Jr., H. A., & Capuano, Jr., J. M. 1992, ApJ, 393, 611

Wright, E. L., Eisenhardt, P. R. M., Mainzer, A. K., et al. 2010, AJ, 140, 1868

Wu, H., Zhu, Y.-N., Cao, C., & Qin, B. 2007, ApJ, 668, 87

Xilouris, E. M., Byun, Y. I., Kylafis, N. D., Paleologou, E. V., & Papamastorakis, J. 1999, A&A, 344, 868

Xilouris, E. M., Kylafis, N. D., Papamastorakis, J., Paleologou, E. V., & Haerendel, G. 1997, A&A, 325, 135

Xilouris, E. M., Madden, S. C., Galliano, F., Vigroux, L., & Sauvage, M. 2004, A&A, 416, 41

Xu, C. & Buat, V. 1995, A&A, 293, L65

York, D. G., Adelman, J., Anderson, Jr., J. E., et al. 2000, AJ, 120, 1579

Young, J. S., Xie, S., Kenney, J. D. P., & Rice, W. L. 1989, ApJS, 70, 699

Young, L. M., Bureau, M., Davis, T. A., et al. 2011, MNRAS, 414, 940

Ysard, N., Abergel, A., Ristorcelli, I., et al. 2013, A&A, 559, A133

Ysard, N., Köhler, M., Jones, A., et al. 2015, A&A, 577, A110

Zacharias, N., Monet, D. G., Levine, S. E., et al. 2004, in Bulletin of the American Astronomical Society, Vol. 36, American Astronomical Society Meeting Abstracts, 1418

Zubko, V., Dwek, E., & Arendt, R. G. 2004, ApJS, 152, 211

Zubko, V. G. & Laor, A. 2000, ApJS, 128, 245